Report No. 171 / UILU ENG-95-4048

An Active-Path-Dissolution Model for Corrosion-Fatigue Cracking of Drill-Pipe Steels in Offshore-Drilling Environments

by

Hung-Yuan Hsieh
and
F. V. Lawrence
Civil Engineering

A report of
MATERIALS ENGINEERING — MECHANICAL BEHAVIOR
College of Engineering, University of Illinois at Urbana-Champaign
October 1995

AN ACTIVE-PATH-DISSOLUTION MODEL FOR CORROSION-FATIGUE CRACKING OF DRILL-PIPE STEELS IN OFFSHORE-DRILLING ENVIRONMENTS

ABSTRACT

The corrosion-fatigue life of drill-pipe steels in simulated offshore-drilling environments was predicted using an analytical model. This model, named the Active-Path-Dissolution (APD) model, simulates a sequence of three corrosion-fatigue processes: chemical notching process, microcrack development, and macroscopic crack growth. The first two processes are combined with mechanical fatigue to simulate corrosion-fatigue crack initiation. A series of fatigue-life simulations for a variety of corrosion-fatigue conditions were carried out. The effects of fluid aeration, electrolytic conductivity (η), electrochemical potential (E_{bulk}), mean stress and stress ratio (R) effects, fluid temperatures (T), material yield strengths (S_y), pre-existing notch (K_t) effects, and test frequencies (f) were studied to provide data to validate the predictions of the APD model. Experience with the APD model suggests that microcrack development is the dominant period in the corrosion-fatigue life.

The APD model partitioning of the corrosion-fatigue cracking into three processes was confirmed by observations of the electrochemical potential (E_{bulk}) and displacement (Δe) during corrosion-fatigue tests. Observations of current/potential transient phenomena under various waveforms of cyclic loading corroborated that film rupture/film formation induced active-path dissolution is responsible for promoting crack initiation. The SEM micrographs of crack-initiation sites on fractured surfaces provided evidence suggesting the occurrence of vigorous anodic dissolution and galvanic coupling effect within a crack, particularly when the crack size is in microscopic level. The corrosion rate (Tafel's behavior) and corrosion-fatigue resistance of an API-S135 drill-pipe steel were also studied experimentally in a simulated offshore drilling environment to verify the proposed APD model. No effect of fluid aeration or the addition of a polymeric inhibitor on the corrosion-fatigue system investigated was observed.

Comparison of experimental results with the APD model simulations showed satisfactory agreement. Both the APD model and the experimental results suggest that altering the electrochemical potential (E_{bulk}) by impressing current or by galvanic coupling with Ion-Vapor-Deposited (IVD) aluminum is an effective and practical means of controlling the corrosion-fatigue phenomenon.

ACKNOWLEDGMENTS

I would like to express my sincere gratitude to Professor Frederick V. Lawrence, Jr. for providing support, inspiration and patient guidance throughout the course of this study.

Special thanks to Dr. James D. Burk in Amoco Research Center for donating fatigue specimens and providing technical assistance. Thanks to Mr. Willie Vasquez in M-I Drilling Fluid Company for donating drilling-fluid components. Thanks to Mr. Mel Faul in Titanium Finishing Company for providing free technical support on the ion-vapor-deposition (IVD) process of aluminum plating.

The invaluable input and assistance from faculty and staff members during the period of author's graduate studies at the University of Illinois are also sincerely acknowledged. Thanks to Professor Ralph G. Nuzzo, Professor Darrell F. Socie, and Professor Leslie J. Struble for serving as committee members and for their invaluable advice. Thanks are extended to Dr. Peter Kurath for his expert assistance in setting up and maintaining the hydraulic equipment; and to Mr. Frederick Rottet for developing and assisting data acquisition. Generous support from Prof. Gerald P. Wirtz, Prof. Carl J. Altstetter, and from Mr. John Bukowski in the Center for Cement Composite Materials for lending test equipment are all acknowledged. Comments and advice from Dr. Ellen G. Segan in Construction Engineering Research Laboratory (CERL) on the electrochemical experiments are appreciated.

I also wish to express my appreciation to my colleagues: Dr. Grzegorz Banas, Dr. C.-Y. Hou, and Dr. Gary T. Fry. Their encouragement during author's difficulties in building the experimental setup is greatly appreciated. Thanks are also extended to Mr. Stamati D. Dimitrakis, Ms. Nong Chen, Ms. Wei Liu and Mr. Z.-H. Zhang for their help in preparing this thesis.

So many thanks to my friends in this campus and to my family members in Taiwan for their uninterrupted encouragement throughout my graduate studies at the UIUC.

This research was supported by the Fracture Control Program (FCP) at the University of Illinois at Urbana-Champaign. This work was also partially supported by the Amoco Research Center through the FCP.

TABLE OF CONTENTS

CHAPTER I: INTRODUCTION 1

1.1 BACKGROUND 1

1.2 THE PROBLEM 1

1.3 OBJECTIVE AND SCOPE 2

1.4 THESIS ORGANIZATION 2

CHAPTER II: LITERATURE REVIEW 4

2.1 ENVIRONMENTAL (AQUEOUS) EFFECTS ON FATIGUE 4

2.2 MECHANISMS OF CORROSION-FATIGUE CRACK INITIATION 4

2.2.1 General 4
2.2.2 Pitting Mechanism on Crack Initiation 5
2.2.3 Hydrogen Embrittlement on Crack Initiation 5
2.2.4 Slip Dissolution/Preferential Dissolution on Crack Initiation 7

2.3 MECHANISMS OF CORROSION-FATIGUE CRACK GROWTH 7

2.3.1 General 7
2.3.2 Transport/Adsorption Phenomena and Local Crack Environments 8
2.3.3 Anodic Dissolution/Film Rupture Mechanism on Crack Growth 8
2.3.4 Hydrogen Embrittlement on Crack Growth 9

2.4 CORROSION-FATIGUE LIFE OF STRUCTURAL STEELS IN SALINE AQUEOUS ENVIRONMENTS 9

2.4.1 General 9
2.4.2 Effects of Strength and Microstructure 9
2.4.3 Effects of Stress Amplitude ($\Delta S/2$) and Stress Ratio (R) 10
2.4.4 Effects of Test Frequency (f) 10
2.4.5 Effects of Loading Waveform 10
2.4.6 Effects of Environmental Variables 11
2.4.7 Effects of Cathodic Protection 12

2.5 CORROSION-FATIGUE CRACK GROWTH OF STRUCTURAL STEELS IN SALINE AQUEOUS ENVIRONMENTS 13

2.5.1 Effects of Strength and Microstructure 13
2.5.2 Time-Dependent Process of Corrosion-Fatigue Crack Growth 13
2.5.3 Effects of Stress-Intensity-Factor Range (ΔK) 13
2.5.4 Effects of Stress Ratio (R) 14
2.5.5 Effects of Test Frequency (f) 14
2.5.6 Effects of Loading Waveform 15
2.5.7 Effects of Environmental Variables 15
2.5.8 Effects of Cathodic Protection 17

2.6 MATHEMATICAL MODELS OF CORROSION FATIGUE 17

2.6.1 General Aspects on Modeling Corrosion-Fatigue Cracking 17
2.6.2 Models for Corrosion-Fatigue Crack Initiation 17
2.6.3 Models for Corrosion-Fatigue Crack Growth 18

2.7 SUMMARY 18

CHAPTER III: DEVELOPMENT OF THE ACTIVE-PATH-DISSOLUTION (APD) MODEL 20

3.1 EXPERIMENTAL OBSERVATIONS OF CORROSION-FATIGUE-LIFE PARTITIONING 20

3.1.1 General Consideration 20
3.1.2 Electrochemical Observations on Chemical Notching 20
3.1.3 Electrochemical Observations on Microcrack Development 21
3.1.4 Electrochemical Observations on Macroscopic Crack Growth 21

3.2 MAJOR MODELING (APD) ASSUMPTIONS 21

3.2.1 Modeling the Three CFC Processes 21
3.2.2 Modeling Total Corrosion-Fatigue Life (N_T) 22

3.3 MODELING (STAGE I) CHEMICAL-NOTCHING PROCESS (N_{pit}) 22

3.3.1 Overview and Major Assumptions 22
3.3.2 Simulating the Cyclic-Strain-Induced Chemical-Notching Process 23
3.3.3 Determining the Critical Depth (a_{pit}) of Chemical Notch 24

3.4 MODELING (STAGE I) MICROCRACK DEVELOPMENT (N_{p1}) 26

3.4.1 Overview and Major Assumptions 26
3.4.2 Modeling the Rate of Microcrack Development 26
3.4.3 Modeling Film Rupture/Film Formation Development of Microcracks 27
3.4.4 The Current-Density-Decay Exponent (λ) 28
3.4.5 Simulating the Fatigue-Life Period of Microcrack Development (N_{p1}) 29

3.5 SIMULATING SYNERGISTIC ELECTROCHEMICAL-MECHANICAL INTERACTIONS FOR MODELING CRACK-INITIATION LIFE (N_i) 30

3.6 MODELING (STAGE II) MACROSCOPIC CRACK GROWTH (N_{p2}) 31

3.7 VARIABLES IN THE APD MODEL 31

CHAPTER IV: EXPERIMENTAL METHODOLOGY 33

4.1 PURPOSE 33

4.2 MATERIALS 33

4.3 FATIGUE TESTS UNDER FREE CORROSION 34

4.3.1 Specimen Preparation 34
4.3.2 Environmental Conditioning 34
4.3.3 Monitoring Devices 35
4.3.4 Testing Procedures 35

4.4 FATIGUE TESTS UNDER POTENTIAL CONTROL OR CATHODIC PROTECTION..... 35

4.4.1 Fatigue Tests under Potential Control..... 35
4.4.2 Preparation of Aluminum-Plated (IVD-Al) Specimens..... 36
4.4.3 Fatigue Tests of IVD-Al Plated Specimens..... 37

4.5 POTENTIODYNAMIC POLARIZATION SCANS..... 37

4.5.1 Preparation of Disk Electrodes..... 37
4.5.2 Potentiodynamic Polarization Scan on Disk Electrodes..... 37
4.5.3 Potentiodynamic Polarization Scan on Straining Electrodes..... 38
4.5.4 Hysteresis Polarization Scan on Disk Electrodes..... 38
4.5.5 Hysteresis Polarization Scan on Straining Electrodes..... 39

4.6 MONITORING OF CURRENT/POTENTIAL TRANSIENT PHENOMENA..... 39

4.6.1 Purpose..... 39
4.6.2 Specimen Preparation..... 40
4.6.3 Experimental Procedures..... 40

4.7 FRACTURE SURFACE ANALYSIS..... 40

4.7.1 Sample Preparation..... 40
4.7.2 Crack Initiation Sites and Fracture Surfaces..... 41

CHAPTER V: EXPERIMENTAL VERIFICATION OF THE APD MODEL..... 42

5.1 GENERAL: MATERIAL PROPERTIES AND ELECTROCHEMICAL PARAMETERS USED IN THE APD MODEL SIMULATIONS..... 42

5.2 VERIFICATION: EFFECTS OF FLUID AERATION..... 43

5.2.1 Effects of Fluid Aeration on the Corrosion Rate (Tafel's Behavior)..... 43
5.2.2 Effects of Fluid Aeration on the Corrosion-Fatigue Life..... 43

5.3 VERIFICATION: EFFECTS OF ELECTROLYTIC CONDUCTIVITY (η) ON THE CORROSION-FATIGUE LIFE..... 43

5.4 VERIFICATION: EFFECTS OF ELECTROCHEMICAL POTENTIAL (E_{bulk}) ON THE CORROSION-FATIGUE LIFE..... 44

5.4.1 Controlled Potential by Potentiostat..... 44
5.4.2 Controlled Potential by Galvanic Coupling with Aluminum..... 44

5.5 VERIFICATION: EFFECTS OF STRESS RATIO (R) OR MEAN STRESS ON THE CORROSION-FATIGUE LIFE..... 44

5.6 VERIFICATION: EFFECTS OF TEMPERATURE (T)..... 45

5.6.1 Effects of Temperature (T) on the General Corrosion Rate (Tafel's Behavior)..... 45
5.6.2 Effects of Temperature (T) on the Stress-Corrosion Rate..... 45
5.6.3 Effects of Temperature (T) on the Corrosion-Fatigue Life..... 45

5.7 VERIFICATION: EFFECTS OF MATERIAL STRENGTH (S_y) ON THE CORROSION-FATIGUE LIFE..... 45

5.8 VERIFICATION: EFFECTS OF PRE-EXISTING NOTCHES (K_t) ON THE CORROSION-FATIGUE LIFE 46

5.9 VERIFICATION: EFFECTS OF LOADING RATE AND TEST FREQUENCY (f) ON THE CORROSION FATIGUE 46

5.9.1 Effects of Loading Rate on Current-Density Transients (Trapezoidal Wave) 46
5.9.2 Effects of Test Frequency (f) on Current-Density Transients (Sinusoidal Wave) 47
5.9.3 Effects of Test Frequency (f) on the Corrosion-Fatigue Life 47

5.10 VERIFICATION: EFFECTS OF MACROSCOPIC CRACK-GROWTH LIFE (N_{p2}) 47

5.11 VERIFICATION: EFFECTS OF ELECTROCHEMICAL DISSOLUTION ON CRACK INITIATION AND GROWTH 48

5.11.1 Appearance of Chemical Notches 48
5.11.2 Appearance of Crack Surfaces on Crack-Initiation Sites 48
5.11.3 Appearance of Macroscopic Crack-Growth Regime 49
5.11.4 Summary of Microscopic Observations 49

CHAPTER VI: DISCUSSION 50

6.1 SUMMARY OF THE INVESTIGATED VARIABLES 50

6.2 OBSERVED AND PREDICTED EFFECTS OF FLUID AERATION 50

6.2.1 Effects of Fluid Aeration on the Corrosion Rate 50
6.2.2 Effects of Fluid Aeration on the Corrosion-Fatigue Life 51
6.2.3 Effects of Fluid Aeration on the Macroscopic Crack Growth 51

6.3 OBSERVED AND PREDICTED EFFECTS OF POLYMERIC INHIBITOR 51

6.3.1 Effects of Polymeric Inhibitor on the Corrosion-Fatigue Life 51
6.3.2 Effects of Polymeric Inhibitor on the Corrosion Inhibition 52
6.3.3 Effects of Polymeric Inhibitor on the Chemical-Notching Characteristics 52

6.4 OBSERVED AND PREDICTED EFFECTS OF ELECTROCHEMICAL POTENTIAL (E_{bulk}) 53

6.4.1 Relationship between the Corrosion Rate and the Corrosion-Fatigue Life 53
6.4.2 Effects of Cathodic Protection on the Corrosion-Fatigue Life 53
6.4.3 Effects of Galvanic Protection on the Corrosion-Fatigue Life 54

6.5 REPORTED AND PREDICTED EFFECTS OF STRESS RATIO (R) AND APPLIED MEAN STRESS 54

6.6 OBSERVED, REPORTED, AND PREDICTED EFFECTS OF TEMPERATURE (T) 55

6.6.1 Effects of Temperature (T) on the General-Corrosion Rate 55
6.6.2 Effects of Temperature (T) on the Stress-Corrosion Rate 56
6.6.3 Effects of Temperature (T) on the Corrosion-Fatigue Life 56

6.7 REPORTED AND PREDICTED EFFECTS OF MATERIAL STRENGTH (S_y) 57

6.8 REPORTED AND PREDICTED EFFECTS OF PRE-EXISTING NOTCHES (K_t) 58

6.9 OBSERVED EFFECTS OF CURRENT/POTENTIAL TRANSIENT PHENOMENA 58

6.9.1 Significance of the Electrochemical-Potential Transients 58
6.9.2 Significance of the Anodic Current-Density Transients 59
6.9.3 Effects of Waveform and Frequency (f) on the Anodic Current-Density Transients 60
6.9.4 Significance of the Cathodic Current-Density Transients 60

6.10 REPORTED AND PREDICTED EFFECTS OF TEST FREQUENCY (f) 60

6.11 OBSERVED AND PREDICTED MACROSCOPIC CRACK-GROWTH LIFE (N_{p2}) 61

6.11.1 Implication from Microscopic Observations on Fracture Surfaces 61
6.11.2 Macroscopic Crack-Growth Life (N_{p2}) 61

6.12 PREDICTIVE ABILITY OF THE APD MODEL 62

6.12.1 The APD Model Simulations on Electrolytic Conductivity (η) and Fluid Aeration 62
6.12.2 The APD Model Simulations on Electrochemical Potential (E_{bulk}) 62
6.12.3 The APD Model Simulations on Material Strength (S_y) 63
6.12.4 The APD Model Simulations on Pre-existing Notches (K_t) 63
6.12.5 The APD Model Simulations on Temperature (T) and Test Frequency (f) 64

6.13 JUSTIFICATION FOR NEGLECTING CORROSION-PRODUCT-INDUCED CRACK CLOSURE IN THE APD MODEL 64

CHAPTER VII: SUMMARY, CONCLUSIONS, AND SUGGESTED FUTURE WORK 66

7.1 SUMMARY 66

7.2 CONCLUSIONS: EXPERIMENTAL OBSERVATIONS 66

7.3 CONCLUSIONS: THE APD MODEL SIMULATIONS 67

7.4 SUGGESTED FUTURE WORK 67

TABLES 69

FIGURES 78

APPENDIX A: CYCLIC-STRAIN-INDUCED CHEMICAL-NOTCHING KINETICS 145

A.1 STRAINING INDUCED SWEEPING POTENTIAL 145

A.2 TRANSIENT LOCALIZED ELECTROCHEMICAL DISSOLUTION 146

A.3 DIFFUSION LIMITED MASS TRANSFER 147

APPENDIX B: COMPUTATION OF BARE-CRACK-TIP CURRENT DENSITY 152

B.1 MICRO-GALVANIC COUPLING AND ELECTROMIGRATION CONTINUITY 152

B.2 SALT-FILM OHMIC DROP AND CRACK-MOUTH POTENTIAL 155

APPENDIX C: DEGREE OF CFC SATURATION FOR CORROSION-ASSISTED MICROCRACK DEVELOPMENT 162

C.1 GENERAL 162

C.2 MAXIMUM SURFACE AREA OF CRACK-TIP ACTIVE SITES (θ_{max}) AT PEAK LOAD 162

C.3 SATURATED DIMINISHING PROCESS OF CRACK-TIP ACTIVE SITES 163

C.4 PARTIALLY-SATURATED DIMINISHING PROCESS OF CRACK-TIP ACTIVE SITES 164

C.5 DEGREE OF CFC SATURATION (φ) 165

APPENDIX D: COMPUTATION OF SALT-FILM OHMIC-DROP COEFFICIENTS 169

D.1 BACKGROUND 169

D.2 SALT-FILM OHMIC-DROP COEFFICIENTS 170

REFERENCES 172

LIST OF SYMBOLS

a	Notch depth or crack length (mm)
a_f	Final crack length for LEFM integration (mm)
a_i	Initial crack length for LEFM integration (mm)
a_n	Maximum tolerable defect size without damaging fatigue limit (mm)
a_{pit}	Depth of a chemical notch (mm)
A	Empirical coefficient for intrinsic reaction-rate constant
b'	Fatigue strength exponent
B	Empirical exponent for intrinsic reaction-rate constant
c	Notch diameter (mm)
c'	Fatigue ductility exponent
C	Paris constant (mm/cycle)
C_{M^+}, C'_{M^+}	Metal ion concentration in the vicinity of a static (filmed), and of a strained (unfilmed) electrode (mole/cm^3)
$C^s_{M^+}$	Saturation limit of metal ions in a given electrolyte (mole/cm^3)
$(da/dN)_{me}$	Crack growth rate of purely mechanical fatigue (mm/cycle)
$(da/dN)_{cfc}$	Crack growth rate of purely corrosion fatigue (mm/cycle)
$(da/dN)_{pit}$	Chemical notching rate (mm/cycle)
$(da/dN)_{p1}$	Rate of microcrack development (mm/cycle)
$(da/dN)_{p2}$	Rate of macroscopic crack growth (mm/cycle)
$(da/dN)_{scc}$	Crack growth rate of stress-corrosion cracking (mm/cycle)
$(da/dN)_T$	Total fatigue-crack growth rate (mm/cycle)
D	Diffusion coefficient of dissolving metal ions (cm^2/sec)
E	Electrochemical potential at position x in a chemical notch
E_{bulk}	Electrochemical potential of an electrode in bulk electrolyte (V)
E_{cm}	Electrochemical potential at crack mouth (V)
E_{corr}, E'_{corr}	Free-corrosion potential of a static (filmed), and of an strained (unfilmed) electrode (V)
E_{eq}, E'_{eq}	Redox potential of an anodic dissolution on a static (filmed), and on a strained (unfilmed) electrode (V)
E^a_{eq}, E^c_{eq}	Redox potential of an anodic dissolution, and of a cathodic reduction (V)
E^o	Redox potential of a redox couple on a static electrode at its standard state (V)
E_{Ref}	Reference free-corrosion potential (mV)

E_{tip}	Electrochemical potential at crack tip (V)
E_x	Electrochemical potential at crack depth x (V)
E_Ω	Salt-film ohmic-drop coefficient (V)
f	Test frequency (Hz)
F	Faraday's constant (coulomb/mole)
i_a, i_c	Anodic, and cathodic current density (A/cm^2)
i_{bare}	Bare-crack-tip current density (A/cm^2)
i_{corr}, i'_{corr}	Free-corrosion rate of a static (filmed), and of a strained (unfilmed) electrode (A/cm^2)
i_o^{pass}	Exchange current density of a cathodic reduction on passivated crack faces (A/cm^2)
$i_o^{plastic}$	Exchange current density of an anodic dissolution on plastically-deformed crack tips (A/cm^2)
i_{out}	Outcome current density at salt film/bulk solution interface (A/cm^2)
i_{Ref}	Reference current density (μA/cm^2)
i(t)	Trace of chemical-notching current density (A/cm^2)
$i_{rp}(t)$	Trace of dissolution-current density at crack tips after film rupture (A/cm^2)
$i^*(N)$, $i^*(t)$	Transient peak-current density of chemical notching (A/cm^2)
I_a	Anodic current flow (A/cm)
J(x)	Dissolving metal ion flux (mole/cm^2 sec)
K_f	Fatigue-notch factor
K_t	Stress-concentration factor
K_{Imax}	Maximum mode I stress-intensity factor (MPa $\sqrt{m}$)
K_{Iscc}	Onset stress-intensity factor of stress-corrosion cracking (MPa $\sqrt{m}$)
K'	Cyclic strength coefficient (MPa)
L_o	Intrinsic crack length (mm)
m	Paris exponent
M	Atomic weight of material (g/mole)
n'	Cyclic strain-hardening exponent
N	Number of fatigue cycles (cycles)
N_f	Fatigue life to failure (cycles)
N_i	Crack-initiation life for initiating a macroscopic crack (cycles)
N_{pit}	Fatigue cycles to produce a chemical notch of given depth (cycles)
N_{p1}	Fatigue cycles of microcrack development (cycles)
N_{p2}	Fatigue cycles of macroscopic crack growth (cycles)

N_{st}	Crack-initiation life based on strain-life approach (cycles)
N_T	Total fatigue life predicted by the APD model simulation
Q	Accumulated charge density transferred per cycle (coulomb/cm^2)
R	Stress ratio of fatigue loading
R'	Gas constant (joule/mole °K)
R_{film}	Electrolytic resistance of salt film (Ω m)
S_{max}, S_{min}	Maximum, and minimum remote applied stress (MPa)
S_u	Ultimate tensile strength of material (MPa)
S_y	Yield strength of material (0.2% offset) (MPa)
t	Time (sec)
t_c	Characteristic period from the onset of unloading to the complete disappearance of crack-tip active sites (sec)
$t_{descend}$	Stress-descending period within a trapezoidal wave (sec)
t_{hold}	Maximum-stress-holding period within a trapezoidal wave (sec)
t_{rest}	Minimum-stress-resting period within a trapezoidal wave (sec)
t_{rise}	Stress-rising period within a trapezoidal wave (sec)
T	Fluid temperature (°K)
v	Sweeping velocity of redox potential under cyclic loading (V/sec)
w	Distance from an electrode where electrochemical potential was measured (cm)
x	Depth of a microcrack from crack mouth (mm)
Y(a,c)	Geometry factor
z	Valence of dissolving cations
α	Constraint factor for a plane strain condition
β_a, β_c	Tafel's slope of anodic polarization, and of cathodic polarization
χ	Elastic modulus of material (MPa)
δ	Crack-tip opening displacement (m)
δ_{max}	Crack-tip opening displacement at maximum applied stress (m)
$\dot{\delta}_{tip}$	Crack-tip opening rate (m/sec)
Δe	Displacement range during cyclic loading (μm)
ΔH_a	Apparent activation energy (KJ/mole)
ΔK	Stress-intensity-factor range (MPa $\sqrt{m}$)
ΔK_{th}	Threshold stress-intensity-factor range of crack growth (MPa $\sqrt{m}$)
ΔS	Applied stress range (MPa)
$\Delta S/2$	Applied stress amplitude (MPa)
ΔS_e	Fatigue limit (stress range) in ambient air (MPa)

Δt	Time increment (sec)
ϕ	Symmetry factor
η	Electrolytic conductivity of unit crack opening ($\Omega^{-1}m^{-1}$)
φ	Degree of CFC saturation
λ	Current-density-decay exponent
λ_o	Intrinsic reaction-rate constant
μ	Proportional constant between active-site generation and crack-tip opening displacement
ν	Flushing rate of electrolyte (cm/sec)
θ_{max}	Maximum surface area of crack-tip active sites (cm^2)
$\theta(t)$	Trace of crack-tip active area (cm^2)
$\theta^u(t)$, $\theta^u{}_{sat}(t)$	Trace of crack-tip active area under a reversible slip (partially saturated CFC), and under a fully irreversible slip (saturated CFC) during unloading reversal (cm^2)
Θ, Θ_{sat}	Integrated surface area of crack-tip active sites under a reversible slip (partially saturated CFC), and under a fully irreversible slip (saturated CFC) accumulated during unloading reversal (cm^2)
ρ	Density of material (g/cm^3)
σ_{yc}	Cyclic yield strength of material (MPa)
τ	Thickness of diffusion buffer (salt film) (cm)

LIST OF ABBREVIATIONS

APD	Active-Path-Dissolution model
CFC	Corrosion-Fatigue Cracking
EDXA	Energy Dispersive X-ray Analyzer
I-P	Initiation-Propagation fatigue-life model
IVD-Al	Ion-Vapor-Deposited Aluminum plating
LEFM	Linear Elastic Fracture Mechanics
$NaCl_{aq}$	NaCl aqueous solution
PSB	Persistent Slip Band
SCC	Stress-Corrosion Cracking
SCE	Saturated Calomel Electrode
SEM	Scanning Electron Microscope
S-N	Stress-life behavior
UHP	Ultra-High Purity

CHAPTER I: INTRODUCTION

1.1 BACKGROUND

The effect of corrosive environments on fatigue life has been the subject of many experimental investigations. However, describing analytically the fatigue-life reduction due to Corrosion-Fatigue Cracking (CFC) has met with only limited success. Many conflicting observations have been made because, in general, corrosion-fatigue cracking (CFC) is not driven by a single mechanism. Moreover, the mechanisms driving crack initiation might not be the same as that for crack growth. This complex situation makes the corrosion-fatigue life generally unpredictable. However, the difficulty of modeling CFC analytically is reduced if only a single corrosion-fatigue mechanism is operative: this may be the case for the problem considered in this study.

1.2 THE PROBLEM

In offshore drilling application, a drill-pipe steel (e.g., API-S135, see Fig. 1.1) is cyclically strained in a hot, viscous and slow-flowing electrolyte (seawater drilling fluid) containing halide salts. The temperature of the drill pipe increases with the drill-hole depth and approaches the boiling point (at atmospheric pressure) of the drilling fluid. The drilling fluid (a mixture of seawater, rock debris and drilling compounds) circulating within the drilling pipe is so viscous that homogenization of acidified crack solution (due to cation hydrolysis) inside existing microcrevices in the drill pipes with bulk solution probably is not achieved. The elevated solution temperature, the high halide salinity[1], and the low crevice pH all prohibit the formation of rigid oxides at crack tips and thus suppress the development of substantial crack closure which would retard developing cracks. All of the above crack-tip conditions, on the other hand, tend to promote active-path-dissolution (APD) crack initiation in which a localized, preferential dissolution of unfilmed high-stress sites is the dominant mechanism in accelerating the initiation of fatigue cracks.

It is thus postulated that one single mechanism, film rupture/film formation induced active-path dissolution (in addition to mechanical fatigue), can successfully describe the corrosion-fatigue-crack initiation processes of drill-pipe steels during offshore drilling operations.

---

[1] The process of cation hydrolysis increases both the concentration of hydrogen ion (pH) and of chloride ion.

1.3 OBJECTIVE AND SCOPE

The objectives of this study are to develop an analytical model (the Active-Path-Dissolution (APD) model) for corrosion-fatigue crack initiation under anodic dissolution, and to verify the fatigue-life predictions of this model with the experimental results of a drill-pipe steel (API-S135) tested in a simulated offshore-drilling environment. Using the APD model, the effects of fluid aeration, electrolytic conductivity (η), electrochemical potential (E_{bulk}), stress ratio (R), fluid temperature (T), material strength (S_y), pre-existing notches (K_t), and test frequency (f) will be examined. The crack-initiation mechanism presumed in the APD model will be examined through potentiostatic measurements of impressed current and the observation of electrochemical potentials (E_{bulk}) under various loading waveforms. The phenomenon of active-path-dissolution (APD) enhanced crack initiation will be explored through fracture-surface observations using a scanning electronic microscope (SEM). Means of improving the corrosion-fatigue resistance of API-S135 steel by adding polymeric inhibitors, applying cathodic protections, and coupling with galvanic Al coating will also be explored in the light of predictions made using the proposed APD model.

1.4 THESIS ORGANIZATION

The main body of the text presents the concept, the predictions, the experimental verifications, and the application of the proposing APD model.

CHAPTER II: LITERATURE REVIEW reviews the mechanisms and mathematical models for describing both corrosion-fatigue crack initiation and corrosion-fatigue crack growth. Effects of environmental, mechanical and microstructural variables on the corrosion-fatigue life and the corrosion-fatigue crack growth of iron-based structural alloys in saline aqueous environments are discussed.

CHAPTER III: DEVELOPMENT OF THE ACTIVE-PATH-DISSOLUTION (APD) MODEL overviews the partitioning of CFC processes and the relevant modeling concepts for each damaging process.

CHAPTER IV: EXPERIMENTAL METHODOLOGY describes the experimental programs conducted to verify the proposed APD model.

CHAPTER V: EXPERIMENTAL VERIFICATION OF THE APD MODEL compares the APD model predictions with test data. The relative significance of environmental variables are model simulated and experimentally verified to provide the perspectives of mitigating corrosion fatigue by controlling these variables.

CHAPTER VI: DISCUSSION discusses the effects of investigated variables on the APD model simulations; and the verification of postulated crack-initiation mechanism upon which the APD model was built with experimental observations. The predictive capability of the APD model are also examined.

CHAPTER VII: SUMMARY, CONCLUSIONS, AND SUGGESTED FUTURE WORK summaries the model predictions and experimental observations for the investigated corrosion-fatigue systems. Future research directions in the light of current study are suggested.

Four appendices giving the theoretical background of the APD model follow the text:

APPENDIX A: CYCLIC-STRAIN-INDUCED CHEMICAL-NOTCHING KINETICS develops a theory to describe the chemical-notching processes of an electrode cyclically straining in electrolytic environments.

APPENDIX B: COMPUTATION OF BARE-CRACK-TIP CURRENT DENSITY computes the bare-crack-tip current density (i_{bare}) evolved instantaneously after the rupture of protective surface film at a microcrack tip which is under the maximum crack-tip opening (δ_{max}) at the maximum applied stress (S_{max}).

APPENDIX C: DEGREE OF CFC SATURATION FOR CORROSION-ASSISTED MICROCRACK DEVELOPMENT derives an analytical model for obtaining the degree of CFC saturation (φ) to describe the development of microcracks under partially-saturated corrosion attack.

APPENDIX D: COMPUTATION OF SALT-FILM OHMIC-DROP COEFFICIENTS illustrates the computation of salt-film ohmic-drop coefficients (E_Ω) to determine the electrochemical potential (E_{bulk}) at the entrance of a microcrack.

CHAPTER II: LITERATURE REVIEW

2.1 ENVIRONMENTAL (AQUEOUS) EFFECTS ON FATIGUE

Combined exposure to corrosive environments and cyclic stress generally results in degrading the fatigue resistance of structural steel components. Experimental studies suggest that surface degradation (pitting) caused by corrosion and its synergistic interaction with the surface-defect initiation from cyclic plasticity of fatigue are responsible for significantly reducing the service life of structural members. The presence of an aggressive environment may also accelerate the accumulation of fatigue damage and result in the disappearance of a fatigue limit [1].

The effects of corrosive environments on fatigue are not caused by a single mechanism. Corrosion reactions may accelerate crack growth by promoting anodic dissolution at the crack tips while retaining crack sharpness, or by facilitating the entry of discharged hydrogen to embrittle the material ahead of the growing crack tips [2]. A crack-growth retardation effect, on the other hand, may also occur if the crack tips are severely blunted by extensive anodic dissolution [2-4]. In addition, insoluble corrosion products may collect inside the crack enclaves and raise the crack-closure stress by wedging the crack tips open. This process reduces the effective stress intensity and retards crack growth [4]. The operative cracking mechanisms vary with the actual combination of material and environmental conditions [1]. It is thus not possible to derive an universal mathematical model based on a particular mechanism to generalize all kinds of corrosion-fatigue processes [2].

2.2 MECHANISMS OF CORROSION-FATIGUE CRACK INITIATION

2.2.1 General

The mechanisms which have been proposed for corrosion-fatigue crack initiation are mainly modifications of theories originally developed for stress-corrosion cracking (SCC). Although different approaches have been suggested, all of them commonly agree that localized-corrosion processes instead of uniform-corrosion processes are responsible for the premature fatigue-crack initiation of materials in corrosive environments [2].

The three major fatigue-crack-initiation mechanisms of steels in saline aqueous environments including: pitting, hydrogen embrittlement, and slip dissolution will be reviewed. None of these mechanisms is commonly accepted for all (or even any particular) material/environment systems. The subcritical microcrack development near the material surface is also considered a part of fatigue-crack initiation process.

2.2.2 Pitting Mechanism on Crack Initiation

The stress-concentrating-pit theory, first proposed by McAdam [5], was favored by the early investigators of corrosion fatigue [5-8]. It was assumed that pits on a metal surface behave as local stress raisers which reduce the fatigue strength of materials by prematurely initiating fatigue cracks.

The formation of corrosion pits is usually associated with autocatalytic reactions under which the passive films on metal surface are locally destroyed [9]. The onset of pitting is attributed to a critical pitting potential (E_{pit}) above which pits grow. The pitting potential (E_{pit}) usually is located around the passive-transpassive borderline of anodic-polarization hysteresis loop and varies according to material/environment combinations.

The actual mechanism for the nucleation of pits at pitting potential is not well understood. The following sequence of events (see Fig. 2.1) for iron in slightly-alkaline chloride-bearing aqueous environments has been suggested by Jones [10] and supported by considerable observations from experiments. He suggested that the copious generation of positively-charged cations (Fe^{2+}) at certain spots (e.g., inclusions [11-12] or microstructural heterogeneity [13]) attracts negatively-charged anions (Cl^-) to precipitate nearby the chloride-salt islands of increasing thickness. The iron underneath the chloride-salt islands undergoes a sequence of vigorous hydrolysis as represented by:

$$Fe^{2+} + 2H_2O + 2Cl^- \Rightarrow Fe(OH)_2 + 2H^+ + 2Cl^- \qquad (2.1)$$

The hydrolysis of iron depresses the pH leading to the further acceleration of the anodic dissolution and the accumulation of chloride ions in the locality. Outside of the pits, an insoluble cap of hydroxide products are deposited as a consequence of Eq. 2.1. This cap impedes the easy escape of ferrous ions but is sufficiently porous to permit the migration of chloride ions for sustaining a high concentration of hydro-chlorine acid within the pits. An anodic polarization of the pit interior (which liberates electrons) occurs by coupling with the exterior passive surface (which consumes electrons) resulting in an autocatalytic pit growth. Pits would grow to various shapes such as hemispherical, undercutting, or tunnel-like depending on the applied electrochemical potential (E_{bulk}) [13-14], anion concentration, or the microstructure of the materials [13].

2.2.3 Hydrogen Embrittlement on Crack Initiation

This mechanism suggests that atomic hydrogen adsorbed on material surface would diffuse into stress concentrating areas (persistent slip band or plastic zone) leading to a local hydrogen embrittlement [15]. As discussed in a comprehensive review by Briant [16],

various mechanisms including hydride formation, build-up of hydrostatic pressure, surface adsorption, and bonding decohesion have been proposed to explain the effects of hydrogen on stress-corrosion cracking (SCC). None of these ideas, however, seems capable of conclusively describing corrosion-fatigue crack initiation for structural steels in chloride-bearing aqueous environments.

Hydrogen-assisted fatigue-crack initiation in aqueous environments has been found to be strongly sensitive to the chemical composition and the microstructure of steels [17]. After having examined the aluminum-plated PH13-8Mo steels of various chemical compositions using notched cantilever specimens tested in distilled water, Asayama et al. [17] found that hydrogen assisted premature cracking did not occur for specimens having carbon contents larger than 0.025% or aluminum contents less than 1.16%. Ray et al. [18] have used a transmission electron microscope (TEM) to examine the crack-initiation sites of a Enl-type mild steel fatigued in 0.6M NaCl solution and argued that the dissolution of sulphur-enriched inclusions was responsible to generate H_2S and the low-energy paths for diffusing hydrogen. The hydrogen so generated then induced the nucleation of microvoids and microcracks which subsequently coalesced by cyclic deformation to initiate macroscopic cracks.

The effect of hydrogen embrittlement seems also to depend on crack size and oxygen supply in aqueous electrolytes. In their Auger-electron-spectroscopic study on the surface oxidation of AISI-4340 steel, Simmons et al. [19] reported that the surface reaction rate of oxygen with iron was at least 10^6 times faster than the reaction rate for water vapor with iron: a process responsible for generating atomic hydrogen. This observation was consistent with the oxygen-inhibition models proposed by Hancock and Johnson [20], and Gangloff [21] who have claimed that the presence of oxygen in humid H_2 or in water-vapor environments arrested hydrogen-assisted subcritical-crack growth for high-strength steels under corrosion fatigue. For those microcrack tips of shallow geometry, an abundant oxygen supply through convection would deposit certain oxide layers of sufficient thickness to prevent the adsorption of atomic hydrogen thus avoiding cracking assistance from crack-tip embrittlement [19,21].

Ouchi [22] has suggested that hydrogen source for steels immersed in aqueous environments was generated primarily through the water-molecular dissociation (Eq. 2.2) and the hydrogen-ion discharging processes occurred at steel/water interface. He also suggested that such steel/water surface reactions proceeded in a similar fashion regardless of the conductivity, or the chloride-ion concentration of investigated electrolytes [22].

$$H_2O \Rightarrow H^+ + OH^- \qquad (2.2)$$

2.2.4 Slip Dissolution/Preferential Dissolution on Crack Initiation

Fatigue-crack initiation under an intrusion/extrusion cyclic slip generally occurs in regions where persistent slip bands (PSB) intensify local strain on the material surface. With the presence of electrolytic environments, these PSB of cyclic deformation are preferentially attacked by the corrosive medium and are subsequently transformed to stress intensification sites leading to an early crack initiation [23-26]. This preferential corrosion attack occurs due to a fact that those plastically-deformed areas (PSB) act as anodes which couple with less deformed metals as cathodes to enforce the localized dissolution [23]. The localized dissolution on areas where the PSB have emerged may also be attributed to the film rupture/repassivation characteristics of materials, as have been suggested by Müller [27] and Daeubler et al. [28]. The emerging slip steps rupture passive films which would otherwise be protective and thus raise local dissolution current at the unfilmed areas. Corrosion processes also tend to enhance an irreversible slip [25] resulting in an increased density of PSB and the number of potential sites for crack initiation.

Markfield [29] has tested HY-80 steel in NaCl solutions and reported that microcracks produced by the dissolution process are so open that they can grow without crack closure at most R ratios. This observation suggests that the dissolution processes which interact with fatigue deformation cause a rapid growth of microcracks leading to a premature fatigue-crack initiation at much lower stress ranges (ΔS) than those that would be observed in ambient air.

2.3 MECHANISMS OF CORROSION-FATIGUE CRACK GROWTH

2.3.1 General

At least six types of processes may play a role to determine the rate of fatigue-crack growth in corrosive aqueous environments [30]. They are:

(1) Rupture of protective surface film by cyclic strain.
(2) Periodic production of freshly-fractured crack surfaces by fatigue cracking.
(3) Supply of reactant to and removal of products from crack-tip regions.
(4) Anodic dissolution at crack tips.
(5) Material/environment reactions to produce deleterious chemical species (e.g., hydrogen) which might diffuse into zones ahead of crack tips to accelerate crack growth.
(6) Buildup of corrosion products on crack surfaces to raise crack-closure stress or to reduce the effective range of stress-intensity factor (ΔK_{eff}) for crack growth.

The relative significance of the above processes must be evaluated individually for each material/environment system.

In general, the most important issues relating to environmentally-assisted crack growth in corrosive aqueous environments are the transport/adsorption phenomena, the anodic dissolution/film rupture process and the hydrogen embrittlement. Each of these issues is reviewed in detail below.

2.3.2 Transport/Adsorption Phenomena and Local Crack Environments

To understand the mechanisms of corrosion-fatigue crack growth requires knowledge of the electrochemical kinetics of various processes. The reactants present in bulk environments must be supplied to crack-tip regions for electrochemical reactions. However, due to the restricted mass transport[1] induced by the crack geometry, the electrochemistry in crack-tip solutions generally is different in nature from that in bulk solutions [31-35]. A significant reduction in pH near crack tips has been reported as a consequence of the occluded hydrolysis (see Fig. 2.2) of steels by local electrolytes [34-35]. The potential drop across a crack depends on: the size, the geometry of the crack; the frequency (f), the stress ratio (R) of fatigue loading [31,35]; and even the types of corrosion products precipitated around crack entrances [31]. For instance, an increased test frequency (f) and a decreased stress ratio (R) were both found to result in an increased potential drop across fatigue cracks and in an enhanced crack-size effect on crack-tip chemistry [31,35].

The local crack-tip chemistry, not the bulk solution chemistry, governs the rate of fatigue crack growth.

2.3.3 Anodic Dissolution/Film Rupture Mechanism on Crack Growth

The anodic dissolution/film rupture mechanism explains the accelerated growth of corrosion-fatigue cracks by the localized anodic dissolution of periodically-exposed fresh crack tips [3]. Corrosion processes usually deposit protective films (oxides or hydroxides) on corroded surfaces. Due to the locally-concentrated plastic strain, the protective films at crack tips are easily broken by the emerging slip steps. The unstrained crack surfaces, on the other hand, remain passivated and cathodic relative to the crack tips. The anodic dissolution occurred at the freshly-exposed crack tips of plastic deformation is thus intensive and localized. After being attacked, the crack tips are subsequently recovered with passive layers during the unloading reversal until the next event of film rupture. The growth of a corrosion-fatigue crack is thus associated with the periodic film rupture, the localized anodic dissolution, and the repassivation of crack tips.

---

[1] The mass transport in crack solution strongly depends on the relative movement (test frequency) of the crack wall.

2.3.4 Hydrogen Embrittlement on Crack Growth

The corrosion reactions near crack tips may generate deleterious chemical species which accelerate crack growth. Hydrogen is the most commonly observed species which embrittles material ahead of the crack tip [36]. Hydrogen ions may be produced by cathodic reductions [37-40] or by water molecular dissociation [22]. These hydrogen ions are subsequently discharged and adsorbed on material surface. The adsorbed atomic hydrogen can then diffuse into the zone ahead of crack tips where it causes localized embrittlement or cavitation by hydrogen gas recombination [18-19] or by local plasticity enhancement [41-42]. The diffusional transport of hydrogen is most likely along dislocations or grain boundaries instead of by bulk diffusion. A more complete review on hydrogen-assisted crack growth can be found in a comprehensive survey by Turnbull [2].

The mechanism of localized hydrogen embrittlement has been recognized responsible for accelerating the fatigue-crack growth of high-strength steels in aqueous or in water-vapor environments [19,22]. This mechanism has also been realized to be the dominant environmental assistance for the fatigue-crack growth of medium/high-strength steels in saline aqueous environments under cathodic protection [17,43-47].

2.4 Corrosion-Fatigue Life of Structural Steels in Saline Aqueous Environments

2.4.1 General

Unless otherwise specified, the following review is focused on the stress-life (S-N) behavior of smooth structural steel specimens fatigued in salt-water environments. The effects of material properties, environmental variables are discussed. High-cycle-fatigue characteristics under free-corrosion conditions are emphasized.

2.4.2 Effects of Strength and Microstructure

In contrast to ambient-air fatigue for which an increasing material strength is beneficial, high-cycle-fatigue behavior of carbon steels and low-alloyed steels have been shown to be approximately independent of tensile strength when fatigued in saline aqueous environments under free corrosion [48-49]. An increasing strength of several high-strength steels, e.g., AISI 4140, AISI 4340, etc., can be even detrimental to their fatigue resistance in 1% NaCl solutions due to the increasing vulnerability of these materials to hydrogen embrittlement [50-51]. The positive dependence of fatigue resistance on tensile strength for steels in salt-water environments could be partially restored, as suggested by Ishiguro [49], with a small addition of alloying elements such as Cr, Ni, etc.

Common modifications of material microstructures to improve air-fatigue properties have been found to be without effect on the fatigue resistance of carbon steels in salt-water environments [52]. Refining the grain size of materials has made no difference on the S-N behavior of carbon steels in 3% NaCl solutions. Similar test results have been obtained after changing the microstructure from lamellar pearlite to dispersed cementite [52].

2.4.3 Effects of Stress Amplitude ($\Delta S/2$) and Stress Ratio (R)

Similar to air fatigue, an increasing stress amplitude ($\Delta S/2$) shortens the fatigue life of structural steels in saline aqueous environments. There is, however, no apparent fatigue-limit behavior for the case of corrosion fatigue [1,53].

An increased stress ratio (R), i.e., the ratio of minimum applied stress to maximum applied stress, can be expected to reduce the corrosion-fatigue resistance of steels in a similar manner as observed in the ambient-air fatigue [1,53-54].

2.4.4 Effects of Test Frequency (f)

Corrosion fatigue is a process which is not only cyclic dependent but also time dependent. A decrease of test frequency (f) causes marked reductions in the strength of high-cycle fatigue for freely corroding steels [55], although little or zero difference has been found in the case of low-cycle fatigue [56]. The S-N curves of various test frequencies (f), as reported by Endo and Miyao [55], tend to diverge from each other at low stress amplitudes ($\Delta S/2$). Pettit et al. [57] have tested API-S135 steel in seawater within a fatigue-life (N_f) range of 10^4 to 10^5 cycles and found a reduction of fatigue life (N_f) by a factor of 2 after reducing test frequency (f) from 20 to 1 Hz. A further reduction of the frequency (f) from 1 to 0.2 Hz gave about 20% further fatigue-life reduction. Therefore, a meaningful application of laboratory S-N curves to engineering designs for structural members cyclically stressed in corrosive environments can be made only when the test frequency (f) of fatigue tests is properly selected to simulate the actual service conditions.

2.4.5 Effects of Loading Waveform

For low-cycle corrosion fatigue, the fatigue resistance of materials generally is affected more by stress waveforms than by test frequency (f) [58]. A typical trapezoidal wave consisting of a stress-rising period (t_{rise}), a maximum-stress-holding period (t_{hold}), a stress-descending period ($t_{descend}$), and a minimum-stress-resting period (t_{rest}), is illustrated in Fig. 2.3. After having tested a 0.9% carbon steel (yield strength: 890 MPa) in 1% NaCl solutions under various trapezoidal waves, Endo and Komai [59] reported that the stress-rising period (t_{rise}) was the most influential period in affecting corrosion-fatigue S-N behavior. They

found that a decreasing corrosion-fatigue life is always associated with an increasing stress-rising period [59]. An extended period of the maximum-stress holding (t_{hold}) or of the minimum-stress resting (t_{rest}), however, diminished environmental influences on the corrosion fatigue. A prolonged maximum-stress-holding period (t_{hold}) could inflict a significant fatigue-life reduction only when the tested systems were stress-corrosion-cracking (SCC) sensitive [59] or when a fluctuation stress of small amplitude was superimposed on the maximum holding stress [58].

2.4.6 Effects of Environmental Variables

The effects of major environmental variables, including fluid temperature (T), hydrostatic pressure, oxygen content, and pH, on the corrosion-fatigue S-N behavior of structural steels in saline aqueous environments will be reviewed below.

Several studies have shown that increasing temperature (T) in the range of 13 °C to 45 °C resulted in a decreasing (although small) fatigue life for structural steels tested in artificial seawater [60-62]. Above 50 °C, Watanabe and Mukai [62] have found a saturated phenomena of the fluid-temperature (T) effect on low-cycle fatigue. There is, however, no corresponding observation available for the corrosion fatigue in high-cycle-fatigue regime.

Jolliff and Thiruvengadam [63] have found that the corrosion-fatigue resistance of HY-80 steel was not affected by a 2000 psi hydrostatic pressure in 3% NaCl solutions. A higher strength materials, e.g., HY-130, in contrast to HY-80, have shown a corrosion-fatigue-life reduction for the presence of the hydrostatic pressure relative to the corrosion fatigue at atmospheric pressure [63]. The above observations on pressure effects, however, are not conclusive for usual engineering application because the test frequency (f) in Jolliff and Thiruvengadam's experiments was as high as 20 kHz. The frequency-dependent behavior (time-dependent process) of corrosion fatigue should not be overlooked (see Sec. 2.4.4).

The effects of oxygen content on the corrosion-fatigue behavior of structural steels appears controversial and operative only in high-cycle-fatigue regime. A significant improvement on the corrosion-fatigue (f = 30 Hz) life of an AISI-4140 steel (ultimate strength: 793 MPa) has been achieved by Lee and Uhlig [50] using fully de-oxygenated 3% NaCl solutions as testing environments. A similar effect was also apparent for a 1015 steel (0.18% C, ultimate strength: 524 MPa) tested in the same conditions by Duquette and Uhlig [64]. Masumoto and Akaishi [65] have reported a more detail investigation on the effect of oxygen content. They found a beneficial effect of reducing oxygen on the corrosion-fatigue life of a SM-41 steel in 3% NaCl solutions having oxygen content below 10 ppm. Above 10 ppm up to the saturation limit of 1980 ppm, no effect of oxygen content was observed. Pettit et al. [57], however, reported that reducing the oxygen content from 6 ppm to 0.02 ppm had

almost obscure influence on the corrosion-fatigue S-N behavior of API-S135 steel tested (f = 1 Hz) in seawater [57]. The effect of oxygen, as pointed out by Velden et al. [66], could also interact with the test frequency (f) of fatigue loading.

Over a broad range of pH from 4 to 10, the pH of the electrolyte has little influence on the corrosion-fatigue resistance of steels [67-68]. Corrosion-fatigue life, in general, decreases with a decreasing solution pH. Pettit et al. [57] examined an API-S135 steel at a test frequency (f) of 1 Hz in seawater drilling mud and found no pH effect on fatigue life for the mud of pH ranging from 9 to 12.

2.4.7 Effects of Cathodic Protection

Applying cathodic protection to improve the corrosion-fatigue resistance of steels has been studied by many investigators [69-72]. The principles of using this technique to protect steels from corrosion fatigue are similar to that for general corrosion, i.e., to reduce the corrosion rate of steels. The electrochemical potential to be maintained for an optimum protection is system dependent but typically has a value of around -0.80 V vs. SCE.

Several investigators have emphasized the importance of forming calcareous deposits, e.g., $CaCO_3$ and $Mg(OH)_2$, for cathodic protection. The formation of the calcareous deposits was beneficial in reducing the input current necessary for achieving required protection. The susceptibility of cathodes (steels under protection) to hydrogen embrittlement could thus be minimized [69-72]. It is worth noting that these deposits appeared only when actual, or well-formulated artificial seawaters were employed as environments for the fatigue tests.

Cathodic overprotection can be detrimental to medium/high-strength steels[2] (HY-130, maraging steels, etc.) in low-cycle-fatigue regime, i.e., a regime consists mainly of crack growth [73-75]. The same steels tested in high-cycle-fatigue regime maintained at the same cathodic protection, however, were effectively protected [74,76-77]. It can be thus deduced that cathodic protection is effective in enhancing the resistance of high-strength steels from initiating corrosion-fatigue cracks, but is not so effective in retarding any existent corrosion-fatigue crack from growth.

Plating steels with a galvanically inferior alloy, e.g., Zn, Cd, Al, etc., also protects the underlying steel substrates (cathodes) from initiating corrosion-fatigue cracks [57,78-80]. These sacrificial coatings have been demonstrated to be more effective than physical-barrier coatings such as tungsten carbide, chromium, or painting, etc. [79]. The density of galvanic current flowing between anodes (coatings) and cathodes (substrates) is an important factor in determining the efficiency of using this technique for mitigating corrosion fatigue [78]. Among the sacrificial alloys (Zn, Cd, Al, etc.), aluminum plating has been shown to be the

[2] These high-strength steels are known to be relatively susceptible to hydrogen embrittlement.

most effective approach to enhance the high-cycle-fatigue resistance of structural steels in saline aqueous environments [78,80].

2.5 Corrosion-Fatigue Crack Growth of Structural Steels in Saline Aqueous Environments

2.5.1 Effects of Strength and Microstructure

HY-130 steels seems to have a greater resistance to the growth of fatigue cracks in salt-water environments than other HY series or pipeline steels (X65, X70, etc.) [44-46,81-82]. This fact implies that the fatigue-crack growth in saline aqueous environments should depend on the strength or the microstructure of steels [83-85]; although, no systematic or conclusive investigation on this subject has been reported to the writer's knowledge.

2.5.2 Time-Dependent Process of Corrosion-Fatigue Crack Growth

In contrast to behavior in ambient-air fatigue for which no time dependence was observed, the fatigue-crack growth of steels in corrosive environments has been recognized to be highly sensitive to test frequency (f) and loading waveforms for a variety of material/environment systems [44,46,54,59,86-92]. The time-dependent fatigue-crack growth requires the presence of aggressive environments which cause metallic corrosion. It is thus suspected that testing variables, e.g., temperature (T) [86], electrochemical potential (E_{bulk}) [46,54,92], loading waveform [59,87-91], test frequency (f) [44,46,54,59,86-92], and applied stress-intensity factor (K_{Imax}, ΔK) [44,46,54,86-91], which affect the extent of corrosion attack should therefore all influence the time-dependent phenomena of corrosion-fatigue crack growth.

2.5.3 Effects of Stress-Intensity-Factor Range (ΔK)

The fatigue-crack growth in saline aqueous environments depends heavily on mechanical-environmental interactions, particularly when the applied range of stress-intensity factor (ΔK) is intermediate [54]. The da/dN vs. ΔK curves often have a plateau shape in the intermediate ΔK regime where da/dN exhibits a ΔK independent behavior and varies greatly with test frequency (f) and stress ratio (R). Little or no environmental effect was observed in the high or in the low ΔK regimes [44-46,54,81].

For a high cyclic range of stress-intensity factor (ΔK), mechanical crack growth is far in advance of any environmental attack which thereby diminishes the latter's relative significance. In the near-threshold ΔK regime, the relative movement of the crack faces is so small that it is difficult to rupture oxide films or to expose fresh crack tips to the electrolyte.

No significant environmental influence can thus be detected at these ΔK values. For intermediate ΔK values, the rate of crack growth is so slow as to allow environmental attack to keep pace with the material freshly exposed at the crack tips. The localized corrosion at the crack tips can hence accelerate the growth of fatigue cracks in the intermediate ΔK regime [54].

2.5.4 Effects of Stress Ratio (R)

The environmental assistance in fatigue-crack growth increases with an increasing stress ratio (R) of applied fatigue loading [93-95]. Vosikovsky [46] has tested HY-130 steel in 3.5% NaCl solutions with three values of stress ratio (R), i.e., 0.05, 0.1 and 0.9, and found that da/dN vs. ΔK curves were shifted upward (increasing da/dN) as the R ratio increased. The diminishing values of threshold stress-intensity range (ΔK_{th}) were also observed with the tests of increasing R ratios [46,85].

Instead of using ΔK, Vosikovsky [46] then proposed that the above R-ratio effects on corrosion-fatigue crack growth can be correlated quite well with a simple parameter ($\Delta K+3R$). Similar R-ratio phenomena was subsequently reported for a X70 pipeline steel by Vosikovsky [45]; and a correlation parameter ($\Delta K+4R$) was suggested. These correlation parameters were intended to take the crack-closure effects of corrosion products into account, as also suggested by some other investigators [66,85,96], to characterize the R-ratio effects on the fatigue-crack growth of steels in saline aqueous environments.

2.5.5 Effects of Test Frequency (f)

It has been often reported that decreasing the test frequency (f) below 10 Hz causes accelerated fatigue-crack growth at intermediate ΔK for structural steels fatigued in saline aqueous environments [44-46,54,86]. This phenomenon was pronounced when a cathodic overprotection was impressed on the systems [44-46,54] or when the test frequency (f) was reduced from 1 to 0.01 Hz [86]. For tests with a test frequency (f) above 10 Hz, there appeared, however, no significant environmental influence on the fatigue-crack growth of HY-130 steel in 3.5% NaCl solutions, as reported by Vosikovsky [46].

In their systematic investigation on the fatigue-crack growth of HY-130 steel in 3.5% NaCl solutions under a varying test frequency (f), temperature (T) and applied stress-intensity range (ΔK), Thomas and Wei [86] have observed the existence of a saturation frequency below which no further environmental assistance on fatigue-crack growth was detected. This saturation frequency represents a lower bound of the fatigue-crack growth depending on both elapsed time (t) and cyclic loading (ΔK) as commonly observed for steels in saline aqueous environments. Below such a frequency, a solely-cyclic-dependent

corrosion-fatigue crack growth resumes. Thomas and Wei [30] have suggested that the saturation frequency strongly depended on the value of stress-intensity-factor range (ΔK) and temperature (T) used in their experiments. Similar phenomena has been also recognized by Jaske et al. [54] after analyzing the fatigue-crack growth data of various steels (HY-130, X65, X70) in 3.5% NaCl solutions published by Vosikovsky [44-46].

2.5.6 Effects of Loading Waveform

The maximum stress-intensity factor (K_{Imax}), in addition to ΔK, of fatigue-loading waves is important to the fatigue-crack growth of steels in saline aqueous environments. Using trapezoidal loading waves with various periods of stress rising, holding, descending, and resting (see Fig. 2.3), Kawai and Koibuchi [87] have found that the stress-rising period[3] (t_{rise}) was the only period within which corrosion-fatigue crack growth was both time and cyclic dependent if the maximum mode I stress-intensity factor (K_{Imax}) was kept below the onset stress intensity for stress-corrosion cracking (K_{Iscc}). The same phenomena has also been recognized by other investigators [88-90], as summarized in Fig. 2.4a. For cases where the maximum-stress-intensity factor (K_{Imax}) was greater than K_{Iscc}, significant amounts of stress-corrosion cracking (SCC) may be added to the total fatigue-crack growth rate (da/dN) [89-91]. The fatigue-crack growth rate (da/dN) under such a condition, i.e., $K_{Imax} > K_{Iscc}$, was proportional to both the stress-rising period (t_{rise}) and the maximum-stress-holding period (t_{hold}). A prolonged period of stress rising (decreasing test frequency) and of stress holding[4] both promote corrosion-fatigue crack growth, as seen in Fig. 2.4b.

For square or negative-sawtooth loading waves where the stress-rising rate is quite rapid, the fatigue-crack growth of high-strength steels in salt-water environments is not different from that obtained in ambient air [88,90]. Significant environmental acceleration of fatigue crack growth has been observed only when the rate of stress rising was slow enough to allow corrosion reactions to attack fresh crack tips opened after fatigue fracture at the maximum stress [87-91]. Therefore, not only the value of K_{Imax} and the period for rising stress (t_{rise}), but also the rising rate of the stress intensity at crack tip is important to the corrosion-fatigue crack growth.

2.5.7 Effects of Environmental Variables

Ryder and Gallagher [97-98] have found that increasing the temperature (T) of 3.5% NaCl solutions from 5 °C up to 85 °C raised fatigue-crack growth rate for HY-130 steel. This temperature effect can be explained by the enhancing rate of surface reactions for the steel

[3] This phenomena is equivalent to the frequency effect discussed in Sec. 2.5.5.
[4] A period for stress-corrosion cracking to take place.

with the testing fluids of an increasing temperature (T) [38]. Similar to that discussed in Sec. 2.5.3, this temperature effect is pronounced only in the intermediate ΔK regime.

The effect of oxygen content on corrosion-fatigue crack growth remains uncertain at present. Controversial results have been reported [61,99]. Reducing oxygen content in testing fluids has significantly retarded the fatigue-crack growth of steels under free corrosion within the range of oxygen content investigated by Scott and Silvester [99]. Such an effect of oxygen content on fatigue-crack growth has been, however, absent when a cathodic potential (-0.82, and -1.02 V vs. SCE) was impressed on the specimens of the same steel [99]. Ouchi et al. [61] have tested ($R = 0.25$, $f = 0.17$ Hz) a structural steel of 667 MPa tensile strength and found no effect of dissolved oxygen on the fatigue-crack growth of the steel freely corroding in an ASTM synthetic seawater of oxygen content ranging from 0.5 ppm to 8 ppm.

In solutions of usual pH (>3), no significance of solution pH on fatigue-crack growth for steels should be expected. Changing solution pH from 5.3 to 11.2, as shown by Misawa and Kobayashi [100], had no significant effect on the fatigue-crack growth of a low carbon steel in 0.5N NaCl solutions at 25 °C. Austen et al. [101] have manipulated solution pH from 7 to 0 and observed obscured difference on the fatigue-crack growth of nickel steels in 0.1M NaCl solutions.

Reducing solution salinity or generating calcareous precipitates[5] [83,96] by using synthetic seawater over NaCl solutions would result in no beneficial effect on the growth behavior of macroscopic fatigue cracks for steels tested under free corrosion at ambient temperature. Ouchi et al. [22] have found no difference in crack-growth behavior for a steel (UTS 667 MPa) tested in various fluids including synthetic seawater, 3.5% NaCl solutions, and distilled water. Similar conclusion has also been drawn by Li et al. [84] from their experiments of fatiguing several medium-strength structural steels in artificial seawater or in 3% NaCl solutions. They observed no difference in fatigue-crack growth rate between the test results of using different testing fluids in their investigation.

The presence of sulphur reducing bacteria producing H_2S in natural seawater would promote hydrogen embrittlement at crack tips and hence facilitate fatigue-crack growth [54]. This argument is supported by an experiment conducted by Bogar and Crooker [102]. They have reported that the fatigue-crack growth rate of HY-130 steel at intermediate ΔK was significantly higher in a flowing natural seawater than in a flowing 3.5% NaCl solution. Using actual seawater for the measurements of corrosion-fatigue crack growth is thereby recommended for characterizing structural members serving under marine environments.

---

[5] Calcareous precipitates within a crack would induce crack closure which retard crack growth.

2.5.8 Effects of Cathodic Protection

In general, once a dominant crack has been initiated by corrosion fatigue, cathodic protection is not capable of prohibiting its subsequent growth. Cathodically protecting a material up to a potential of -0.78 V vs. SCE or higher can even accelerate fatigue-crack growth above those observed under free-corrosion fatigue [22,44,46-47,83,94,99,103]. The crack-growth acceleration by cathodic over-protection is apparent particularly at intermediate ΔK or at a test frequency (f) below 1 Hz. Embrittling the plastic zone ahead of growing crack tips by atomic hydrogen has been often speculated as the cause of the accelerated fatigue-crack growth [38,54]. The detrimental effect of cathodic over-protection on HY-80 steel was found to be greater in a flowing natural seawater than in a flowing 3.5% NaCl solution [102].

A few studies have shown that applying moderate cathodic protections (up to -0.78 V SCE) is beneficial in retarding corrosion-fatigue crack growth when cracks are shallow, the environment is not stagnant, and the stress ratio (R) is below 0.1 [99,102].

2.6 Mathematical Models of Corrosion Fatigue

2.6.1 General Aspects on Modeling Corrosion-Fatigue Cracking

Mechanistic modeling is important in characterizing environmentally-assisted fatigue-crack growth; however, its application to life prediction may be limited to specific systems because of the complexities arising from the multiple crack nucleation, crack coalescence, crack-tip wedging and the highly-uncertain synergistic electrochemical-mechanical interaction. An intelligent combination of empirical formulation supported by insights from mechanistic models is an effective approach in estimating the environmental assistance on fatigue-crack initiation and growth [2].

2.6.2 Models for Corrosion-Fatigue Crack Initiation

It is known that the influence of corrosion on crack initiation is much greater than on crack growth [1,104]. Müller [27] first proposed a fatigue-crack initiation model for general corrosion, pitting corrosion, and passive corrosion. The pit-growth kinetics in his model were based on a simple power law which required tedious experiments to obtain the involved kinetics parameters. Daeubler et al. [28] modified Müller's passive-corrosion model by considering a critical-slip-step height as the transition from an intense slip band to an incipient crack. The crack-initiation process was then viewed as an interaction and competition between the rate of emerging slip steps (film rupture events) and the rate of repassivation. Kondo [104] suggested an empirical criterion for a crack emanating from a

corrosion pit. The transition condition was a critical stress-intensity-factor range of 1.2 MPa$\sqrt{m}$. The corrosion pit was modeled as a sharp crack regardless of its size.

2.6.3 Models for Corrosion-Fatigue Crack Growth

A superposition model was first proposed by Wei [105] to describe corrosion-fatigue crack-growth rate. The rate of fatigue-crack growth in corrosive environments was computed as the summation of a purely mechanical-fatigue cracking, an environmental-mechanical interaction, and a stress-corrosion cracking. Hoeppner [8] used a four-parameter Weibull fit to characterize the threshold stress-intensity-factor range (ΔK_{th}) for systems undergoing pitting corrosion. Numerous linear-elastic-fracture-mechanics (LEFM) approaches can also be found in literature [4,83,106-108]. Among those, Zhang and Song [4] provided a crack-closure blunting model, Weiss [107] combined LEFM with a linear damage-accumulation theory, while Imhof and Barsom [108] suggested an empirical curve-fitting scheme with no physical basis.

More recently, Ford and Emigh [3] gave an estimation of maximum corrosion-fatigue crack-growth rate. They modeled the crack growth by combining Faraday's law with the number of film rupture events at crack tips. However, to estimate the fracture strain of oxide layers and the crack-tip strain rate for computing the number of film rupture events was not straightforward. Wei and Gao [109] reconstructed their superposition model to be a weighted combination of a purely mechanical-fatigue cracking and a purely corrosion-fatigue cracking. Masuda et al. [110] provided a more sophisticated alternative for the film rupture/repassivation approach. They calculated the acceleration of crack growth due to corrosion by evaluating the amount of the slip plane dissolved during each loading cycle. Using such an approximation, however, the da/dN vs. ΔK curves for all environments were forced to be parallel because the crack-growth acceleration ratio in their model was independent of the applied stress-intensity-factor range (ΔK). Harlow and Wei [111] proposed a fairly complicated probability model to predict statistically the service lives of engineering components operated under corrosive environments.

2.7 SUMMARY

The actual mechanisms of crack initiation and crack growth for structural steels fatigued in saline aqueous environments are still under debate. Conclusive experimental evidence supporting any existing hypothesis has not been reported for both issues: the corrosion-fatigue crack-initiation process, particularly, is still poorly understood. Recently, the mechanism of hydrogen embrittlement has become more widely accepted as an

explanation of the accelerated fatigue-crack growth for high-strength steels in saline aqueous environments. However, the existence of a single mechanism controlling crack-growth processes for steels under all kinds of corrosion fatigue is still very unlikely. Various combinations of multiple mechanisms for cracks at different length or for varying material/environment systems are probably the most reasonable approaches to characterize the processes of crack initiation and crack growth for metallic fatigue in corrosive environments.

Experimental observations on corrosion fatigue are usually controversial and system dependent. The stress ratio (R) and test frequency (f) are probably the most important mechanical parameters affecting both fatigue life and fatigue-crack growth for steels in saline aqueous environments at given values of stress amplitude ($\Delta S/2$). Efforts to mitigate corrosion fatigue by reducing the corrosivity of testing environments do not appear effective.

Applying cathodic over-potentials or sacrificial coatings prolongs corrosion-fatigue life for most structural steels in salt-water environments. These cathodic-protection techniques, however, cause little influence or even detrimental effects on corrosion-fatigue crack growth. It could be thus deduced that applying cathodic protection should protect steels from initiating macroscopic cracks of a critical size but not from propagating any existing dominant cracks to fatigue fracture.

A commonly accepted corrosion-fatigue model for crack initiation or crack growth is currently not available. Most models proposed in literature are purely conceptual, or are entirely empirical in nature and rely heavily on experiments to obtain curve-fitting parameters. Models for predicting corrosion-fatigue life which have been experimentally verified are rare. A systematic investigation of structural steels in saline-aqueous environments to develop an analytical model with theoretical background is needed to promote further understanding of this complicated subject.

The ambitious purpose of this study was to develop an analytical model, based on electrochemical principles, capable of simulating corrosion-fatigue S-N behavior of structural steels in saline aqueous environments. The predicted fatigue life was experimentally verified; and the cracking mechanisms upon which the model was built were validated by experimental observations.

CHAPTER III: DEVELOPMENT OF THE ACTIVE-PATH-DISSOLUTION (APD) MODEL

3.1 EXPERIMENTAL OBSERVATIONS OF CORROSION-FATIGUE-LIFE PARTITIONING

3.1.1 General Consideration

The APD model considers the corrosion-fatigue life (N_T) to be governed by a sequence of three processes and to be the sum of their corresponding life periods:

Chemical-Notching Process (N_{pit}),
Microcrack Development (N_{p1}),
Macroscopic Crack Growth (N_{p2}).

These three processes can be roughly correlated with experimentally observed changes of electrochemical potential (E_{bulk}) and mechanical displacement range (Δe) as shown in Fig. 3.1.[1] As seen in Fig. 3.1b, a first subtle increase in the displacement range (Δe) appears within a fatigue-life region (shaded in Fig. 3.1) labeled as "A" and occurs at less than 50% of total fatigue life (N_f). This increase[2] represents the (broad) transition between chemical-notching process and microcrack development. A second major change (labeled "B") in the displacement range (Δe) versus life (N) behavior occurs at the transition between microcrack development and macroscopic crack growth. The fatigue life devoted to macroscopic crack growth (N_{p2}) is brief.

The background relating to this partitioning of corrosion-fatigue life (N_f) is discussed in detail below.

3.1.2 Electrochemical Observations on Chemical Notching

The stable growth of chemical notches (pits) is usually associated with a "potential dip" toward an active potential [9,112-113]. The appearance of such a "potential dip" on the electrochemical potential (E_{bulk}) verse fatigue cycle (N) plot seen in Fig. 3.1a represents a period during which protective surface films are locally destroyed. The emergence of an active dissolution at those unfilmed area (active path) drops[3] the electrochemical potential (E_{bulk}) before the film-formation process on those spots is fully restored.

---

[1] An API-S135 steel was fatigued (R = 0.1, f = 2 Hz) in deaerated seawater drilling fluid at 93.3 °C. The experimental details for obtaining Fig. 3.1 will be given later in Chapter IV.

[2] This increase in measured mechanical displacement range (Δe) during cyclic loading might be caused by cyclic softening effects induced by chemical-notching process which degrades the surface of tested material (API-S135) and by the subsequent development of multiple microcracks.

[3] More discussion about the current/potential response for film rupture/film formation mechanism will be given later in Chapter VI.

3.1.3 Electrochemical Observations on Microcrack Development

The electrochemical potential (E_{bulk}) exhibits a continuous drift towards noble potentials during microcrack development (see Fig. 3.1a). The dropping pH caused by cation (e.g., Fe^{2+} and Fe^{3+}) hydrolysis (Eq. 2.1) inside microcracks together with stress intensification make preferential anodic dissolution at opened microcrack tips on a straining electrode a feasible process. Because the anodic zone is confined at the crack tips (see Fig. 3.2a), the cathodic current density decays with a rising cathode/anode ratio as the microcrack lengthens. The corresponding electrochemical potential (E_{bulk}) versus life (N) behavior (Fig. 3.1a) reflects the expanding cathodic area and the diminishing cathodic-current density (i_c) as a shift of electrochemical potential (E_{bulk}) towards a more noble potential. This potential drift is equivalent to the film-formation current/potential response as sketched in Fig. 3.2b.

3.1.4 Electrochemical Observations on Macroscopic Crack Growth

During macroscopic crack growth, the anodic dissolution at crack tips makes no significant contribution to the crack-growth rate dominated by stress-intensity-factor range (ΔK). The rapid creation of fresh surface dramatically increases the cathodic current density and significantly enlarges the corresponding deviation of electrochemical potential (E_{bulk}) seen in Fig. 3.1a at the onset indication of macroscopic crack growth (see Fig. 3.1b).

3.2 Major Modeling (APD) Assumptions

3.2.1 Modeling the Three CFC Processes

The chemical-notching process (N_{pit}) is modeled as a process which generates a hemispherical surface notch. This process creates an initial active path (see Fig. 3.3a) through an uniform dissolution current at the attacked area until the simulated "chemical notch" (corrosion pit) grows to a depth having its fatigue-notch factor (K_f) above unity.

The microcrack-development process (N_{p1}) is modeled by focusing the electrochemical dissolution along the stress-intensification sites (secondary active path, see Fig. 3.3b) to simulate the development of microcracks. This mechanism prevails until the crack[4] size is macroscopically significant. From there on, the APD model assumes that purely-mechanical fatigue-crack growth occurs with a diminishing contribution from electrochemical processes.

The macroscopic crack-growth process (N_{p2}) is modeled using linear elastic fracture mechanics (LEFM). The stress-intensity-factor range (ΔK) drives fatigue-crack growth until fracture (Fig. 3.3c).

---

[4] An emanating crack at crack-initiation stage is equivalent to the active path of dissolution in the APD model.

3.2.2 Modeling Total Corrosion-Fatigue Life (N_T)

The APD model divides the total corrosion-fatigue life (N_T) into two stages: stage I: crack initiation[5] (including microcrack growth) and stage II: macroscopic crack growth. The crack-initiation stage is postulated to consist of a sequence of two processes: chemical notching (N_{pit}) and microcrack development (N_{p1}). The APD model simulates the total corrosion-fatigue life (N_T) as the summation of stage I: crack-initiation life (N_i) and stage II: macroscopic crack-growth life (N_{p2}):

$$N_T = (N_{pit} + N_{p1}) + N_{p2} = N_i + N_{p2} \tag{3.1}$$

Modeling stage II, macroscopic crack-growth life (N_{p2}), is relatively uncomplicated and involves only the integration of the Paris power law. Modeling stage I, the crack-initiation life (N_i), is complicated and will be discussed in detail in Sections 3.3-3.5 below.

3.3 Modeling (Stage I) Chemical-Notching Process (N_{pit})

3.3.1 Overview and Major Assumptions

The nucleation of chemical notches is a thermodynamically spontaneous process for systems susceptible to pitting corrosion and does not necessarily require cyclic strain for incubation [114]. It is thus assumed that the nucleation of chemical notches occurs immediately after the onset of loading with no lengthy incubation period. Some nucleated chemical notches are "stable" and continue to grow while others are "unstable" and cease to grow [9,112-113]. The unstable (repassivated) chemical notches will be ignored in this work because they are seldom reactivated [9,112-113] and because they are also too small to be detrimental to the fatigue resistance of a material.

A fully irreversible electrochemical dissolution is assumed in modeling the cyclic-strain-induced chemical-notching process (see detail in Appendix A). The bulk electrolyte is assumed to be so dilute ($[C^b_{M^+}] \approx 0$, Fig. 3.4) that excess cations in the vicinity of a straining electrode can be completely conducted away to satisfy the need for dropping[6] redox potential (E_{eq}) during the loading reversal. During unloading, the subsequent exponentially-increasing demand of cations (recharging) is assumed to be limited by a diffusion process through a salt film[7] to restore the redox potential (E_{eq}) back[8] to its static state. This conducting/recharging process is simulated and is taken as the driving force which periodically promotes the growth

[5] Modeling corrosion-fatigue crack initiation life will be made clearer in Sec. 3.5.
[6] Film-rupture process accompanying with observed dropping electrochemical potential (see Fig. 3.2b).
[7] Equivalent to a diffusional buffer shown in Fig. 3.4 to compensate the concentration gradient of metal ions.
[8] Film-formation process accompanying with observed rising electrochemical potential (see Fig. 3.2b).

of a chemical notch on the surface of material. The current density at a chemical notch is considered to be uniform since chemical notches grow in depth but remain nearly unchanged in shape (approximately hemispherical). This notching process is applied until a simulated chemical notch reaches a depth producing a fatigue-notch factor (K_f) greater than unity. After which, the preferential dissolution at the notch tips is modeled to dominate further penetration; and the chemical notch is modeled as a part of a microcrack.

3.3.2 Simulating the Cyclic-Strain-Induced Chemical-Notching Process

Cyclic strain should promote the growth of nucleated chemical notches although (as argued above) it has no effect on their nucleation [104]. The stable growth of a chemical notch leads to the formation of a severe notch and the nucleation of a microcrack. Unfortunately, there have been very few studies concerning chemical-notching kinetics particularly for systems subjecting to an applied strain. In the present study, the chemical-notching kinetics were derived from the electrochemical principles relating to localized electrochemical dissolution as discussed in Appendix A. Assuming an uniform current-density distribution at an active chemical notch (see model chemical notch in Fig. 3.4), a model which simulates the required fatigue life to produce a notch of a given depth (a_{pit}) was derived from Faraday's law:

$$N_{pit} = \frac{\rho f a_{pit}}{2M}\left[\frac{a_{pit}}{D C^{s}_{M^{+}}} + \frac{2zF}{i^{*}}\right] \tag{3.2}$$

where:

N_{pit}	=	Fatigue cycles to produce a chemical notch of a given depth (cycles)
ρ	=	Density of material (g/cm^3)
f	=	Test frequency (cycle/sec, Hz)
a_{pit}	=	Depth of a chemical notch (cm)
M	=	Atomic weight of material (g/mole)
D	=	Diffusion coefficient of dissolving metal ions (cm^2/sec)
C^{S}_{M+}	=	Saturation limit of metal ions in a given electrolyte (mole/cm^3)
z	=	Valence of dissolving cations
F	=	Faraday's constant (coulomb/mole)
i^*	=	Transient peak-current density of chemical notching (A/cm^2)

The transient peak-current density (i^*) in Eq. 3.2 depends upon the cyclic strain ($\Delta\varepsilon$) and is evaluated separately in Appendix A. The parameters in Eq. 3.2, except for the depth

of chemical notch (a_{pit}), are constants of the material, the environment and fatigue testing conditions. The critical depth of chemical notch (a_{pit}) which determines the fatigue-life period of chemical notching (N_{pit}) will be determined below.

3.3.3 Determining the Critical Depth (a_{pit}) of Chemical Notch

A chemical notch produced in the chemical-notching process is so small as to be incapable of introducing significant damage to the fatigue limit of smooth specimen until it grows to certain critical depth. The critical chemical-notch depth is a material-dependent quantity which reflects the "notch sensitivity" of a material. This quantity will be modeled in this section to determine the fatigue-life period of chemical notching process (N_{pit}).

The APD model considers that the uniformly penetrating chemical notch continues to degrade the surface of material until the notch is large enough to cause significant stress intensification. The development of significant stress at these notches should make notch tips (secondary active path, see Fig. 3.3b) electrochemically active in dissolution relative to the previous, more uniform chemical-notching processes (Fig. 3.3a).

The fatigue cycles prior to the preferential dissolution (microcrack development) of secondary active path (sites of stress intensification) is modeled as the fatigue-life period of chemical-notching process (N_{pit}). The following reported models will be adopted and assembled to characterize the critical chemical-notch depth (a_{pit}) which separates the first CFC process (chemical notching) of uniform penetration from the second CFC process (microcrack development) of preferential anodic dissolution.

Ting and Lawrence [115] have proposed the following formula to characterize the maximum non-damaging notch depth for steels:

$$a_n = \frac{1}{Y(a,c)}\left[\ 2.5 + 0.79\,\frac{L_o}{K_t}\ \right] \tag{3.3}$$

$$L_o = \frac{1}{\pi}\left(\frac{\Delta K_{th}}{\Delta S_e}\right)^2 \tag{3.4}$$

where:

a_n	=	Maximum tolerable defect size without damaging fatigue limit (μm)
$Y(a,c)$	=	Geometry factor
a	=	Notch depth or crack length (μm)
c	=	Notch diameter (μm)
L_o	=	Intrinsic crack length (μm)

K_t	=	Stress concentration factor (2.0-2.25)
ΔK_{th}	=	Threshold stress-intensity-factor range of crack growth (MPa $\sqrt{m}$)
ΔS_e	=	Fatigue limit (stress range) in ambient air (MPa)

Hagn [116] has derived the geometry factor (Y) as a function of notch depth (a) and notch diameter (c) for chemical notches (corrosion pits):

$$Y(a,c) = \frac{1.13 - 0.07\sqrt{\frac{a}{c}}}{\sqrt{1 + 1.47\left(\frac{a}{c}\right)^{1.64}}} \tag{3.5}$$

while Ahn and Lawrence [117] suggested the stress-concentration factor (K_t) for elliptical chemical notches:

$$K_t = 1 + 1.25\sqrt{\frac{2}{1 + \left(\frac{c}{2a}\right)^2}} \tag{3.6}$$

As shown in Fig. 3.5, a typically observed[9] chemical notch leading to a final fracture has an aspect ratio (a/c) of 0.4 and a stress-concentration factor (K_t) about 2.1. Therefore, a stress-concentration factor (K_t) ranging from 2.0 to 2.25 (a hemispherical notch) should be a reasonable approximation for Eq. 3.6.

Upon inserting Eqs. 3.4-3.6 into Eq. 3.3, the critical depth of chemical notch (a_{pit}) which begins inducing preferential dissolution of notch apex (microcrack development) is determined by equating the maximum non-damaging defect size[10] (a_n) in Eq. 3.3 with the depth of chemical notch (a_{pit}) in Eq. 3.2:

$$a_{pit} = a_n \tag{3.7}$$

the fatigue-life period (N_{pit}) of chemical notching process (first CFC process) before the initiation of microcracks[11] (second CFC process) is then simulated using Eq. 3.2.

---

[9] API-S135 steel fatigued in deaerated drilling fluid at 93.3 °C as will be detailed in Chapter IV.

[10] It must be emphasized that the maximum non-damaging defect size (a_n) evaluated in Eq. 3.3 does not imply the disappearance of the chemical-notching process. The real physical meaning of a_n simulated in Eq. 3.3 is the maximum defect size below which the fatigue-notch factor (K_f) remains unity. A chemical notch with its depth greater than a_n is considered to preferentially dissolve at the notch apex causing the uniform notching to become a relatively less competitive process (see Fig. 3.3).

[11] A chemical notch greater than a_n is simulated as a microcrack with an electrochemically-active crack tip and cathodically-protected crack faces.

3.4 MODELING (STAGE I) MICROCRACK DEVELOPMENT (N_{pl})

3.4.1 Overview and Major Assumptions

Short crack phenomena were reported to be essentially obscured for high-strength martensitic steel (AISI-4340) tested in ambient air [118]. An AISI-4340 steel tested in 3% NaCl solutions, however, has shown a pronounced acceleration of short crack propagation [21,119]. It is thus postulated that electrochemical reactions in electrolytic environments overcome mechanical-fatigue barriers in promoting microcrack development.

The development of microcracks is modeled as the preferential dissolution of crack tips using Faraday's law. An exponential-decay transient of rupture-current density at crack tips (Fig. 3.6) is employed to model the film rupture/film formation phenomena induced by cyclic loading: see Fig. 3.2. The bare-crack-tip current density is simulated based on a Tafel's relationship after obtaining the crack-tip potential from an electromigration-continuity theory (see details in Appendix B). A micro-galvanic coupling of microcrack tips (anodes) with passivated crack walls (cathodes) is assumed to localize anodic dissolution at the fresh crack tips (secondary active path) of plastic deformation. The simulation of the microcrack development is terminated when a characteristic crack length (a_i) is reached. Beyond this crack length (a_i), the electrochemical reactions at crack tips is considered to start losing their relative significance in comparison with the macroscopic crack growth of purely mechanical fatigue. The fatigue cycles spent between the end of chemical-notching period and the onset of macroscopic crack growth are modeled as the fatigue-life period of microcrack development (N_{pl}).

3.4.2 Modeling the Rate of Microcrack Development

We start with a most general description of corrosion-fatigue crack growth. In 1983, Wei and Gao [109] have suggested that fatigue-crack growth in a corrosive environment should be composed of mechanical-fatigue cracking, corrosion-fatigue cracking (CFC) and stress corrosion cracking (SCC) in the superposed manner seen in Eq. 3.8:

$$\left(\frac{da}{dN}\right)_T = (1-\varphi)\left(\frac{da}{dN}\right)_{me} + \varphi\left(\frac{da}{dN}\right)_{cfc} + \left(\frac{da}{dN}\right)_{scc} \tag{3.8}$$

where:

$\left(\frac{da}{dN}\right)_T$ = Total fatigue-crack growth rate (mm/cycle)

$\left(\frac{da}{dN}\right)_{me}$ = Crack growth rate of purely mechanical fatigue (mm/cycle)

$\left(\frac{da}{dN}\right)_{cfc}$ = Crack growth rate of purely corrosion fatigue (saturated) (mm/cycle)

$\left(\frac{da}{dN}\right)_{scc}$ = Crack growth rate of stress-corrosion cracking (mm/cycle)

φ = Degree of CFC "saturation" or "dominance" ($0 \le \varphi \le 1$)

The purely mechanically-induced microcrack development has been found to be negligible for medium/high strength martensitic steels [21,118]. For microcrack development under $K_{Imax} << K_{Iscc}$ in saline aqueous environments, we could further ignore (as discussed in Sec. 2.5.6) the stress-corrosion-cracking contribution in Eq. 3.8. Thus, for the microcrack development of medium-strength martensitic steels, e.g., API-S135, in certain saline-aqueous environments, e.g., thermally-elevated seawater drilling fluids, Eq. 3.8 can be reduced to:

$$\left(\frac{da}{dN}\right)_{pl} = \varphi \left(\frac{da}{dN}\right)_{cfc} \tag{3.9}$$

where:

$\left(\frac{da}{dN}\right)_{pl}$ = Rate of microcrack development (mm/cycle)

K_{Imax} = Maximum mode I stress-intensity factor (MPa $\sqrt{m}$)

K_{Iscc} = Onset stress-intensity factor of stress-corrosion cracking (MPa $\sqrt{m}$)

Equation 3.9 is adopted in the APD model to simulate microcrack development. The fully saturated corrosion-fatigue crack growth, $(da/dN)_{cfc}$, is modeled based on a postulated film rupture/film formation mechanism (see Fig. 3.2) as detailed in the following section.

The degree of CFC saturation (φ) in Eq. 3.9 is employed to simulate microcrack development in which the corrosion reaction is so slow[12] as to be incapable of establishing a fully saturated cracking assistance. The degree of CFC saturation ($0 \le \varphi \le 1$) for corrosion-assisted microcrack development strongly depends on fluid temperature (T) and test frequency (f). The details for obtaining φ are given in Appendix C.

3.4.3 Modeling Film Rupture/Film Formation Development of Microcracks

Assuming that an alternative dissolution/repassivation occurs at advancing crack tips (see Fig. 3.2), the development of microcracks can be modeled through a correlation with the total amount of charge dissipated during each fatigue cycle: see Fig. 3.6. Film rupture is

[12] For tests of high frequency or low fluid temperature where corrosion reaction rate is relatively slow.

assumed to occur once a cycle, and the bare crack tip is assumed to be subsequently repassivated (refilmed) during each unloading reversal.

The current-density trace following each film-rupture event is simulated using a well-known exponential decay phenomena [27-28,86,120]:

$$i_{rp}(t) = i_{bare} \exp(-\lambda t) \tag{3.10}$$

where:

$i_{rp}(t)$	=	Trace of dissolution-current density at crack tips after film rupture (A/cm^2)
i_{bare}	=	Bare-crack-tip current density (A/cm^2)
λ	=	Current-density-decay exponent
t	=	Time (sec)

The accumulated charge transferred (Q) per each film rupture/film formation event[13] is hence modeled by integrating the area under the rupture-current-density trace seen in Fig. 3.6:

$$Q = \int_0^{\frac{1}{2f}} i_{bare} \exp(-\lambda t)\, dt = \frac{i_{bare}}{\lambda}\left(1 - \exp\left(-\frac{\lambda}{2f}\right)\right) \tag{3.11}$$

By applying Faraday's law to simulate an active-path (crack-tip) penetration rate, one obtains:

$$\left(\frac{da}{dN}\right)_{cfc} = \frac{MQ}{zF\rho} = \frac{M\, i_{bare}}{zF\rho\lambda}\left(1 - \exp\left(-\frac{\lambda}{2f}\right)\right) \tag{3.12}$$

The details for modeling the bare-crack-tip current density (i_{bare}) in Eq. 3.12 are given separately in Appendix B. The modeling of current-density-decay exponent (λ) is discussed below.

3.4.4 The Current-Density-Decay Exponent (λ)

The current-density-decay exponent (λ) considered in Eq. 3.12, was derived empirically from experimental observations. The following Arrhenius-type relationship for λ suggested by Thomas and Wei [86] is adopted in the APD model:

---

[13] Each rupture/repassivation event corresponds to the damage occurred per each fatigue cycle.

$$\lambda = \lambda_o \exp\left(\frac{-\Delta H_a}{R' T}\right) \tag{3.13}$$

$$\lambda_o = A\left(\Delta K\right)^B \tag{3.14}$$

where:

λ_o	=	Intrinsic reaction-rate constant
ΔH_a	=	Apparent activation energy (KJ/mole)
R'	=	Gas constant (joule/mole °K)
T	=	Fluid temperature (°K)
ΔK	=	Applied stress-intensity-factor range (MPa $\sqrt{m}$)
A, B	=	Empirical coefficient and exponent
Q	=	Accumulated charge density transferred per cycle (coulomb/cm^2)

Thomas and Wei [86] have suggested that an apparent activation energy (ΔH_a) for HY-130 martensitic steel was about 27.83 KJ/mole. A series of current-density-decay exponents (λ) were reported. These values were obtained indirectly from a saturation concept of corrosion-fatigue cracking [86]. Figure 3.7 examines the correlation of Eqs. 3.13 and 3.14 by plotting λ values reported by Thomas and Wei [86]. The correlation is fairly satisfactory as suggesting that Eqs. 3.13-3.14 are good empirical measures to model the current-density-decay exponent (λ) for simulating the microcrack development in Eq. 3.12 .

3.4.5 Simulating the Fatigue-Life Period of Microcrack Development (N_{pl})

Microcracks are assumed to develop according to Eq. 3.9 until a characteristic crack length (a_i) is reached. At such a crack length (a_i), a rapid coalescence of multiple microcracks should produce a macroscopic crack of a sufficient size which permits the legitimate use of linear elastic fracture mechanism (LEFM) to describe subsequent crack growth. This characteristic crack length (a_i) is set to be equal to the initial crack length for LEFM integration and is assumed to have a value of 0.5 mm in the current study. The fatigue-life period of microcrack development (N_{pl}) is thus modeled as:

$$N_{pl} = \int_{a_{pit}}^{a_i} \frac{1}{\left(\frac{da}{dN}\right)_{pl}} da \tag{3.15}$$

For a crack having a length greater than the characteristic crack length (a_i), the electrochemical reactions occurring at its crack tip should lose their relative significance, in comparison with ΔK, on the subsequent crack growth, and should thus indicate the termination crack-initiation period. More discussion on the determination of corrosion-fatigue crack-initiation life is given below.

3.5 Simulating Synergistic Electrochemical-Mechanical Interactions for Modeling Crack-Initiation Life (N_i)

We have defined the fatigue life before macroscopic crack growth to be the crack-initiation life (N_i):

$$N_i = N_{pit} + N_{pl} \tag{3.16}$$

The crack-initiation life (N_i) obtained from Eq. 3.16 is expected to give a good estimate for low-strain-rate CFC but only when electrochemical processes[14] dominate. Equation 3.16 is not capable of predicting high strain-rate CFC in which mechanical straining is the primary driving force for crack initiation. For such an instance, high strain-rate CFC, a purely mechanical model, e.g., the strain-life approach [121], should be used.

A corrosive environment tends to shorten the fatigue-crack initiation life. The synergistic interaction of mechanical straining and electrochemical dissolution is believed to accelerate the crack-initiation process. A simple electrochemical-mechanical interaction rule suggested by the form of Miner's rule [107] is thus suggested by the writer:

$$\frac{N_i}{N_{st}} + \frac{N_i}{(N_{pit} + N_{pl})} = 1 \tag{3.17}$$

For a high-strain-rate CFC (e.g., $N_i < 3.0 \times 10^5$ at a frequency of 2 Hz), the simulated crack-initiation life should be dominated by the strain-life approach (N_{st}); for a low-strain-rate CFC (e.g., $N_i > 1.0 \times 10^6$ at a frequency of 2 Hz), the crack-initiation life should mainly be determined by the active-path dissolution of chemical-notching process and microcrack development (Eq. 3.16): see APD model simulation shown in Fig. 3.8. For an intermediate-strain-rate CFC, a strong synergistic electrochemical-mechanical interaction should be anticipated (see Fig. 3.8).

---

[14] The modeling of chemical-notching process (N_{pit}) and microcrack development (N_{pl}) in the APD model considered only electrochemical dissolution processes without taking any mechanical effects into consideration.

Utilizing Eq. 3.17 to model the synergistic electrochemical-mechanical interaction is merely a suggested way of overcoming our poor understanding of this complex phenomena. Further development of this concept (Eq. 3.17) is desirable and necessary.

3.6 MODELING (STAGE II) MACROSCOPIC CRACK GROWTH (N_{p2})

The observed patterns of crack growth in corrosive environments which induce chemical notching suggest the occurrence of multiple crack interaction and intensive crack coalescence during macroscopic crack growth [1,53,122]. The macroscopic crack-growth (stage II) rate in saline aqueous environments can thus be modeled by the Paris power law using parameters (C and m) obtained in ambient air from the same material together with a properly formulated crack-shape-development model for ΔK.

Alternatively, one could use actual test data (C, m) from the crack growth of a similar material in aqueous solutions containing chloride salts (e.g., 3.0~3.5% NaCl) to model the rate $(da/dN)_{p2}$ of macroscopic crack growth and its corresponding life period (N_{p2}) by the integration of the crack growth rate $(da/dN)_{p2}$:

$$\left(\frac{da}{dN}\right)_{p2} = C\left(\Delta K\right)^m \tag{3.18}$$

$$N_{p2} = \int_{a_i}^{a_f} \frac{1}{\left(\frac{da}{dN}\right)_{p2}} da \tag{3.19}$$

where:

$\left(\frac{da}{dN}\right)_{p2}$	=	Rate of macroscopic crack growth (mm/cycle)
C, m	=	Paris constants in tested environment
N_{p2}	=	Fatigue cycles of macroscopic crack growth (cycles)
a_i	=	Initial crack length for LEFM integration (mm)
a_f	=	Final crack length for LEFM integration (mm)

3.7 VARIABLES IN THE APD MODEL

The proposed APD model requires several electrochemistry parameters (as listed in Table 3.1) such as: the electrochemical potentials (E_{bulk}), the exchange current densities (i_o),

the redox potentials (E_{eq}), the apparent activation energy (ΔH_a), the valence (z), and the Tafel's slopes (β_a, β_b) of material as well as the temperature (T), the electrolytic conductivity (η, R_{film}), the cation diffusivity (D), and the cation saturation limits (C^s_{M+}) of electrolytes to make fatigue-life predictions. Most of these parameters can be easily obtained from the literature or from electrochemical measurements. However, the parameters of the exchange current density of anodic dissolution at crack tips which involve plastic deformation are not available and are very difficult to measure. In the present study, a value of 1.5×10^{-5} A/cm^2 is adopted and is validated later by examining the polarization behavior (will be shown in Chapter V) of an electrode (API-S135) subjected to a stress greater than material yield strength (S_y). This value ($i_o^{plastic}$) leads to obtain reasonable estimates of fatigue life of steels in saline aqueous environments as will be presented later in Chapter V.

The material properties (M, ρ, S_y), strain-life parameters (σ_f', ε_f', etc.) and crack-growth parameters (Paris constants, C and m) are also needed: Table 3.1 summaries the variables appearing in the APD model.

CHAPTER IV: EXPERIMENTAL METHODOLOGY

4.1 PURPOSE

In order to verify the proposed APD model, fatigue tests and polarization experiments on a drill-pipe steel (API-S135) in simulated offshore-drilling environments (seawater drilling fluids at 93.3 °C and 1 atmosphere pressure) were conducted. The effects of electrochemical potentials (E_{bulk}), varying conditions of fluid aeration[1] and the addition of a polymeric inhibitor (Conquor 404) on the corrosion-fatigue life of API-S135 were studied. The effectiveness of using cathodic over-potentials or galvanic aluminum plating for mitigating the corrosion fatigue of API-S135 was also evaluated.

The corrosion rate of API-S135 in the drilling fluids of various aeration conditions and temperature (T) were interpreted using Tafel's slopes of measured polarization diagrams. The mechanism (anodic or cathodic) driving crack initiation for the investigated CFC system was clarified by monitoring current/potential transients of each fatigue cycle. The cracking susceptibility caused by cathodic reduction reactions (hydrogen embrittlement) on the stress-corrosion cracking (SCC) and on the corrosion-fatigue life of API-S135 were also studied under impressed electrochemical potentials (E_{bulk}) down to -1.0 V (SCE).

4.2 MATERIALS

The chemical composition and mechanical properties of API-S135 drill-pipe steel[2] can be found in Tables 4.1 and 4.2, respectively. This material was selected because it represents one of the highest-strength-grade drill-pipe steel used in offshore drilling industry. API-S135 has been given the standard heat treatment consisting of quenching from 840 ~ 870 °C at a quenching rate of 10.7 m/minute followed by tempering at 550 °C. The microstructures[3] of API-S135 steel as revealed by etching with Vilella's reagent[4] are shown in Fig. 4.1 and Fig. 4.2 for sections parallel and perpendicular to the longitudinal axis of drill pipe, respectively. No orientation difference in the microstructure was observed. API-S135 steel appeared to have predominantly fine-martensitic structure with austenitic-grain size around 10 ~ 25 μm.

The composition of the seawater drilling fluids[5] is tabulated in Table 4.3. The fluid containing no polymeric inhibitor (Conquor 404, phosphate ester salt) is designated as

---

[1] Aerated with medical air and deaerated with ultra-high purity (UHP) nitrogen.
[2] Specimens were machined and donated by Amoco Research Center, Naperville, IL.
[3] Dptiphot APX-II, Nikon, Japan.
[4] 5 ml HCl, 1 g picric acid, 100 ml ethyl alcohol (95%).
[5] Drilling fluid compounds and inhibitor were donated by M-I Drilling Fluid Company, Houston, TX.

ordinary fluid while the other containing a polymeric inhibitor of 0.11 ~ 0.3% is termed "chemically-inhibited fluid". The test fluid was refreshed for each specimen.

4.3 FATIGUE TESTS UNDER FREE CORROSION

4.3.1 Specimen Preparation

The specimens of uniaxial-tensile fatigue were machined from standard 4 inch O.D. drill pipes to the dimension shown in Fig. 4.3. All specimens were machined from the pipe sections oriented parallel to the longitudinal axis of the pipes. The surface of the specimens was ground and polished (≈ 600 grit). The specimens were then ultrasonically degreased in an ethanol bath three times for 10 minutes using fresh ethanol each time. The residual ethanol on the specimen surface was evaporated thoroughly in dry air before coating the specimen with fully-cured silicon rubber to selectively expose the middle portion (about 20 mm) of gauge section to testing environments.

4.3.2 Environmental Conditioning

The test set-up is shown in Fig. 4.4. A 20 liter polypropylene reservoir contained the seawater drilling fluid (0.4 M [Cl^-], 3.1% NaCl, see Table 4.3) and maintained it at a constant temperature (93.3 °C). This reservoir also permitted a constant control of environmental species (anions and pH). A closed-loop circulation of seawater drilling fluid[6] between the reservoir and testing chamber was carried out by a peristaltic pump.[7] The circulating fluid was confined within a Norprene tubing without any possible contamination from a pump head. To avoid galvanic coupling with dissimilar metals, the whole system was constructed with thermal-resistant polypropylene, Teflon, and glass. The fluid was thus allowed no contact with any other metal except for the specimen.

A proportional thermostat[8] with a thermistor probe[9] (0.2 °C accuracy) positioned near sample surface supplied additional heat to the testing chamber to compensate for the heat loss of the testing fluid during transmission. Moisture loss was minimized by condensing water vapor and by water-saturating air[10] or nitrogen[11] by bubbling them through de-ionized water.

---

[6] Thermal degradation of seawater drilling fluid was observed. The agglomeration of decomposed drilling-fluid components reduced both the pH and the viscosity of testing fluid. Mixture of solution and agglomerates was pumped within the closed-loop circulation system.

[7] MasterFlex tubing pump, Cole-Parmer Instrument Company, Niles, IL.

[8] YSI Model 72 Proportional Temperature Controller, YSI Company, Inc., Yellow Springs, OH.

[9] YSI series 400 tubular temperature probe, YSI Company, Inc., Yellow Springs, OH.

[10] Medical air, breathing quality.

[11] Ultra-high purity nitrogen (99.99%).

4.3.3 Monitoring Devices

A schematic representation of the environmental chamber is shown in Fig. 4.5. This set-up offers a continuous measurement of electrochemical potential (E_{bulk}) and displacement during a fatigue test. Both measured quantities (electrochemical potential and displacement) were recorded by a data acquisition system[12] with a 400-cycle recording interval.

The electrochemical potential[13] (E_{bulk}) was monitored by an electrometer[14] having its internal resistance up to 10^{14} ohms which thus allowed zero polarization due to the measurement. A saturated calomel electrode[15] (SCE) was used as a reference. No correction concerning the electrical junction between dissimilar metals at electrical connections was performed. A salt-bridge probe having ceramic junctions[16] at both ends was positioned 1 ~ 2 mm away from the specimen with one end while connected to the reference electrode with the other end in a saturated KCl solution.

An extensometer (MTS,[17] 50.8 mm) was mounted on the extension arms attached to the grip section of a specimen. This device gave the peak values of displacement which were correlated with the observations of the electrochemical potential (E_{bulk}) during a fatigue test.

4.3.4 Testing Procedures

A degreased specimen was first surrounded by an O-ring sealed environmental chamber shown in Fig. 4.5. The specimen was then mounted in a MTS frame using hydraulic collet grips. After introducing the well-conditioned seawater drilling fluid into the environmental chamber, the whole circulation system was permitted to stabilize for 2.5 ~ 3.0 hours before starting a test. This pre-exposure period was intended to generate a thin oxide layer (passive film) on specimen surface to minimize the possible scatter in test results. The fatigue loading was maintained at a stress ratio (R) of 0.1 and a test frequency (f) of 2 Hz under a sinusoidal loading control throughout the program.

4.4 Fatigue Tests under Potential Control or Cathodic Protection

4.4.1 Fatigue Tests under Potential Control

A schematic representation of potential-controlled set-up is given in Fig. 4.6. A potentiostat[18] was utilized to control electrochemical potential (E_{bulk}) during fatigue tests.

[12] LabVIEW for Macintosh, National Instruments, Austin, TX.
[13] Mixed-electrode potential under free corrosion.
[14] Model 610B electrometer, Keithley Instruments, Inc., Cleveland, OH.
[15] Standard glass-body calomel reference electrode, Fisher Scientific, Pittsburgh, PA.
[16] Replacement ceramic junctions, Corning Glass Works, Corning, NY.
[17] MTS Systems Corp., Eden Prairie, MN.
[18] Model 273 Potentiostat/Galvanostat, EG & G Princeton Applied Research, Princeton, NJ .

D.C. current as required was passed via a counter electrode of woven platinum gauze (99.9 Pt, 50 mm × 50 mm) to maintain the working electrode (fatigue specimen) at specified potentials with respect to a saturated calomel electrode (SCE). The working electrode (fatigue specimen) was electrically insulated from fatigue frame using inserts[19] made of Garolite. After setting up the specimen with well-conditioned drilling fluid circulating, the system was polarized to a desired potential and then allowed to stabilize for 2.5 ~ 3.0 hours before applying load. The same testing parameters as given in Sec. 4.3.4 were employed for the fatigue tests.

4.4.2 Preparation of Aluminum-Plated (IVD-Al) Specimens

Some fatigue specimens were aluminum plated[20] to examine the suitability of using galvanic coatings for protecting drill pipes from corrosion fatigue during offshore-drilling operation. Specimens as seen in Fig. 4.3 were first ultrasonically degreased under an ethanol bath as described in Sec. 4.3.1 and then solvent cleaned with trichloroethylene. Any surface oxides on specimens were then blast away to expose fresh metal by an abrasive blast at 0.138 MPa (20 psi) using the aluminum-oxide (Al_2O_3) powder of 150 mesh. Great care was taken to minimize surface roughness or irregularities imposed at this stage.

Once the specimens were hung on a rack, the vacuum chamber was pumped down to 0.001 MPa (10 ~ 5 Torr) to sufficiently outgas the chamber and to remove previously absorbed gases or vapors from the specimens. The plating chamber was then backfilled with inert gas (argon) before impressing a negative D.C. potential upon the substrate specimens for plating. Under such a bias potential, positive ions were produced in local atmosphere through the collisions between high-energy electrons and gas atoms. Plasma bombardment was established by attracting those positive ions to the negatively charged substrate. The plasma bombardment which further eliminates surface contamination on the substrates was allowed to last for 10 ~ 20 minutes or until a phenomena of "glow discharge" appeared.

An Ion-Vapor-Deposition (IVD-Al) process followed to plate aluminum on the specimens. Once the aluminum wires were vaporized by a high current source, the aluminum atoms were ionized[21] through collisions with high-energy electrons or with metastable gas atoms. These positively charged ions were attracted to and deposited on the substrates of negative charges. The feeding rate of aluminum wire was carefully controlled to ensure an efficient growth and a good adhesion of the aluminum plating until a plating thickness[22] of about 25.4 μm (1 mil) on the substrates was achieved.

---

[19] The Garolite inserts has a dimension: 19 mm (3/4") O.D., 11 mm (7/16") I.D., 38 mm (1.5") long.
[20] Coating processes were conducted and donated by Titanium Finishing Company, East Greenville, PA.
[21] This process is called peening ionization.
[22] Satisfied MIL-C 83488, Class I, type II, 0.001" thickness.

A burnishing process followed to consolidate the porous IVD plated aluminum using glass media at an applied pressure of 0.14 ~ 0.21 MPa (20 ~ 30 psi). This process of compressing yielded a more uniform, less porous and more durable aluminum plating than before. A chromate-converted topcoat was then applied to seal remaining coating porosity for achieving a maximum corrosion protection. More detailed information about the ion-plating process can be obtained from review papers by Nevill [123], and by Ahmed [124].

4.4.3 Fatigue Tests of IVD-Al Plated Specimens

The fatigue test of IVD-Al plated specimens used the same testing parameters and procedures given in Sec. 4.3.4.

4.5 POTENTIODYNAMIC POLARIZATION SCANS

4.5.1 Preparation of Disk Electrodes

Sample disks (11.1 mm in diameter, see Fig. 4.7) of 2 mm thickness were cut[23] from the grip sections of fatigue specimens using a low-speed diamond saw.[24] Sample disks were ultrasonically cleaned under an ethanol bath, air dried and then cast with epoxy.[25] The surface of sample disks was exposed by grinding the casts with silicon carbide (SiC) papers until a surface finish of 20 μm (1200 grit) was reached. Sample disks were then free from the casts by dissolving the casting epoxy away using fresh acetone. The polished sample disks were ultrasonically cleaned under an acetone bath, air dried, and re-polished using SiC papers of 20 μm (1200 grit) to ensure a clean surface finishing of no epoxy contamination. A Teflon coated hook-up wire (26 AWG) was then soldered on the back face of a sample disk and the connection was secured with a silicon rubber of full maturity. The sample disks were then installed in Teflon electrode holders[26] (Fig. 4.7) and were exposed only the polished surfaces to environments. The disk electrodes were stored in a desiccator before polarization tests.

4.5.2 Potentiodynamic Polarization Scan on Disk Electrodes

The intent of this experiment was to study the corrosion rate of API-S135 under various seawater drilling fluids. The fluids of various temperature (T) and conditions of aeration were used in this study.

The disk electrode prepared in Sec. 4.5.1 was mounted on an environmental chamber as sketched in Fig. 4.8. A fully aerated or deaerated drilling fluid was then introduced into

[23] Cutting was lubricated with a mixture of polishing oil and propylene glycol.
[24] Isomet low speed diamond saw, Buehler Ltd., Lake Bluff, IL.
[25] Castolite mounting epoxy, Buehler Ltd., Lake Bluff, IL.
[26] The electrode holder is 12.7 mm (0.5") in diameter and 89 mm (3.5") long.

the chamber and was circulated between the chamber of disk electrode and the environmental reservoir. The temperature of the disk electrode was monitored by a digital thermistor thermometer[27] via the thermistor probe. A salt-bridge probe filled with KCl was positioned near disk-electrode surface at about 1 mm apart with one end while connected to a reference-electrode unit with the other end. System was allowed to stabilized for about 30 minutes before the free-corrosion potential (E_{corr}) was recorded. A potentiostat then automatically polarized (anodically up to -0.2 V SCE or cathodically down to -1.5 V SCE) the disk electrode with a scan rate of 0.2 mV/sec. This unit passed polarization current via a platinum counter electrode to instantaneously maintain the disk electrode at specified electrochemical potentials (E_{bulk}) with respect to a saturated calomel electrode (SCE) during scanning. The polarization current and electrochemical potential (E_{bulk}) were recorded every 20 ~ 30 seconds by the data acquisition system. The effects of fluid temperature (T) and fluid-aeration conditions on the corrosion rate (Tafel's slope) of API-S135 were both investigated.

4.5.3 Potentiodynamic Polarization Scan on Straining Electrodes

The intent of this experiment was to study the effect of applied stress on the corrosion rate of API-S135 in seawater drilling fluids. The fluid used in this study were heated to 93.3 °C and fully deaerated with UHP N_2.

A working electrode having the same preparation described in Sec. 4.3.1 was immersed in fully-conditioned drilling fluid after setting up the testing chamber as shown in Fig. 4.6. Garolite inserts as seen in Fig. 4.6 were gripped with the electrode to ensure an electrical insulation between the working electrode and fatigue frame. The working electrode was then loaded to various stress states including: zero stress, 80% of yield strength (S_y), onset of yielding, and post-yielding stress. The straining electrode was allowed to stabilize under free corrosion for about 30 minutes before impressing polarization current. An anodic potentiodynamic polarization scan was then imposed from free-corrosion potential (E_{corr}) up to -0.4 V (SCE) with a scan rate of 0.2 mV/sec. The electrochemical potential (E_{bulk}) and polarization current during the polarization scans were recorded.

4.5.4 Hysteresis Polarization Scan on Disk Electrodes

The intent of this experiment was to study the effect of electrochemical-potential perturbation on the surface roughening[28] of API-S135 in seawater drilling fluids. The fluid used in this study were thermally elevated to 93.3 °C and fully deaerated with UHP N_2.

---

[27] Thermistor thermometer Model 8402-20, Cole Parmer Instrument Company, Niles, IL.

[28] The chemical-notching rate in the APD model was characterized with the velocity of potential perturbation caused by cyclic loading as detailed in Appendix A. The intent of this experiment is to verify the above modeling assumption.

The preparation of disk electrodes and the experimental set-up for hysteresis polarization scans were the same as those described in Sec. 4.5.1 and Sec. 4.5.2, respectively. The drilling fluid was first fully deaerated and raised to a temperature of 93.3 °C. After introducing drilling fluid into environmental chamber, system was allowed to stabilized for 3 hours. A hysteresis polarization ranging from -0.8 to -0.6 V (SCE) with a varying scan rates: 0.05, 0.2, 1.0, 5.0, and 30 mV/sec, was then imposed on the disk electrodes for additional 3 hours. A disk electrode freely corroded for the same period of immersion was also prepared for a comparison purpose. After the polarization experiment was finished, sample disks were removed from their electrode holders, rinsed with cold water and then air dried. Additional ultrasonic cleaning was carried out twice in an ethanol bath for 5 minutes. The disks were then air dried and kept in a desiccator before examining their surfaces under a microscope.

4.5.5 Hysteresis Polarization Scan on Straining Electrodes

The intent of this experiment was to clarify the type of corrosion (anodic or cathodic) responsible for the fracture of statically-stressed API-S135 steel in seawater drilling fluids. The fluids used in this study were fully deaerated with UHP N_2 at various temperature.

Same test set-up as in Sec. 4.5.3 was employed for straining hysteresis-polarization scans. After stabilizing without applying stress under free corrosion for 2.5 ~ 3.0 hours, the working electrode was loaded up to 80% of material yield strength (S_y) and was kept at this load through out the duration of polarization scans. A hysteresis polarization with a scan rate of 0.05 mV/sec was then imposed on the straining electrode with electrochemical potentials ranging from -1.0 V (SCE) to -0.2 V (SCE). The initial loop was polarized from free-corrosion potential (E_{corr}) up to the upper potential boundary of -0.2 V (SCE) and then decreased down to the lower potential boundary of -1.0 V (SCE). Simultaneously imposing static stress with hysteresis polarization was sustained until the electrode fractured (fully separated). The electrochemical potential (E_{bulk}) at which fracture occurred was recorded to determine the relative significance of anodic effects (active-path dissolution) in comparison with cathodic effects (hydrogen embrittlement) on the crack initiation of the straining electrode. Fluids at temperature of 25.5 °C and of 93.3 °C were both used.

4.6 Monitoring of Current/Potential Transient Phenomena

4.6.1 Purpose

The intent of this experiment was to study the mechanism which accelerates the fatigue-crack initiation of API-S135 due to the presence of seawater drilling fluids. The perturbation of electrochemical potential (E_{bulk}) under free corrosion and the trace of

anodic/cathodic current transient caused by cyclic loading of various waveforms under potentiostatic control were investigated.

4.6.2 Specimen Preparation

A specimen of tensile-fatigue configuration (see Fig. 4.3) was used to simulate the crack tips of the corrosion fatigue. The specimen was coated with silicon rubber to expose only the middle-gauge section (about 20 mm long) to the test environment.

Another specimen with a semi-circular-circumferential notch as shown in Fig. 4.9 was employed to simulate the crack walls. The specimen was coated with fully-cured silicon rubber except for the portion where the notch was located. A salt-bridge probe was positioned toward the wall of the notch to monitor/control electrochemical potential (E_{bulk}) at such a traction-free surface during corrosion fatigue.

4.6.3 Experimental Procedures

The seawater drilling fluid was first fully deaerated with UHP N_2 and well conditioned according to Sec. 4.3.2. The specimen was electrically insulated from fatigue frame using Garolite inserts installed within hydraulic grips. After introducing the seawater drilling fluid into the environmental chamber, the system was allowed to stabilized for 30 minutes before applying load. Various waveforms of cyclic loading were then applied on the specimen for at least 100 cycles together with a potentiostatic or galvanostatic control via a potentiostat. The potential perturbation under galvanostatic control or under free corrosion and the input current under potentiostatic control were recorded within the period of each loading cycle.

Various waveforms (trapezoidal and sinusoidal) of cyclic loading were applied to study current/ potential transient phenomena. For all trapezoidal waveforms, the maximum-stress-holding period (t_{hold}) was kept constant at 5 seconds. The stress-rising period (t_{rise}) was symmetrical to the stress-descending period ($t_{descend}$). A sequence of stress-rising periods consisting of 0.1, 0.25, 0.5, and 5 seconds which correspond to the sinusoidal waveforms of 5 Hz, 2 Hz, 1 Hz, and 0.1 Hz, respectively, were used. The tests using sinusoidal waveforms at frequencies of 5 Hz, 2 Hz, 1 Hz, and 0.1 Hz were also conducted for comparison.

4.7 Fracture Surface Analysis

4.7.1 Sample Preparation

Fracture surfaces of tested specimens after corrosion-fatigue fracture were first rust-cleaned by pressing the fracture surface against a tissue soaking with polishing oil.[29] Many

[29] Polishing oil, Buehler Ltd., Lake Bluff, IL.

large, loose rust particles were observed to be removed from the fracture surface by this process. The fracture-surface samples were then cut from these fractured specimens using the low-speed diamond saw lubricated with a mixture of polishing oil and propylene glycol. The samples were ultrasonically de-oiled under an acetone bath for 5 minutes before being cleaned twice under a fresh ethanol bath for another 5 minutes. After being air dried, the samples were mounted on sample stubs using a graphite cement and examined using a scanning electron microscope (SEM).[30]

4.7.2 Crack Initiation Sites and Fracture Surfaces

Crack initiation sites were studied using a SEM equipped with an energy dispersive X-ray analyzer (EDXA).[31] The chemical composition of observed corrosion precipitates on fracture surfaces were analyzed by the EDXA. An electron acceleration voltage of 25 KV was applied for all the analysis. The fracture surfaces of corrosion fatigue were compared with those of ambient-air fatigue.

[30] Model S-530, Hitachi Corp., Tokyo, Japan.
[31] PGT EDXA detector, Princeton Gamma Technical Corp., Princeton, PA.

CHAPTER V: EXPERIMENTAL VERIFICATION OF THE APD MODEL

5.1 GENERAL: MATERIAL PROPERTIES AND ELECTROCHEMICAL PARAMETERS USED IN THE APD MODEL SIMULATIONS

The chemical composition of the materials to be investigated can be found in Table 4.1 and Table 5.1 for martensitic steels (API-S135) and hot-rolled steels (JIS SS41, JIS SM50A), respectively. The fatigue-life properties including strain-life parameters (σ_f', ε_f', etc.), crack-growth parameters (Paris constants, C and m), and ambient-air fatigue limit (ΔS_e) are tabulated in Table 5.2. For predicting the mechanical crack-initiation life (N_{si}) of smooth specimens in saline aqueous environments, the fatigue-notch factor (K_f) applied in the strain-life approach was taken as 1.2 for all the corrosion-fatigue systems investigated in this study. This K_f having a value greater than unity was arbitrarily selected to simulate the effects of surface roughening[1] due to the presence of a corrosive environment on the mechanical fatigue-crack initiation.

The electrochemical parameters in the APD model simulations for API-S135 steel in deaerated seawater drilling fluid (0.4M [Cl^-]) at 93.3 °C are listed in Table 5.3. The electrochemical parameters obtained from potentiodynamic polarization scans on API-S135 in various seawater drilling fluids (varying condition of aeration, varying temperature) are compared in Table 5.4. These parameters will be applied to the corrosion fatigue of JIS SS41 and JIS SM50A steels in 3.0% NaCl (≈ 0.5M [Cl^-]) solution as well since that it is the major chemical component (Fe) and the corrosive agent (Cl), but not the mechanical strength (S_y), which would affect the electrochemical characteristics. The computation of salt-film ohmic drop for determining the electrochemical potential (E_{bulk}) at the entrance of microcracks is illustrated in Appendix D.

The electrochemical potential (E_{bulk}) at the onset of microcrack development under free corrosion is set to be -0.73 ~ -0.74 V (SCE) (see Fig. 3.1a) for the corrosion fatigue in seawater drilling fluids at 93.3 °C, and to be -0.55 ~ -0.56 V[2] (SCE) for those in NaCl solutions at 25 °C.

The curve-fitting parameters A and B obtained in Fig. 3.7 for HY-130 steel will be utilized to approximate the current-density-decay exponent (λ) for all the following APD model simulations. The mechanical properties, microstructure, and chemical composition of HY-130 steel are very similar to that of API-S135 steel as can be seen in Tables 4.1-4.2.

---

[1] Upon contacting with a saline aqueous solution, the surface of a smooth specimen can no longer be as smooth as that in ambient air; although it was originally polished before a corrosion-fatigue test.

[2] This will be checked later by potentiodynamic polarization measurements.

5.2 VERIFICATION: EFFECTS OF FLUID AERATION

5.2.1 Effects of Fluid Aeration on the Corrosion Rate (Tafel's Behavior)

The potentiodynamic polarization scans (both anodic and cathodic) of API-S135 steel in seawater drilling fluid (93.3 °C) purged with ultra-high-purity (UHP) N_2 (deaerated fluid) and those purged with medical air (aerated fluid) are compared in Fig. 5.1. Both anodic and cathodic Tafel's slopes are indicated with the polarization curves. The condition of fluid aeration affects only the cathodic polarization. Fluid aeration has, however, no effect on the anodic polarization behavior.

5.2.2 Effects of Fluid Aeration on the Corrosion-Fatigue Life

A summary of the fatigue-test results performed in seawater drilling fluids at 93.3 °C are presented in Fig. 5.2. Corrosion-fatigue life decreases with an increasingly applied stress amplitude ($\Delta S/2$). The presence of seawater drilling fluids greatly reduces the fatigue resistance of API-S135 relative to the test results (also seen in Fig. 5.2) obtained in ambient air. There is, however, no significant effect of varying fluid aeration on the corrosion-fatigue S-N behavior of API-S135. Adding a polymeric inhibitor (Conquor 404, 0.11%), does not cause any noteworthy effect of fluid aeration either as demonstrated in Fig. 5.3.

Various conditions of aeration also produce no influence on the macroscopic crack growth of the corrosion fatigue as seen in Tables 5.5 and 5.6 for tests in seawater drilling fluids without and with adding a polymeric inhibitor (Conquor 404), respectively.

The S-N curves (see Figs. 5.2-5.3) simulated by the APD model predict no significant influence of fluid aeration and give a satisfactory agreement with the test results.

5.3 VERIFICATION: EFFECTS OF ELECTROLYTIC CONDUCTIVITY (η) ON THE CORROSION-FATIGUE LIFE

The effect of adding a polymeric inhibitor (Conquor 404, 0.11%) upon the CFC resistance of API-S135 can be seen in Figs. 5.4 and 5.5 for tests in aerated fluids and in deaerated fluids, respectively. The improvement on corrosion-fatigue resistance by adding this inhibitor is essentially obscured. Although adding the polymeric inhibitor mainly reduces the electrolytic conductivity of the drilling fluids, the APD model predicts no effect of adding such an inhibitor on the S-N behavior of the corrosion fatigue as also seen in Figs. 5.4 and 5.5. The S-N curves simulated by the APD model agree with the test results.

5.4 VERIFICATION: EFFECTS OF ELECTROCHEMICAL POTENTIAL (E_{bulk}) ON THE CORROSION-FATIGUE LIFE

5.4.1 Controlled Potential by Potentiostat

The fatigue life of API-S135 in seawater drilling fluid at 93.3 °C is greatly reduced by raising the electrochemical potential (E_{bulk}) toward noble potentials (less negative) as shown in Fig. 5.6. The APD model simulations seen in the same figure also appear sensitive to the electrochemical potential (E_{bulk}) and appear to be in good agreement with the test data. A comparison of corrosion-fatigue test results under cathodic protection with those obtained in ambient air is given in Table 5.7.

5.4.2 Controlled Potential by Galvanic Coupling with Aluminum

The corrosion-fatigue life should be extended by galvanically protecting API-S135 according to the APD model simulations and according to the experimental evidence both shown in Fig. 5.6. Ion-vapor-deposited Al (IVD-Al) appears to partially restore the immunity of API-S135 (see Table 5.7) from corrosion fatigue in seawater drilling fluid.

5.5 VERIFICATION: EFFECTS OF STRESS RATIO (R) OR MEAN STRESS ON THE CORROSION-FATIGUE LIFE

To check the validity of the APD model at various stress ratios (R), data [57] obtained from the fatigue tests of API-S135 steel in seawater at 25 °C with a constant mean stress (517.2 MPa) are plotted against a S-N curve (see Fig. 5.7) simulated by the APD model. Agreement between the test data and the model prediction is satisfactory. Another corrosion-fatigue system of API-S135 in seawater under reversed bending (R = -1) [133] was also examined and is presented in Fig. 5.8. The APD model again provides a good estimation of the corrosion-fatigue life. The presence of the seawater, regardless of the stress ratio (R) or the applied mean stress of fatigue loading, causes a large reduction in the fatigue life relative to the fatigue-test results obtained in ambient air.

The initiation-propagation (I-P) model was examined with test data in ambient air to check the suitability of fatigue-life parameters tabulated in Table 5.2. As seen in Figs. 5.7 and 5.8, the I-P model predictions using the strain-life and the Paris parameters of AISI-4340 steel reasonably approximates the ambient-air S-N behavior for API-S135 steel.

5.6 VERIFICATION: EFFECTS OF TEMPERATURE (T)

5.6.1 Effects of Temperature (T) on the General Corrosion Rate (Tafel's Behavior)

A different temperature (T) produces a different polarization behavior for API-S135 in both anodic and cathodic branches as shown in Fig. 5.9. The corrosion rate (current density) of a given electrochemical potential (E_{bulk}) at ambient temperature (T = 25°C) appears lower than that at elevated temperature (T = 93.3°C). This temperature effect is also apparent when electrodes are subjected to a static stress up to 80% of material yield strength (see Fig. 5.10). The free-corrosion potential, mixed-electrode potential (E_{corr}), in contrast to current density, is raised with decreasing temperature (E_{corr} = -0.60 V at T = 25 °C; E_{corr} = -0.73 V at T = 93.3 °C) as shown in Fig. 5.9.

5.6.2 Effects of Temperature (T) on the Stress-Corrosion Rate

Stress-corrosion-cracking (SCC) susceptibility of API-S135 decreases with increasing temperature (T): compare Fig. 5.11 with Fig. 5.12. When an electrode is subjected to static stress greater than the yield stress in seawater drilling fluid at 25 °C, the polarization current density is significantly increased (see Fig. 5.11). No difference in polarization current density for a varying applied stress, however, is detected in case the electrode is polarized in seawater drilling fluid at 93.3 °C (see Fig. 5.12). A plastically pre-deformed electrode in Fig. 5.12 exhibits a noticeable increase of current density only when the impressed electrochemical potentials (E_{bulk}) are greater than -0.6 V.

5.6.3 Effects of Temperature (T) on the Corrosion-Fatigue Life

A comparison of fatigue life obtained in seawater drilling fluid at 93.3 °C with that observed [133] in seawater at 25 °C is presented in Fig. 5.13. The API-S135 sustains a shorter fatigue life when tested at ambient temperature than tested at elevated temperature, particularly under the applied stress amplitudes ($\Delta S/2$) of high-cycle fatigue. Frequency effect from 1 to 2 Hz is considered non-significant for the above comparison. For both temperature (T), the APD model simulated S-N curves are in good agreement with test data.

5.7 VERIFICATION: EFFECTS OF MATERIAL STRENGTH (S_y) ON THE CORROSION-FATIGUE LIFE

The effects of material strength (S_y) on corrosion-fatigue resistance and on the APD model simulations were also investigated. Three materials of various yield strength (S_y) are studied including JIS SS41 (S_y = 300 MPa) [78], JIS SM50A (S_y = 420 MPa) [78], and API-

S135 (S_y = 931 MPa) [133]. Figure 5.8, Fig. 5.14, and Fig. 5.15 compare the test data of fully-reversed bending (R = -1) fatigue with model simulations for API-S135, JIS SS41, and JIS SM50A, respectively. Both ambient-air fatigue and corrosion fatigue[3] in saline aqueous environments were studied. The ambient-air fatigue was modeled with initiation-propagation (I-P) model to check the suitability of fatigue-life properties listed in Table 5.2. The corrosion fatigue in saline aqueous environments were simulated using the APD model. As shown in Figs. 5.8, 5.14-15, the APD model provides good estimates of corrosion-fatigue life for all these low-alloy structural steels regardless of their mechanical strengths.

5.8 VERIFICATION: EFFECTS OF PRE-EXISTING NOTCHES (K_t) ON THE CORROSION-FATIGUE LIFE

The S-N behavior of notched (K_t = 4.0) API-S135 in seawater under a constant mean stress (517.2 MPa) was compared with the APD model simulation as shown in Fig. 5.16.[4] The presence of seawater reduces the fatigue resistance of the notched API-S135. A simulated S-N curve based on a two-stage APD model simulation (microcrack development plus macroscopic crack growth) without considering chemical-notching process gives a reasonable agreement with test results as also seen in Fig. 5.16.

5.9 VERIFICATION: EFFECTS OF LOADING RATE AND TEST FREQUENCY (f) ON THE CORROSION FATIGUE

5.9.1 Effects of Loading Rate on Current-Density Transients (Trapezoidal Wave)

The anodic-current-density transients of unnotched API-S135 under trapezoidal-wave loading of various loading rates in seawater drilling fluid at 93.3 °C were measured and are presented in Fig. 5.17. The maximum anodic-current density decreases with a decreasing loading rate. The total charge transferred under the current-density trace of each loading cycle (shown within shaded area), however, increases with a decreasing loading rate.

The cathodic-current-density transients of unnotched API-S135 under trapezoidal-wave loading of various loading rates in seawater drilling fluid at 93.3 °C are compared in Fig. 5.18. No significant cathodic-current-density transient phenomena are observed.

For the corresponding experiments on the stress-free surface of a notched API-S135, neither anodic nor cathodic current-density transient phenomena (not shown) were detected.

---

[3] JIS SS41 and JIS SM50A steels were tested in 3.0% NaCl solution [78] while API-S135 steel was tested in seawater [133].

[4] Data from the summary reports of project Moholes by Battelle Memorial Institute [134-135].

5.9.2 Effects of Test Frequency (f) on Current-Density Transients (Sinusoidal Wave)

The anodic-current-density transients of unnotched API-S135 under sinusoidal-wave loading of various test frequencies (f) in seawater drilling fluid at 93.3 °C are shown in Fig. 5.19. The maximum current density appears at the maximum stress for a test frequency (f) of 2 Hz. Opposite is true, however, when the test frequency (f) is reduced to 0.1 Hz for which the minimum current density is observed at the maximum stress.

No significant transient phenomena of cathodic-current-density for unnotched API-S135 in seawater drilling fluid at 93.3 °C under sinusoidal-wave loading are observed. Changing test frequency (f) (see Fig. 5.20) or changing stress ratio (R) (see Fig. 5.21) does not affect the cathodic current-density response of the corrosion fatigue.

5.9.3 Effects of Test Frequency (f) on the Corrosion-Fatigue Life

A comparison of fatigue-life data [57,135] of API-S135 obtained at various test frequencies (f) in seawater with the APD model simulations is given in Fig. 5.22. The environmental degradation of fatigue resistance decreases with an increasing test frequency (f). Only limited data are available to verify the predicted S-N curve at a test frequency as high as 20 Hz. Reasonable agreement is obtained between the test data and the simulated effects of test frequency (f) on the corrosion fatigue by the APD model.

5.10 Verification: Effects of Macroscopic Crack-Growth Life (N_{p2})

Figure 5.23 illustrates the determination of macroscopic crack-growth life (N_{p2}) for an API-S135 specimen fatigued in an aerated and chemically-inhibited drilling fluid at 93.3 °C. The fatigue life devoted in growing a macroscopic crack is determined by examining the displacement (Δe) changes of the corrosion fatigue at its final stage.

The remaining fatigue life following the transition (labeled B in Fig. 3.1b) between microcrack development and macroscopic crack growth in the displacement range (Δe) versus number of fatigue cycle (N) plots of tested specimens are summarized in Tables 5.5 and 5.6 for the corrosion fatigue without and with adding polymeric inhibitor, respectively. Various testing environments have no effect on the macroscopic crack growth (R = 0.1).

5.11 VERIFICATION: EFFECTS OF ELECTROCHEMICAL DISSOLUTION ON CRACK INITIATION AND GROWTH

5.11.1 Appearance of Chemical Notches

A typical crack-initiation sites of an ambient-air fatigue observed under a scanning electron microscope (SEM) is presented in Fig. 5.24. Generation of persistent slip bands (PSB) might be identified from the magnified vision of the crack-initiation site in the same micrograph. The presence of thermally-elevated seawater drilling fluid (93.3 °C) replaces these PSB with a chemical notch, as seen in Fig. 5.25, which leads to the fatigue-crack initiation for an API-S135 specimen. Upon comparing Fig. 5.24 (fatigue in ambient air) with Fig. 5.25 (CFC in drilling fluid), one can imagine that the chemical-notching process is a consequence of localized dissolution at areas suffering local plasticity (PSB). The formation of persistent slip bands (PSB) interrupts the protective surface films and then localizes the dissolution current leading to the formation of the chemical notch.

Another chemical notch obtained under different test condition was presented earlier in Fig. 3.5. The size of the chemical notch leading to the development of a microcrack appears small (20 ~ 30 μm) and does not depend on the applied stress amplitude (ΔS/2): compare Fig. 3.5 with Fig. 5.25. This observation is consistent with the maximum tolerable defect size (a_n) modeled using Eq. 3.3:

$$a_n = \frac{1}{Y(a,c)}\left[\ 2.5 + 0.79\,\frac{L_o}{K_t}\ \right] \tag{3.3}$$

where no dependence on stress amplitude (ΔS/2) is included but material properties (ΔK_{th}, ΔS_e) and geometrical factors (Y, K_t) are.

5.11.2 Appearance of Crack Surfaces on Crack-Initiation Sites

The crack-initiation site adjacent to a chemical notch is found to be heavily etched and featureless as shown in a micrograph of Fig. 5.26. Evidence of intense anodic dissolution on these surfaces can be recognized. This micrograph thus supports the postulate made in the APD model for which the development of microcracks is considered to be dominated by the preferential anodic dissolution occurring at microcrack tips.

For specimens under cathodic protection at a controlled electrochemical potential (E_{bulk}) as low as -1.0 V (SCE), an extensive amount of deposited iron (identified by EDXA) were accumulated around the crack-initiation site seen in Fig. 5.27. This observation supports the galvanic-coupling effect of model microcrack simulated in the APD model. As

detailed in Appendix B, microcrack tips are assumed to suffer a preferential anodic dissolution (lose electrons) while crack surfaces are assumed to undergo predominantly cathodic reduction (acquire electrons) reactions. This phenomena is expected to be enhanced when an intense cathodic current is externally imposed on the system. The presence of deposited iron[5] on the crack-initiation site shown in Fig. 5.27 confirms that crack surfaces undergo cathodic reduction reactions.

5.11.3 Appearance of Macroscopic Crack-Growth Regime

The fracture surfaces of an API-S135 under ambient-air fatigue exhibits a ductile-striation fracture during macroscopic fatigue-crack growth (see Fig. 5.28). A specimen fatigued in seawater drilling fluid at 93.3 °C showed a mixed mode of ductile-striation fracture with intergranular fracture (see Fig. 5.29). The intergranular fracture is also apparent in the fatigue tests under cathodic protection as seen in Fig. 5.30 for an IVD-Al plated specimen. It is interesting to note that after been galvanically sacrificed under corrosion fatigue, an IVD-plated aluminum (see Fig. 5.31) has not been fully dissolved away but remains nearly intact and adherent on the fatigue-fractured substrate (API-S135 steel). For specimens under an intense cathodic protection (E_{bulk} = -1.0 V SCE), the deposited-iron cluster (identified by EDXA) on fracture surfaces is again wide spread as seen in Fig. 5.32.

The fracture surface in the last ligament to fracture exhibits a high concentration of microvoids (a characteristic of ductile fracture) regardless of testing environments, as shown in Fig. 5.33 and Fig. 5.34, for an ambient-air fatigue and for the corrosion fatigue under cathodic protection, respectively. The ductile fracture of final tearing should not be much influenced by environmental effects.

5.11.4 Summary of Microscopic Observations

The environmental (anodic-dissolution) effects on corrosion fatigue should decrease with an increasing crack length. During the chemical-notching process (first CFC process), electrochemical kinetics is the only driving force. The etched crack surface on crack-initiation sites reveals a major contribution from electrochemical dissolution for microcrack development (second CFC process). Environmental effects decrease continuously with the growth of macroscopic cracks (third CFC process) although evidence of intergranular fracture induced by corrosion attack is still apparent on the fracture surfaces. Finally, a purely mechanical tearing under plastic flow induces a final ductile fracture without any environmental assistance.

---

[5] The ferrous (or ferric) ions dissolved from microcrack tips are electrochemically reduced and resided on crack surfaces.

CHAPTER VI: DISCUSSION

6.1 SUMMARY OF THE INVESTIGATED VARIABLES

The variables studied (both analytically and experimentally) in this investigation are summarized in Table 6.1. Most of these variables will be discussed in the following sections. The relative significance of each variable on the high-cycle corrosion-fatigue life of structural steels in saline aqueous environments is rated qualitatively in this Table. As seen in Table 6.1, the most influential variables are: stress range (ΔS), test frequency (f), pre-existing notch (K_t), electrochemical potential (E_{bulk}), and anodic Tafel's slope (β_a).

6.2 OBSERVED AND PREDICTED EFFECTS OF FLUID AERATION

6.2.1 Effects of Fluid Aeration on the Corrosion Rate

The condition of fluid aeration should not affect anodic polarization but should affect cathodic polarization behavior. As seen in Fig. 5.1, no influence of fluid aeration on the anodic polarization was observed; although an enhanced current density for the cathodic polarization[1] was noted upon comparing results using the air-saturated (medical air) drilling fluid with results using drilling fluid de-oxygenated with ultra-high purity (UHP) N_2.

It is known that dissolving oxygen into a de-oxygenated electrolyte can raise the free-corrosion potential (E_{corr}) by introducing cathodic reactions involving oxygen. Hence, saturating the electrolyte with oxygen-containing air can accelerate[2] free corrosion for an electrode in its active regime. This effect, however, is not apparent upon examining the mixed polarization diagrams (Fig. 5.1) of API-S135 in seawater drilling fluids at 93.3 °C. As seen in Fig. 5.1, the contrast in overall free-corrosion potential (E_{corr}) and free-corrosion current density (i_{corr}) between the results measured under various conditions of fluid aeration are essentially small, having a value of 10 ~ 20 mV (SCE) and 40 $\mu A/cm^2$, respectively. This lack of sensitivity should occur because the oxygen saturation limit decreases with an increasing solution salinity and temperature [136]. For the conditions of free corrosion in the electrolyte (0.4 M [Cl^-]) saturated with medical air at a nearly boiling temperature (93.3 °C) used in this study, the ability of oxygen cathodic reduction to raise the free-corrosion potential (E_{corr}) above that of deaerated tests (purged with UHP N_2) should thus be limited.

---

[1] Oxygen reduction reactions are involved in air-saturated systems but not in de-oxygenated systems.
[2] This effect is restricted to the polarization within the active regime of no passive behavior.

6.2.2 Effects of Fluid Aeration on the Corrosion-Fatigue Life

The oxygen concentration is expected to be sharply depleted (deaerated) within a chemical notch or a microcrack tip due to the limiting effects of mass transport [33]. The electrochemical influence of fluid aeration on crack initiation should thus be increasingly reduced as a microcrack lengthens. Therefore, there should be no significant effect of fluid aeration on the corrosion-fatigue life of API-S135 in seawater drilling fluids at elevated temperature when crack initiation dominates the fatigue process.

The experimental results and the APD model simulations, as seen in Figs. 5.2 and 5.3, both show no fluid aeration effect and thus support the above arguments. This lack of influence of fluid aeration on the S-N behavior observed in this study is consistent with test results obtained by Pettit et al. [78] presented in Fig. 5.7.

6.2.3 Effects of Fluid Aeration on the Macroscopic Crack Growth

Aerating seawater drilling fluids with medical air does not prolong the period devoted to macroscopic crack growth (see Tables 5.5-5.6). This observation can be explained by a diminishing oxygen concentration at the crack tip leading to lesser amounts of oxide-induced crack closure as the crack lengthens. The concentration of oxygen is depressed at the outset by raising the fluid temperature (T) close to its boiling point (93.3 °C). In addition, the mobility of oxygen transporting toward the crack tip is limited by the insufficient homogenization of the crack solution with viscous bulk solution. Finally, the shortage of oxygen together with local crack-tip pH (< 3.0) favor no precipitation (refer to Pourbaix diagram for steels) of oxides at the crack tip; although the bulk solution was saturated with oxygen-containing air. This lack of oxide at crack tips thus reduces the possibility of inducing significant crack closure to retard macroscopic crack growth. Therefore, the conditions of fluid aeration should not influence macroscopic crack growth.

The above view point is strengthened[3] by the appearance of specimens taken out of an environmental chamber immediately after fatigue fracture. The fracture surface of these specimens appears clean implying that a substantial amount of oxide-induced crack closure to retard macroscopic crack growth did not occur.

6.3 Observed and Predicted Effects of Polymeric Inhibitor

6.3.1 Effects of Polymeric Inhibitor on the Corrosion-Fatigue Life

A polymeric inhibitor depresses the electrolytic conductivity (η) of drilling fluids and hence should reduce the susceptibility of API-S135 on microcrack development. In this

[3] This argument is based solely on writer's experience in corrosion-fatigue tests. No photograph was taken.

study, adding a polymeric inhibitor (Conquor 404) caused a only modest improvement of the observed corrosion-fatigue resistance of API-S135 for the concentration (0.11 ~ 0.3%) used (see Figs. 5.4 and 5.5).

The APD model simulations seen in Figs 5.4-5.5 show a very small influence of adding inhibitor and agree with the experimental observations. Reducing the conductivity of the electrolytes from 45 to 30 $\Omega^{-1}m^{-1}$ to simulate the environmental change upon adding the inhibitor predicts no difference in S-N behavior.

6.3.2 Effects of Polymeric Inhibitor on the Corrosion Inhibition

Polymeric inhibitors may also assist in stabilizing the film-formation processes to protect the electrode from corrosion attack. This anticipated effect, however, does not seem at work for API-S135 and Conquor 404 at 93.3 °C. The observed thermal degradation or decomposition of viscosifier (bentonite) and fluid-loss reducers (cellulose and starch) included in drilling fluids may give rise to solution acidification: the pH of a post-heated drilling fluid was 2 ~ 3 in comparison with a pH of 8 for unheated fluid. An increasing solution acidification leads to an increasing retardation or even a prohibition of the film-stabilizing process favored by the polymeric inhibitor. This thermally-activated fluid-acidification effect which damage the film-stabilizing process may not be offset by increasing the dosage of the inhibitor.

6.3.3 Effects of Polymeric Inhibitor on the Chemical-Notching Characteristics

The potential-perturbation rate (sweeping velocity of potential, v) during cyclic loading is observed to be slower upon adding the inhibitor (Conquor 404). According to Eq. A.7 in Appendix A, the transient peak-current density ($i^*(t)$) of chemical-notching process should decrease with a decreasing sweeping velocity of potential (v) (see Appendix A). A relative low chemical-notching rate should thus be simulated, according to the APD model, for the corrosion fatigue in the fluids upon adding the inhibitor.

The above speculation is strengthened by comparing (using naked eyes) the sample disks of API-S135 after being potentiodynamically scanned under a hysteresis polarization in seawater drilling fluid. A tendency of decreasing surface roughness is observed for samples polarized under a decreasing scan rate; although the experiments were carried out over the same range of electrochemical potential (E_{bulk}) for the same duration of polarization. However, the above comparison is based solely upon observation using naked eyes. Further justification of this phenomenon invoking surface-roughness measurement (which has not been carried out in this study) using confocal microscopic is required.

According to the above indirect evidence and the APD model simulation, a prolonged, though not substantially, chemical-notching fatigue life (N_{pit}) should thus be expected as a consequence of adding this polymeric inhibitor. However, the lack of direct evidence warrants further study of this phenomenon.

6.4 Observed and Predicted Effects of Electrochemical Potential (E_{bulk})

6.4.1 Relationship between the Corrosion Rate and the Corrosion-Fatigue Life

An increasing electrochemical potential (E_{bulk}) raises the dissolution rate (anodic current density) of API-S135 steel quickly as seen in Fig. 5.1. The initiation of corrosion-fatigue cracks can be assumed to be controlled by an anodic-dissolution mechanism if the corrosion-fatigue life (N_f), like the corrosion rate (i_a), depends sensitively on the electrochemical potential (E_{bulk}). Figure 5.6 shows a strong dependence of corrosion-fatigue life (N_f) on electrochemical potential (E_{bulk}) and thus confirms the above idea.

Such a strong dependence of N_f with E_{bulk} is also predicted in the APD model. The APD model considers the bare-crack-tip current density (i_{bare}) to be the driving force of microcrack development. In the APD model, the bare-crack-tip current density (i_{bare}) increases exponentially with the crack-tip over-potential ($E_{tip} - E^a_{eq}$) obeying the Tafel's relationship (see Eq. B.12 in Appendix B). The rate of microcrack development, $(da/dN)_{pl}$, which dominates most of the corrosion-fatigue life should thus exponentially increase with a rising (less negative) electrochemical potential (E_{bulk}) according to Eq. 3.12:[4]

$$\left(\frac{da}{dN}\right)_{cfc} = \frac{MQ}{zF\rho} = \frac{M\, i_{bare}}{zF\rho\lambda}\left(1 - \exp\left(-\frac{\lambda}{2f}\right)\right) \tag{3.12}$$

The APD model simulation of the effects of electrochemical potential (E_{bulk}) are shown in Fig. 5.6 together with the limited test results under various electrochemical potentials (E_{bulk}). The APD model simulations agree with the test results.

6.4.2 Effects of Cathodic Protection on the Corrosion-Fatigue Life

In light of Sec. 6.4.1, electrochemical-potential (E_{bulk}) control is thought to be an effective approach in inhibiting corrosion fatigue. The effect of cathodic protection on fatigue life (N_f) is demonstrated in Fig. 6.1. Shifting the electrochemical potential (E_{bulk}) from free-corrosion potential ($\approx$ -0.73 V vs. SCE) to -0.8 V (SCE) significantly prolongs

[4] $(da/dN)_{pl}$ is linearly proportional to $(da/dN)_{cfc}$ with a proportional factor: degree of CFC saturation (φ) as seen in Eq. 3.9.

fatigue life (N_f) in seawater drilling fluid at 93.3 °C; although this shift does not fully restore the fatigue resistance of API-S135 back to that in air.

Figure 6.2 shows the predicted effect of impressing an active (more negative) electrochemical potential (E_{bulk}) using the APD model: crack initiation is retarded. After combining strain-life[5] effects (N_{st}) with the effects[6] of chemical notching (N_{pit}) and microcrack development (N_{pl}) based on a linear damage accumulation (see Sec. 3.5), one predicts (see Fig. 6.2) an extension of crack-initiation life (N_i) resulting from shifting the electrochemical potential (E_{bulk}) from -0.7 V (SCE) to -0.8 V (SCE).

The APD model simulated S-N curves agree with the experimental observations of cathodic protection (see Fig. 6.1) for both by impressing cathodic current and by plating with a sacrificial aluminum (Fe/Al galvanic couple).

6.4.3 Effects of Galvanic Protection on the Corrosion-Fatigue Life

Galvanic protection by aluminum plating is effective (see Fig. 5.6) even after a long-term exposure in seawater drilling fluid at 93.3 °C: a micrograph in Fig. 5.31 shows a residual aluminum plating after a corrosion-fatigue fracture. An equivalent electrochemical potential of a Fe/Al galvanic couple is assigned to be about -0.8 V (SCE) for the APD model simulation. This assignment of electrochemical potential (E_{bulk}) is evaluated below.

The galvanic current density flowing between a scratched Al coating and a Fe substrate in a deaerated 0.1 M NaCl solution has been measured to be 20 ~ 30 $\mu A/cm^2$ [137]. By correlating this value of current density with the cathodic polarization diagram shown in Fig. 5.1, an equivalent electrochemical potential (E_{bulk}) of approximately -0.8 V (SCE) is obtained. This equivalent electrochemical potential (E_{bulk}) of the Fe/Al galvanic couple is confirmed (see Fig. 5.6) by comparing the S-N behavior of IVD-Al plated API-S135 with the fatigue life of the same substrate cathodically protected at a controlled electrochemical potential (E_{bulk}) of -0.8 V (SCE). A consistent pattern of behavior between the test results of the above two techniques at an electrochemical potential (E_{bulk}) of -0.8 V (SCE) is observed.

6.5 Reported and Predicted Effects of Stress Ratio (R) and Applied Mean Stress

The effect of mean stress is illustrated in Fig. 6.3 in which a comparison of the corrosion-fatigue S-N behavior of API-S135 steel under an uniaxial fatigue at a constant mean stress of 517.2 MPa in seawater (Fig. 5.7) with those obtained under a fully-reversed

[5] Crack-initiation life based on strain-life prediction does not depend on electrochemical potential (E_{bulk}).

[6] Both chemical-notching process and microcrack development are effects caused by active-path dissolution.

bending at zero mean stress in the same environment (Fig. 5.8) is given. The mean-stress effect diminishes with an increasing corrosion-fatigue life.

The above observation suggests that mean stress does not affect high-cycle corrosion-fatigue crack initiation and appears to be consistent with results from simulations made using the APD model. No mean stress effect but only stress range (ΔS) is considered in the APD model as being responsible for assisting the processes of chemical notching[7] and microcrack development[8] to initiate macroscopic cracks for the high-cycle corrosion fatigue (Fig. 3.8). The APD model predictions in Fig. 6.3 agree with the test results.

The lack of mean stress effect for the above corrosion-fatigue (f = 1 Hz) results also suggests that a microcrack would be so open (because of the anodic crack-tip dissolution) that the influence of crack-closure effect induced by corrosion products on the development of the microcrack would be diminished. The oxide-induced crack-closure effect will be further discussed in Sec. 6.13.

6.6 Observed, Reported, and Predicted Effects of Temperature (T)

6.6.1 Effects of Temperature (T) on the General-Corrosion Rate

A different temperature (T) produces a different polarization behavior in both anodic and cathodic branches of the polarization diagram. The mixed[9] polarization diagram of API-S135 in seawater drilling fluid at 93.3 °C is compared with that in the same fluid at 25 °C and is shown in Fig. 5.9. An increasing temperature (T) induces an increasing anodic dissolution rate (see anodic branches in Fig. 5.9) at a given electrochemical potential (E_{bulk}). Although a large difference in free-corrosion potential (E_{corr}) exists (-0.6 V SCE at 25 °C in comparison with -0.73 V SCE at 93.3 °C), little difference in the free-corrosion current density (i_{corr}) is observed. Within the range of electrochemical potential (E_{bulk}) explored, API-S135 in the seawater drilling fluid at 93.3 °C, in contrast to that at 25 °C, does not show any active-passive transition behavior. The concentration-polarization effect, i.e., difference between Tafel's slope and polarization current density, on cathodic branch appears more pronounced at ambient temperature.

---

[7] See Eqs. A.4-A.5 in Appendix A for chemical notching kinetic where the sweeping velocity of redox potential is assumed to depend on stress range (ΔS).

[8] See Eq. 3.14 in Sec. 3.4.4 where the intrinsic reaction-rate constant (λ_0)which determines current-density-decay exponent (λ) is assumed to depend on stress-intensity-factor range (ΔK).

[9] Showing both anodic and cathodic polarization behavior.

6.6.2 Effects of Temperature (T) on the Stress-Corrosion Rate

In the presence of a static applied stress, an electrode might exhibit different corrosion characteristics from those in the same environment without stress. As seen in Fig. 5.11 for instance, although imposing a static stress up to 80% of its yield strength (S_y) does not influence the anodic polarization behavior, an electrode subjected to a static stress above the yield stress in seawater drilling fluid at ambient temperature (25 °C) exhibits a substantial increase in anodic dissolution compared with the observed behavior of an electrode under no applied stress. This phenomena suggests that API-S135 is stress-corrosion-cracking (SCC) sensitive in such an environment.

It is inadvisable to deduce a temperature effect on stress-corrosion behavior based on the general corrosion phenomena observed in Fig. 5.9. The stress-enhanced corrosion of a metal might also behave differently in the same fluid of different temperatures (T). For instance, API-S135 is stress-corrosion-cracking sensitive in seawater drilling fluid at ambient temperature (Fig. 5.11); the API-S135 tested in thermally elevated drilling fluid (see Fig. 5.12) shows, however, no evidence of stress-corrosion-cracking (SCC) susceptibility.

It can thus be deduced that an elevated temperature (T) in seawater drilling fluid not only promote general corrosion[10] but also activate the film-formation process[11] which prohibits an excessive dissolution on the electrodes under static stresses above the yield stress. This phenomena is consistent with the effect of temperature (T) on corrosion-fatigue crack initiation simulated by the APD model as will be discussed in the next section.

6.6.3 Effects of Temperature (T) on the Corrosion-Fatigue Life

The effects of temperature (T) on the corrosion-fatigue S-N behavior of API-S135 in saline aqueous environments is presented in Fig. 6.4. This figure compares results in Fig. 5.13 with their corresponding fatigue performance in ambient air. Surprisingly, the seawater drilling fluid at elevated temperature is less damaging to the corrosion-fatigue resistance of API-S135 steel than seawater at ambient temperature. This observation on the effect of temperature (T) can be explained by invoking the same mechanism, i.e., thermally-activated film-formation process proposed in Sec. 6.6.2.

The temperature effects on corrosion-fatigue crack initiation in the APD model were simulated using a parameter of the current-density-decay exponent (λ) which characterizes the speed at which anodic dissolution decays (film-formation process). As seen in Eq. 3.13 (Sec. 3.4.4), the current-density-decay exponent (λ) increases exponentially with increasing temperature (T). The amount of charge transfer (Q) for microcrack development (see Eq.

[10] General corrosion rate corresponds to the bare-crack-tip current density (i_{bare}) in the APD model.
[11] Film-formation rate corresponds to the current-density-decay exponent (λ) in the APD model.

3.11) within each fatigue cycle should thus decrease accordingly; although an increasing general-corrosion rate (i_{bare}) may also be produced by increasing temperature (T). An increasing corrosion-fatigue life (N_f) should thus be predicted with increasing temperature (T). As seen in Fig. 6.4, the APD model correctly predicts the effects of temperature (T) on the corrosion-fatigue S-N behavior.

For high-cycle corrosion fatigue of steels in saline aqueous environments, temperature (T) of the testing environment is more influential than the mean stress or the R ratios of fatigue loading. As seen in Fig. 6.4, the fatigue life in ambient air is greatly extended by lowering the stress ratio (R). However, such an effect of stress ratio[12] (R) on fatigue life appears insignificant for the case of the high-cycle corrosion fatigue (also seen in Fig. 6.4) in which the effect of temperature (T) is far more influential. The influence of test frequency[13] (f) within a range of 1 to 2 Hz is considered to be negligible for the above comparison.

6.7 Reported and Predicted Effects of Material Strength (S_y)

A comparison of ambient-air-fatigue performance of steels with varying yield strength (S_y), including JIS SS41 of 300 MPa, JIS SM50A of 520 MPa, and API-S135 of 931 MPa, under a fully-reversed-bending fatigue (R = -1) is given in Fig. 6.5. An increasing material yield strength (S_y) generally lengthens the fatigue life in ambient air.

For high-cycle corrosion fatigue, as seen in Fig. 6.6, no effect of material strength (S_y) was observed. The test data of the above materials of different strength converge at the life regime of high-cycle corrosion fatigue. Distinguishing between corrosion-fatigue resistance of these materials is only possible at fatigue lives shorter than 2.0×10^5 cycles. Therefore, for high-cycle corrosion fatigue, only the major compositional element, e.g., Fe, and the major electrolytic agent, e.g., Cl^- (but not the mechanical strength or microstructure) significantly affect the corrosion-fatigue crack initiation of these low-alloy structural steels.

By using the same electrochemical parameters to model chemical-notching process (N_{pit}) and microcrack development (N_{pl}), the APD model provides satisfactory simulations for the effect of material yield strength (S_y) on the fatigue life of steels in salt-water environments as shown in Fig. 6.6. The predicted difference in high-cycle-fatigue regime is attributed to the differences in the characteristics of crack-tip opening (see Appendix B) and of macroscopic crack growth (Paris parameters) seen in Table 5.2.

---

[12] See discussions in Sec. 6.5 for effects of R ratio and mean stress on the corrosion-fatigue life.

[13] Changing frequency from 1 to 2 Hz should have no significance: refer to Fig. 5.22 for the effect of frequency ranging from 1-20 Hz.

6.8 Reported and Predicted Effects of Pre-existing Notches (K_t)

A summary plot of notch effects on both the ambient-air fatigue and the corrosion fatigue of API-S135 with a constant uniaxial mean stress (517.2 MPa) is given in Fig. 6.7. The presence of a pre-existing mechanical notch ($K_t = 4.0$) reduces fatigue life relative to the behavior of the same material without notch in both ambient air and seawater environments.

The above test data clearly indicate that corrosion fatigue is not solely a problem of mechanical stress intensification. The presence of saline aqueous environments together with a pre-existing notch causes a reduction in fatigue life (see Fig. 6.7) greater than reduction produced by the solely presence of pre-existing notch (mechanical stress-concentration effect) relative to the ambient-air fatigue without notch. Therefore, the influence of stress intensification and of electrochemical kinetics are both important; and both must be taken into consideration to characterize corrosion-fatigue behavior.

To use the APD model to simulate corrosion-fatigue life for API-S135 with pre-existing notches, the chemical-notching process (N_{pit}) was assumed to be negligible. As discussed in Sec. 3.3.3, the fatigue-life period of chemical-notching process (N_{pit}) for a smooth specimen is the fatigue life required to generate a chemical notch capable of producing a fatigue-notch factor (K_f) greater than unity. Therefore with the presence of a macroscopic pre-existing notch having stress-concentration factor (K_t) as high as 4.0 in Fig. 6.7, the APD model logically should ignore the chemical-notching life period (N_{pit}).

In the APD model, the stress-concentrating effect from a pre-existing notch intensifies both mechanical-fatigue (strain-life) damage and the localized electrochemical kinetics of microcrack development to initiate macroscopic cracks. Fig. 6.7 demonstrates the capability of the APD model in simulating the corrosion-fatigue S-N behavior of API-S135 with and without pre-existing mechanical notches in seawater environments.

6.9 Observed Effects of Current/Potential Transient Phenomena

6.9.1 Significance of the Electrochemical-Potential Transients

Cyclically straining an electrode causes a perturbation of the free-corrosion potential (E_{corr}) as shown in Fig. 6.8. The investigated electrode was fatigued under a trapezoidal-waveform having a stress-holding period (t_{hold}) of 5 seconds and a stress-rising period (t_{rise}) of 0.1 seconds (sinusoidal waveform of 5 Hz) in seawater drilling fluid at 93.3 °C. The free-corrosion potential reaches the maximum at the minimum stress and resumes a stabilized potential during the stress-holding period (t_{hold}) of the maximum stress ($\approx 92\%\ S_y$).

The above phenomena would seems to be the result of a film-rupture/film-formation process. As illustrated in Fig. 6.9, a sudden tensile straining of an electrode causes a rupture (or thinning) process of the protective surface film. This process drops the free-corrosion potential toward the redox potential (E_{eq}), i.e., a potential equivalent to the free-corrosion potential of a completely unfilmed electrode, of a metallic half-cell reaction. On the other hand, reverse straining during unloading causes a thickening of the surface film and raises the free-corrosion potential back to the potential of a fully-refilmed electrode. The inset sketches of potential (E) versus current density (i) along with the trapezoidal-loading wave shown in Fig. 6.8 illustrate this postulated film-rupture/film-formation process.

It is worth noting that the film-formation process continues during stress-holding period (t_{hold}), as well. The growth of a protective film on a strained electrode during stress-holding period (t_{hold}) slowly raises the free-corrosion potential from the valley potential of film rupture at the onset maximum holding stress (see second half of Fig. 6.8). The free-corrosion potential of the electrode stabilizes after the completion of the film-formation process without being affected by the applied strain under the maximum holding stress.

6.9.2 Significance of the Anodic Current-Density Transients

The perturbation of the free-corrosion potential induced by cyclic straining gives rise to a current-density transient phenomena. The rupture (or thinning) process of a protective film after sudden straining raises the anodic dissolution-current density while the free-corrosion potential of the electrode drops toward active potential as sketched in Fig. 6.10.

The current-density transient phenomena as postulated above was experimentally observed using a potentiostat which monitors the response of impressed current while maintaining a cyclically-straining electrode at a specified electrochemical potential (E_{bulk}). Figure 6.11 presents the current-density transient of API-S135 under a trapezoidal-wave loading in seawater drilling fluid at 93.3 °C. The significance of this plot is discussed below.

A sudden reduction of applied stress facilitates the thickening of film which reduces anodic dissolution current (the first half in Fig. 6.11) evolved on the straining electrode at an electrochemical potential (E_{bulk}) of -0.73 V (SCE). The opposite is true after raising applied stress up to 92% of material yield strength (S_y) within a period[14] of 0.25 seconds. During the stress-rising period (t_{rise}), the anodic current density increases with an increasingly applied stress as an indication of a progressively film-rupture process on the electrode. Although the stress is thereafter sustained after reaching the maximum applied stress (S_{max}), the anodic current density decays (the second half in Fig. 6.11) implying an undergoing process of film formation despite of the stress state on the electrode.

[14] The loading rate is equivalent to a cyclic sinusoidal-waveform loading of 2 Hz.

6.9.3 Effects of Waveform and Frequency (f) on the Anodic Current-Density Transients

A specimen subjected to a sinusoidal-waveform loading with a test frequency (f) of 2 Hz in the same environment exhibits a similar behavior of anodic current-density transient phenomena (see Fig. 6.12). However, the anodic current density starts decaying before reaching the maximum stress while stabilizing before the termination of unloading reversal.

The shape of the anodic current-density transient should depend not only on loading waveform but also on loading rate (frequency, f), as suggested in Figs. 5.17 and 5.19. For a loading rate as low as 0.17 S_y/sec (sinusoidal waveform of 0.1 Hz), the film-rupture process would not be fast enough relative to the simultaneous film-formation process to give rise to a rupture dissolution current during loading reversal. The maximum current density would rather occur at the minimum stress instead (as seen in Figs. 5.17 and 5.19). The appearance of the reverse current transient might result from the protective films which grow during tensile loading would be subjected to an overload compressive strain during unloading and could thus buckle giving rise to the observed film-rupture dissolution current (see Fig. 5.17).

6.9.4 Significance of the Cathodic Current-Density Transients

The cyclic loading processes have no effect on cathodic current response (Figs. 5.18, 5.20-5.21) irrespective of the waveform or the test frequency (f) of applied fatigue loading. As presented in Figs. 6.11-6.12, no influence of cyclic loading on cathodic-current density is observed after maintaining an electrochemical potential (E_{bulk}) of -0.8 V (SCE) on an API-S135 electrode in seawater drilling fluid at 93.3 °C. The little fluctuation of the cathodic-current density with loading wave suggests that the film rupture and the film formation are competing and are proceeding simultaneously regardless of applied strain on the electrode.

6.10 Reported and Predicted Effects of Test Frequency (f)

Corrosion-fatigue crack initiation and growth are both time and frequency dependent. A loading of high test frequency (f) usually retards crack initiation and prolongs corrosion-fatigue life as illustrated in Fig. 5.22. This frequency effect at high test frequency (f) is probably due to the reduced time available for corrosion reactions to assist in developing microcracks. As shown in Figs. 5.17 and 5.19, the total amount of charge transferred, i.e., the amount[15] of metal ionized, within each fatigue cycle decreases with an decreasing period for rising stress (t_{rise}), or equivalently an increasing test frequency (f) of fatigue loading. A detailed discussion regarding the effect of test frequency (f) on time-dependent corrosion-fatigue cracking and its saturation is given in Appendix C.

[15] Area under the transient traces of anodic current density in the shaded regions of Fig. 5.17 and Fig. 5.19.

6.11 Observed and Predicted Macroscopic Crack-Growth Life (N_{p2})

6.11.1 Implication from Microscopic Observations on Fracture Surfaces

The presence of intergranular fracture on the fracture surfaces of corrosion fatigue has been attributed to corrosion attack from testing environments [2,28]. As shown in Fig. 5.29 for a fracture surface of an API-S135 specimen fatigued in seawater drilling fluid, the intergranular fracture can be seen although the ductile-striation fracture is also apparent. The accumulation of deposited iron on the fatigue-fracture surface (see Fig. 5.32) of an API-S135 specimen cathodically protected at an electrochemical potential (E_{bulk}) of -1.0 V (SCE) also indicates an undergoing electrochemical process during macroscopic crack growth. From the above observations, it is postulated that the macroscopic crack growth of the investigating systems may also be assisted by electrochemical reactions. The acceleration mechanism or the magnitude of the environmentally-assisted macroscopic-crack growth remains, however, undefined[16] in the current investigation.

6.11.2 Macroscopic Crack-Growth Life (N_{p2})

The experimentally observed macroscopic crack-growth life (N_{p2}) illustrated in Fig. 5.23 is summarized and compared with the linear-elastic-fracture-mechanics (LEFM) predictions in Fig. 6.13. Various testing fluids have no effect on macroscopic crack growth ($R = 0.1$). This observation demonstrates that once a crack reaches a critical size, e.g., $a > 0.5$ mm, the stress-intensity-factor range (ΔK) is the dominant factor driving crack growth.

The Paris parameters (C, m) from a similar material (AISI-4340, see Table 5.2) tested in air [108] do not give a satisfactory prediction (Fig. 6.13) for the test results of API-S135 in this investigation. However, the prediction so obtained could significantly overestimate the macroscopic crack-growth life (N_{p2}) for a system tested in thermally-elevated drilling fluids containing chloride[17] ions (0.4M [Cl^-]). The presence of saline aqueous environments (e.g., NaCl solution) may accelerate macroscopic crack growth relative to that in ambient air by electrochemical kinetics [2] (anodic dissolution, hydrogen embrittlement) or by multiple crack coalescence (crack shape development) [122].

Using the corresponding parameters (C, m) obtained from studies in a 3.0% NaCl solution [108] gives a better agreement with the test data, as also seen in Fig. 6.13. Such a correlation also supports adopting 0.5 mm as the critical crack length (a_i) to separate

---

[16] The environmental assistance in macroscopic crack growth is implicitly included in the measured Paris parameters (C and m) of corrosion-fatigue crack growth in saline aqueous environments.

[17] A substance which is responsible for causing multiple chemical notching (pitting) for steels.

macroscopic crack growth (LEFM) from microcrack development (see Fig. 3.1) for the CFC processes of steels in saline aqueous environments.

6.12 PREDICTIVE ABILITY OF THE APD MODEL

6.12.1 The APD Model Simulations on Electrolytic Conductivity (η) and Fluid Aeration

A comparison of the APD model-simulated fatigue life (N_T) with observed free-corrosion fatigue life (N_f) of API-S135 under various conditions of fluid aeration or addition of polymeric inhibitor (varying electrolytic conductivity, η) is presented in Fig. 6.14. In general, a satisfactory agreement between model predictions and experimental observations was obtained. However, the APD model seems to overestimate the corrosion-fatigue resistance of API-S135 steel for the observed fatigue life (N_f) below half a million cycles. The divergence of model prediction with test results in this life regime (electrochemical-mechanical interaction regime: see Fig. 3.8) is attributed to the poor understanding of the synergistic electrochemical-mechanical interaction which probably is not adequately handled by the simple linear damage-accumulation rule used (see Sec. 3.5).

6.12.2 The APD Model Simulations on Electrochemical Potential (E_{bulk})

The polarization hysteresis of a straining electrode suggests that within the hysteresis range (from -0.2 to -1.0 V vs. SCE) of electrochemical potential (E_{bulk}) impressed, an API-S135 electrode under a statically applied stress in seawater drilling fluids always fractures at a potential value around -0.2 ~ -0.4 V (SCE) regardless of the temperature (T) of testing. For the electrochemical potential (E_{bulk}) range explored, an anodic dissolution process which reduces the cross section of the electrode and gives rise to stress concentration leading to the final fracture is thus far more significant than the damage from hydrogen induced crack initiation and growth. To apply anodic-dissolution principles to model the crack-initiation processes, i.e., chemical-notching process (N_{pit}) and microcrack development (N_{pl}), of corrosion fatigue is thus qualitatively validated.

Reducing electrochemical potential (E_{bulk}) toward active potential is beneficial to the corrosion-fatigue resistance of API-S135 because this condition suppresses the crack-tip anodic over-potential ($E_{tip} - E^a_{eq}$) and, as a consequence, the microcrack development (see Appendix B). This anticipated improvement occurs because the APD model treats the microcrack development as an anodic dissolution process which is greatly retarded by a decreasing crack-tip over-potential (see Eq. B.12 in Appendix B). A demonstration of the APD model simulated effects of the electrochemical potential (E_{bulk}) on corrosion-fatigue life (N_f) accompanied with limited experimental data is given in Fig. 6.15.

It must be emphasized that it would be unwise to extend the APD model to cathodic protection in systems protected at an electrochemical potential (E_{bulk}) close to or even less than the redox potential (E^a_{eq}) of the investigated electrode. Although no anodic current can be computed, a vigorous hydrogen reduction at crack faces would promote cathodic damage, e.g., hydrogen induced surface energy reduction or hydrogen induced local plasticity, to initiate macroscopic cracks. For those systems, hydrogen embrittlement can no longer be ignored but should be treated as the dominant mechanism. The APD model is not designed for systems under intense cathodic protections and does not take any cathodic damaging mechanisms into consideration either.

A failure of the APD model to simulate cathodic protection is presented in Fig. 6.15. A specimen failed at about four million cycles under a controlled electrochemical potential (E_{bulk}) of -1.0 V (SCE). The APD model predicts no failure for the above case because no environmentally-assisted crack initiation under such an electrochemical potential (E_{bulk}) can be estimated by this model. Additional research of hydrogen effects is required before the fatigue life of systems under an intense cathodic protection can be predicted.

6.12.3 The APD Model Simulations on Material Strength (S_y)

Although good agreement with the APD model simulations of the fatigue life for structural steels of low to medium strength in saline aqueous environments was obtained (Fig. 6.16), there is potential danger in applying the APD model to predict corrosion-fatigue life for high-strength structural steels (S_y > 1240 MPa). It is known that the susceptibility to hydrogen embrittlement of steels increases with material strength (S_y) [38,54]. Before a quantitative measure of hydrogen effects in assisting crack initiation is available, it is not recommend to use the APD model (which is solely based on anodic-dissolution principles) to simulate the fatigue behavior of high-strength steels in saline aqueous environments.

6.12.4 The APD Model Simulations on Pre-existing Notches (K_t)

A successful simulation of corrosion-fatigue life for specimens without a mechanical notch using the APD model does not ensure the suitability of using the same model for the corresponding systems with pre-existing notches. Fig. 6.17 illustrates a failure of applying the APD model for a notched (K_t = 3.5) JIS SM50A steel in 3.0% NaCl solution; although a successful simulation for the same steel without notch is obtained in Fig. 5.15. Due to the presence of pre-existing notch of severe stress concentration, the crack-initiation life (N_i) simulated by the APD model appears brief even under a small amplitude of applied cyclic stress ($\Delta S/2$). The predicted total fatigue life (N_T) is almost equal to the life computed by the LEFM of macroscopic crack growth (N_{p2}). An improper characterization of macroscopic

crack growth at the stress-intensity-factor range (ΔK) near threshold regime (ΔK_{th}) is thus speculated as being responsible for such a difference between model predictions and test results. The discrepancy between the model prediction and the test data of a smooth JIS SM50A at low applied-stress amplitude ($\Delta S/2$) seen in Fig. 5.15 supports the above reasoning.

6.12.5 The APD Model Simulations on Temperature (T) and Test Frequency (f)

Both temperature (T) and test frequency (f) affect the degree of CFC saturation[18] (φ) on microcrack development. A detailed discussion on this subject can be found in Appendix C. The APD model is primarily suitable for the corrosion fatigue of sufficiently low test frequency (f) at a given temperature (T) to ensure a saturated anodic dissolution for developing microcracks. This requirement, however, may not be met at low temperatures (T) or at high test frequencies (f).

High-frequency corrosion fatigue would also tend to induce substantial crack closure from oxides [66] which retards[19] crack initiation (developing microcracks) and macroscopic crack growth. The prediction made for the test frequency of 20 Hz in Fig. 5.22 based on the CFC saturation theory derived in Appendix C should thus be viewed with caution until the CFC saturation or the effects of the oxide-induced crack closure can be clarified.

6.13 Justification for Neglecting Corrosion-Product-Induced Crack Closure in the APD Model

In their systematic investigation on anomalous crack-growth retardation, Velden et al. [66] have asserted that oxide-induced crack closure was essentially obscured for steels tested under a frequency as low as 2 Hz with a circulating seawater of low flushing rate. They attributed the disappearance of the oxide-induced crack closure to the insufficient "pumping" of crack faces and the consequently insufficient oxygen supply. Moreover, the increasing acidification of crack solution toward the crack tip due to metal-ion hydrolysis together with the insufficient solution homogenization should further limit the stability[20] of any rigid oxide to sustain a substantial contribution to crack closure. The above arguments can be confirmed by corrosion-fatigue crack-growth data in the literature. The apparent retardation of crack growth due to the presence of oxide films can only be found from the CFC growth-rate tests under a high fluid-flow rate or a test frequency (f) greater than 5 Hz [66,138].

---

[18] The time allowing anodic dissolution (corrosion) to take place.
[19] Both microscopically and macroscopically.
[20] Refer to the Pourbaix diagram of steels for the stability of oxides.

However, any corrosion product (if present) collected inside a fatigue microcrack appears to have only a limited effect on the anodic dissolution[21] at microcrack tips. The passivated iron (Fe_2O_3) on crack faces has been reported to behave similar to a n-type semiconductor which would not prohibit ionic diffusion, but provides auto-catalytic electrodes for cathodic reductions to couple with active crack tips[22] for completing a micro-galvanic cell [139] in developing microcracks (major CFC crack-initiation process).

Therefore, taking the oxide-induced crack closure into account would not make any significant improvement in the predictive capability (in both crack initiation and macroscopic crack growth) of the APD model for electrodes slowly cyclic strained in saline aqueous environments. This phenomenon will be ignored for the present; although its possible significance warrants further attention [2,140].

[21] The major driving force considered in the APD model for developing microcracks to initiate macroscopically significant cracks (corrosion-fatigue crack initiation).

[22] The active crack tips is plastically deformed and bare after the rupture of protective films.

CHAPTER VII: SUMMARY, CONCLUSIONS, AND SUGGESTED FUTURE WORK

7.1 SUMMARY

The proposed APD model works quite satisfactory for the variables examined; however, the APD model is at present restricted to low-alloy structural steel of medium strength fatigued in saline aqueous environments at low[1] test frequencies (f). Despite the non-conservative predictions for systems under an intense[2] cathodic protection, the APD model should simulate systems operated under usual electrochemical potentials (E_{bulk}) which are not too far away from the potential (E_{corr}) for free corrosion.

7.2 CONCLUSIONS: EXPERIMENTAL OBSERVATIONS

1. API-S135 drill-pipe steel fatigued in simulated offshore drilling environments exhibited a corrosion-fatigue-cracking (CFC) behavior consisting of three processes, i.e., chemical-notching process (N_{pit}), microcrack development (N_{p1}), and macroscopic crack growth (N_{p2}). These corrosion fatigue cracking processes can be partitioned using electrochemical potential (E_{bulk}) or displacement range (Δe) vs. fatigue cycle (N) observations. Both mechanical fatigue and electrochemical reactions contribute to reduce the fatigue resistance of API-S135 steel.

2. No significant effect of modifying the test environment by means of fluid aeration or by adding a polymeric inhibitor (Conquor 404, 0.11 ~ 0.3%) on the corrosion-fatigue S-N behavior of API-S135 steel in seawater drilling fluids at 93.3 °C was observed.

3. Corrosion-fatigue-crack initiation of API-S135 steel in seawater drilling fluids was driven by a mechanism of film rupture/film formation induced active-path dissolution. The integrated amount of anodic dissolution depended upon the loading waveforms and upon the loading rates (test frequency). A decreasing loading rate (decreasing test frequency) gave rise to an increasing environmental attack.

4. The corrosion-fatigue-crack initiation of API-S135 steel can be retarded by impeding preferential dissolution at microcrack tips using cathodic protections. Ion-Vapor-Deposition (IVD) plated aluminum provided an effective sacrificial anode to galvanically protect the substrate steels (API-S135) from initiating macroscopic fatigue cracks.

---

[1] Generally, less than 2 Hz for most stress range of fatigue loading.
[2] Impressed potential close to or even lower than the redox potential of the corroding metal.

7.3 CONCLUSIONS: THE APD MODEL SIMULATIONS

1. The APD model simulations were verified for eight important corrosion-fatigue variables: fluid aeration, electrolytic conductivity (η), electrochemical potential (E_{bulk}), mean stress and stress ratio (R), fluid temperature (T), material yield strength (S_y), notch (K_t) effect, and test frequency (f). Corrosion-fatigue life predictions made using the proposed Active-Path-Dissolution (APD) model exhibited a satisfactory agreement with the experimental results.

2. Electrochemical potential (E_{bulk}) was found to be the major factor affecting the corrosion-fatigue S-N behavior of API-S135 steel in seawater drilling fluids. An impressed negative electrochemical potential (E_{bulk}) retards mainly the dominant process of the corrosion fatigue: microcrack development.

3. The chemical notching process was found to be sensitive to the film-rupture perturbation of free-corrosion potential (E_{corr}).

4. Microcrack development was found to be governed by the electromigration of anodic dissolution-charge carriers.

7.4 SUGGESTED FUTURE WORK

1. Because a flawless surface finish or a perfectly-bonded galvanic coating on any substrate is highly unlikely and should not be expected, it is essential to study the effect of galvanic-coating defects on corrosion-fatigue protection for substrate steels with and without mechanical notches. This study should provide useful background information to evaluate the applicability of galvanic coating for protecting real (notched) structural members serving in corrosive environments from CFC damage.

2. The effect of high test frequency on corrosion fatigue should be further investigated to verify the predictive capability of the APD model for systems under partially-saturated corrosion attack. The importance of corrosion-product-induced crack closure might also have to be studied to clarify the effects of test frequency on corrosion-fatigue cracking saturation.

3. Environmentally-assisted macroscopic crack growth at a stress-intensity-factor range near threshold regime should be studied before reasonable fatigue-life estimations for notched members at near threshold conditions in corrosive environments can be obtained.

4. The possibility of cathodic damage, e.g., hydrogen embrittlement, which might assist crack initiation has to be explored before fatigue-life predictions on high-strength steels or on systems under intense cathodic protection can be made. This subject is still highly controversial. No definite cracking mechanism or theory is commonly accepted at present.

5. The direct evidence of fatigue life spending in developing microcracks (the dominant CFC process in the APD model) during corrosion fatigue is required. More sophisticated experimental investigation in monitoring the development of microcracks (up to 0.5 mm) before the initiation of a macroscopic crack is highly desirable to verify the fatigue-life partitioning and the fatigue-life prediction of the proposed APD model.

TABLES

Table 3.1 Variables Required in the APD Model

Classification	Variables	Symbols
Applied Stress & Geometry	Stress Amplitude	$\Delta S/2$
	Stress Ratio	R
	Test Frequency	f
	Stress Concentration Factor of Notch	K_t
Material Properties (Mechanical)	Yield Strength (0.2%)	S_y
	Tensile Strength	S_u
	Atomic Weight	M
	Density	ρ
	Fatigue Strength Coefficient	σ_f'
	Fatigue Strength Exponent	b'
	Fatigue Ductility Coefficient	ε_f'
	Fatigue Ductility Exponent	c'
	Cyclic Strength Coefficient	K'
	Cyclic Strain-Hardening Exponent	n'
	Paris Constant	C
	Paris Exponent	m
	Fatigue Limit (Stress Range)	ΔS_e
	Threshold Stress-Intensity-Factor Range	ΔK_{th}
Environmental & Electrochemical Properties	Temperature of Aqueous Solution	T
	Electrolytic Conductivity	η
	Electrochemical Potential	E_{bulk}
	Redox Potentials	E^a_{eq}, E^c_{eq}
	Exchange Current Densities	i_o
	Tafel's Slopes	β_a, β_c
	Valence of Dissolving Cations	z
	Saturation Limit of Metal Ions	$C^s_{M^+}$
	Electrolytic Resistance of Salt Film	R_{film}
	Apparent Activation Energy of Film Formation	ΔH_a

Table 4.1 Chemical Composition of Martensitic Steels

Steel	C	Si	Mn	P	S	Al	Cr	Mo	Ni	Fe
API-S135	0.40	0.25	0.92	0.013	0.001	0.054	1.09	0.27	---	balance
AISI-4340[108]	0.40	0.33	0.70	0.008	0.022	0.005	0.89	0.22	1.72	balance
HY-130[86]	0.08	0.23	0.70	0.010	0.004	0.020	0.40	0.39	4.66	balance

Table 4.2 Mechanical Properties of Martensitic Steels (weight %)

Steel	Yield Strength S_y (0.2% offset) (MPa)	Tensile Strength S_u (MPa)	Elongation (%)	K_{Ic} (MPa$\sqrt{m}$)
API-S135	918.2	1047.2	18.6	190.6
AISI-4340[108]	905.8	992.7	18.5	155.0
HY-130[86]	932.0	974.0	-----	275.0

Table 4.3 Composition of Seawater Drilling Fluids (weight %)

Bentonite	Cellulose	Starch	$BaSO_4$	NaOH	Na_2CO_3
0.557	0.271	0.157	0.043	0.217	0.111

$NaHCO_3$	NaCl	Seawater	Fresh Water	Phosphate Ester Salt[1]
0.023	0.043	71.8	26.6	0.114

[1] Polymeric inhibitor, "Conquor 404", from M-I Drilling Fluid Company, Houston, TX.

Table 5.1 Chemical Composition of Hot-Rolled Medium-Strength Steels

Steel	C	Si	Mn	P	S	Cu	Cr	Mo	Ni	Fe
JIS SS41[78]	0.18	0.01	0.35	0.006	0.011	0.030	0.01	-----	0.02	balance
JIS SM50A[78]	0.17	0.35	1.35	0.023	0.025	0.020	0.02	-----	0.02	balance

Table 5.2 Fatigue-Life Properties of Investigated Steels

Properties	API-S135[2]	JIS SS41[3]	JIS SM50A[4]
Yield Strength (0.2%), S_y (MPa)	918.2	299.9[78]	420.4[78]
Tensile Strength, S_u (MPa)	1047.2	519.4[78]	603.7[78]
Fatigue Strength Coefficient, σ_f' (MPa)	1655.0[125]	1092.1[126]	1130.3[126]
Fatigue Strength Exponent, b'	-0.076[125]	-0.108[126]	-0.09[126]
Fatigue Ductility Coefficient, ϵ_f'	0.73[125]	0.47[126]	1.81[126]
Fatigue Ductility Exponent, c'	-0.62[125]	-0.52[126]	-0.749[126]
Cyclic Strength Coefficient, K' (MPa)	1579.0[125]	904.6[126]	1042.1[126]
Cyclic Strain-Hardening Exponent, n'	0.14[125]	0.21[126]	0.12[126]
Paris Constant (R = 0~0.1, Air), C (mm/cycle)	1.817×10^{-8}[108]	3.137×10^{-10}[43]	1.033×10^{-9}[127]
Paris Exponent, m, in Air	2.67[108]	3.698[43]	3.458[127]
Paris Constant (R = 0~0.1, $NaCl_{aq}$), C (mm/cycle)	(0.1 Hz, 3.0%) 4.163×10^{-8}[108]	(1 Hz, 3.5%) 4.925×10^{-8}[43]	(0.3 Hz, 3.0%) 9.47×10^{-10}[110]
Paris Exponent, m, in $NaCl_{aq}$	2.63[108]	2.615[43]	3.825[110]
Fatigue Limit in Air, ΔS_e (MPa)	760.0[57]	630.0[78]	325.0[78]
Threshold ΔK, ΔK_{th} (MPa$\sqrt{m}$)	6.0[118]	6.0[118]	6.0[118]

[2] Fatigue-life properties were taken from AISI 4340 steel of same mechanical strength (see Tables 4.1-4.2).
[3] Crack propagation parameters were taken from a similar material: A516-60 hot-rolled steel.
[4] Crack propagation parameters in saline aqueous environment were taken from JIS SM50B steel.

Table 5.3 Electrochemical Parameters Used in the APD Model Simulations for API-S135 Steel in Deaerated Seawater Drilling Fluid at 93.3 °C

Parameter	Value	Unit
Redox Potential of Ferrous Ion (Fe^{2+}) Half-Cell Reaction at Standard State (E^{o}_{a} vs. SCE)	-0.68[128]	(V)
Redox Potential of Hydrogen Ion (H^{+}) Half-Cell Reaction at Standard State (E^{o}_{c} vs. SCE)	-0.24[128]	(V)
Redox Potential of Ferrous Ion (Fe^{2+}) Half-Cell Reaction in Seawater Drilling Fluid (E^{a}_{eq} vs. SCE)	-0.90[5]	(V)
Redox Potential of Hydrogen Ion (H^{+}) Half-Cell Reaction in Seawater Drilling Fluid (E^{c}_{eq} vs. SCE)	-0.37[6]	(V)
pH of Bulk Electrolyte	~8.0[7]	
pH of Crack Electrolyte	~3.5[34]	
Ferrous Ion Concentration in Very Dilute Electrolyte [C_{M+}]	1.0×10^{-6}	(mole/liter)
Exchange Current Density of Fe^{2+} at Crack Tip ($i_o^{plastic}$)	1.5×10^{-5}	(A/cm^2)
Exchange Current Density of H^{+} at Crack Face (i_o^{pass})	1.0×10^{-7}[129]	(A/cm^2)
Electrolytic Conductivity of Drilling Fluid (η)	45.0[130]	($\Omega^{-1}m^{-1}$)
Electrolytic Conductivity of Inhibited Fluid (η)	30.0	($\Omega^{-1}m^{-1}$)
Atomic Weight of Electrode (M)	55.8	(g/mole)
Density of Electrode (ρ)	7.9	(g/cm^{-3})
Tafel's Slope of Fe^{+2} Oxidation (β_a)	0.050	
Tafel's Slope of H^{+} Reduction (β_c)	-0.180	
Diffusion Coefficient of Fe^{+2} (D)	3.5×10^{-7}[131][8]	(cm^2/sec)
Saturation Limit of Fe^{+2} (C^{s}_{M+})	4.0×10^{-3}[131]	($mole/cm^3$)
Electrolytic Resistance of Salt Film (R_{film})	5.5×10^{3}[132]	(Ω-cm)
Apparent Activation Energy of Film Formation (ΔH_a)	27.8	(KJ/mole)

[5] Redox potential value of ferrous ions was obtained from Nerst's equation for very dilute (cations) electrolyte.
[6] A potential value corresponds to cathodic exchange current density in observed cathodic polarization diagram.
[7] Checked with pH paper.
[8] Value was adjusted by Stokes Einstein relation for a solution having its viscosity 15-20 times the value of pure water.

Table 5.4 Comparison of Electrochemical Parameters Obtained from Polarization Experiments on API-S135 Steel in Various Seawater Drilling Fluids

Parameter	Case I	Case II	Case III	Unit
Fluid Temperature (T)	93.1~93.4	93.1~93.4	25.3~26.0	°C
Gas Purged	UHP N_2	Medical Air	UHP N_2	
Redox Potential of Ferrous Ion (Fe^{2+}) Half Cell (E^a_{eq} vs. SCE)	-0.90	-0.90	-0.78	V
Redox Potential of Hydrogen Ion (H^+) Half Cell (E^c_{eq} vs. SCE)	-0.37	-0.13	-0.173	V
Tafel's Slope of Fe^{+2} Oxidation (β_a)	0.05	0.05	0.075	
Tafel's Slope of H^+ Reduction (β_c)	-0.18	-0.22	-0.227	

Table 5.5 Summary of Fatigue-Test Results of API-S135 Steel in Seawater Drilling Fluids at 93.3 °C under Free Corrosion (R = 0.1, f = 2 Hz)

Stress Amplitude $\Delta S/2$ (MPa)	Aeration	Crack Initiation N_i (cycles)	Crack Growth N_{p2} (cycles)	Total Life N_f (cycles)
127.9	Medical Air	3,259,000	84,000	3,343,300
150.6	Medical Air	-------	-------	4,115,310
170.5	Medical Air	1,862,000	45,000	1,907,500
170.7	Medical Air	436,000	35,000	470,810
170.5	Medical Air	1,473,000	31,000	1,504,050
181.9	Medical Air	1,537,000	25,000	1,562,000
181.9	Medical Air	1,644,000	25,000	1,669,440
191.8	Medical Air	529,000	23,000	551,950
198.9	Medical Air	1,637,000	20,000	1,657,340
227.4	Medical Air	1,783,000	17,000	1,800,000
270.0	Medical Air	888,000	11,000	899,360
298.4	Medical Air	306,000	6,400	312,090
170.5	UHP N_2	2,073,000	23,000	2,095,840
170.5	UHP N_2	1,367,000	39,000	1,406,210
170.5	UHP N_2	-------	-------	3,865,110
191.8	UHP N_2	1,839,000	22,000	1,860,590
191.8	UHP N_2	2,078,000	34,000	2,111,730
213.1	UHP N_2	495,000	14,000	508,990
227.4	UHP N_2	1,663,420	10,000	1,673,420
241.6	UHP N_2	512,400	16,200	528,600
255.8	UHP N_2	1,220,460	8,480	1,228,940
270.0	UHP N_2	812,420	10,300	822,720

Table 5.6 Summary of Fatigue-Test Results of API-S135 Steel in Chemically Inhibited[9] Drilling Fluids at 93.3 °C under Free Corrosion (R = 0.1, f = 2 Hz)

Stress Amplitude ΔS/2 (MPa)	Aeration	Crack Initiation N_i (cycles)	Crack Growth N_{p2} (cycles)	Total Life N_f (cycles)
170.5	Medical Air	2,945,800	25,000	2,970,800
184.7	Medical Air	1,847,400	22,600	1,870,000
184.7	Medical Air	2,330,700	22,100	2,352,800
213.1	Medical Air	1,504,000	17,000	1,521,200
227.4	Medical Air	--------	------	1,161,200
241.6	Medical Air	945,900	15,300	961,200
255.8	Medical Air	853,250	9,750	863,000
270.0	Medical Air	777,550	7,250	784,800
284.2	Medical Air	415,400	7,000	422,400
170.5	UHP N_2	3,767,000	34,000	3,801,350
191.8	UHP N_2	2,385,000	24,000	2,409,200
191.8	UHP N_2	2,296,000	25,000	2,320,530
204.6	UHP N_2	1,451,000	21,000	1,472,200
204.6	UHP N_2	946,000	21,000	967,400
213.1	UHP N_2	272,000	16,000	287,600
213.1	UHP N_2	2,028,000	26,000	2,054,000
227.4	UHP N_2	1,476,000	17,000	1,492,800
255.8	UHP N_2	943,000	11,000	954,000
298.4	UHP N_2	825,000	7,400	832,000
326.8	UHP N_2	199,000	8,700	208,000
355.2	UHP N_2	233,000	5,300	238,400

[9] Conquor 404 polymeric inhibitor, 0.11%.

Table 5.7 Comparison of Fatigue-Test Results of API-S135 Steel Obtained in Ambient Air with those Obtained in Deaerated Seawater Drilling Fluid at 93.3 °C under Cathodic Protection (R = 0.1)

Stress Amplitude ΔS/2 (MPa)	Environment	Protection Method	Frequency f (Hz)	Total Life N_f (cycles)
213.1	Ambient Air	----------	8	>10,375,510[10]
284.2	Ambient Air	----------	8	>10,319,000
353.7	Ambient Air	----------	10	>10,118,000
394.1	Ambient Air	----------	10	>10,328,000
404.2	Ambient Air	----------	10	6,229,000
414.3	Ambient Air	----------	10	356,000
414.3	Ambient Air	----------	10	77,000
429.4	Ambient Air	----------	10	24,000
213.1	Drilling Fluid[11]	E_{bulk}= -0.75 V (SCE)	2	3,866,510
227.4	Drilling Fluid	E_{bulk}= -0.75 V (SCE)	2	3,152,970
270.0	Drilling Fluid	E_{bulk}= -0.75 V (SCE)	2	2,972,360
255.8	Drilling Fluid	E_{bulk}= -0.8 V (SCE)	2	9,543,290
255.8	Drilling Fluid	E_{bulk}= -1.0 V (SCE)	2	4,096,340
312.6	Drilling Fluid	IVD Al (25 μm)	2	5,233,850
326.8	Drilling Fluid	IVD Al (25 μm)	2	10,282,800
341.0	Drilling Fluid	IVD Al (25 μm)	2	605,350
355.2	Drilling Fluid	IVD Al (25 μm)	2	1,485,400
376.6	Drilling Fluid	IVD Al (25 μm)	2	609,600
397.9	Drilling Fluid	IVD Al (25 μm)	2	120,000

[10] Specimen did not fail.

[11] All drilling fluids for tests under cathodic protection were purged with UHP N_2.

Table 6.1 A Summary of the Effects of Controllable Variables on the High-Cycle Corrosion-Fatigue Life of Structural Steels in Saline Aqueous Environments

Classification	Variables	Influence on Fatigue Life	Significance	Referred Section in Thesis
Mechanical	Stress Range (ΔS)	($\downarrow$)[12]	STRONG[15]	Sec. 2.4.3
	Stress Ratio (R)	($\downarrow$)	Weak[16]	Sec. 2.4.3, 5.5
	Frequency (f)	($\uparrow$)[13]	STRONG	Sec. 2.4.4, 5.9.3
	Notches (K_t)	($\downarrow$)	STRONG	Sec. 5.8
	Strength (S_y)	N/A[14]	N/A	Sec. 2.4.2, 5.7
Environmental	Pressure (P)	($\downarrow$)	Weak	Sec. 2.4.6
	Temperature (T)	($\uparrow$)	Medium	Sec. 2.4.6, 5.6.2
	pH	($\uparrow$)	Weak	Sec. 2.4.6
	Oxygen [O_2]	N/A	N/A	Sec. 2.4.6, 5.2.2
Electrochemical	Potential (E_{bulk})	($\downarrow$)	STRONG	Sec. 2.4.7, 5.4
	Conductivity (η)	($\downarrow$)	Weak	Sec. 5.3
	Anodic TS[17] (β_a)	($\uparrow$)	STRONG	Appendix B
	Cathodic TS (β_c)	($\downarrow$)	Medium	Appendix B

[12] Symbol represents a decrease in fatigue life for an increasing value of the corresponding variable.
[13] Symbol represents an increase in fatigue life for an increasing value of the corresponding variable.
[14] Not known or uncertain because it's influence or significance may interact with other variables.
[15] Producing orders of magnitude difference in fatigue life is classified as STRONG significance.
[16] Producing more than 200% magnitude difference in fatigue life is classified as Medium significance.
[17] TS represents an abbreviation of Tafel's slope.

FIGURES

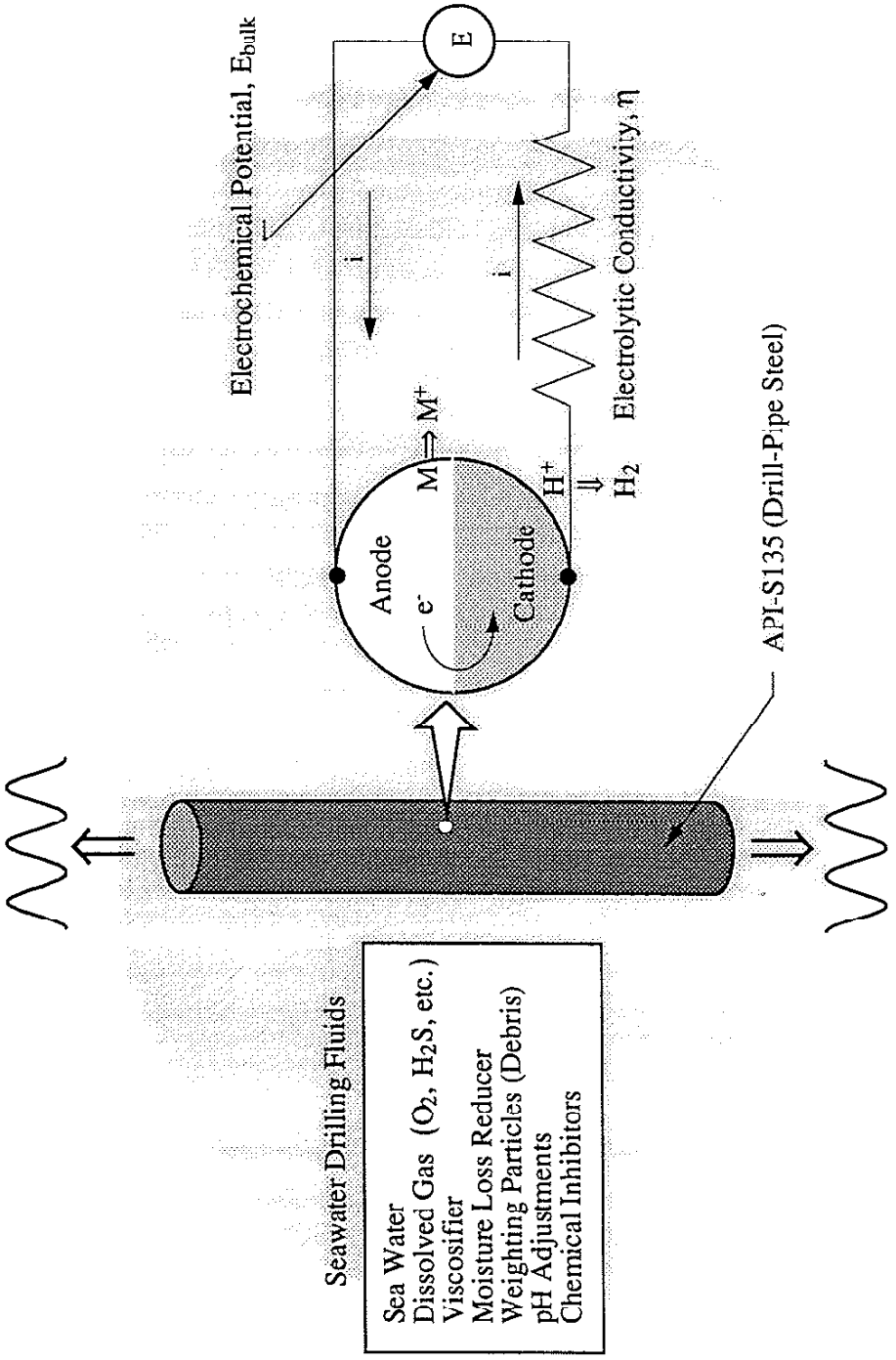

Figure 1.1 Schematic presentation of a smooth drill-pipe-steel specimen cyclically loaded in seawater drilling fluid during offshore drilling operation.

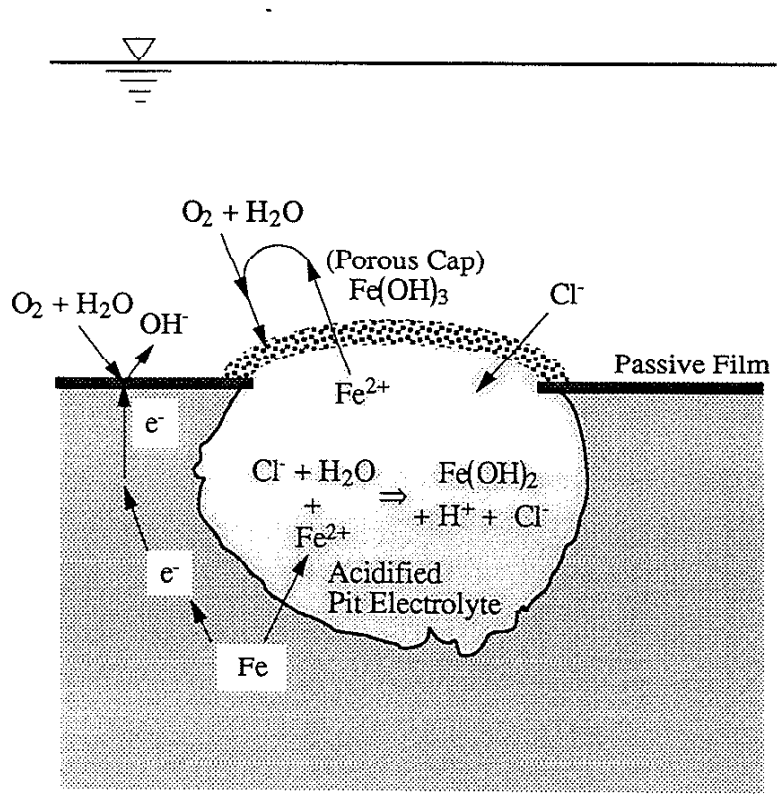

Figure 2.1 Schematic of processes occurring within an actively growing pit in iron [after 10].

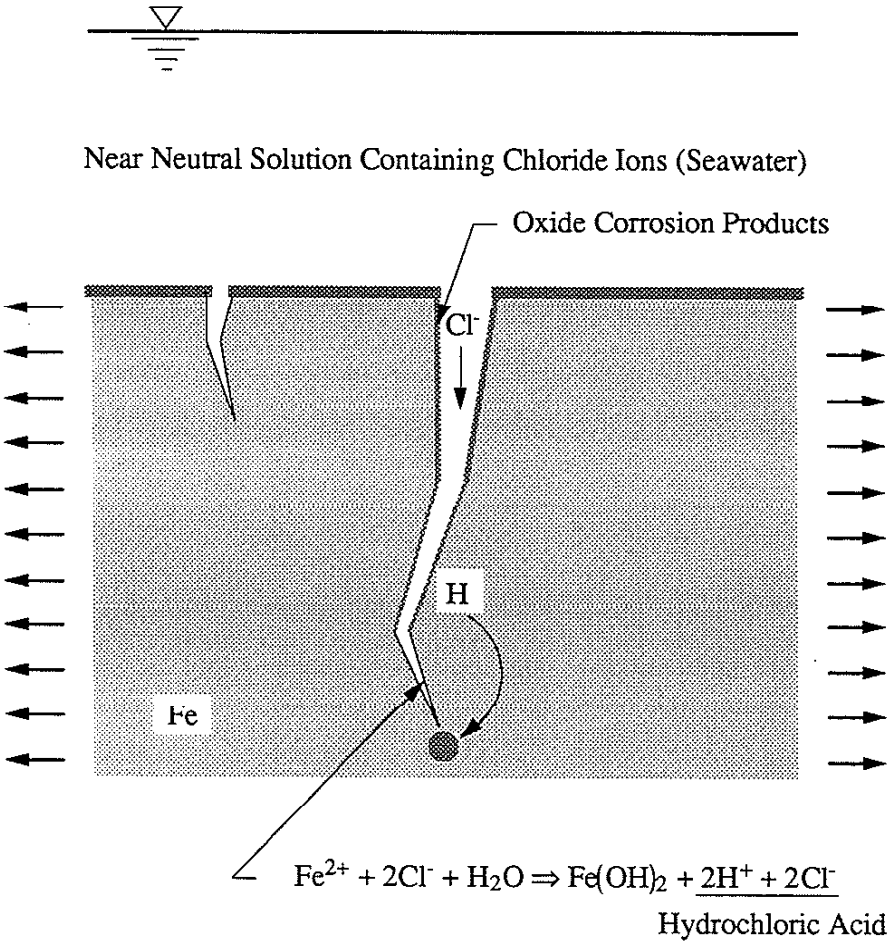

Figure 2.2 Chemistry and pH change in a growing crack under stress in seawater.

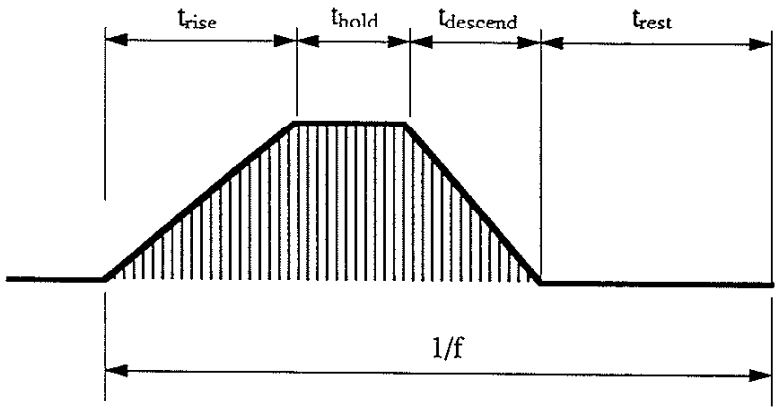

Figure 2.3 A trapezoidal cyclic loading waveform.

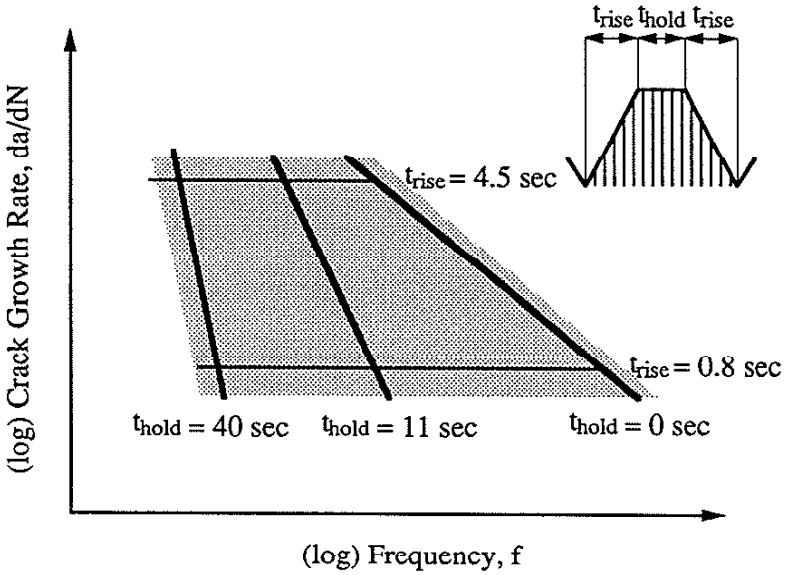

(a) $K_{Imax} < K_{Iscc}$

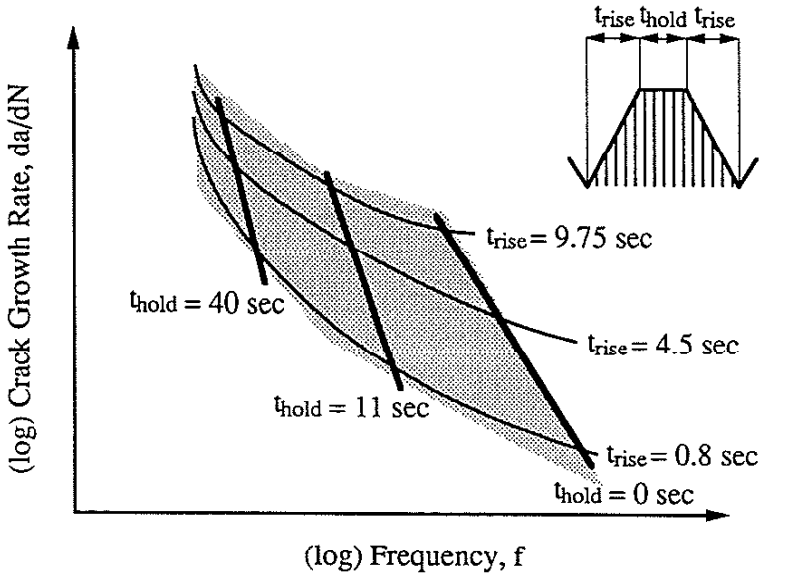

(b) $K_{Imax} > K_{Iscc}$

Figure 2.4 Effects of cyclic loading waveform and frequency on corrosion-fatigue crack growth [after 89]: (a) $K_{Imax} < K_{Iscc}$; (b) $K_{Imax} > K_{Iscc}$.

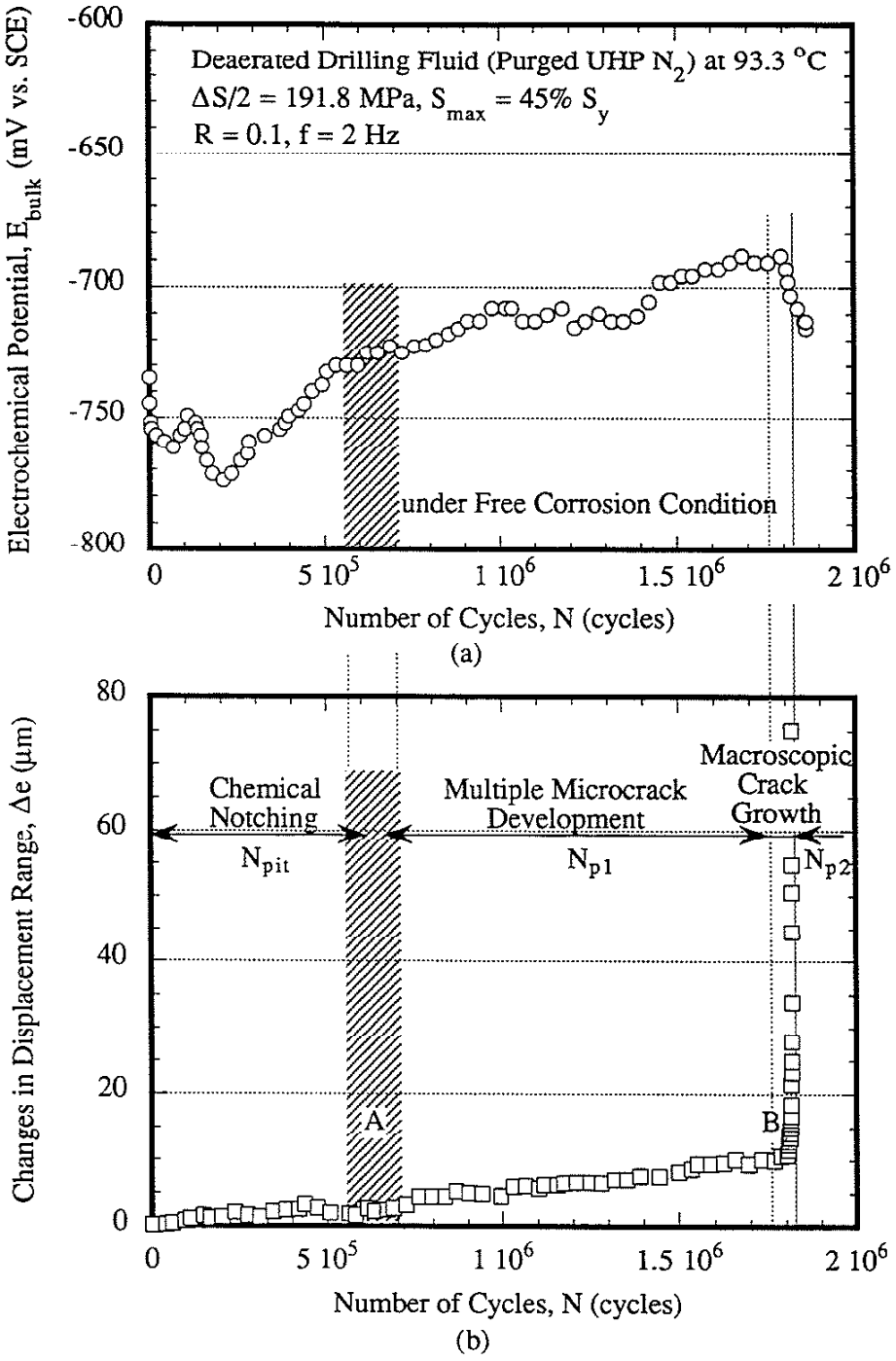

Figure 3.1 Observed accumulation of damage during corrosion-fatigue cracking: (a) electrochemical potential (E_{bulk}); (b) changes in displacement range (Δe) (note: "A" represents a transition region between chemical notching and microcrack development; "B" represents a transition between microcrack development and macroscopic crack growth).

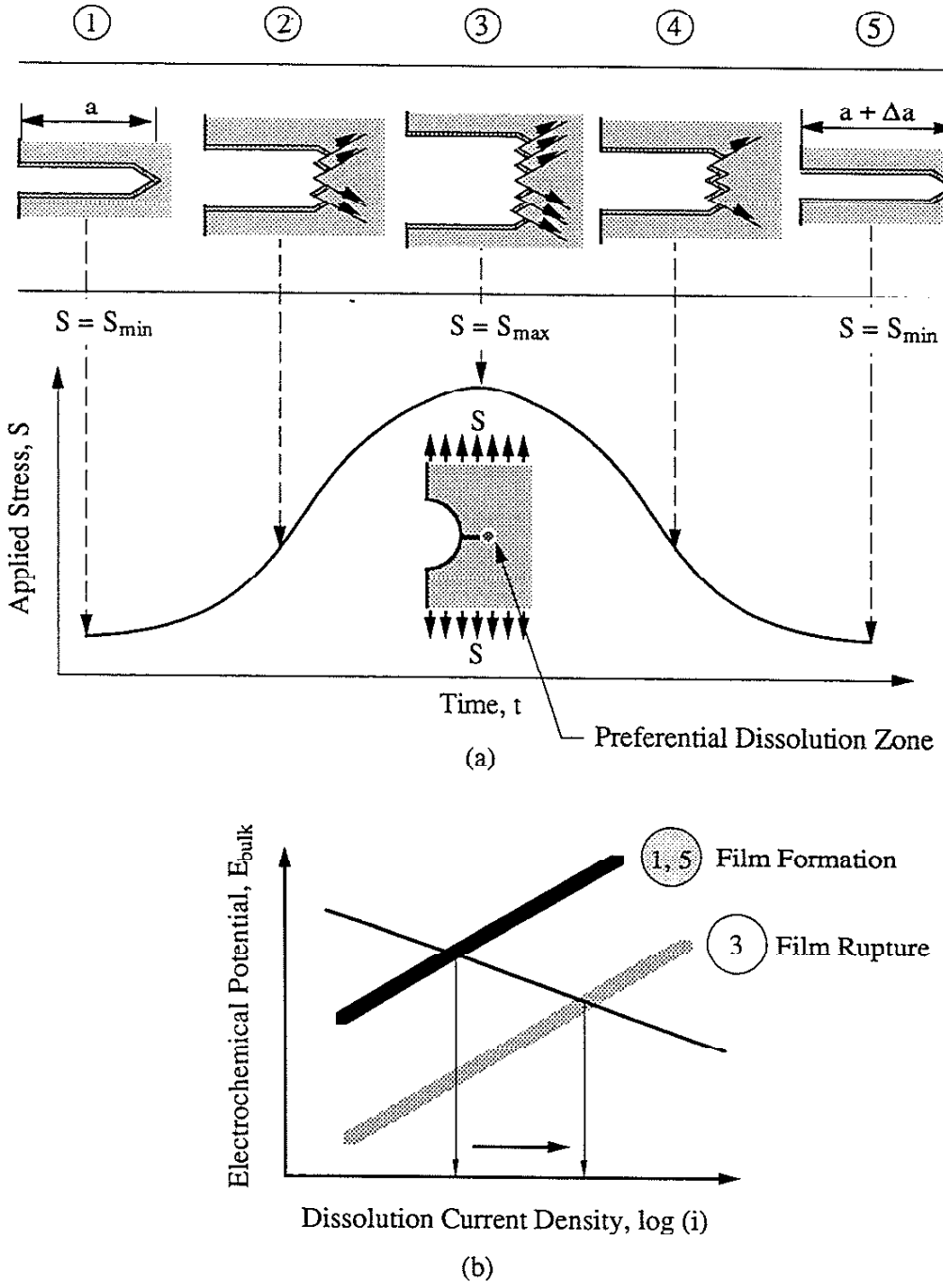

Figure 3.2 Microcrack development processes:
(a) cyclic-loading-induced film-rupture process causing preferential dissolution at a microcrack tip;
(b) potential/current density perturbation for responding film rupture/film formation process occurred at preferential dissolution zone due to the cyclic loading.

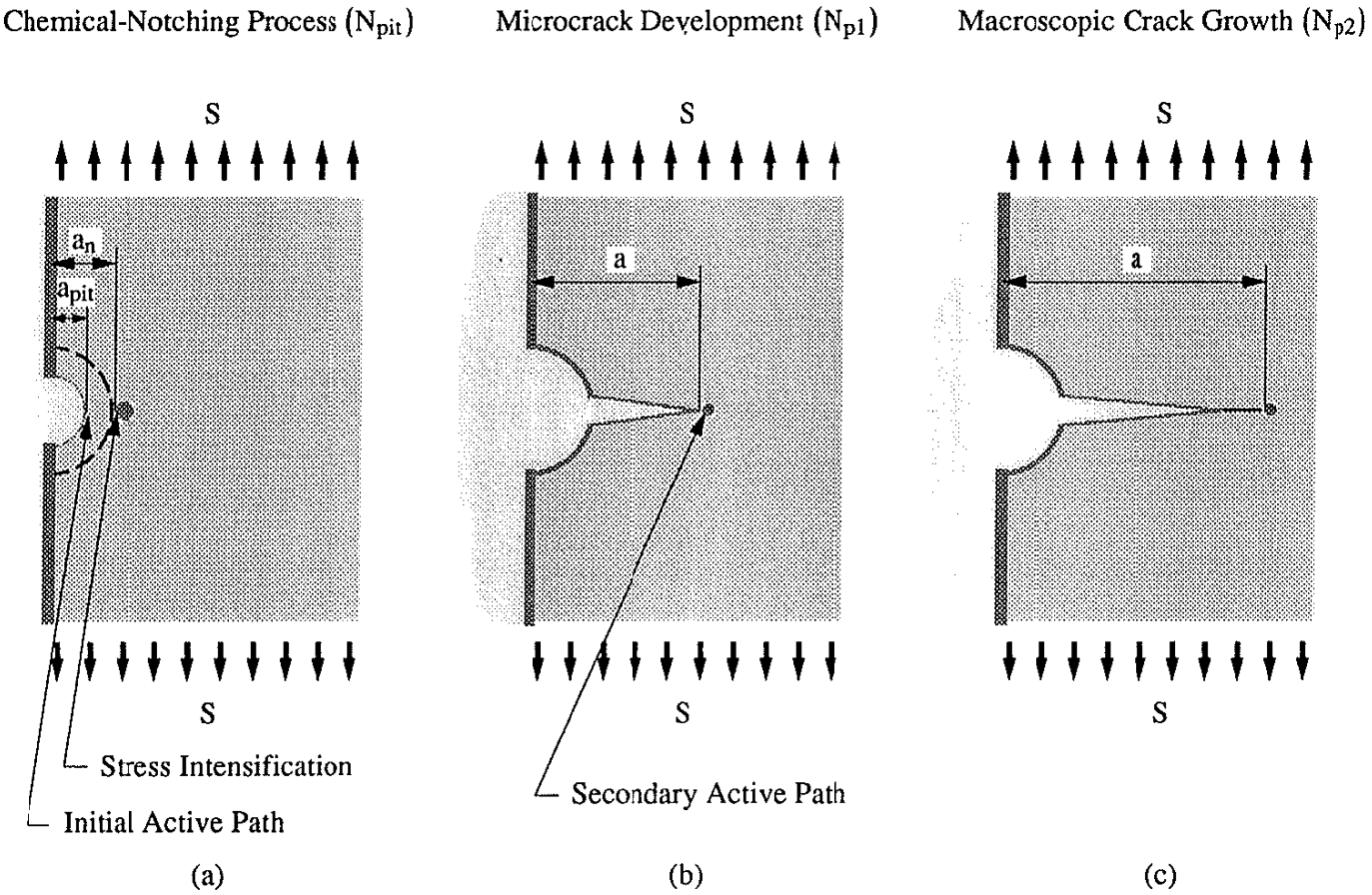

Figure 3.3 Illustration of progressive Active-Path-Dissolution (APD) crack initiation and growth: (a) chemical-notching process; (b) microcrack development; (c) macroscopic crack growth.

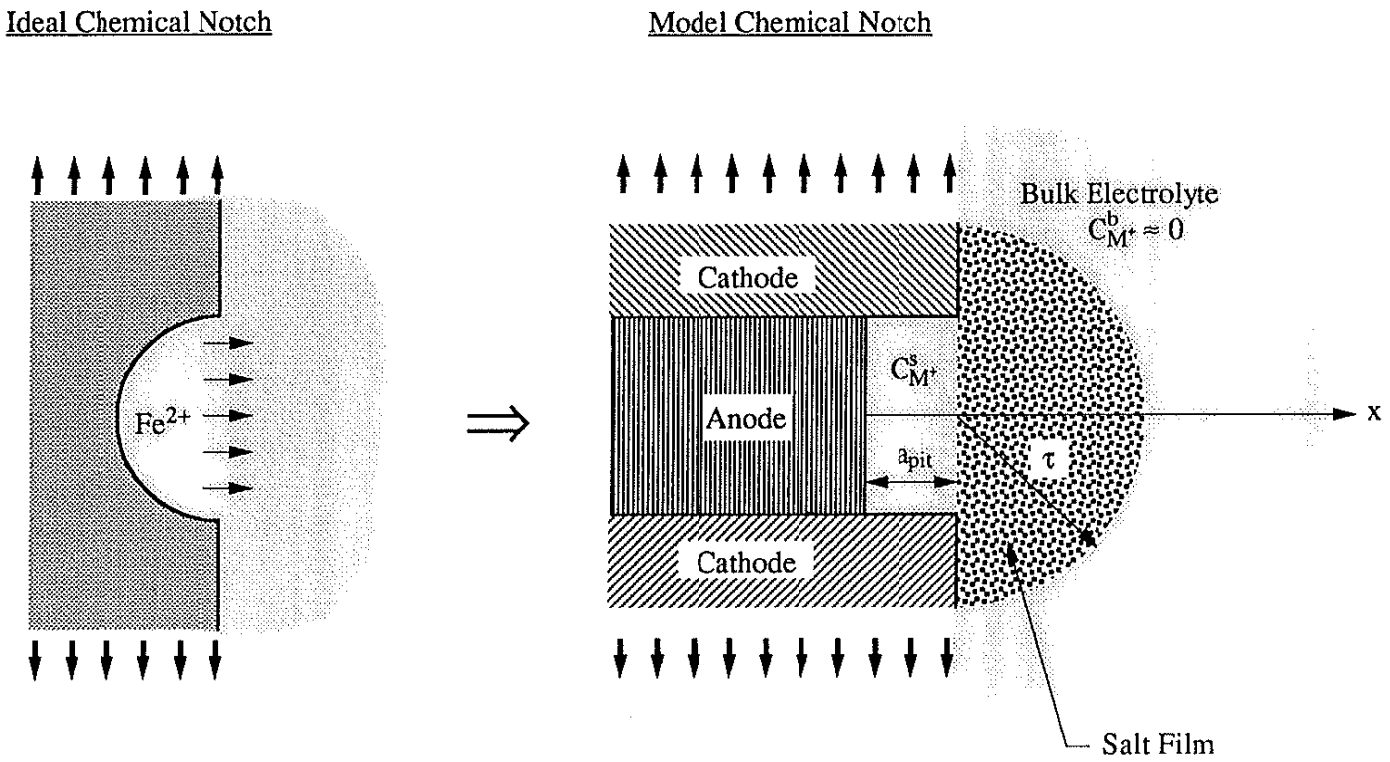

Figure 3.4 Construction of a model chemical notch (corrosion pit).

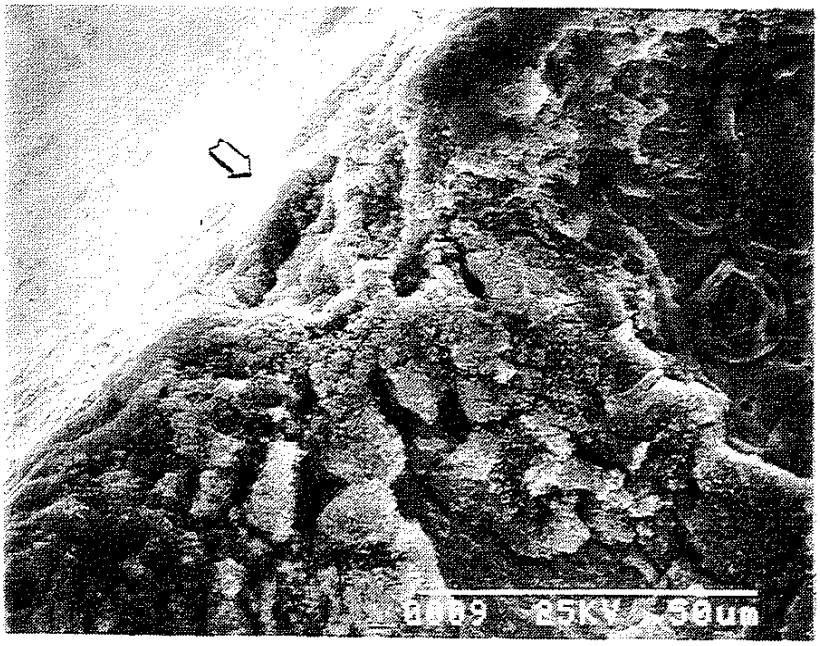

Figure 3.5 A micrograph showing a chemical notch (arrow) on a crack-initiation site of an API-S135 fatigued in deaerated seawater drilling fluid (T = 93.3 °C, $\Delta S/2$ = 213.1 MPa, R = 0.1, f = 2 Hz).

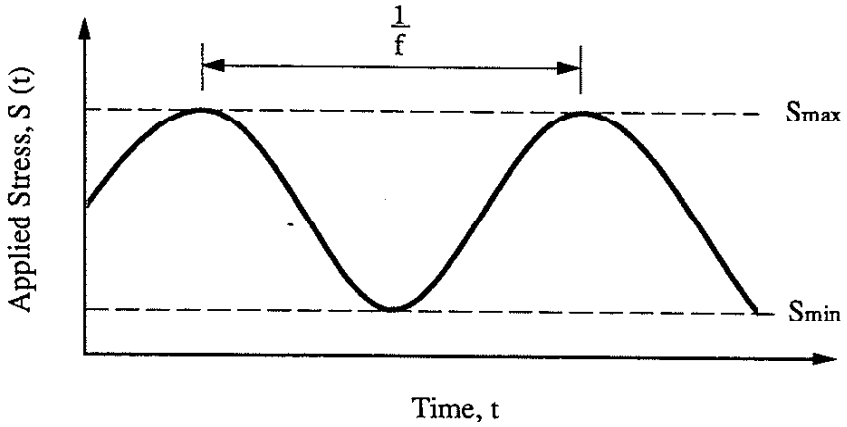

(a)

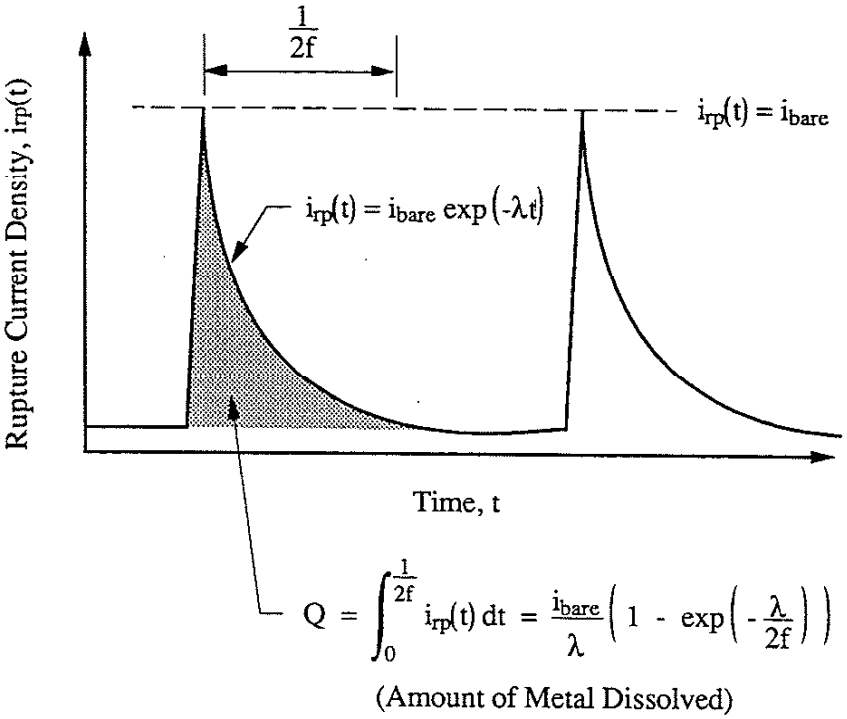

(b)

Figure 3.6 Current-density transient as the consequence of film rupture/ film formation process induced by cyclic loading: (a) cyclic loading wave; (b) rupture current-density trace.

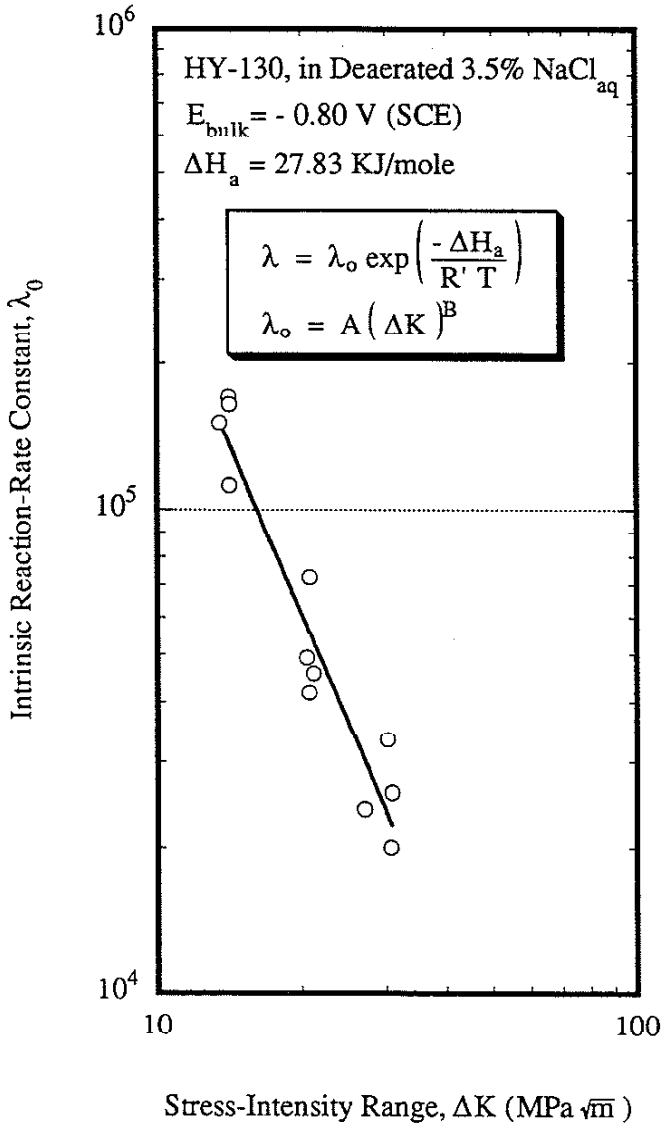

Figure 3.7 Correlation of intrinsic reaction-rate constant (λ_o) with stress-intensity-factor range (ΔK) for modeling current-density-decay exponent (λ) [after 86].

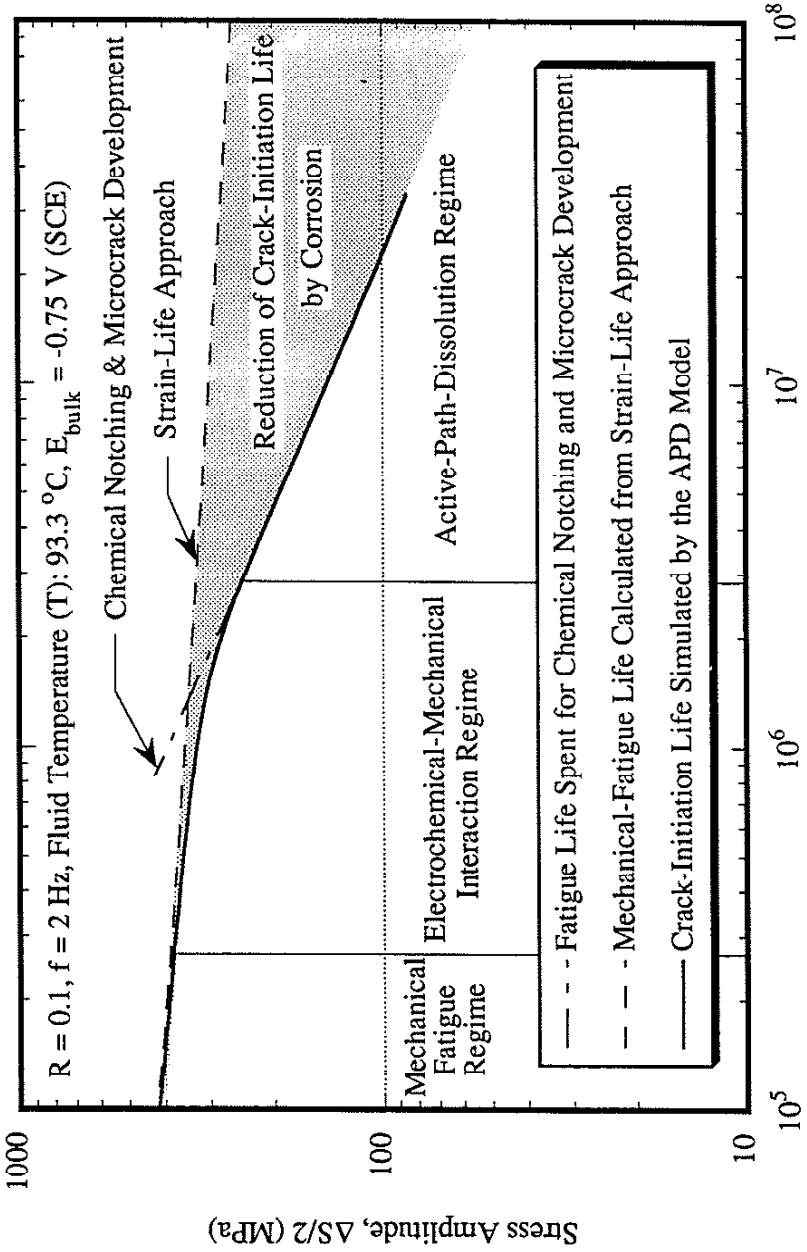

Figure 3.8 Determination of crack-initiation life by the linear damage accumulation of the mechanical-fatigue life predicted by strain-life approach and the life period spent for chemical-notching process and microcrack development in the APD model (sinusoidal wave, R = 0.1, f = 2 Hz, η = 45 $\Omega^{-1}m^{-1}$, E_{bulk} = -0.75 V vs. SCE).

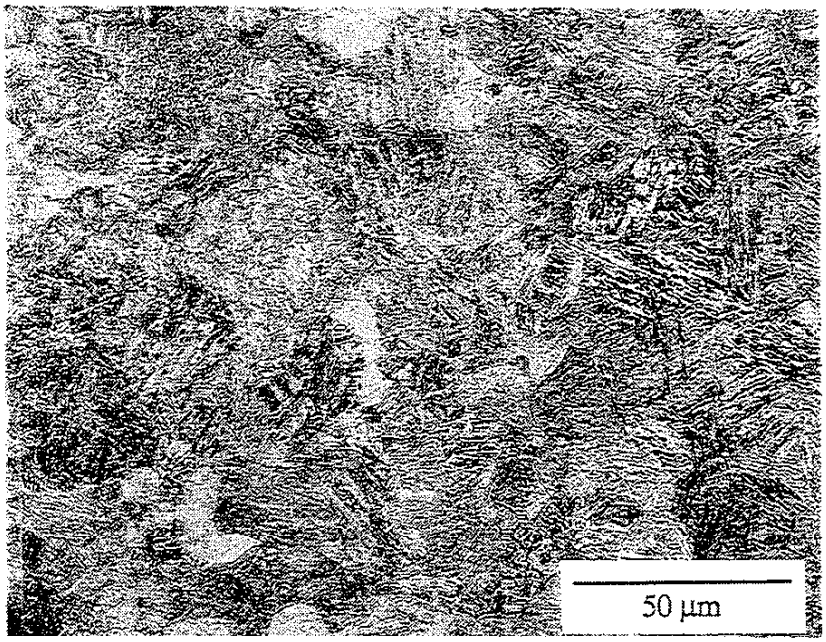

Figure 4.1 The microstructure of an API-S135 steel sectioned parallel to the longitudinal axis of a drill pipe (Vilella's reagent, 600 X).

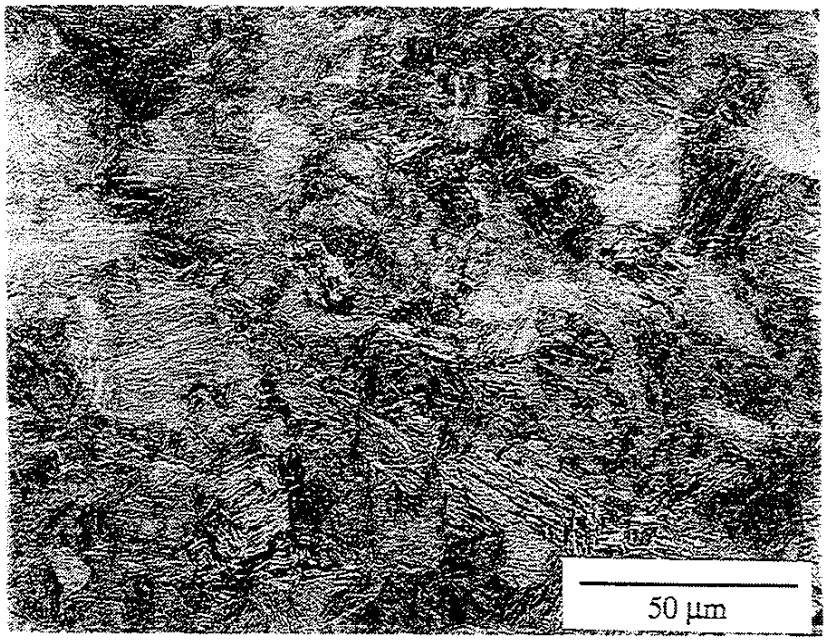

Figure 4.2 The microstructure of an API-S135 steel sectioned perpendicular to the longitudinal axis of a drill pipe (Vilella's reagent, 600 X).

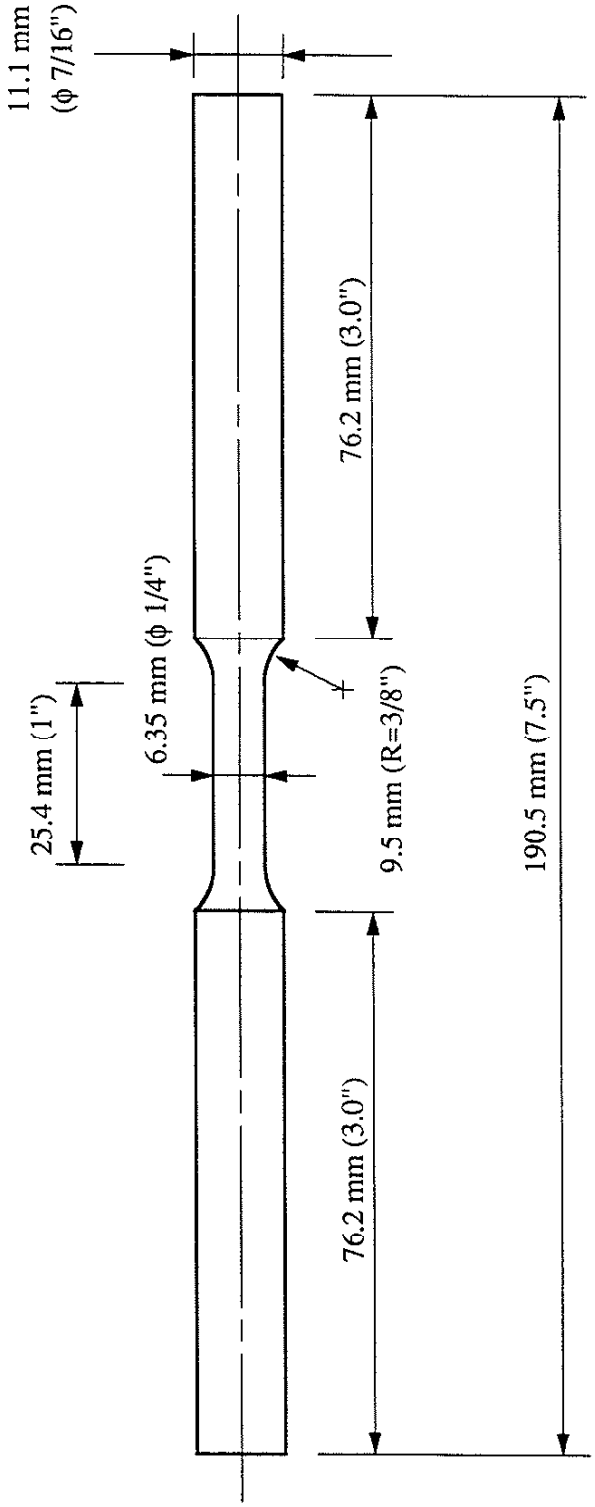

Figure 4.3 Dimensions of a corrosion-fatigue specimen.

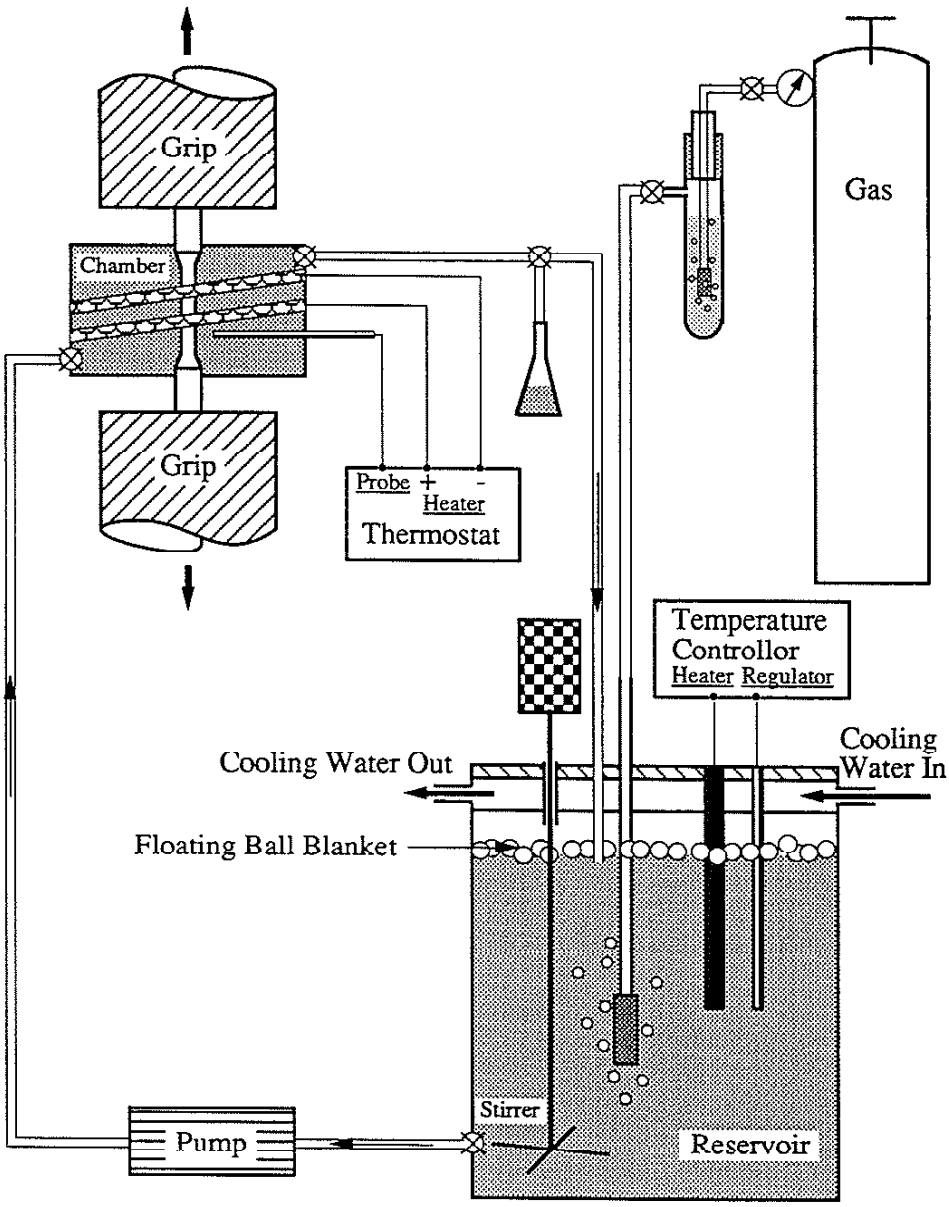

Figure 4.4 A closed-loop circulation set-up for corrosion-fatigue tests.

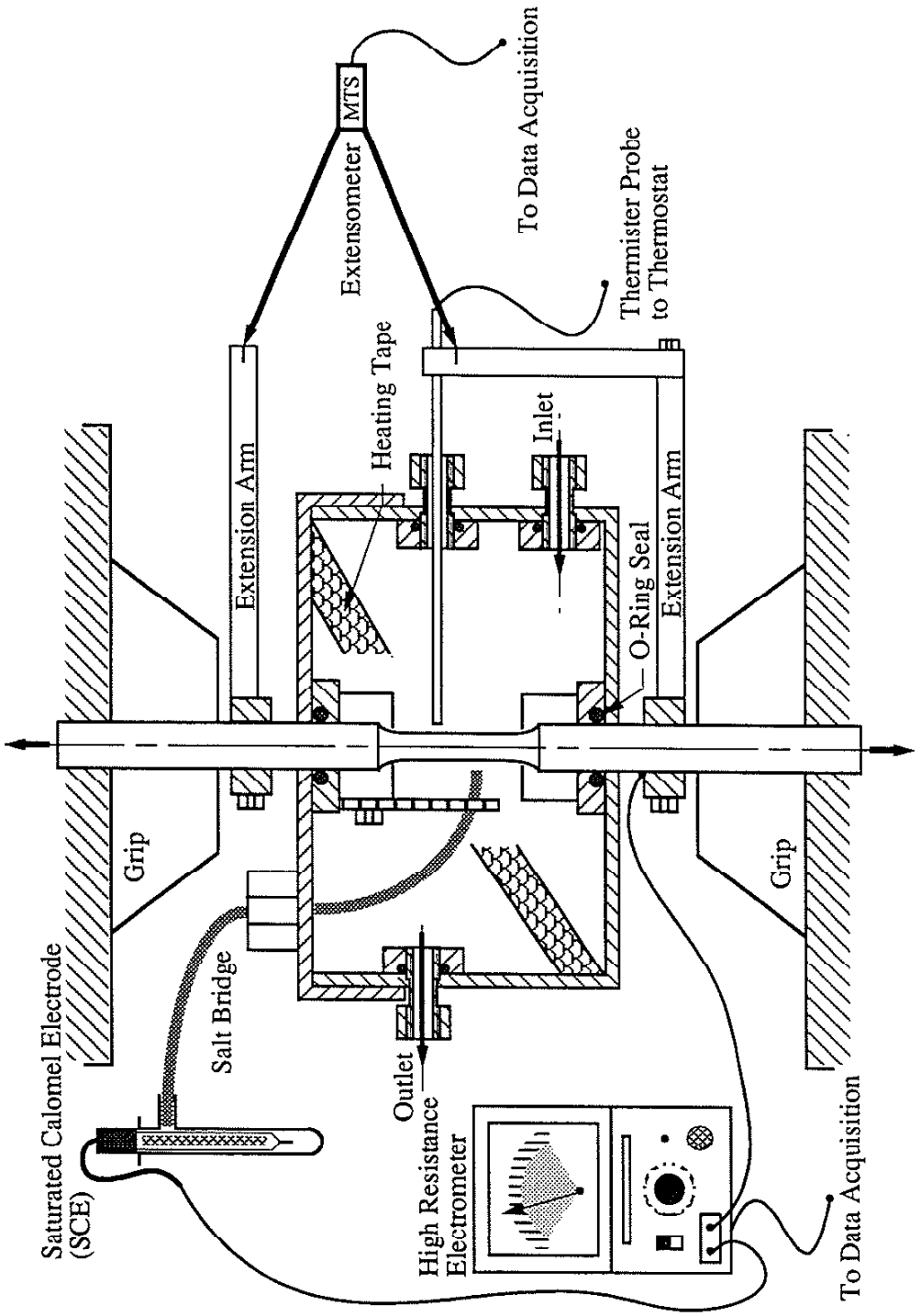

Figure 4.5 The set-up of environmental chamber.

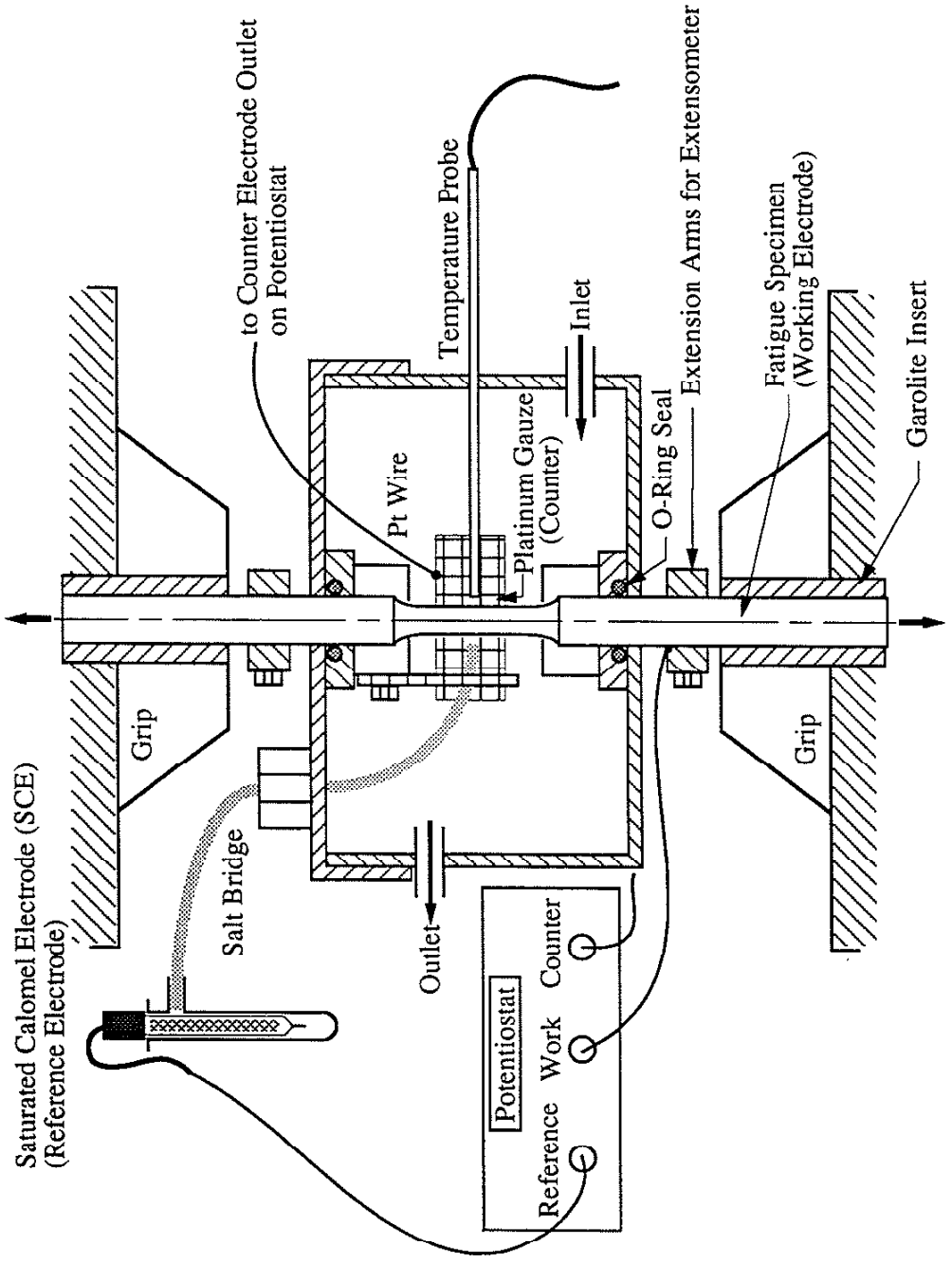

Figure 4.6 The fatigue test under potential control by a potentiostat.

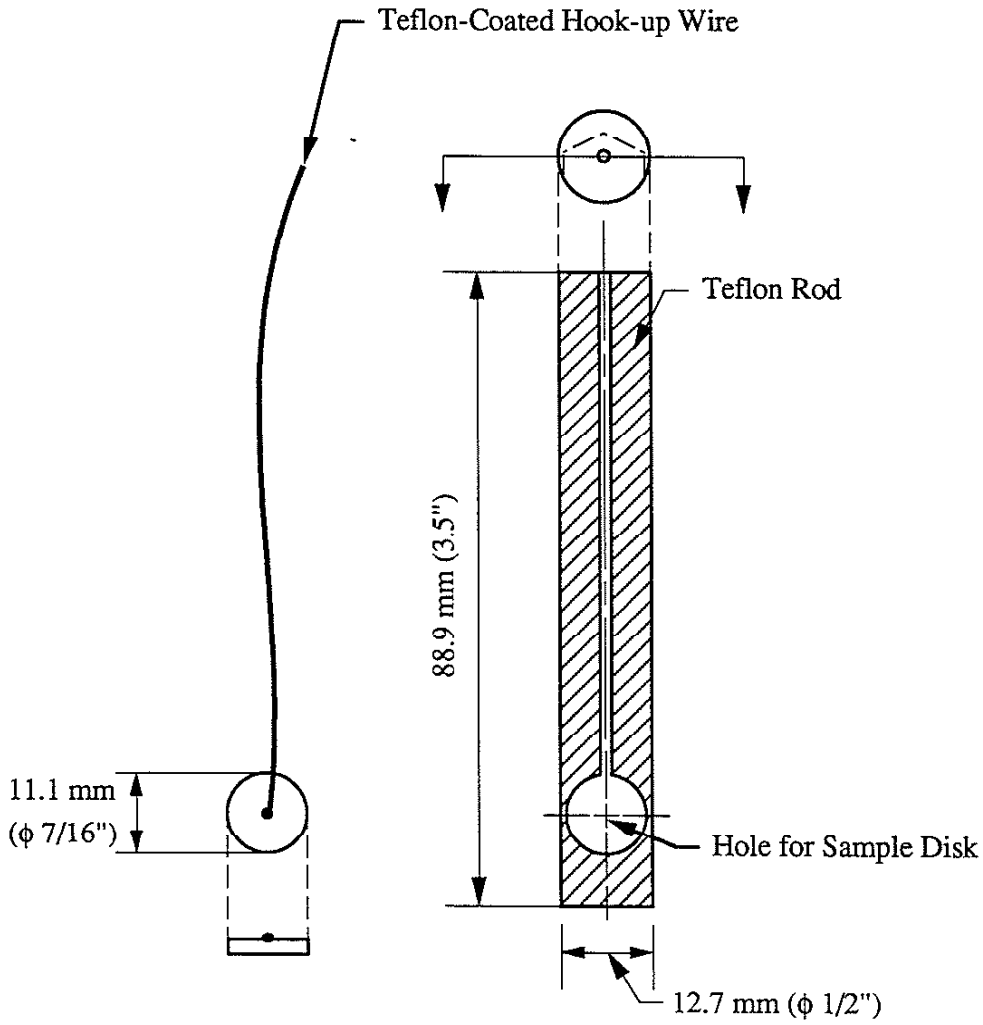

Figure 4.7 Sample disk and electrode holder for potentiodynamic polarization analysis.

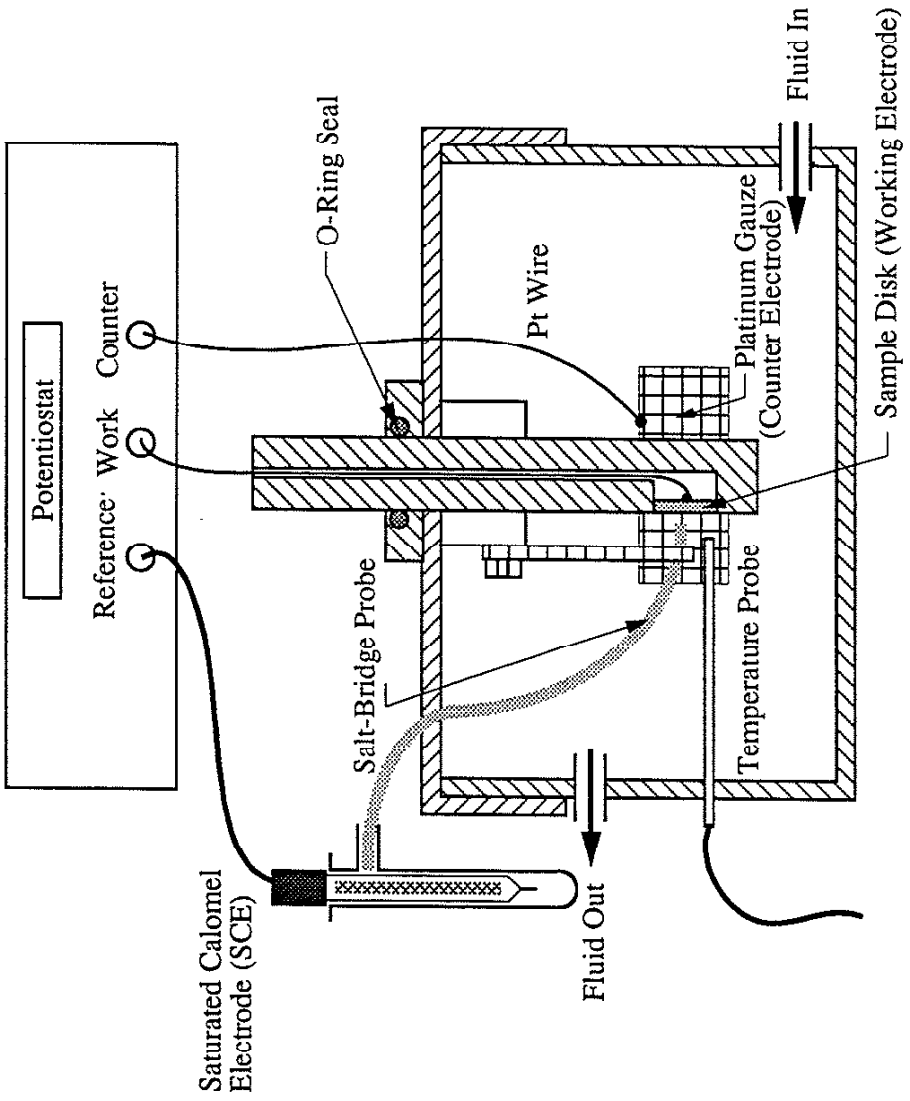

Figure 4.8 The set-up for potentiodynamic polarization scan.

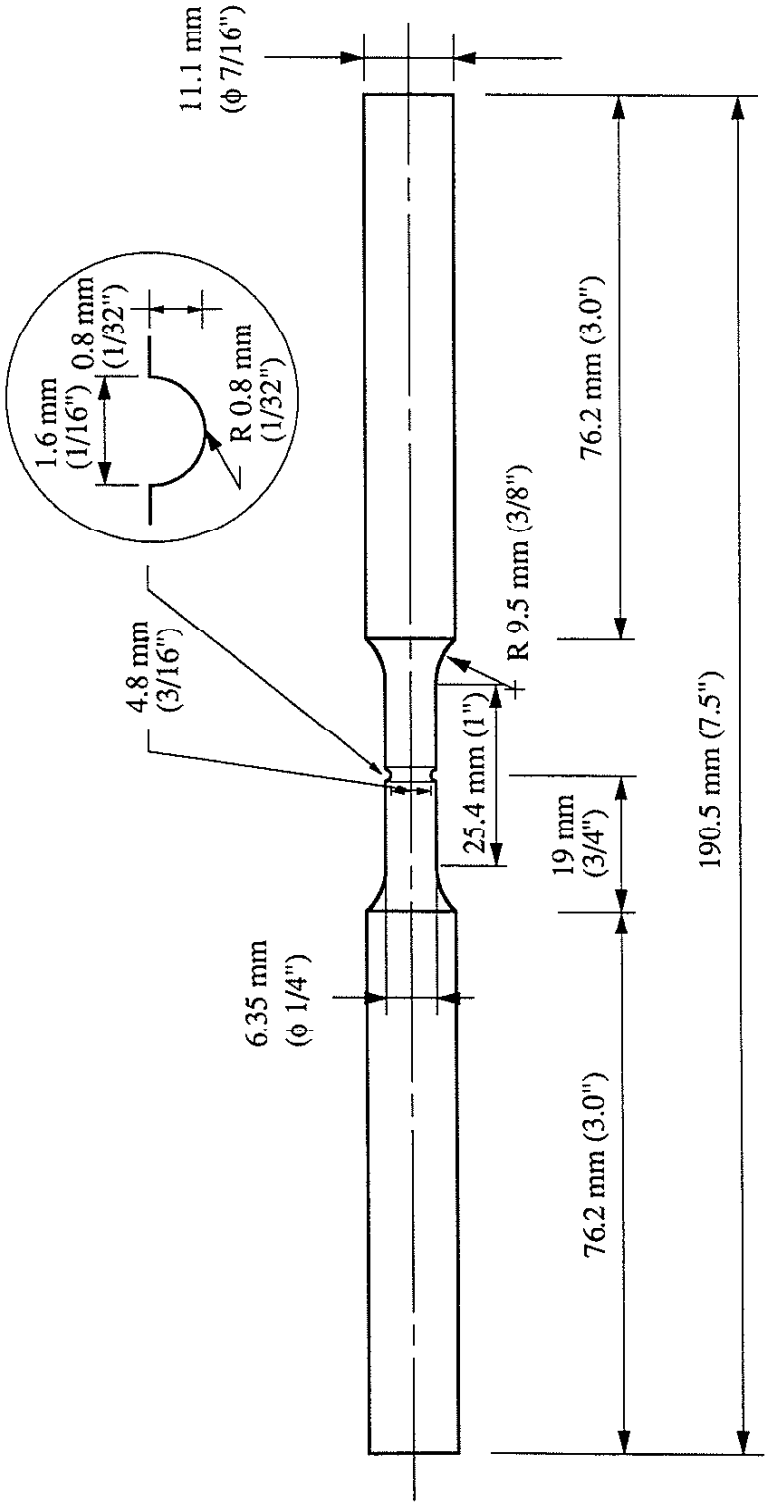

Figure 4.9 Dimensions of notched corrosion-fatigue specimen for current/potential transient measurements.

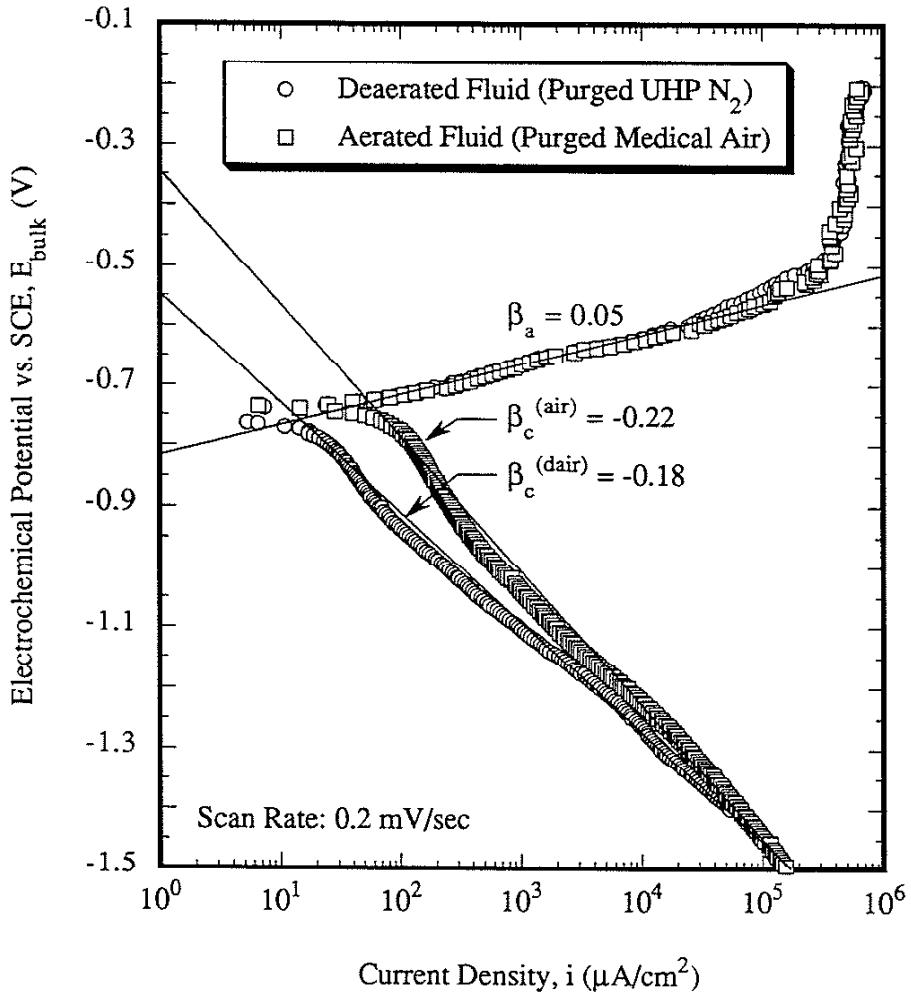

Figure 5.1 Aeration effects on the potentiodynamic polarization behavior of API-S135 steel in seawater drilling fluids at 93.3 °C (note: β_a is the Tafel's slope of the anodic branch while β_c the cathodic branch, scan rate: 0.2 mV/sec).

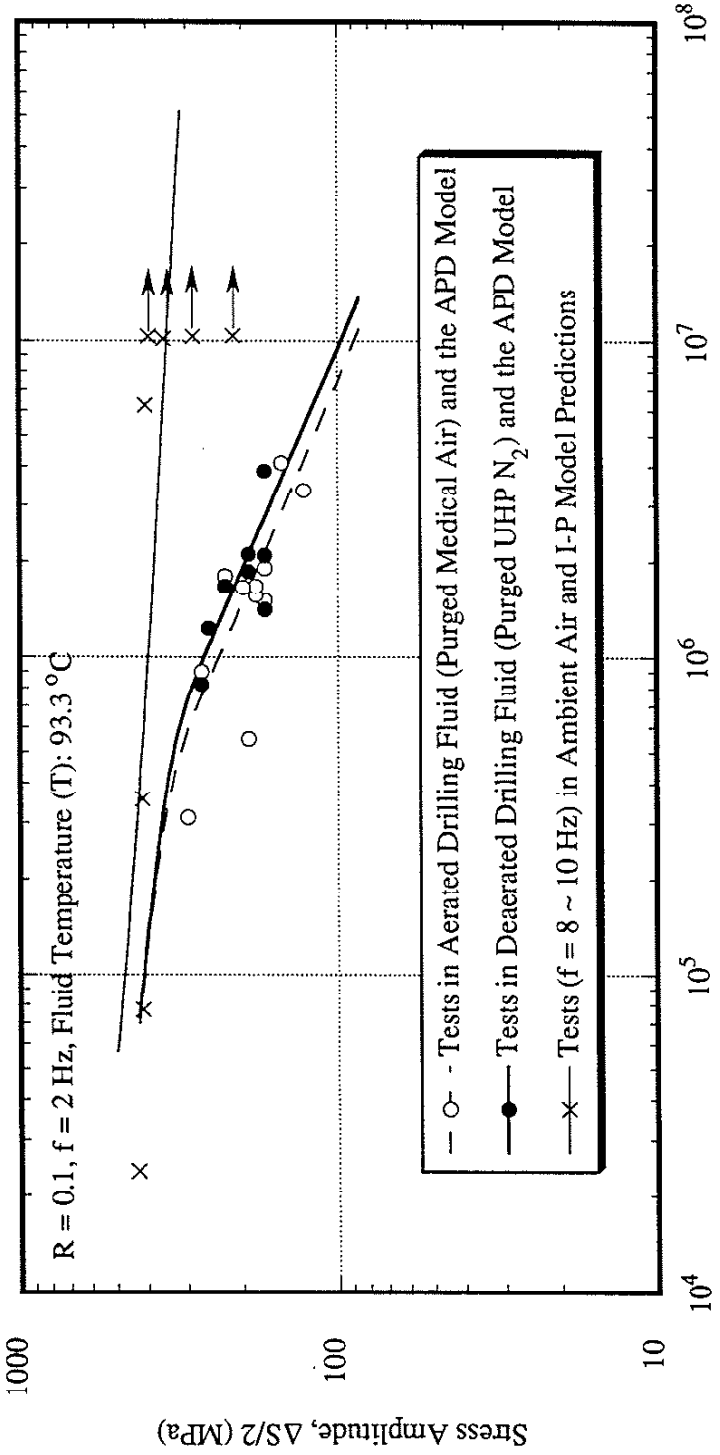

Figure 5.2 Comparison of experimentally observed S-N behavior of API-S135 steel tested (f = 2 Hz) in seawater drilling fluids at 93.3 °C with test (f = 8 ~ 10 Hz) results in ambient air, and the APD model simulations (sinusoidal wave, R = 0.1, $\eta = 45\ \Omega^{-1}m^{-1}$).

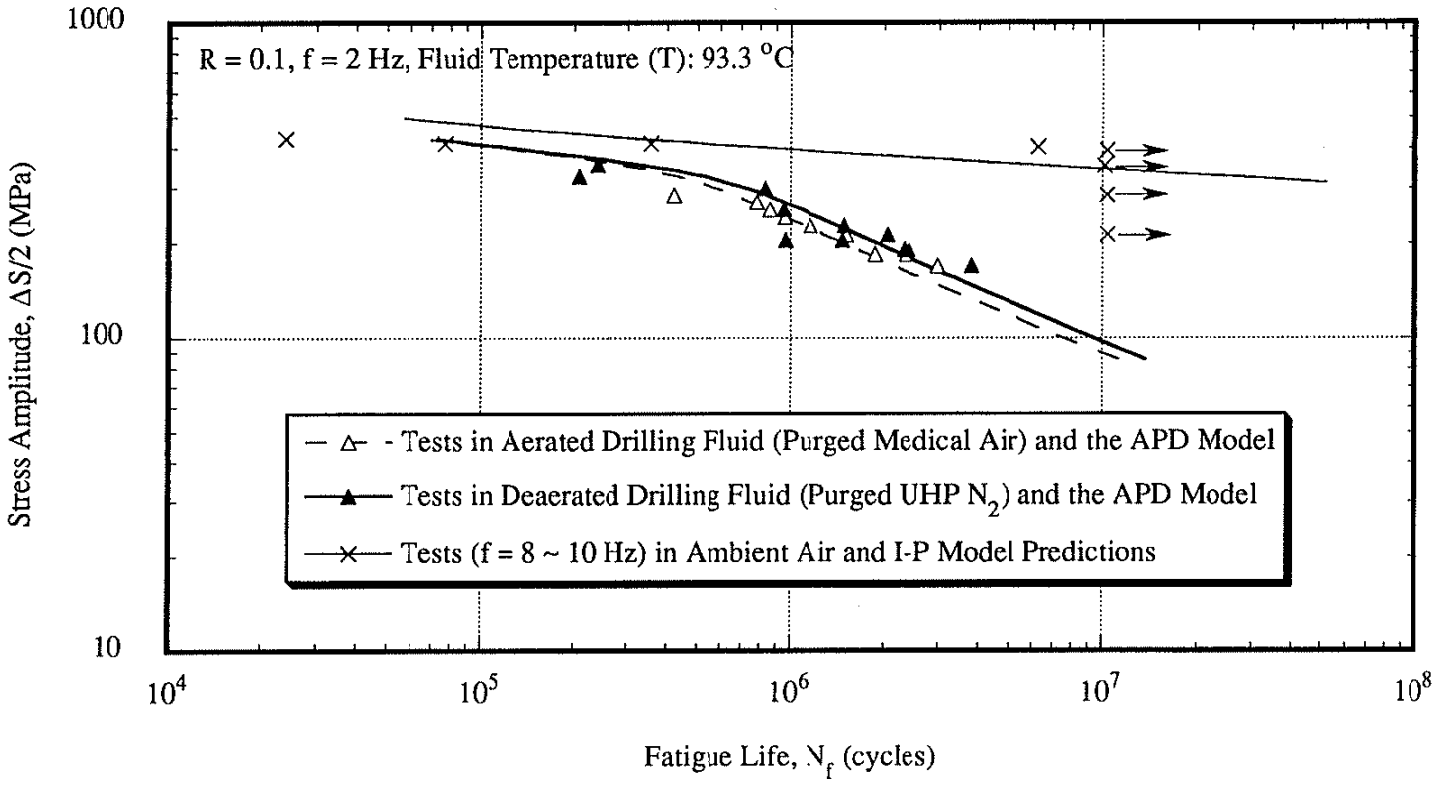

Figure 5.3 Comparison of experimentally observed S-N behavior of API-S135 steel tested (f = 2 Hz) in chemically inhibited drilling fluids (0.11% phosphate ester salt) at 93.3 °C with test (f = 8 ~ 10 Hz) results in ambient air, and the APD model simulations (sinusoidal wave, R = 0.1, $\eta = 30\ \Omega^{-1}m^{-1}$).

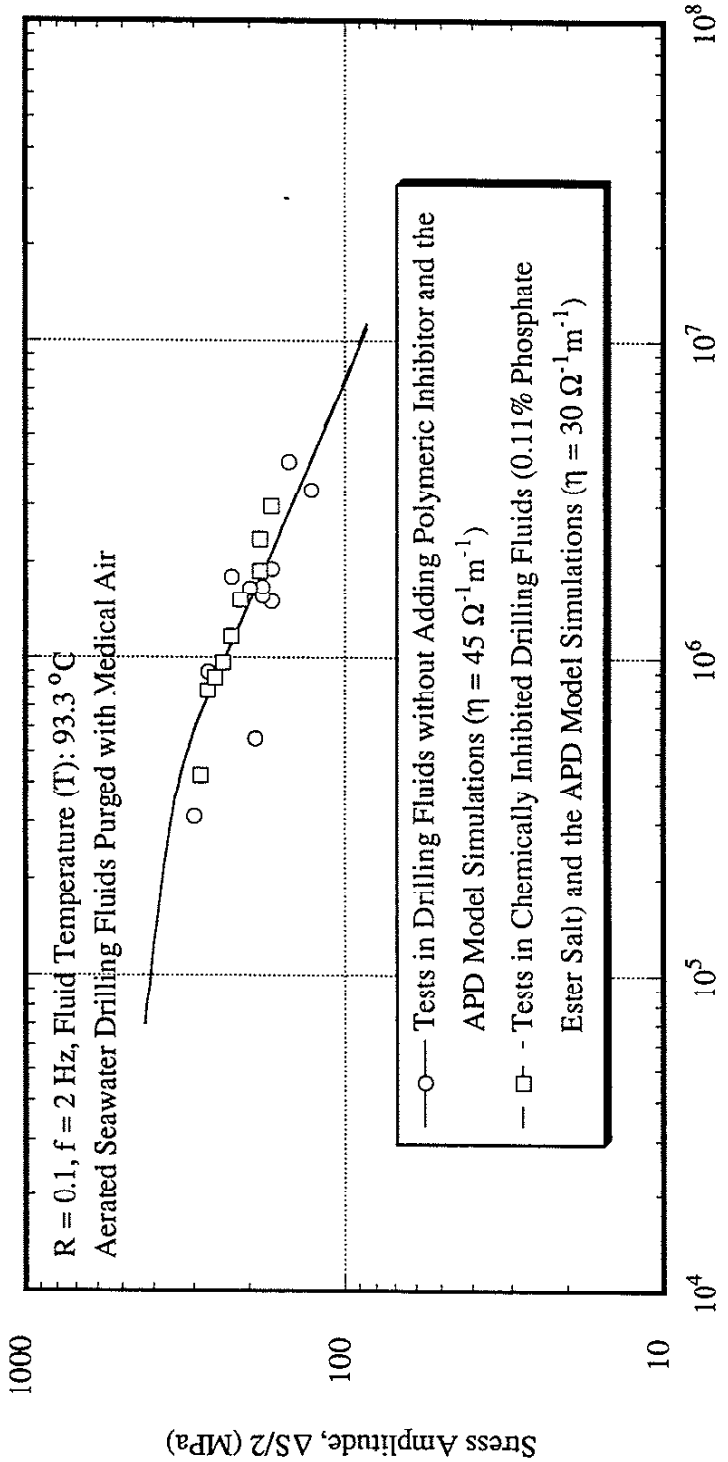

Figure 5.4 Comparison of experimentally observed S-N behavior of API-S135 steel tested in fully aerated (purged medical air) drilling fluids at 93.3 °C (with or without adding polymeric inhibitor) with the corresponding APD model simulations (sinusoidal wave, R = 0.1, f = 2 Hz, $\eta = 30 \sim 45\ \Omega^{-1}m^{-1}$).

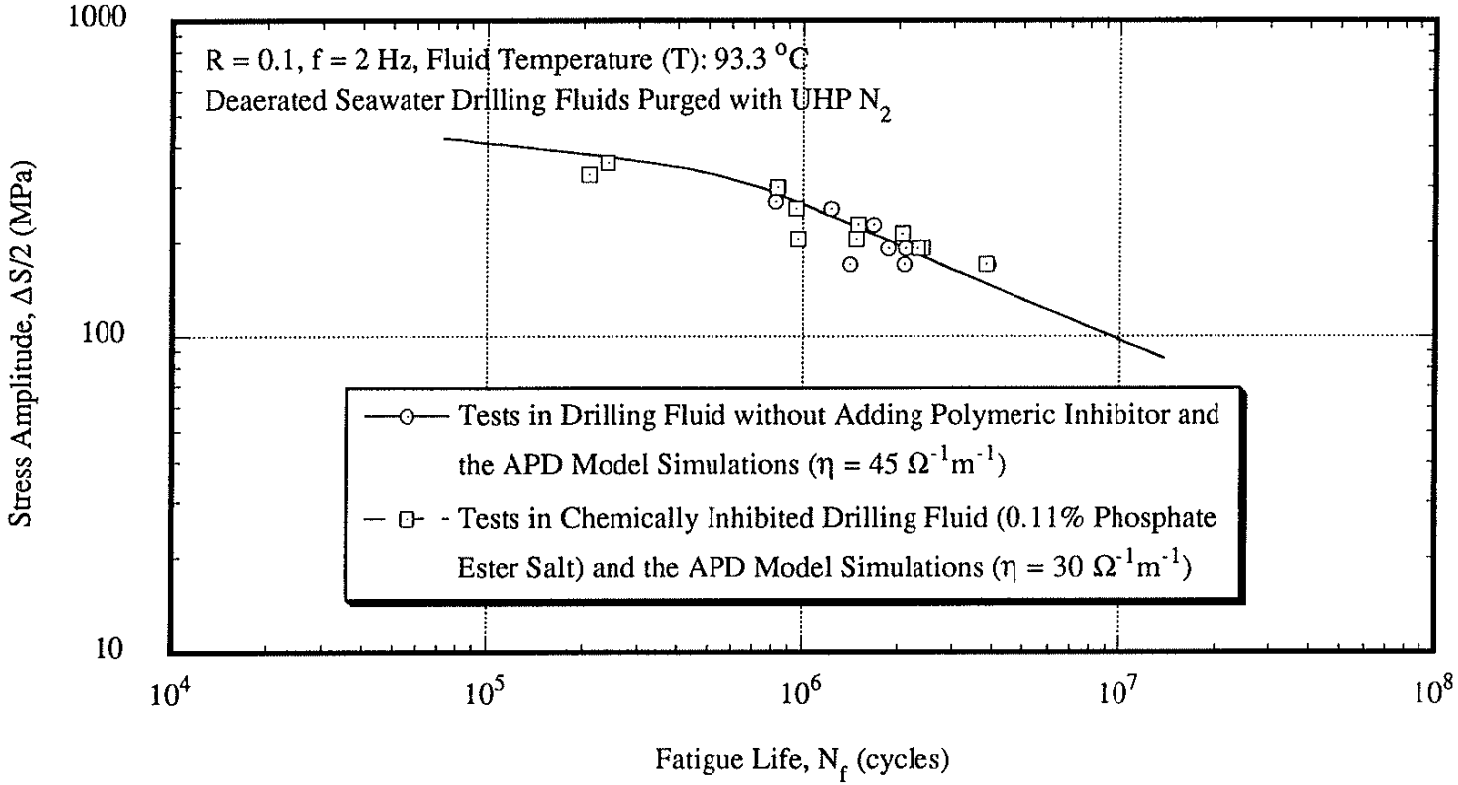

Figure 5.5 Comparison of experimentally observed S-N behavior of API-S135 steel tested in fully deaerated (purged UHP N_2) drilling fluids at 93.3 °C (with or without adding polymeric inhibitor) with the corresponding APD model simulations (sinusoidal wave, R = 0.1, f = 2 Hz, $\eta = 30 \sim 45\ \Omega^{-1}m^{-1}$).

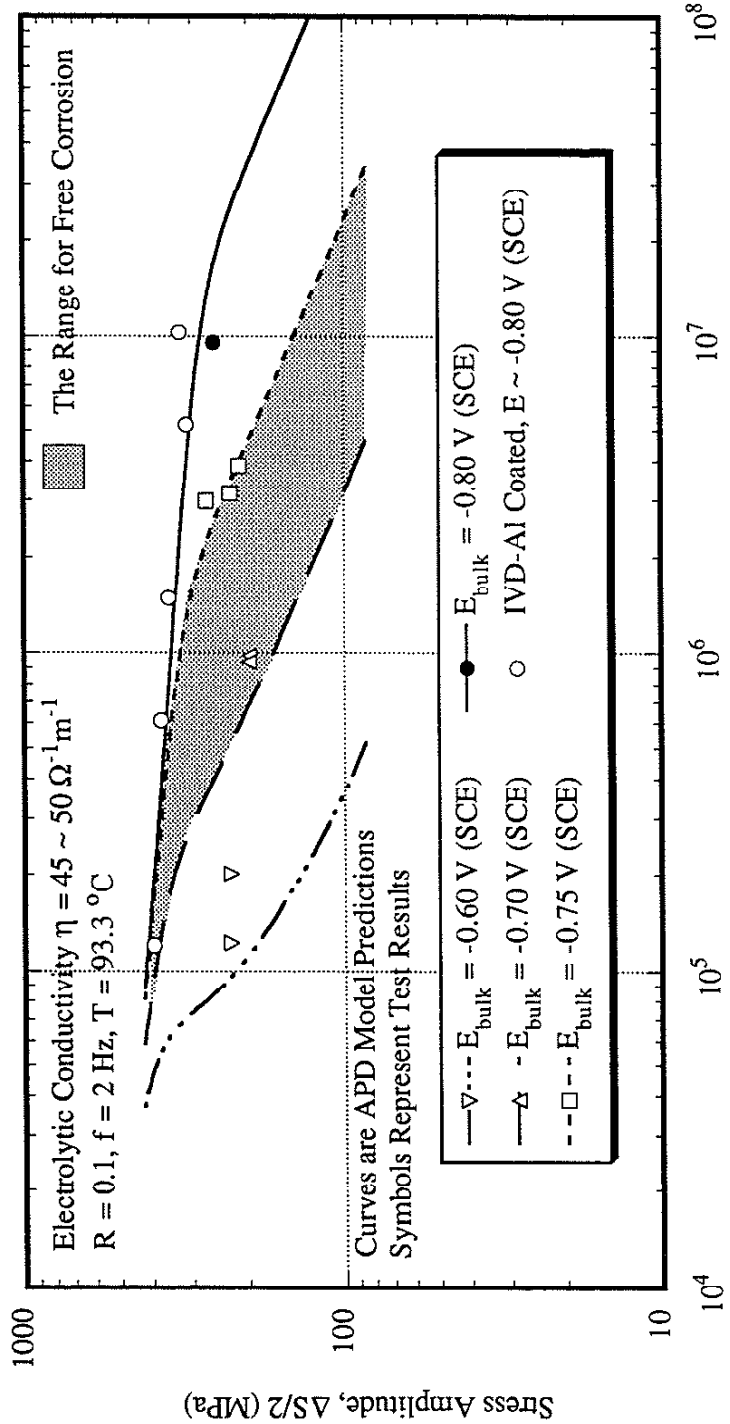

Figure 5.6 Verification of the effects of electrochemical potential (E_{bulk}) on the corrosion-fatigue S-N behavior of API-S135 steel tested in deaerated (purged UHP N_2) seawater drilling fluid at 93.3 °C (sinusoidal wave, R = 0.1, f = 2 Hz, η = 45 ~ 50 $\Omega^{-1}m^{-1}$).

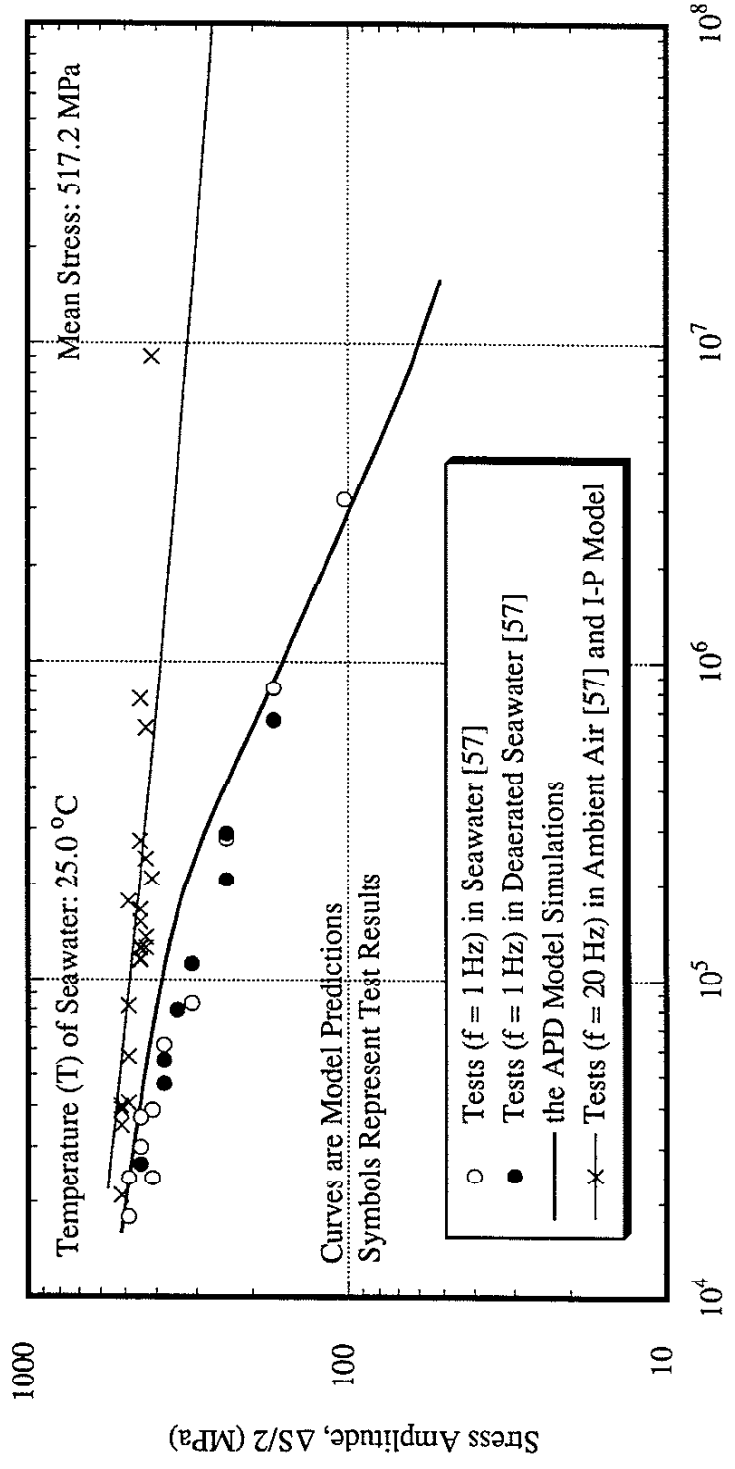

Figure 5.7 Comparison of the corrosion-fatigue S-N behavior of API-S135 steel tested (f = 1 Hz) under a constant mean stress (517.2 MPa) in seawater at 25 °C with test (f = 1 ~ 20 Hz) results in ambient air, and the APD model simulations (data taken from reference [57], sinusoidal wave).

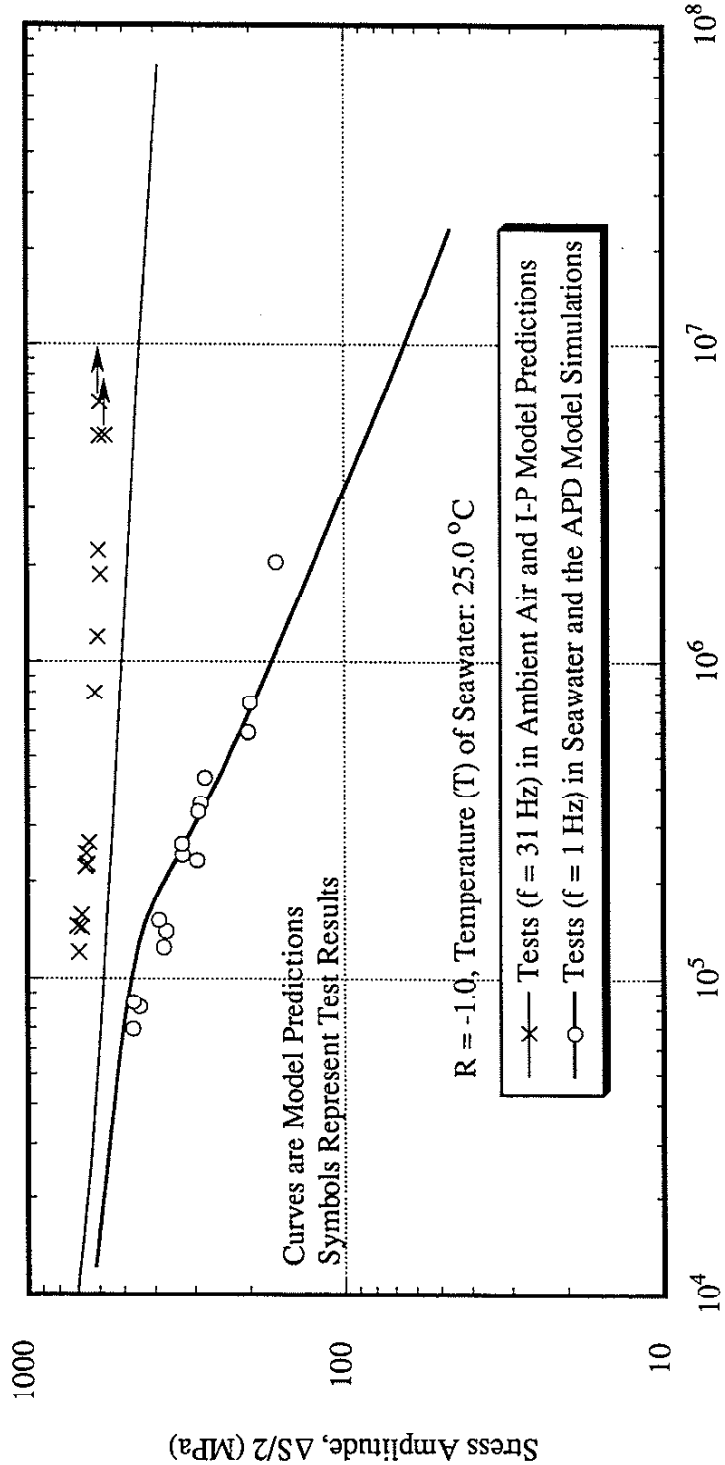

Figure 5.8 Comparison of corrosion-fatigue S-N behavior of API-S135 steel tested (f = 1 Hz) under fully reversed bending (R = -1.0) in seawater at 25 °C with test (f = 31 Hz) results in ambient air, and the APD model simulations (data taken from reference [133], sinusoidal wave).

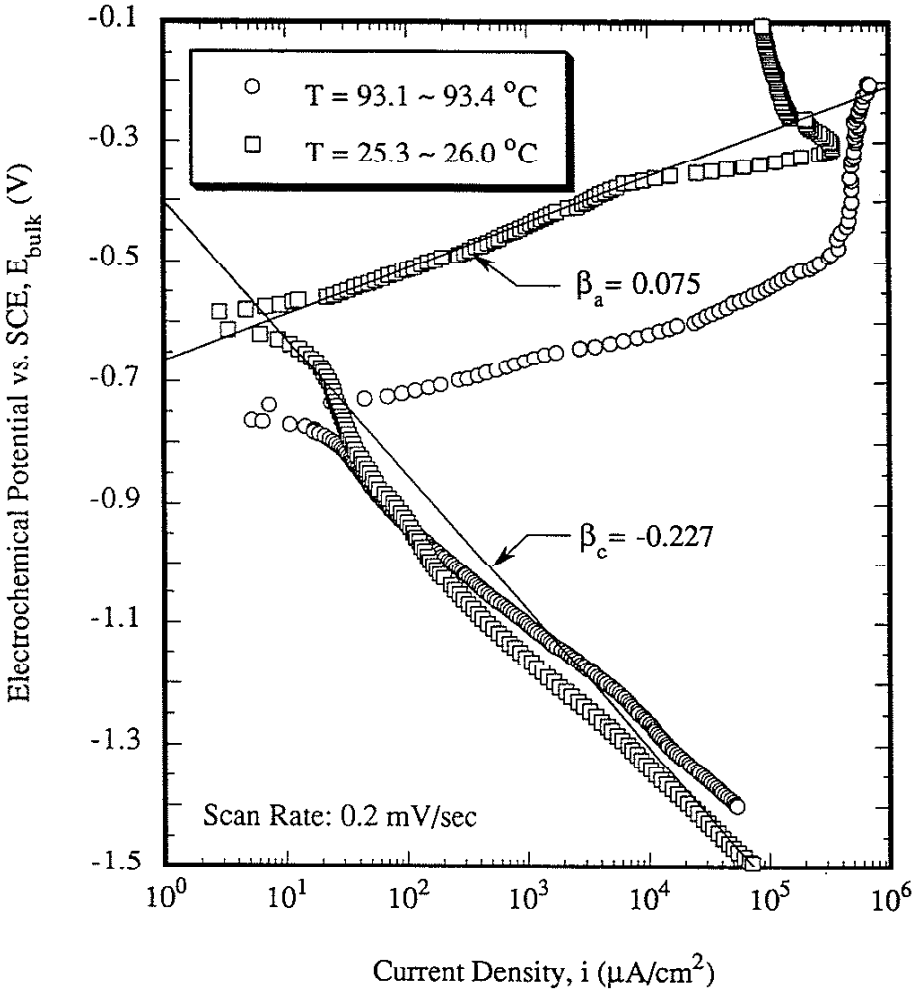

Figure 5.9 Fluid temperature effects on potentiodynamic polarization behavior of API-S135 steel in deaerated (purged UHP N_2) seawater drilling fluids (β_a is the Tafel's slope of the anodic branch while β_c the cathodic branch, scan rate: 0.2 mV /sec).

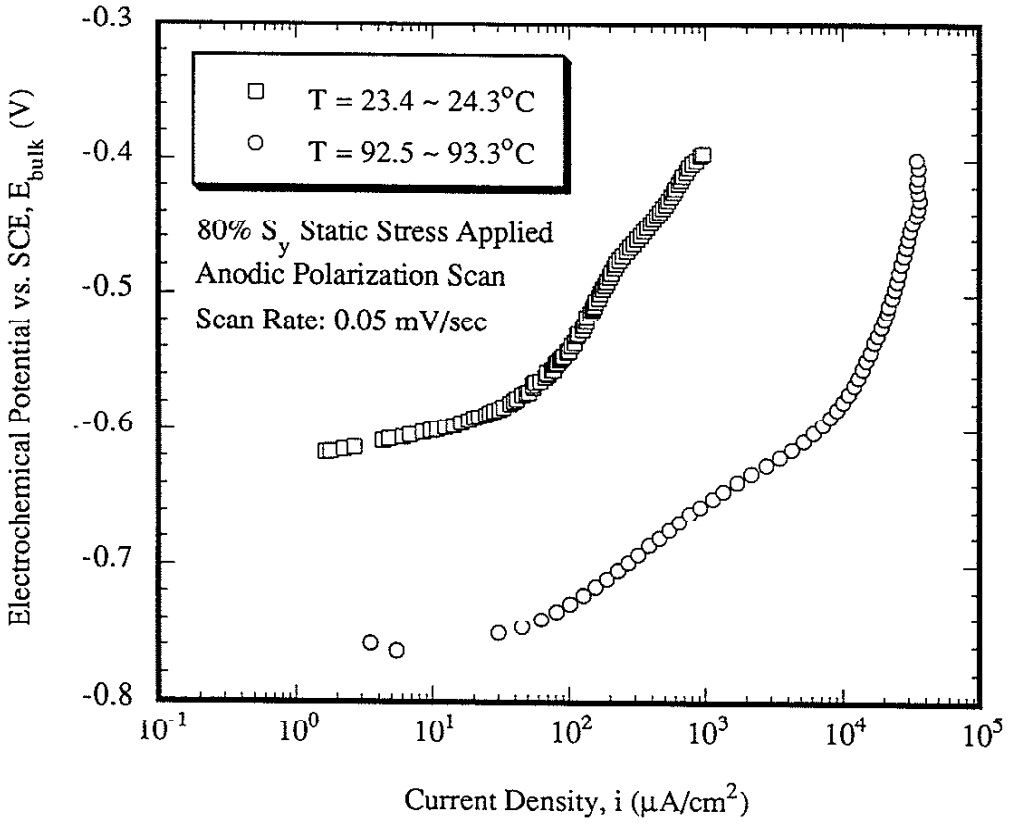

Figure 5.10 Temperature effects on anodic potentiodynamic polarization behavior of API-S135 steel under a static stress of 80% S_y in deaerated (purged UHP N_2) seawater drilling fluids (scan rate: 0.05 mV/sec).

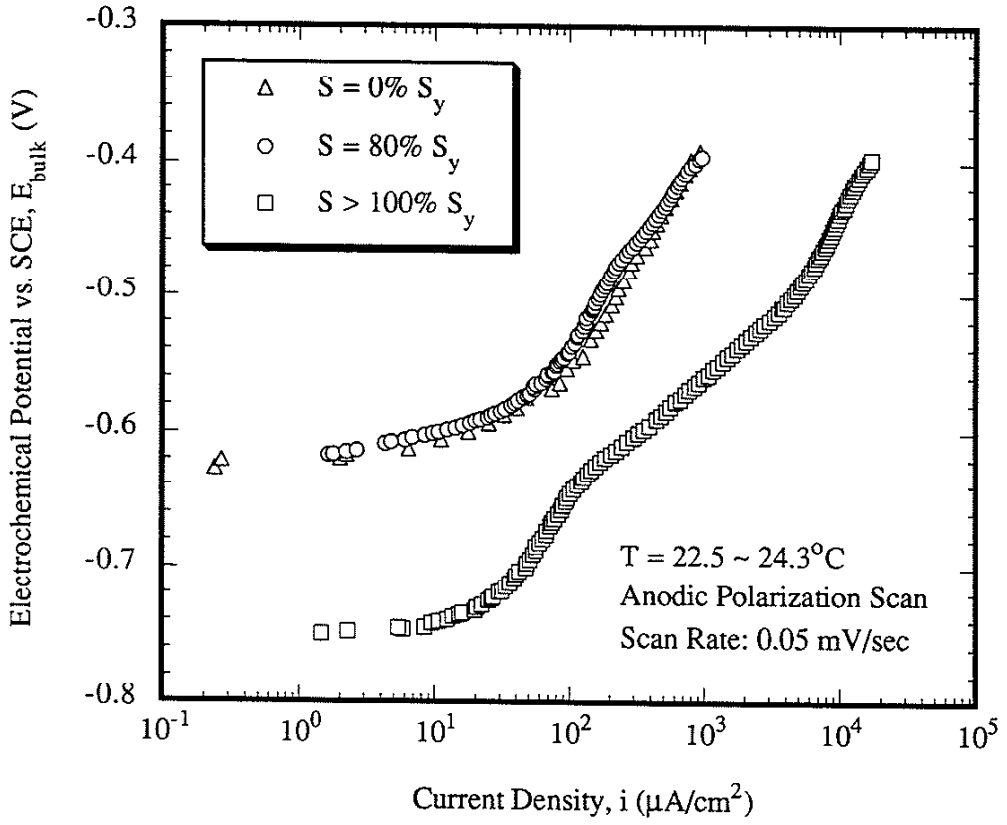

Figure 5.11 Anodic potentiodynamic polarization behavior of API-S135 steel in deaerated (purged UHP N_2) seawater drilling fluid at ambient temperature under various applied static stresses (scan rate: 0.05 mV/sec).

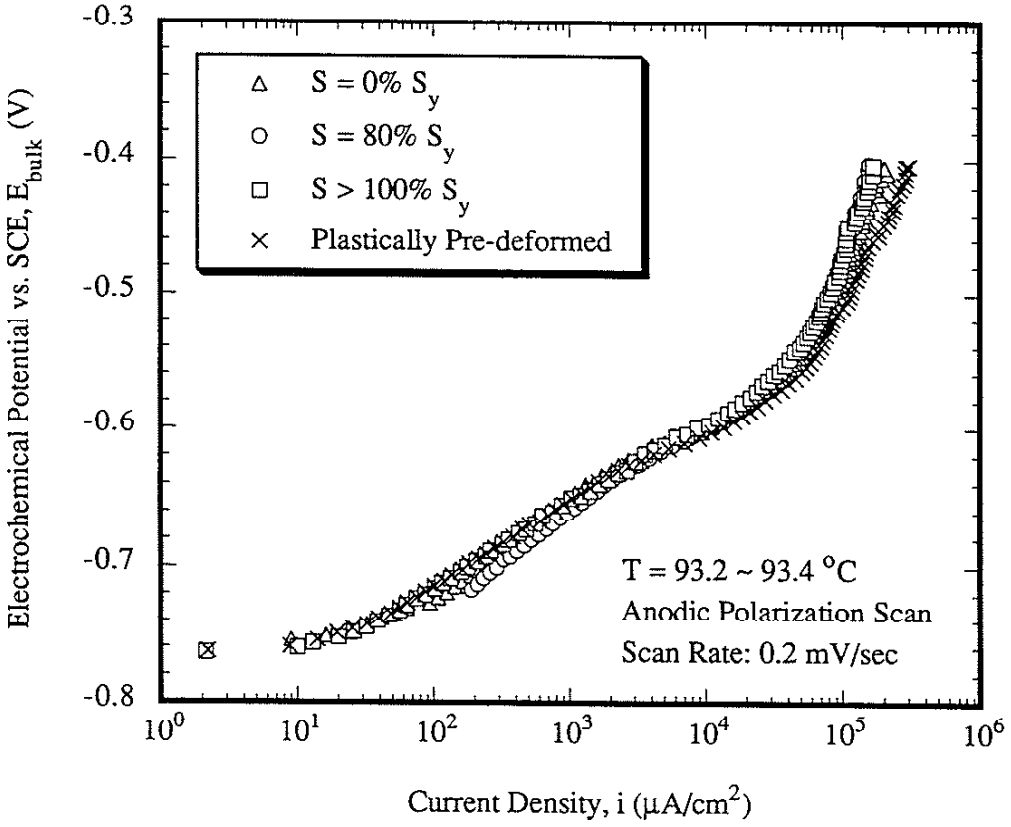

Figure 5.12 Anodic potentiodynamic polarization behavior of API-S135 steel under various applied static stresses in deaerated (purged UHP N_2) seawater drilling fluid at 93.3 °C (scan rate: 0.2 mV/sec).

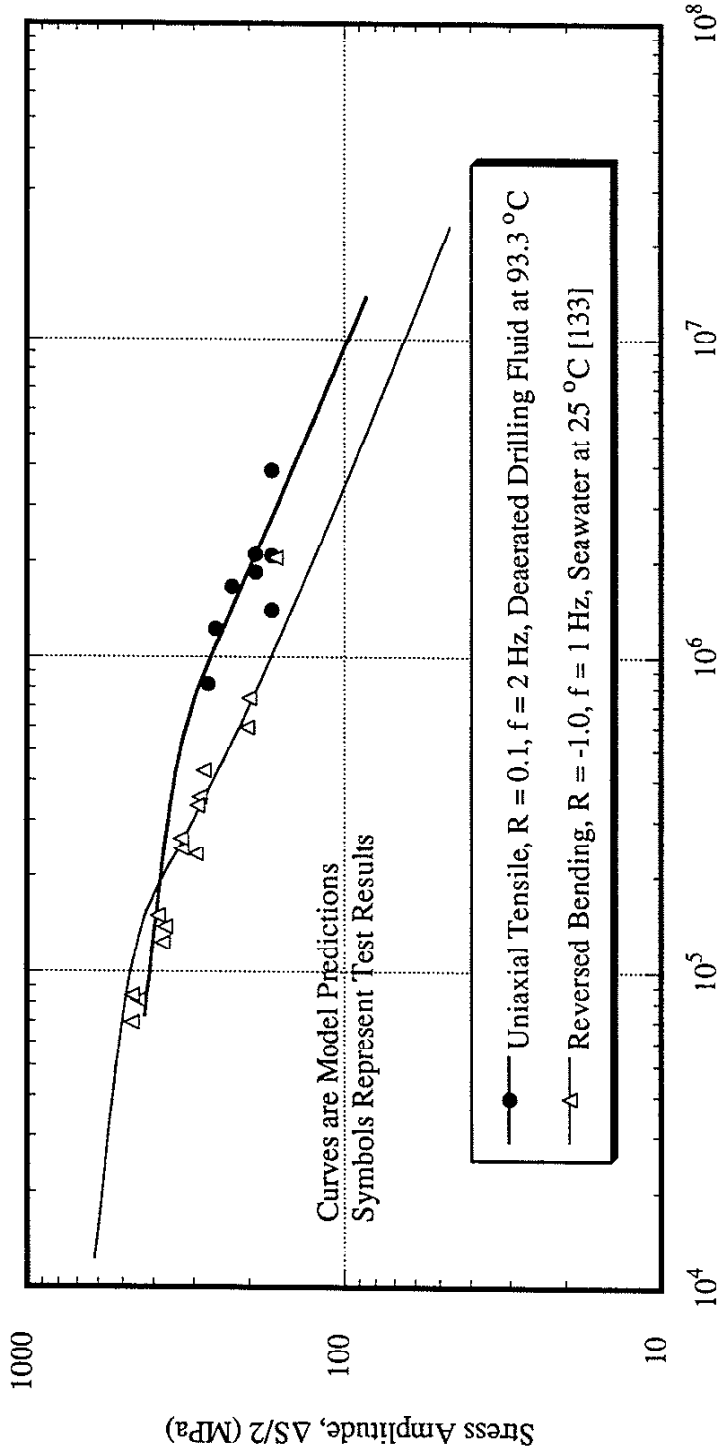

Figure 5.13 Comparison of experimentally observed effects of fluid temperature (T) and stress ratio (R) on the corrosion-fatigue S-N behavior of API-5135 steel in seawater bearing aqueous environments with the corresponding effects simulated by the APD model.

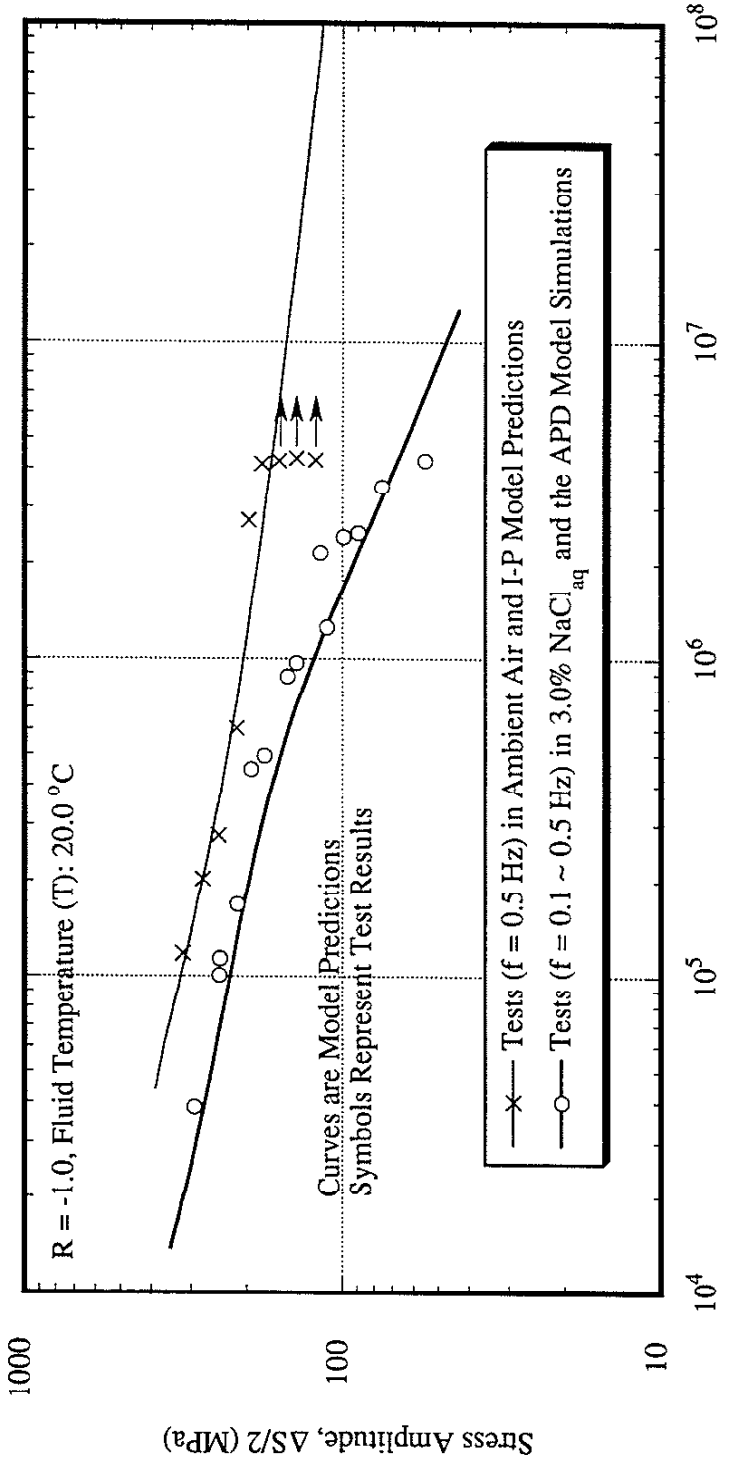

Figure 5.14 Comparison of corrosion-fatigue S-N behavior of JIS SS41 steel tested (f = 0.1 ~ 0.5 Hz) under reversed bending (R = -1.0) in 3.0% NaCl solution at 20 °C with test (f = 0.5 Hz) results in ambient air, and the APD model simulations (data taken from reference [78], sinusoidal wave).

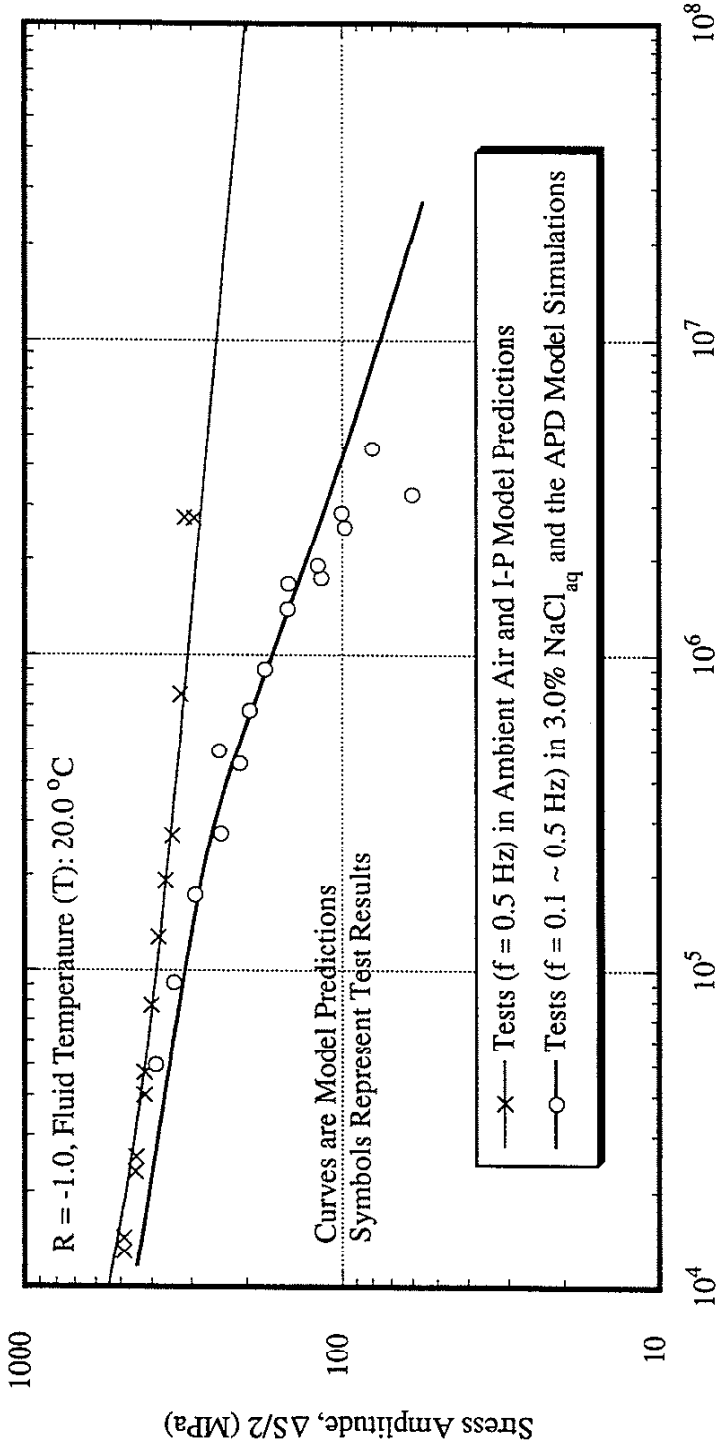

Figure 5.15 Comparison of corrosion-fatigue S-N behavior of JIS SM50A steel tested (f = 0.1 ~ 0.5 Hz) under reversed bending (R = -1.0) in 3.0% NaCl solution at 20 °C with test (f = 0.5 Hz) results in ambient air, and the APD model simulations (data taken from reference [78], sinusoidal wave).

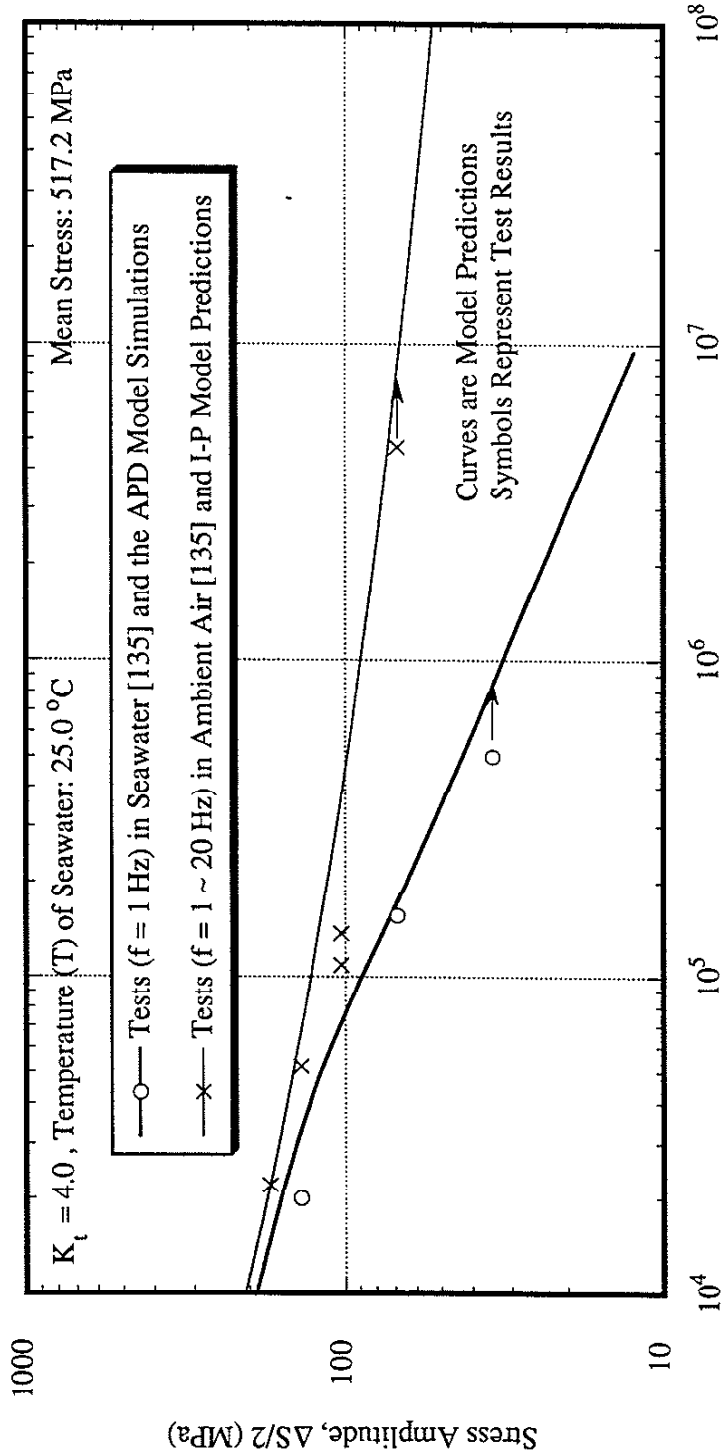

Figure 5.16 Comparison of corrosion-fatigue S-N behavior of notched (K_t = 4.0) API-S135 steel tested (f = 1 Hz) under a constant mean stress (517.2 MPa) in seawater at 25 °C with test (f = 1 ~ 20 Hz) results in ambient air, and the APD model simulations (data taken from reference [135], sinusoidal wave).

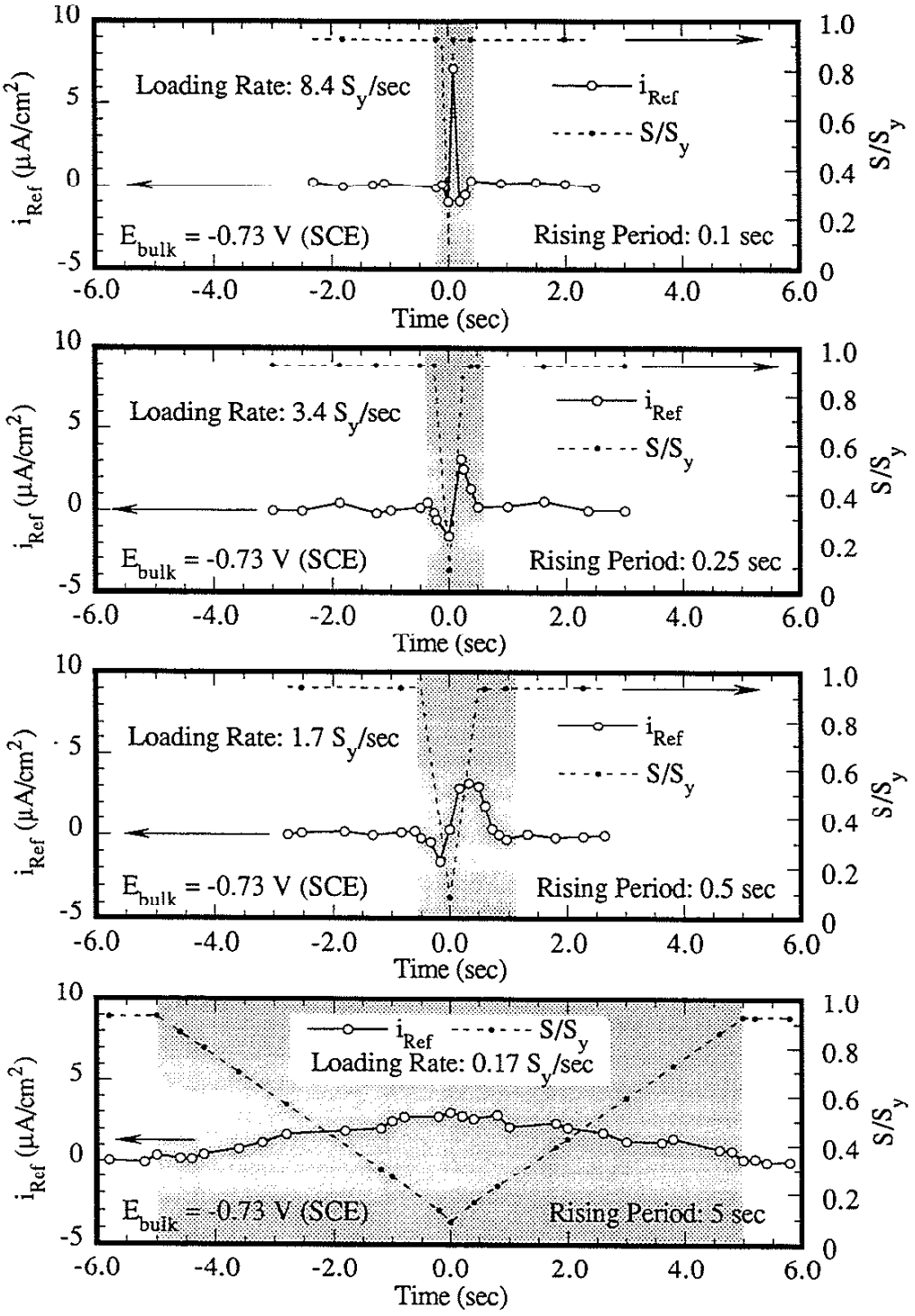

Figure 5.17 Comparison of anodic current-density transients of API-S135 steel in deaerated seawater drilling fluid (93.3 °C) under trapezoidal waveform loadings of various loading rates (R = 0.1, E_{bulk} = -0.73 V).

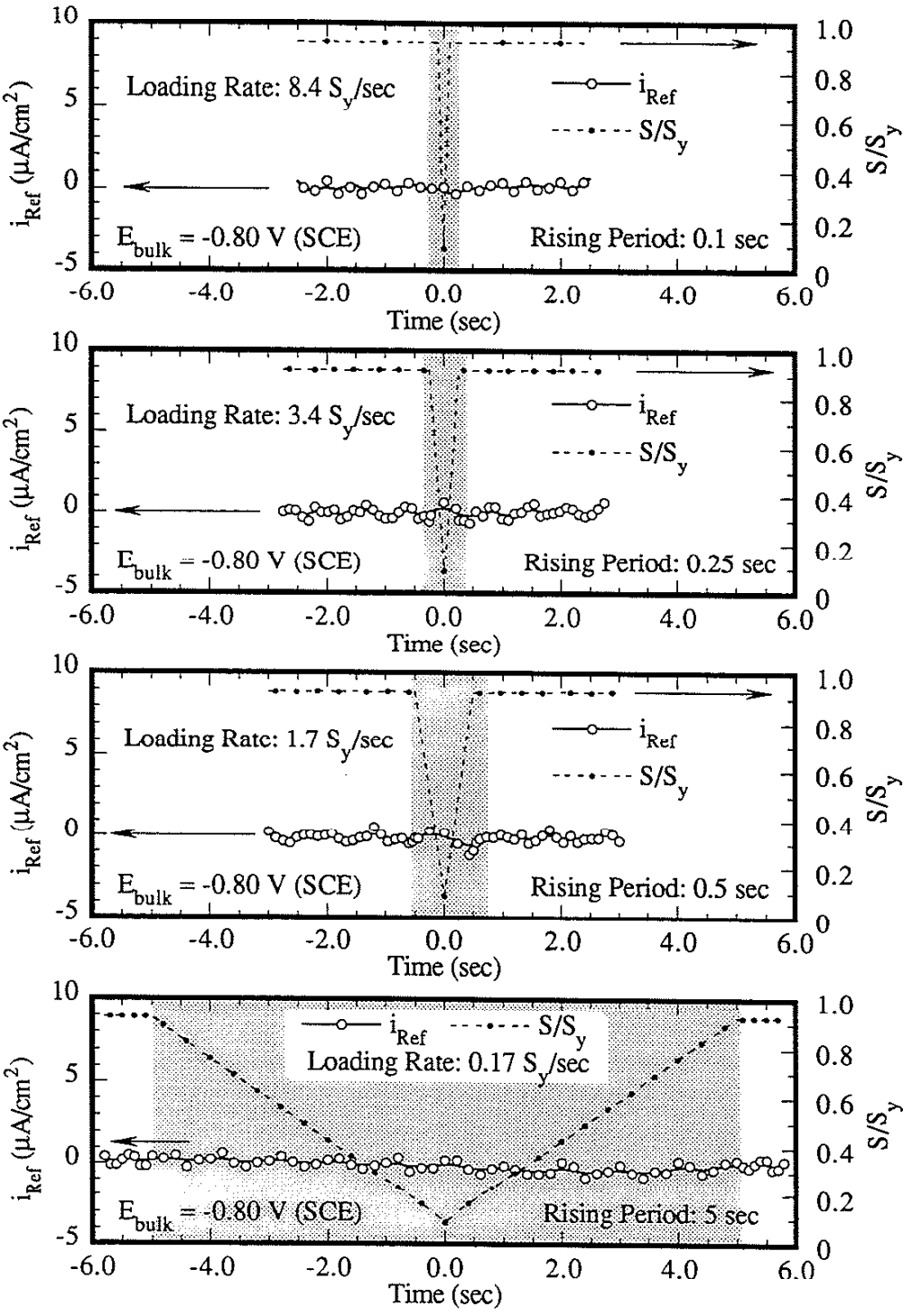

Figure 5.18 Comparison of cathodic current-density transients of API-S135 steel in deaerated seawater drilling fluid (93.3 °C) under trapezoidal waveform loadings of various loading rates (R = 0.1, E_{bulk} = -0.80 V).

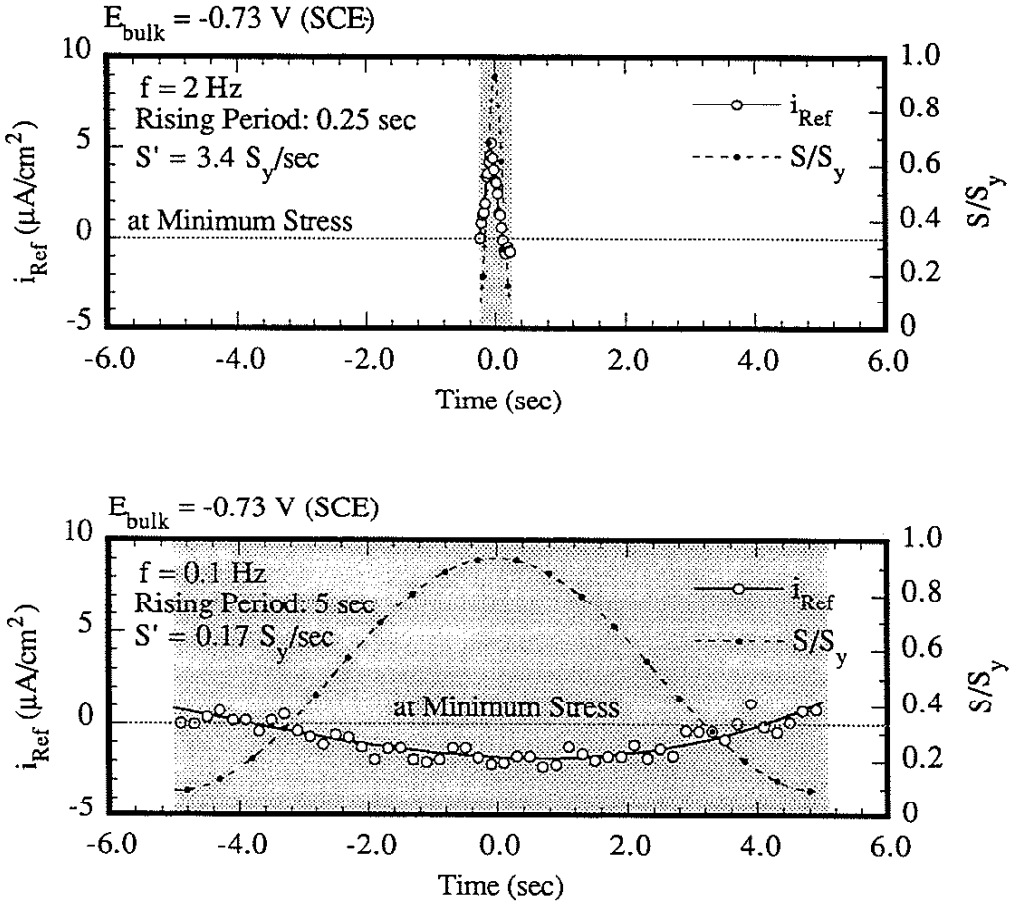

Figure 5.19 Comparison of anodic current-density transients of API-S135 steel in deaerated seawater drilling fluid (93.3 °C) under sinusoidal waveform loadings of various test frequencies (f) (R = 0.1, E_{bulk} = -0.73 V vs. SCE, S' is loading rate).

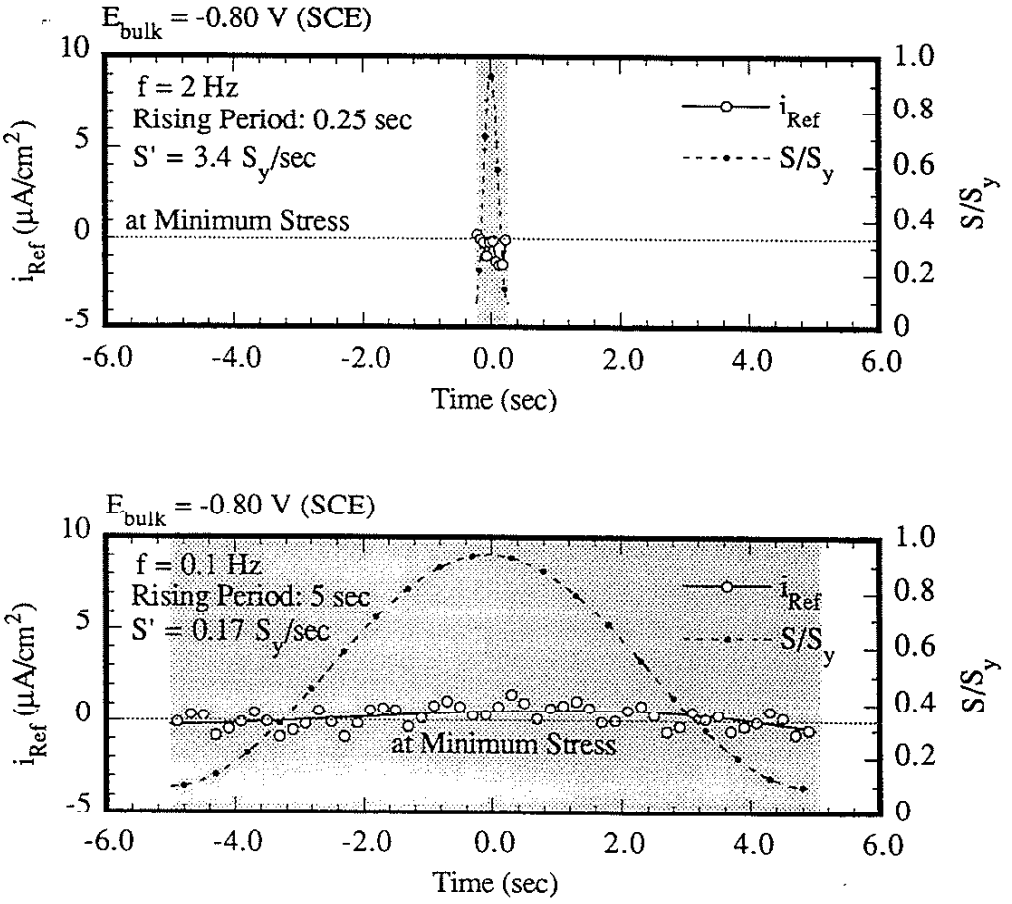

Figure 5.20 Comparison of cathodic current-density transients of API-S135 steel in deaerated seawater drilling fluid (93.3 °C) under sinusoidal waveform loadings of various test frequencies (f) (R = 0.1, E_{bulk} = -0.80 V vs. SCE, S' is loading rate).

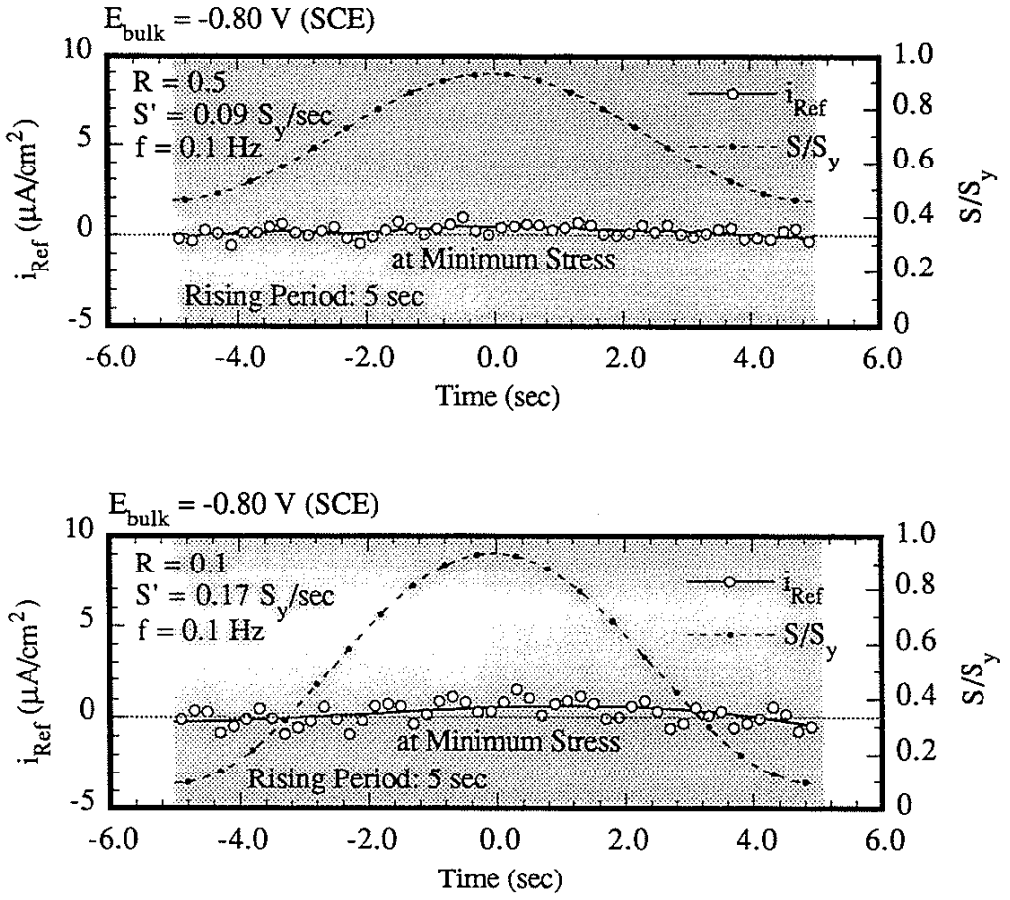

Figure 5.21 Comparison of cathodic current-density transients of API-S135 steel in deaerated seawater drilling fluid (93.3 °C) under sinusoidal waveform loadings of various R ratios (f = 0.1 Hz, E_{bulk} = -0.80 V vs. SCE, S' is loading rate).

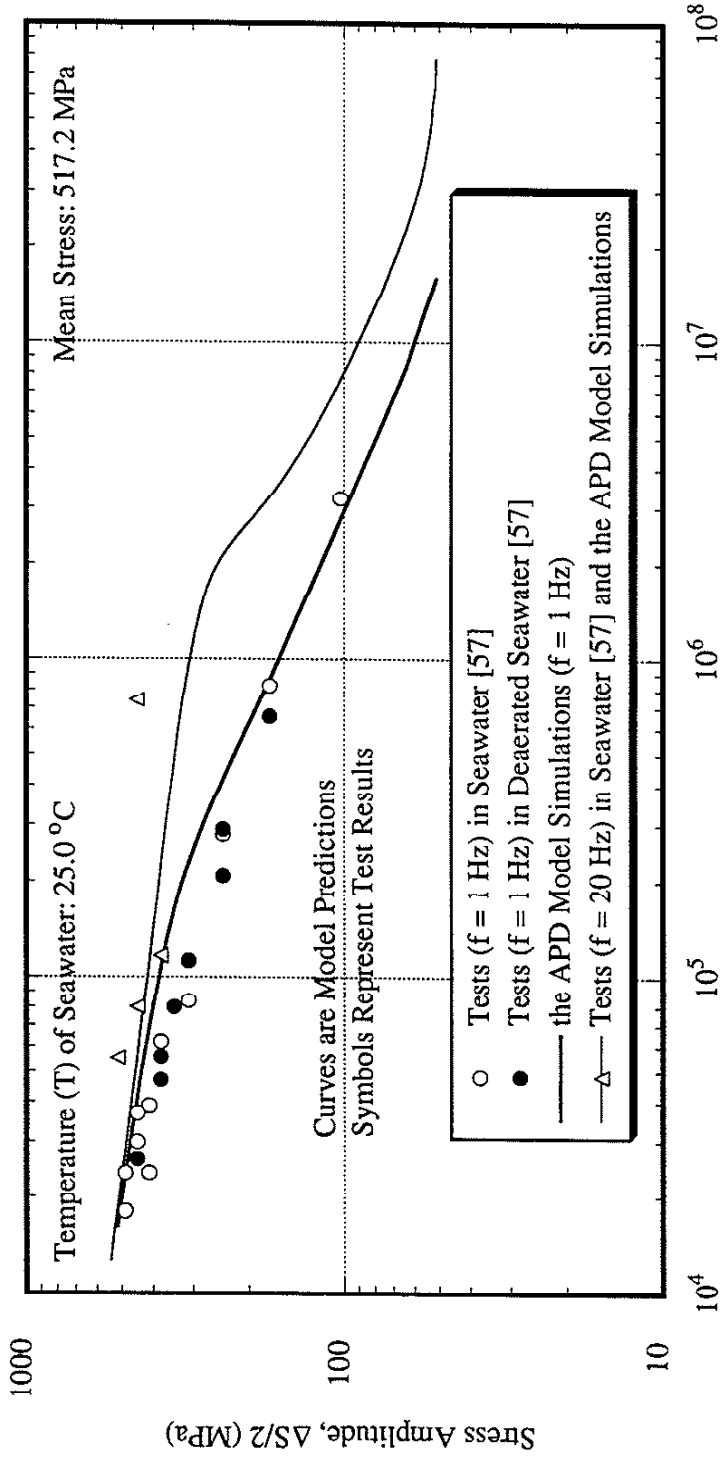

Figure 5.22 Comparison of experimentally observed effects of test frequency (f) on the corrosion-fatigue S-N behavior of API-S135 steel under a constant mean stress (517.2 MPa) in seawater at 25 °C with the corresponding APD model simulations (data taken from reference [57], sinusoidal wave).

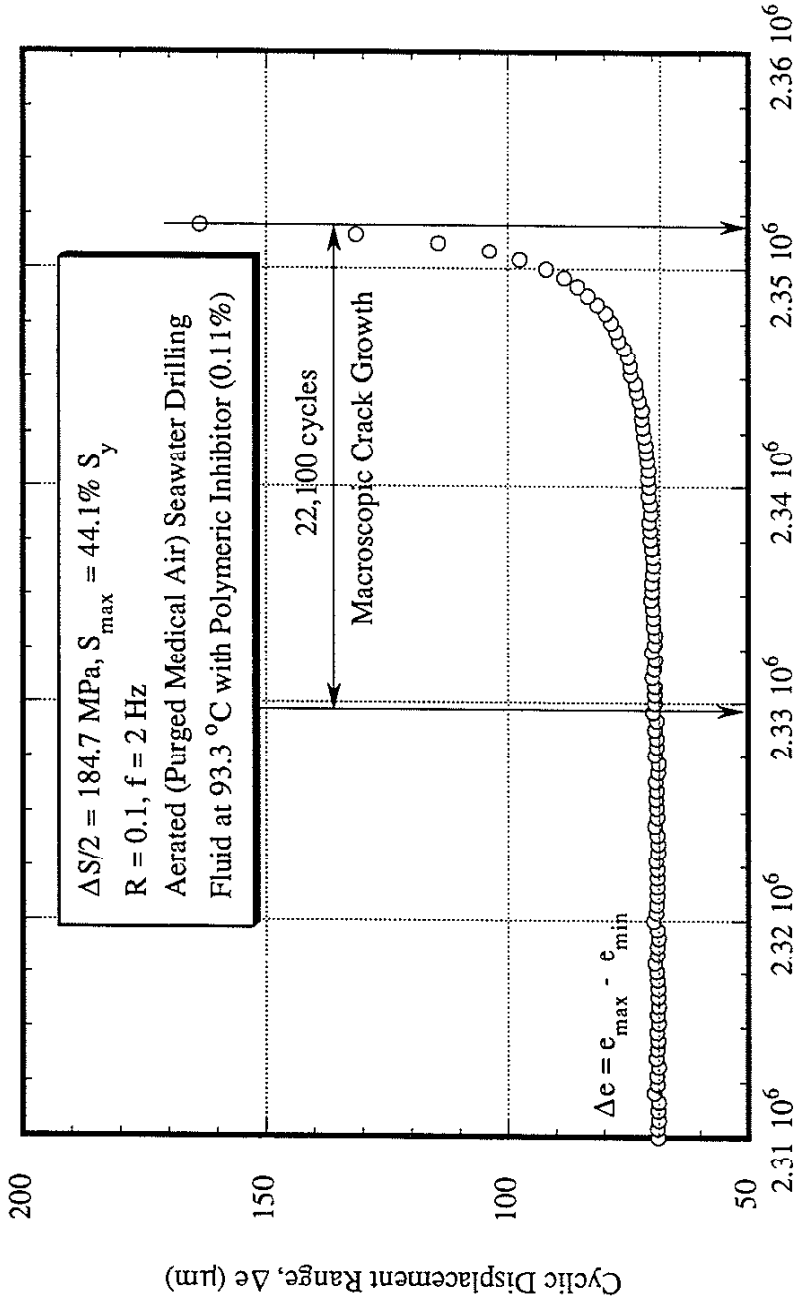

Figure 5.23 Determination of the life period of macroscopic crack growth from cyclic displacement range (Δe) vs. fatigue cycle (N) plot by arbitrarily selecting an onset fatigue life at which a significant change in cyclic displacement range (Δe) was first noticed by an extensometer at the final stage of a fatigue test.

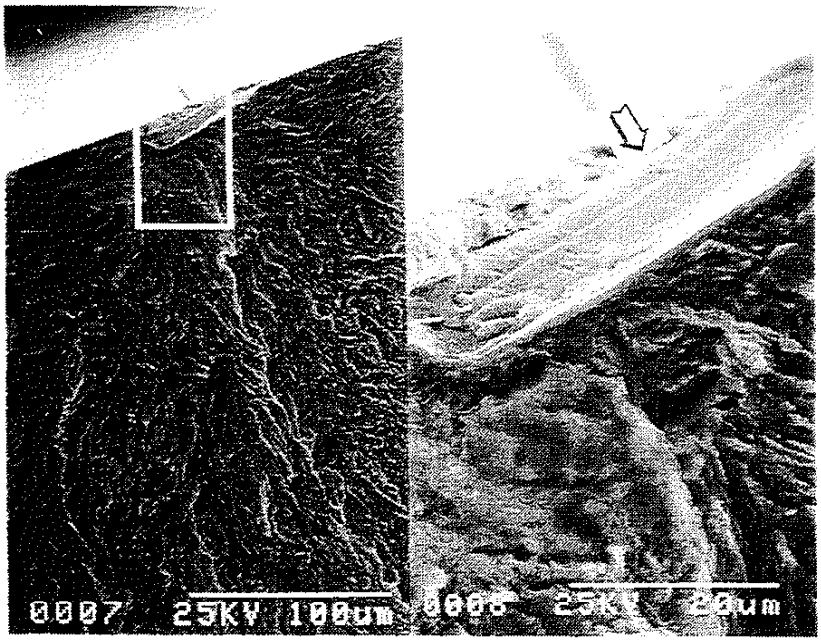

Figure 5.24 A micrograph showing the generation of persistent slip bands (PSB, arrow) on a crack-initiation site of an API-S135 fatigue fractured in ambient air ($\Delta S/2$ = 429.4 MPa, R = 0.1, f = 10 Hz).

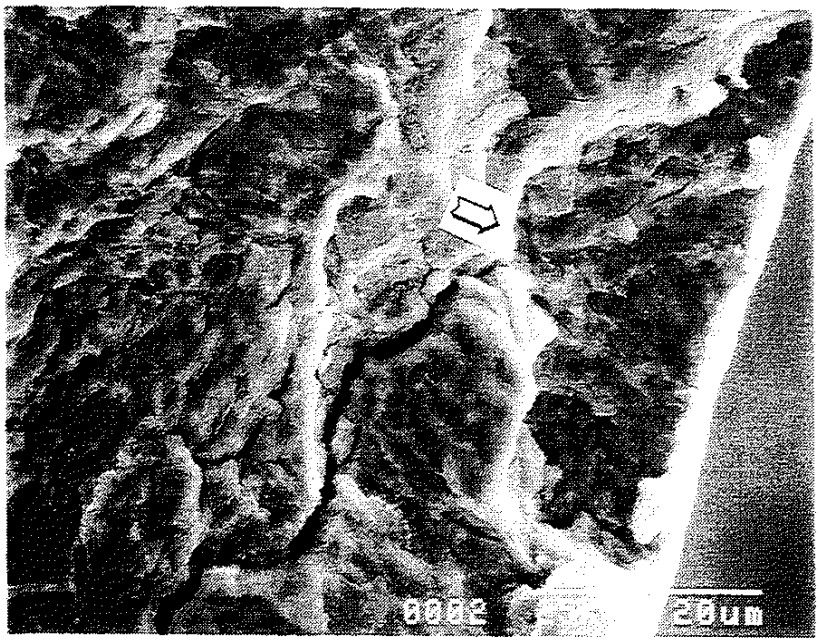

Figure 5.25 A micrograph showing a chemical notch (arrow) on a crack-initiation site of an API-S135 fatigue fractured in deaerated drilling fluid (T = 93.3 °C, $\Delta S/2$ = 255.8 MPa, R = 0.1, f = 2 Hz).

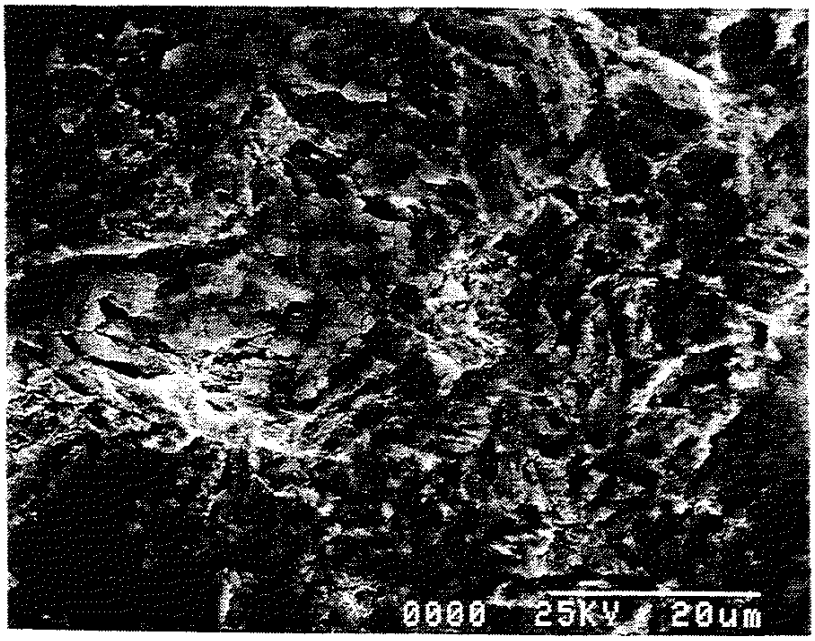

Figure 5.26 A heavily etched crack-initiation site of an API-S135 fatigue fractured in aerated seawater drilling fluid (T = 93.3 °C, $\Delta S/2$ = 127.9 MPa, R = 0.1, f = 2 Hz).

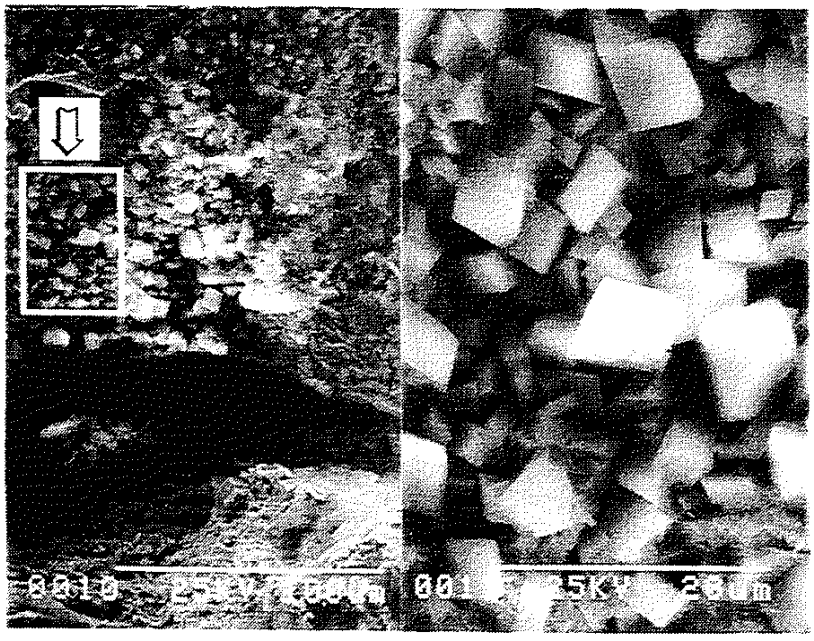

Figure 5.27 Accumulation of deposited iron (arrow) on a crack-initiation site of an API-S135 fatigue fractured in deaerated seawater drilling fluid under cathodic protection (T = 93.3 °C, E_{bulk} = -1.0 V vs. SCE, $\Delta S/2$ = 255.8 MPa, R = 0.1, f = 2 Hz).

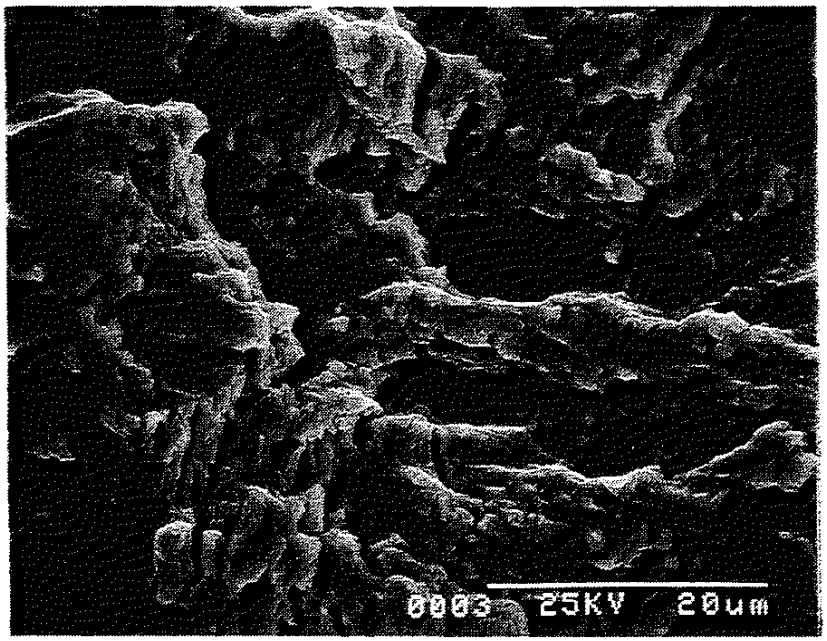

Figure 5.28 Ductile-striation fracture of an API-S135 fatigue fractured in ambient air ($\Delta S/2$ = 414.3 MPa, R = 0.1, f = 10 Hz).

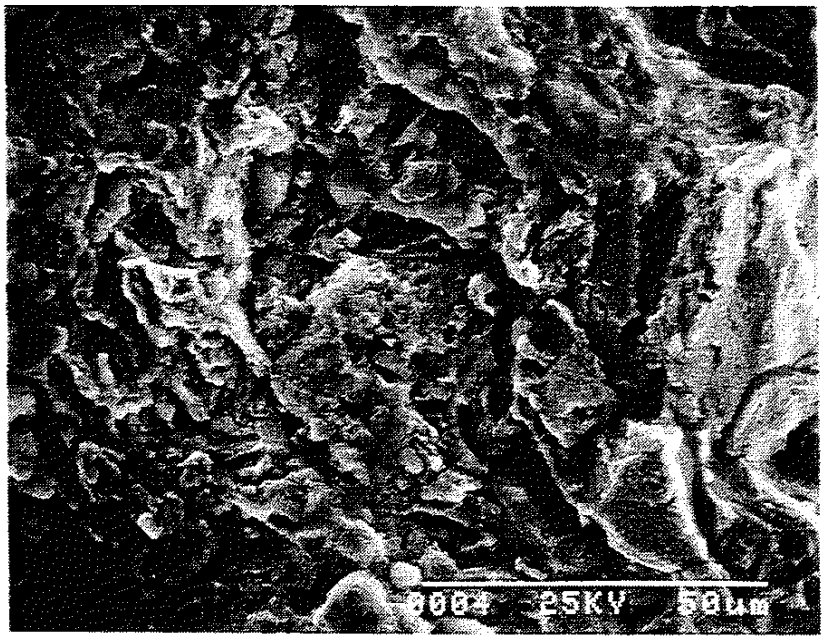

Figure 5.29 Mixed ductile-striation/intergranular fracture of an API-S135 fatigue fractured in deaerated seawater drilling fluid with a polymeric inhibitor (0.3% phosphate ester salt, T = 93.3 °C, $\Delta S/2$ = 198.9 MPa, R = 0.1, f = 2 Hz).

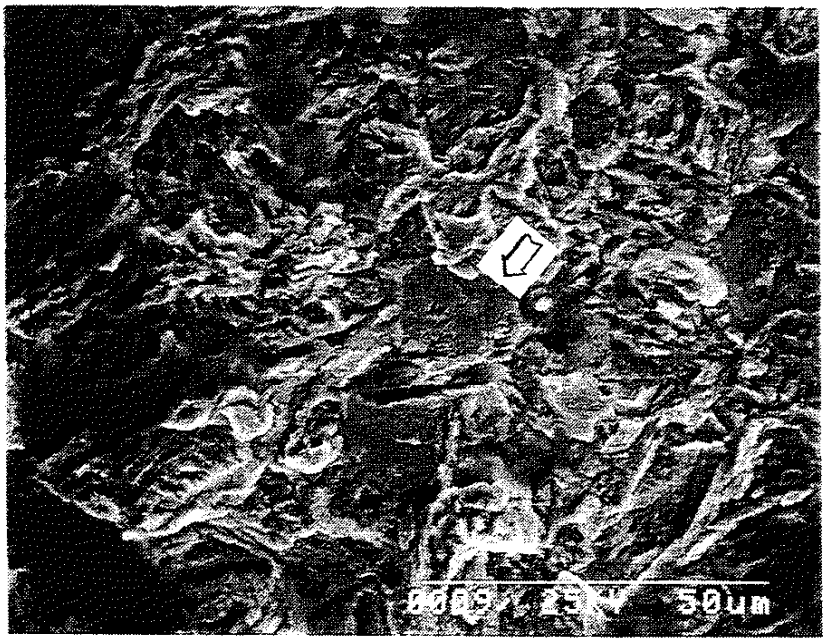

Figure 5.30 Intergranular fracture (arrow) of an IVD-Al plated API-S135 fatigue fractured in deaerated seawater drilling fluid (T = 93.3 °C, ΔS/2 = 376.6 MPa, R = 0.1, f = 2 Hz).

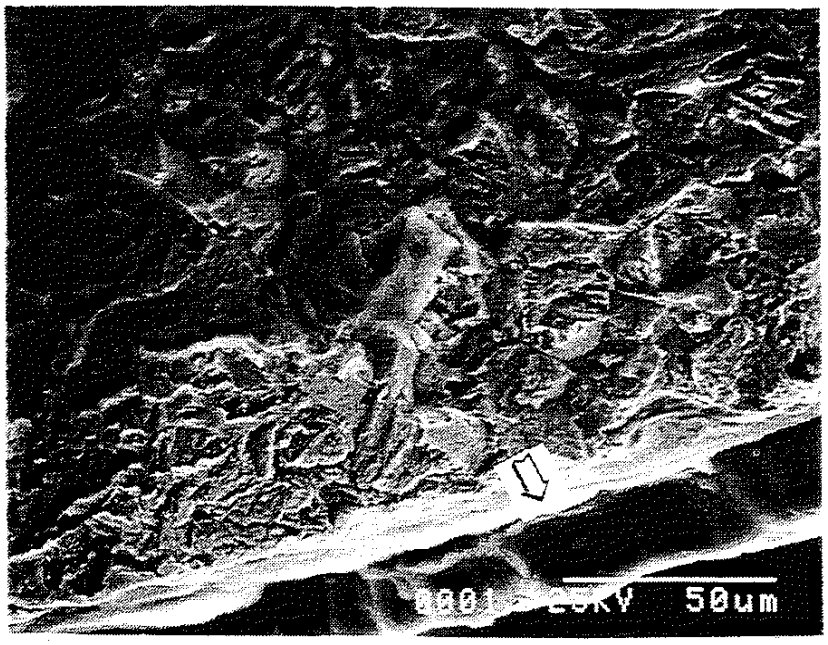

Figure 5.31 Residual IVD-Al plated aluminum (arrow) on an API-S135 substrate fatigue fractured in deaerated seawater drilling fluid (T = 93.3 °C, ΔS/2 = 397.9 MPa, R = 0.1, f = 2 Hz).

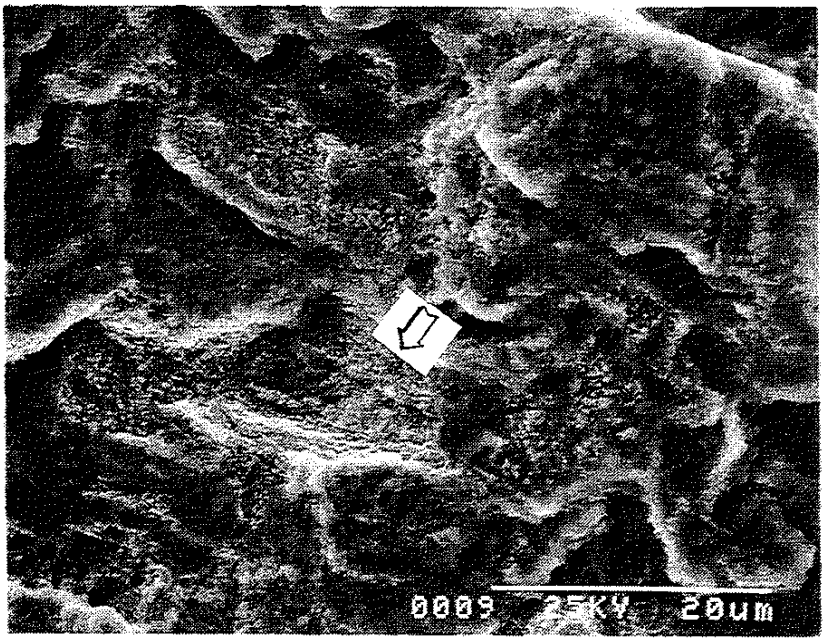

Figure 5.32 Accumulation of deposited iron (arrow) on a fracture surface of an API-S135 fatigue fractured in deaerated seawater drilling fluid under cathodic protection (T = 93.3 °C, E_{bulk} = -1.0 V vs. SCE, $\Delta S/2$ = 255.8 MPa, R = 0.1, f = 2 Hz).

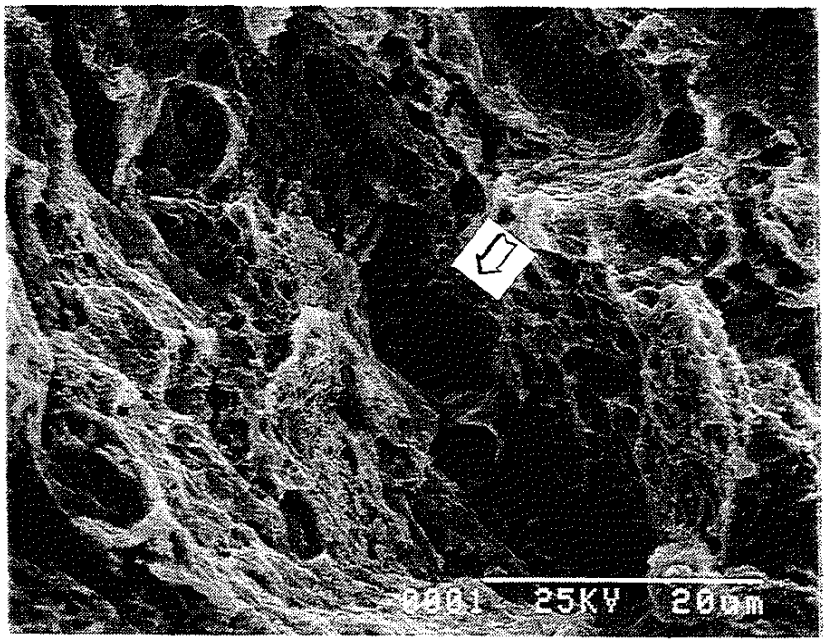

Figure 5.33 Appearance of high-density microvoids (arrow) induced by plastic flow in the last ligament to fracture of an API-S135 fatigued in ambient air ($\Delta S/2$ = 404.2 MPa, R = 0.1, f = 10 Hz).

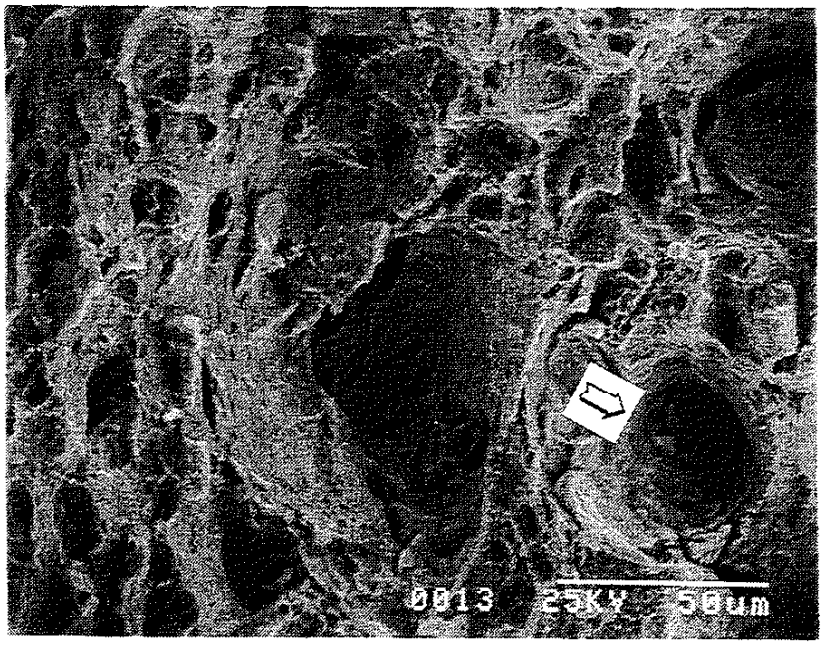

Figure 5.34a Appearance of high-density microvoids (arrow) in the last ligament to fracture of an API-S135 fatigue fractured in deaerated seawater drilling fluid under cathodic protection (T = 93.3 °C, E_{bulk} = -1.0 V vs. SCE, $\Delta S/2$ = 255.8 MPa, R = 0.1, f = 2 Hz).

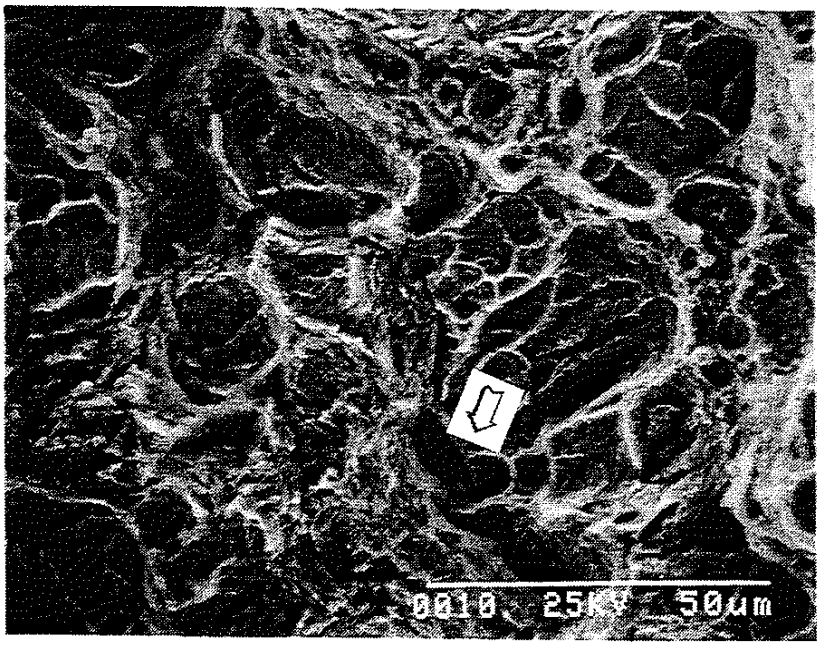

Figure 5.34b Appearance of high-density microvoids (arrow) in the last ligament to fracture of an IVD-Al plated API-S135 fatigue fractured in deaerated seawater drilling fluid (T = 93.3 °C, $\Delta S/2$ = 376.6 MPa, R = 0.1, f = 2 Hz).

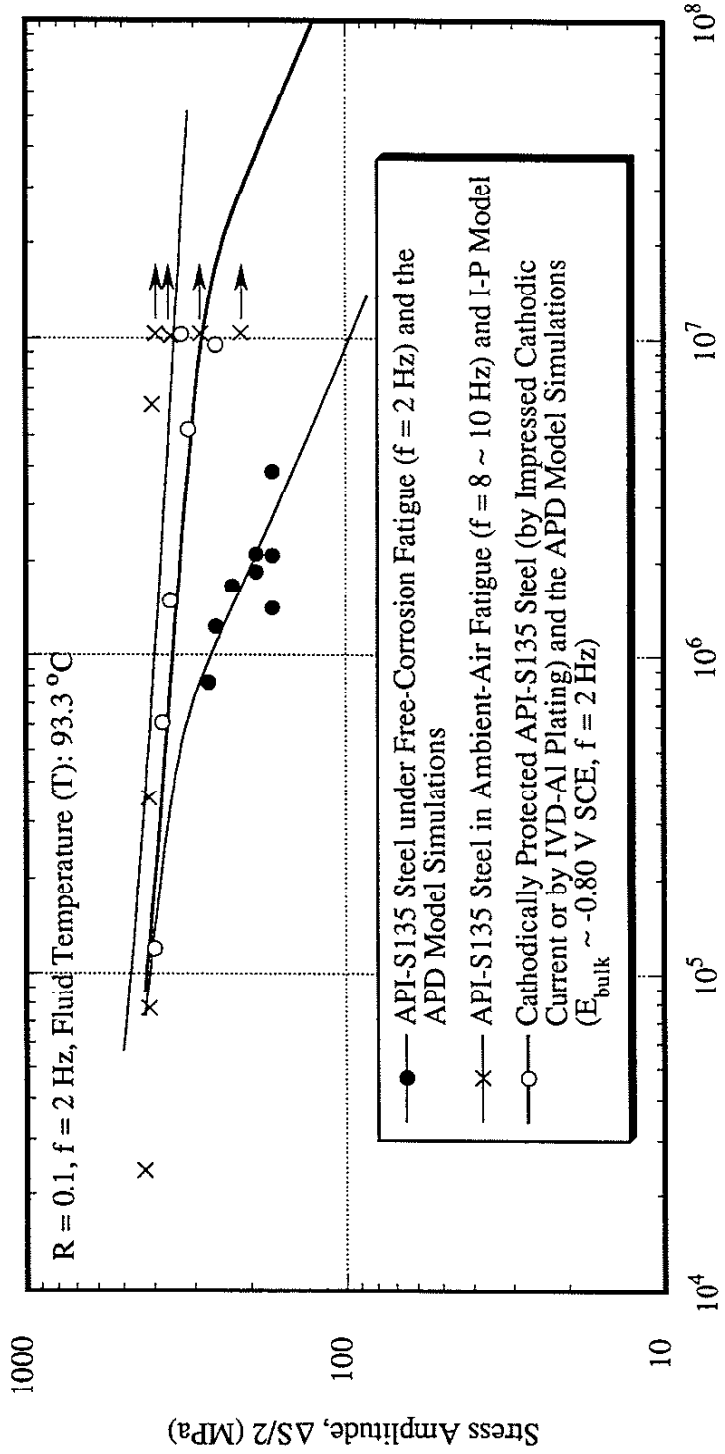

Figure 6.1 Experimentally observed improvement in corrosion-fatigue resistance of API-S135 steel in deaerated (purged UHP N_2) seawater drilling fluid (93.3 °C) by cathodic protection (externally impressed current or IVD-Al plating) relative to that of free-corrosion fatigue (f = 2 Hz); in comparison with test (f = 8 ~ 10 Hz) results in ambient air and the simulated effects by the APD model (sinusoidal wave, R = 0.1, η = 45 Ω^{-1} m^{-1}).

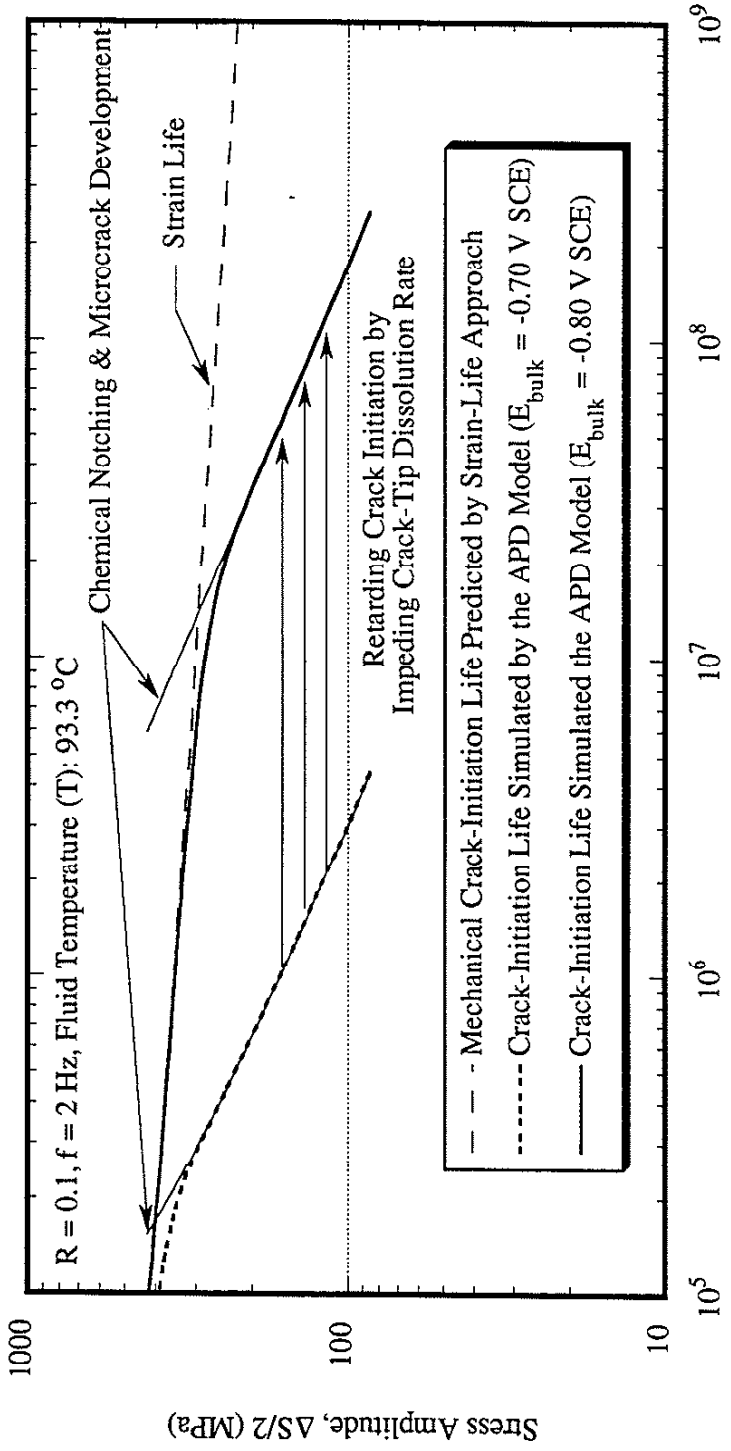

Figure 6.2 Effects of electrochemical potential (E_{bulk}) on the crack-initiation life (N_i) simulated by the APD model (sinusoidal wave, R = 0.1, f = 2 Hz, η = 45 $\Omega^{-1}m^{-1}$).

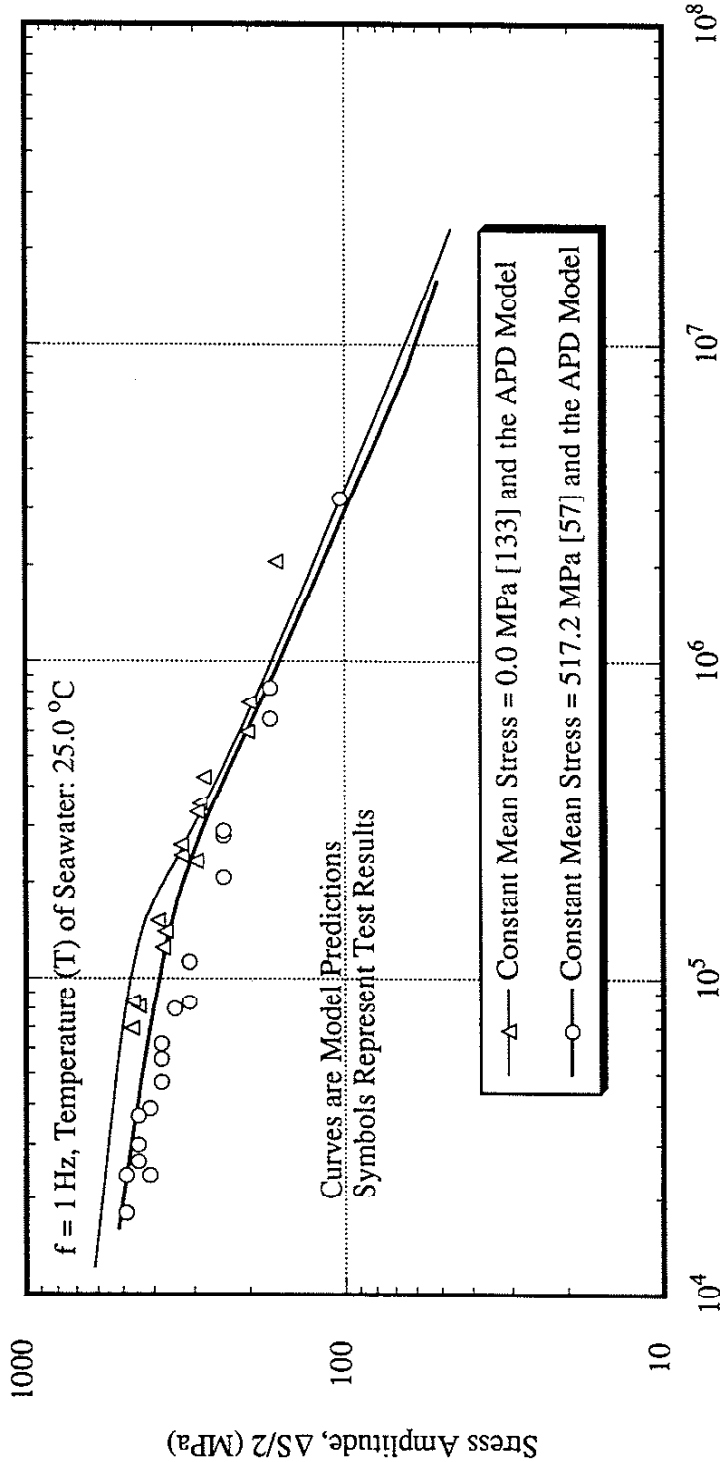

Figure 6.3 Comparison of experimentally observed effects of mean stress on the corrosion-fatigue S-N behavior of API-S135 steel in seawater at 25 °C with which simulated by the APD model (data taken from reference [57,133], sinusoidal wave, f = 1 Hz).

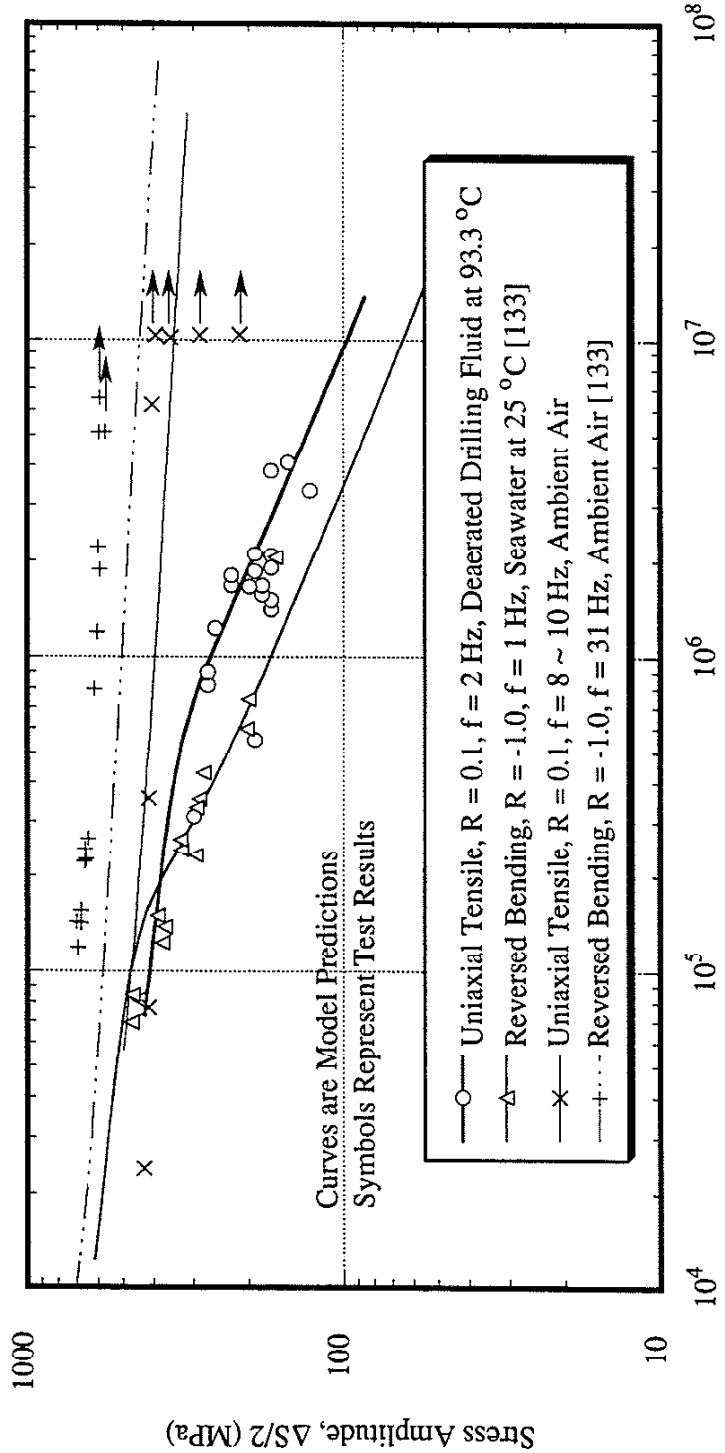

Figure 6.4 Comparison of experimentally observed effects of fluid temperature (T) and stress ratio (R) on the corrosion-fatigue S-N (f = 1 ~ 2 Hz) behavior of API-S135 steel in seawater bearing aqueous environments with test (f= 8~31 Hz) results in ambient air, and the corresponding effects simulated by the APD model.

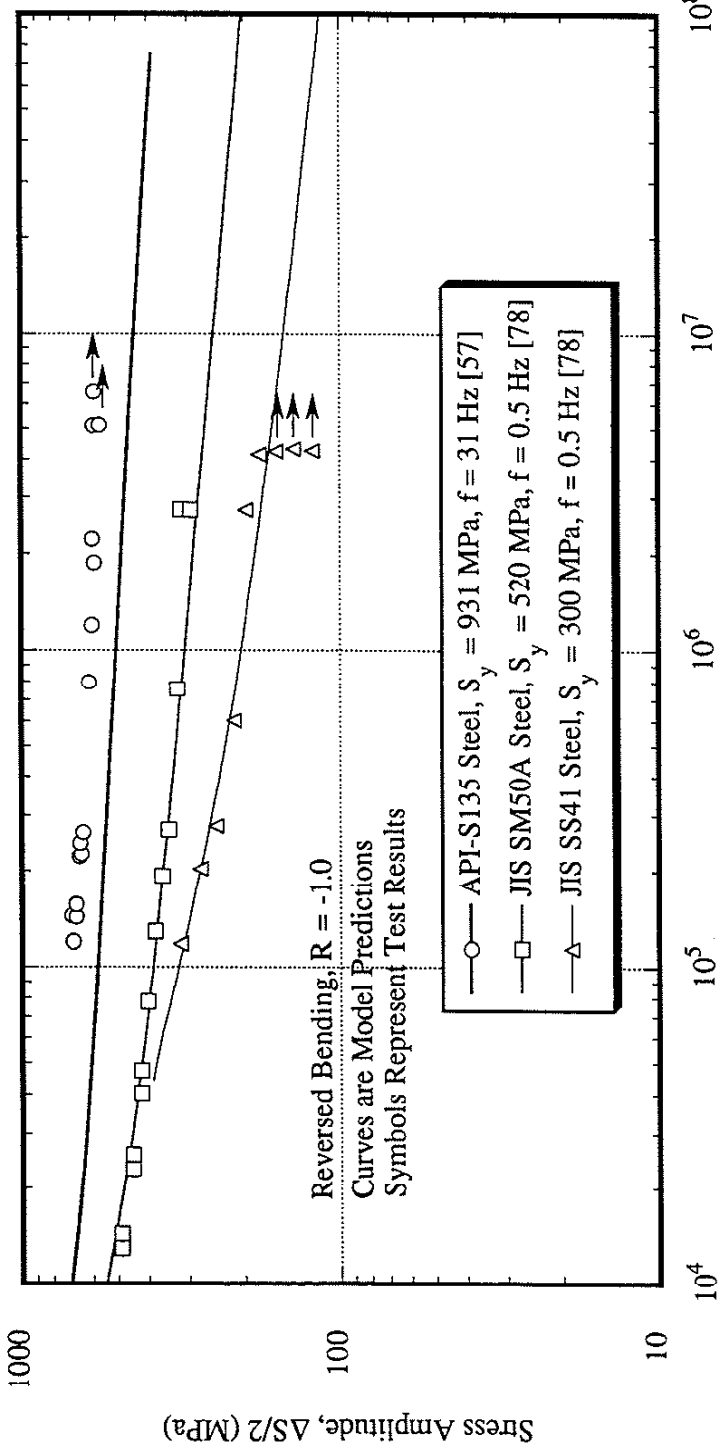

Figure 6.5 Comparison of experimentally observed effects of material strength (S_y) on reversed-bending (R= -1.0) S-N behavior in ambient air (25°C) with the corresponding I-P model predictions (data taken from reference [57,78], reversed bending, R = -1.0, sinusoidal wave).

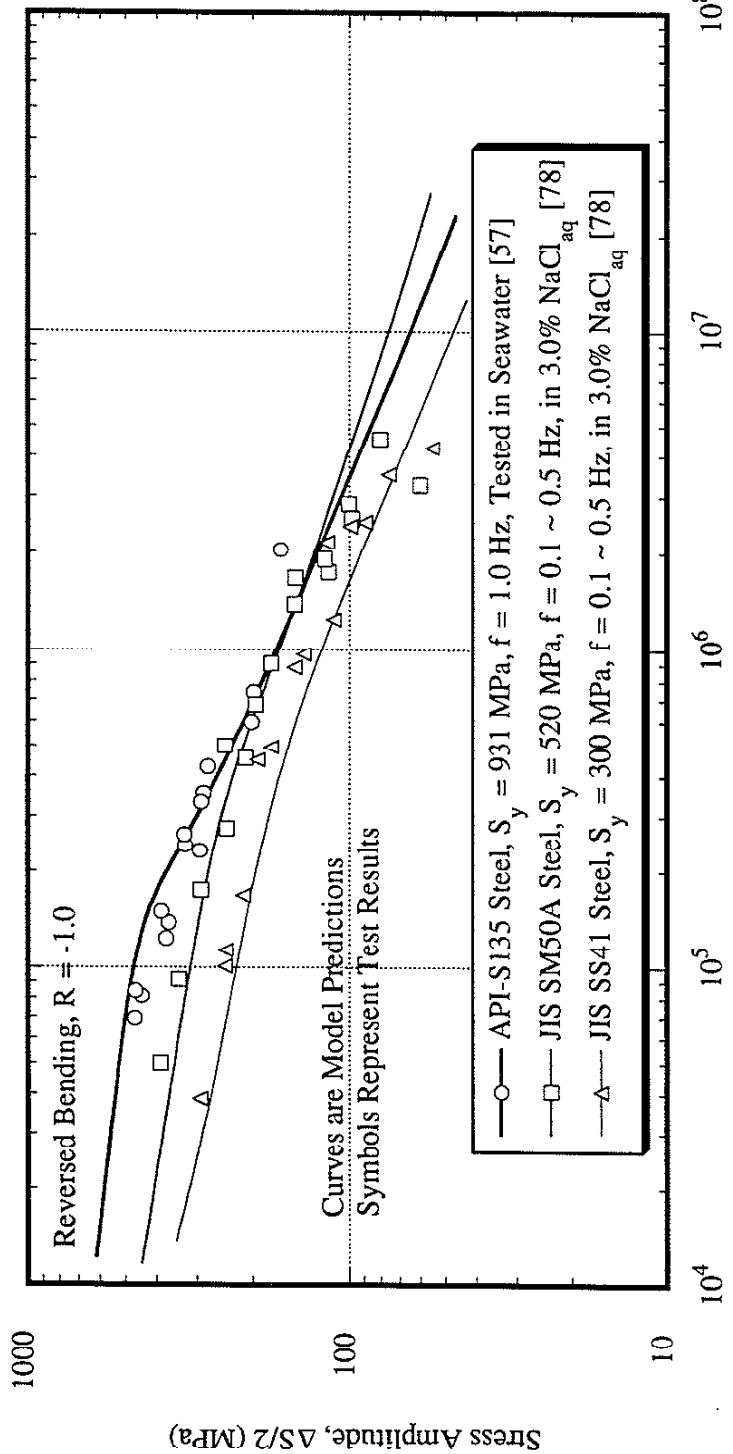

Figure 6.6 Comparison of experimentally observed effects of material strength (S_y) on reversed-bending (R = -1.0) corrosion-fatigue S-N behavior in saline aqueous environments at ambient temperature (20 ~ 25 °C) with the corresponding APD model simulations (data taken from reference [57,78], reversed bending, R = -1.0, sinusoidal wave).

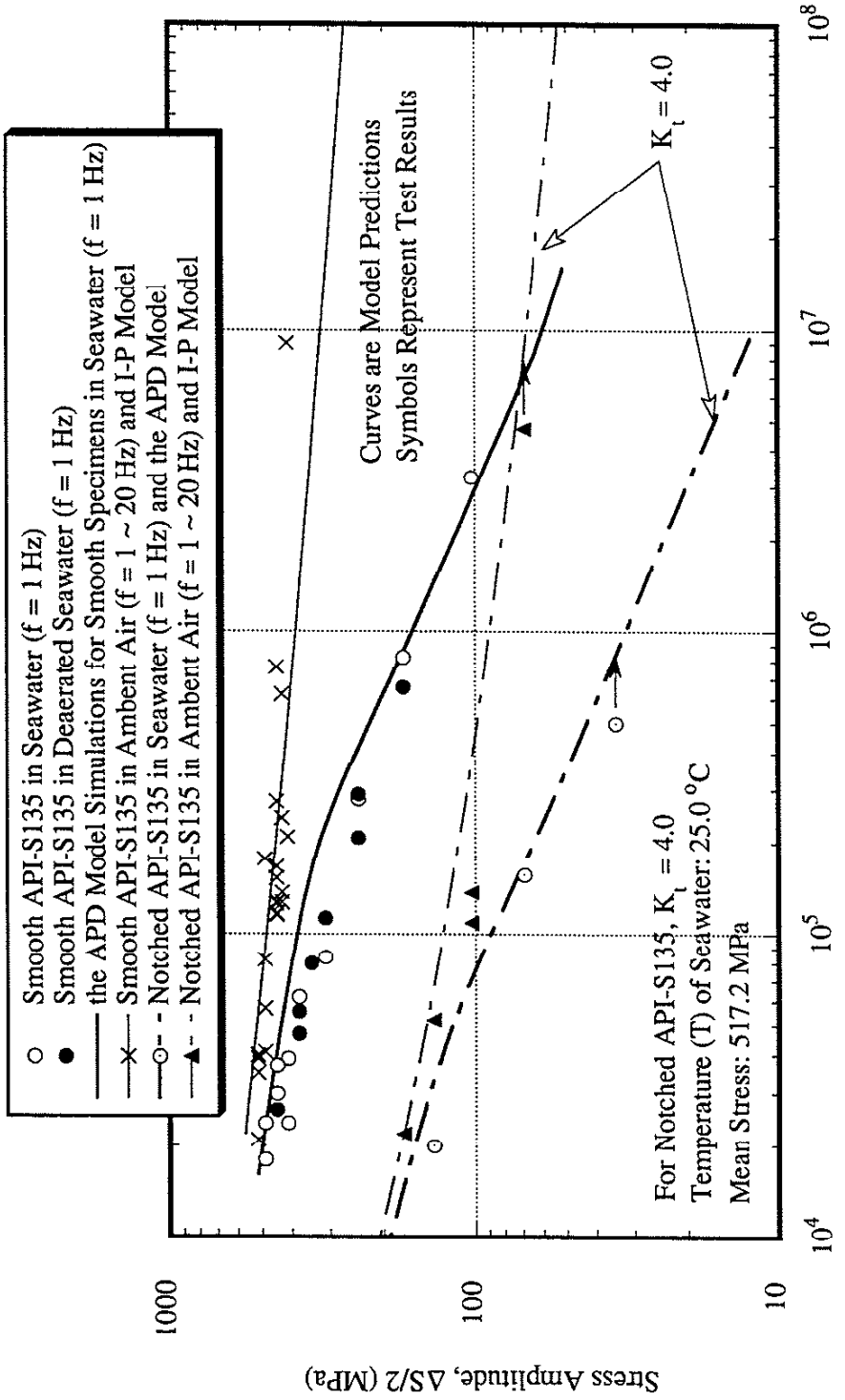

Figure 6.7 Comparison of the experimentally observed effects of mechanical notch (K_t) on the corrosion-fatigue S-N behavior of API-S135 steel tested (f = 1 Hz) under a constant mean stress (517.2 MPa) in seawater at 25 °C with the observed effects (f = 1 ~ 20 Hz) in ambient air, and the corresponding APD model, I-P model predictions (data taken from reference [135], sinusoidal wave).

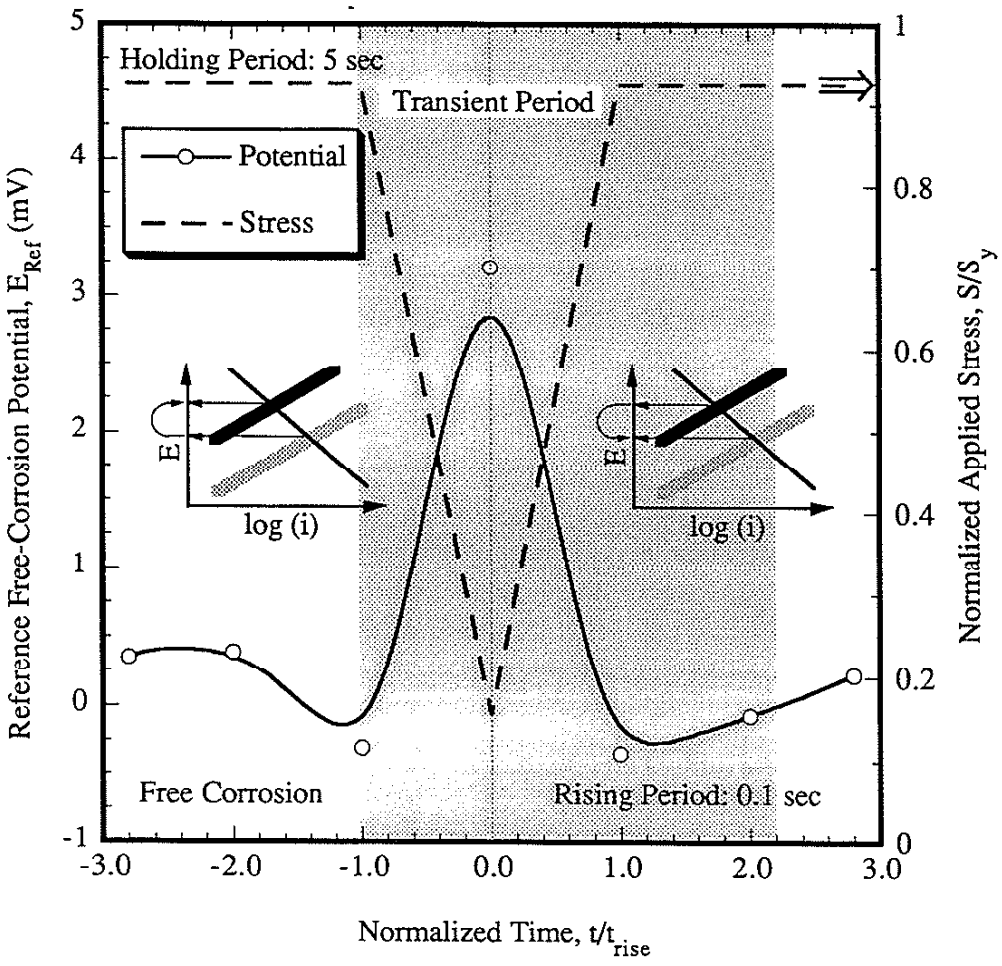

Figure 6.8 Free-corrosion-potential perturbation phenomena of an API-S135 steel subjected to a trapezoidal waveform loading (R = 0.1) having a stress-rising period (t_{rise}) of 0.1 sec (sinusoidal waveform of 5 Hz) in deaerated (purged UHP N_2) seawater drilling fluid at 93.3 °C.

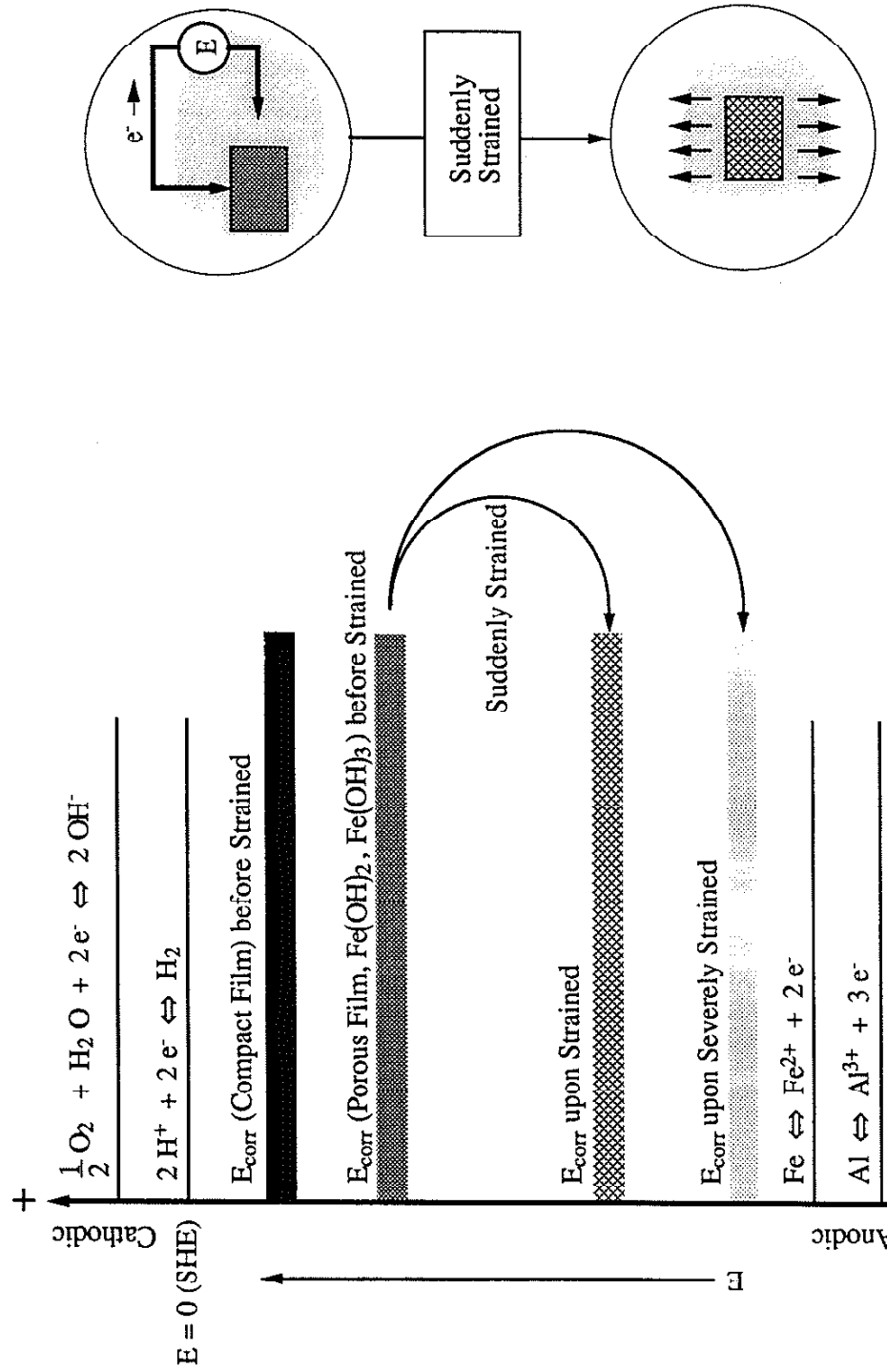

Figure 6.9 Perturbation of free-corrosion potential on a suddenly strained electrode responding to the rupture (or thining) process of surface films which would otherwise protect the electrode from anodic dissolution.

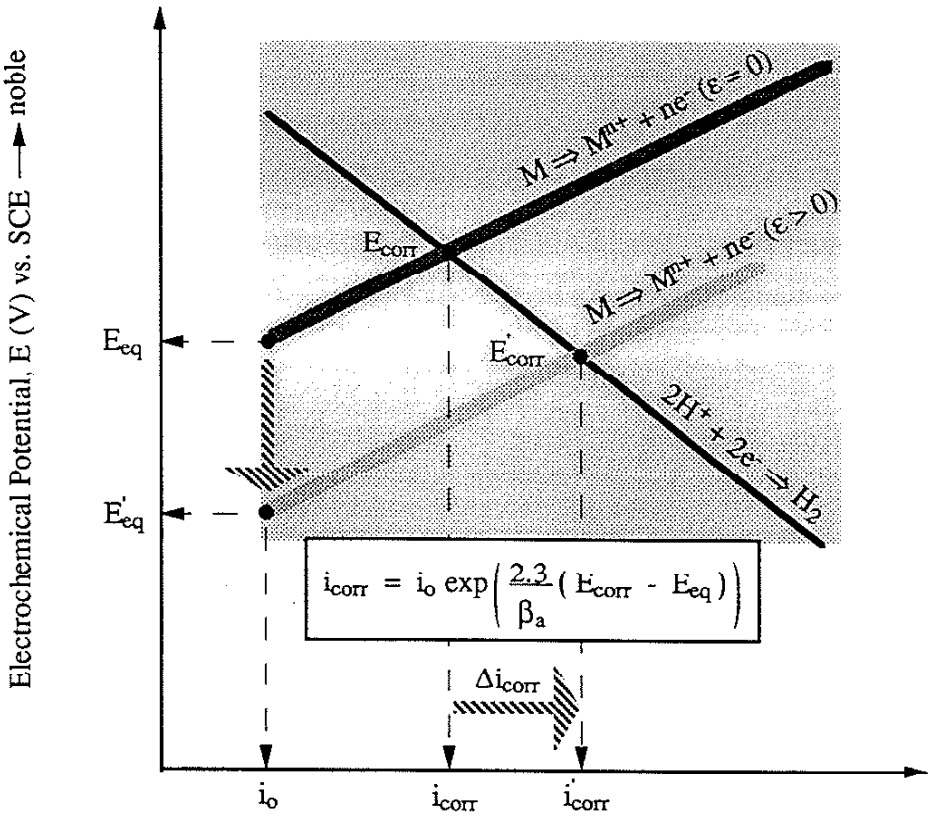

Figure 6.10 Straining induced sweeping perturbation of potentials and transient free-corrosion current density responding to the rupture (or thining) process of protective surface films due to the application of sudden strain.

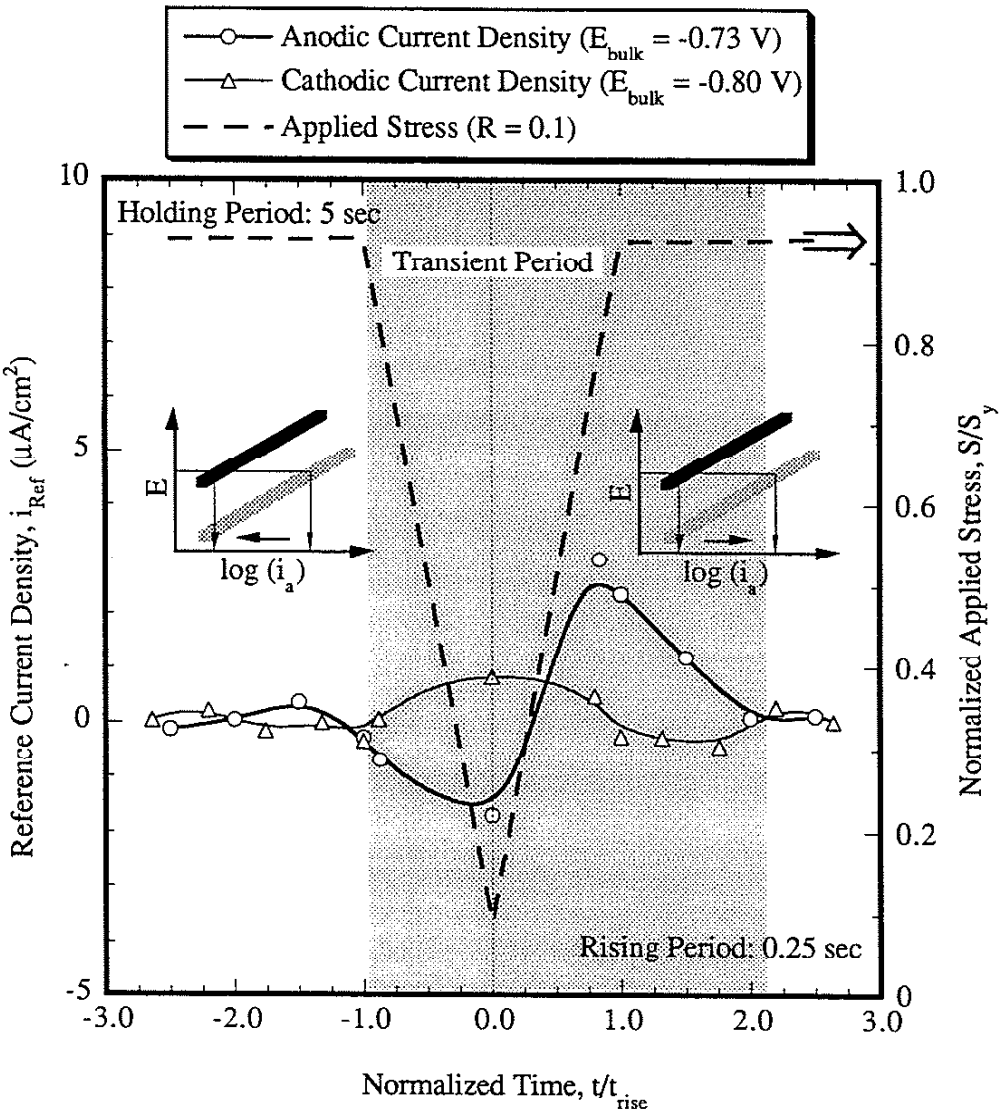

Figure 6.11 Comparison of anodic current-density transient with cathodic current-density transient of an API-S135 steel subjected to a trapezoidal waveform loading (R = 0.1) having a stress-rising period (t_{rise}) of 0.25 sec (sinusoidal waveform of 2 Hz) in deaerated (purged UHP N_2) seawater drilling fluid at 93.3 °C.

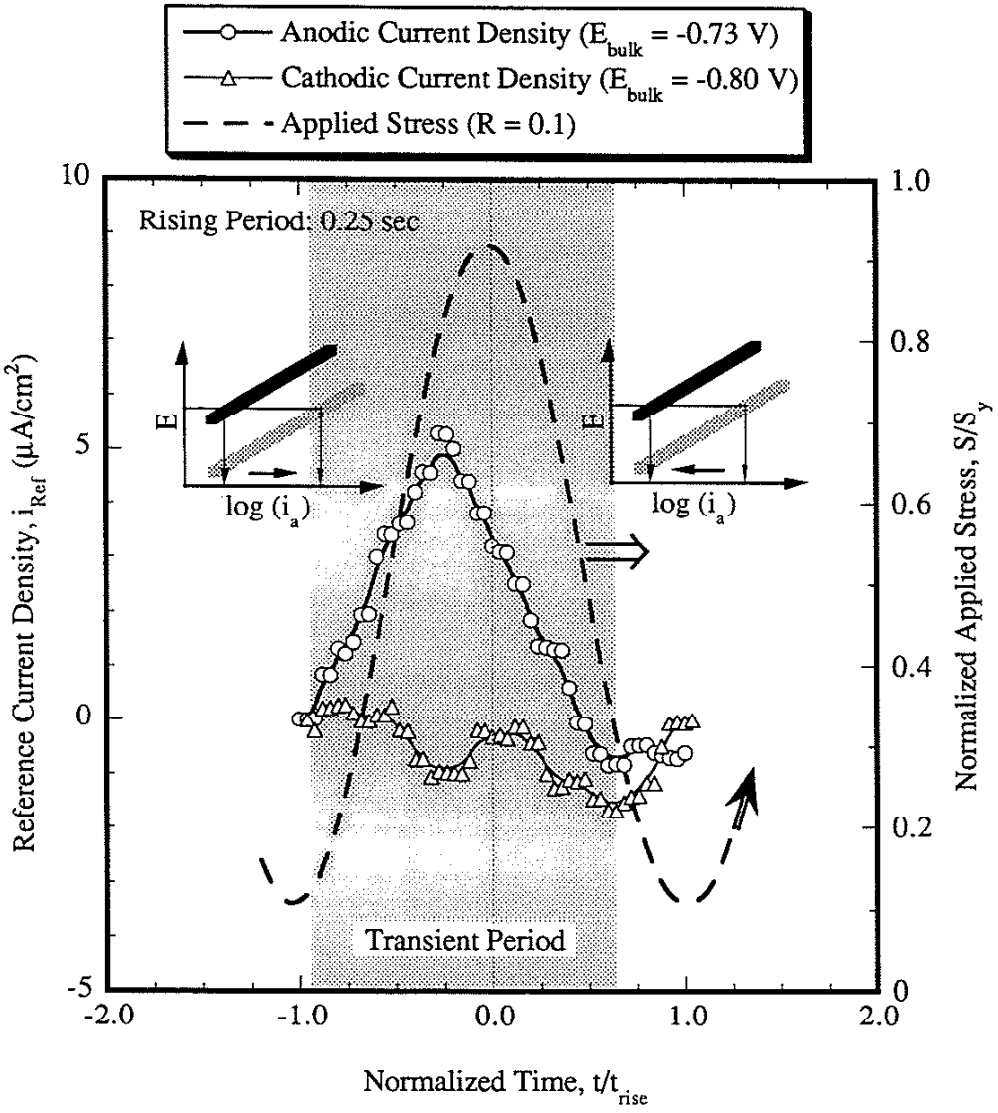

Figure 6.12 Comparison of anodic current-density transient with cathodic current-density transient of an API-S135 steel subjected to a sinusoidal waveform loading (R = 0.1) of 2 Hz having a stress-rising period (t_{rise}) of 0.25 sec in deaerated (purged UHP N_2) seawater drilling fluid at 93.3 °C.

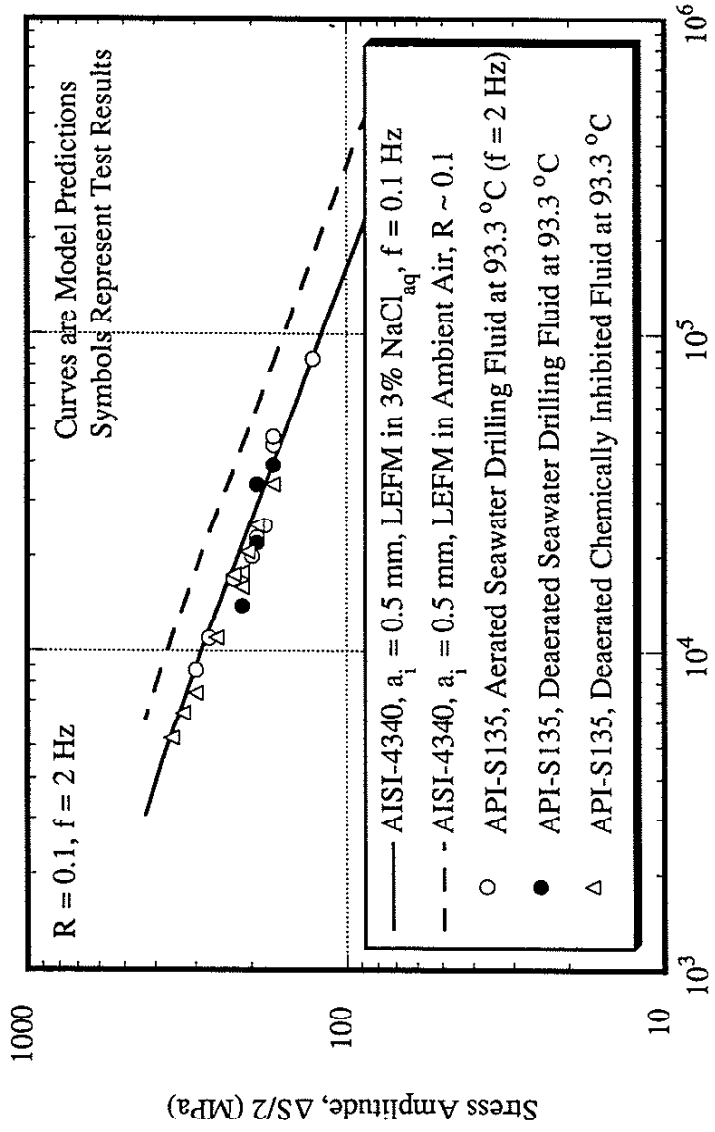

Figure 6.13 Comparison of experimentally observed life period of macroscopic fatigue-crack growth (N_{p2}) of API-S135 steel in seawater drilling fluids at 93.3 °C with the LEFM predictions (R ~ 0.1, f = 0.1 Hz) for an AISI-4340 steel [108] of the same yield strength (S_y) in both air and 3.0% NaCl solution at ambient temperature (20 ~ 25 °C).

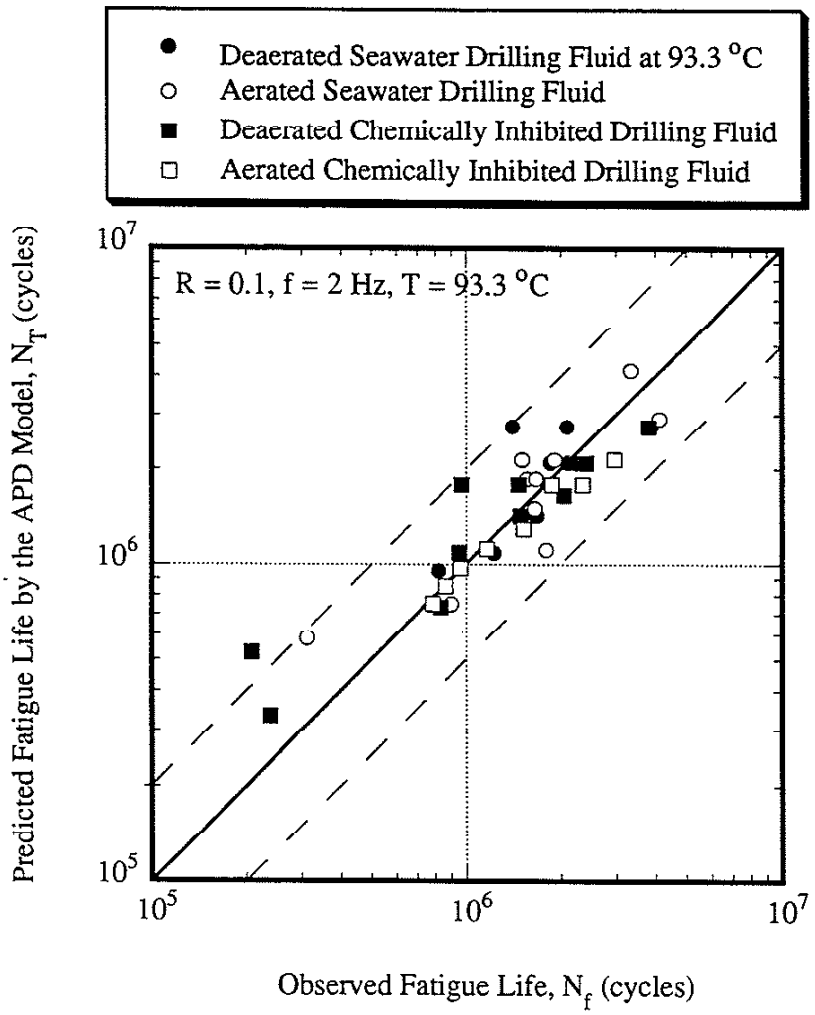

Figure 6.14 Comparison of experimentally observed corrosion-fatigue life (N_f) of API-S135 steel in seawater drilling fluids at 93.3 °C with the fatigue life (N_T) simulated by the APD model (uniaxial-tensile fatigue, unnotched specimen, sinusoidal wave, R = 0.1, f = 2 Hz).

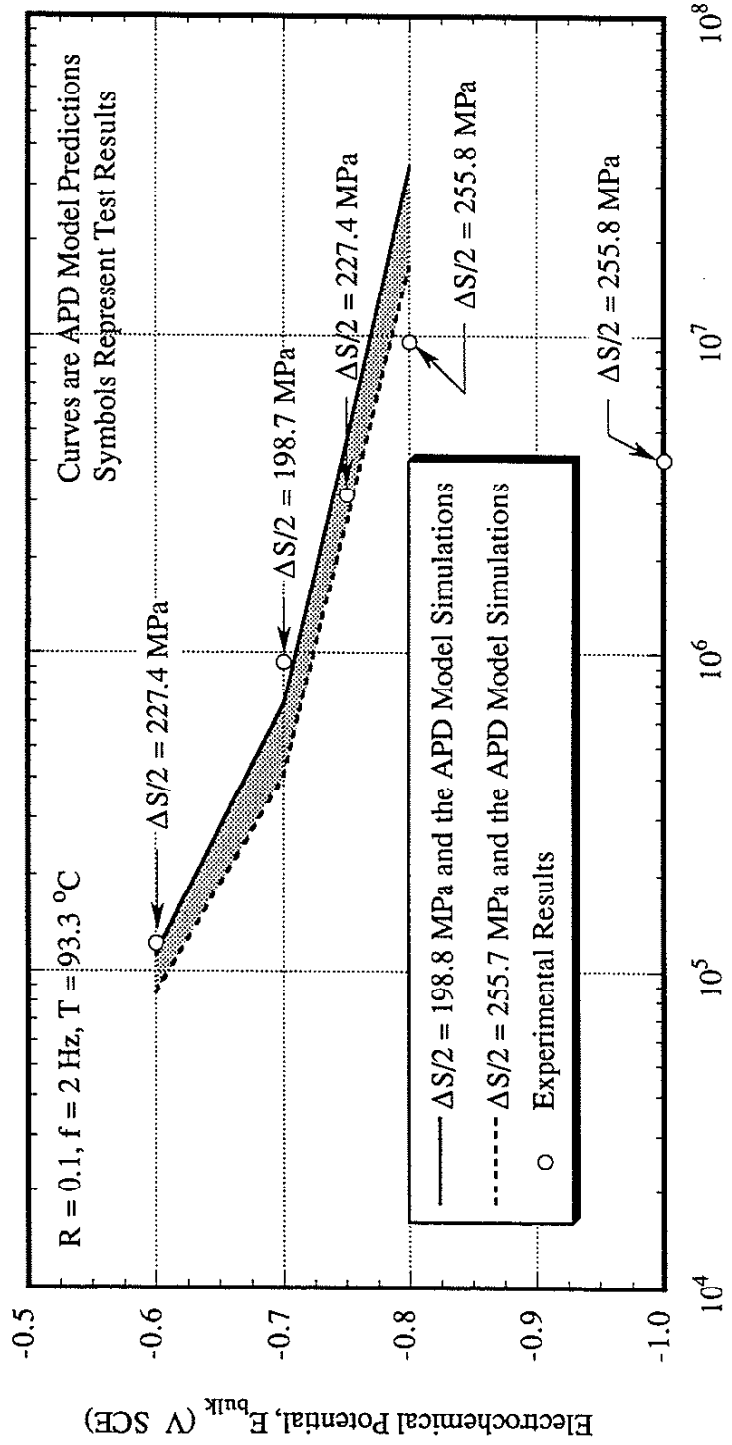

Figure 6.15 Validity limit of the APD model simulated effects of electrochemical potential (E_{bulk}) on the corrosion-fatigue life of API-S135 steel in deaerated (purged UHP N_2) seawater drilling fluid at 93.3 °C (sinusoidal wave, R = 0.1, f = 2 Hz).

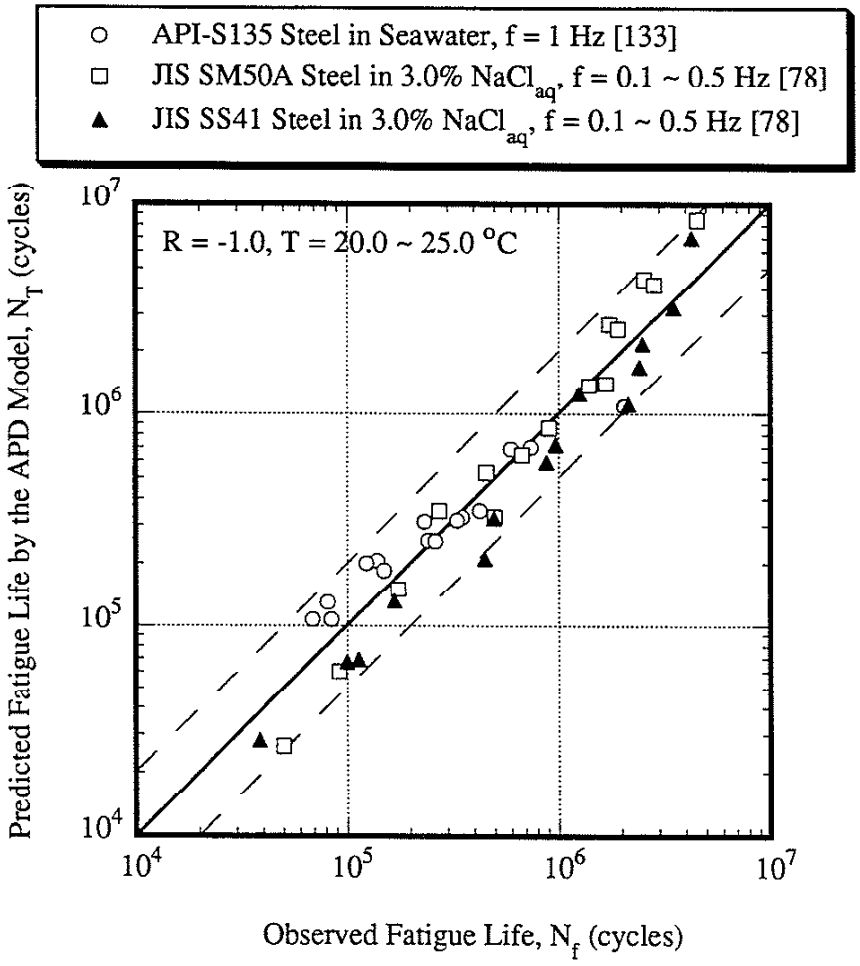

Figure 6.16 Comparison of experimentally observed corrosion-fatigue life of structural steels of various yield strength (S_y) in saline aqueous environments with the fatigue life (N_T) simulated by the APD model (data taken from reference [78,133], reversed-bending fatigue, R = -1.0, unnotched specimen, sinusoidal wave, f = 0.1 ~ 1 Hz).

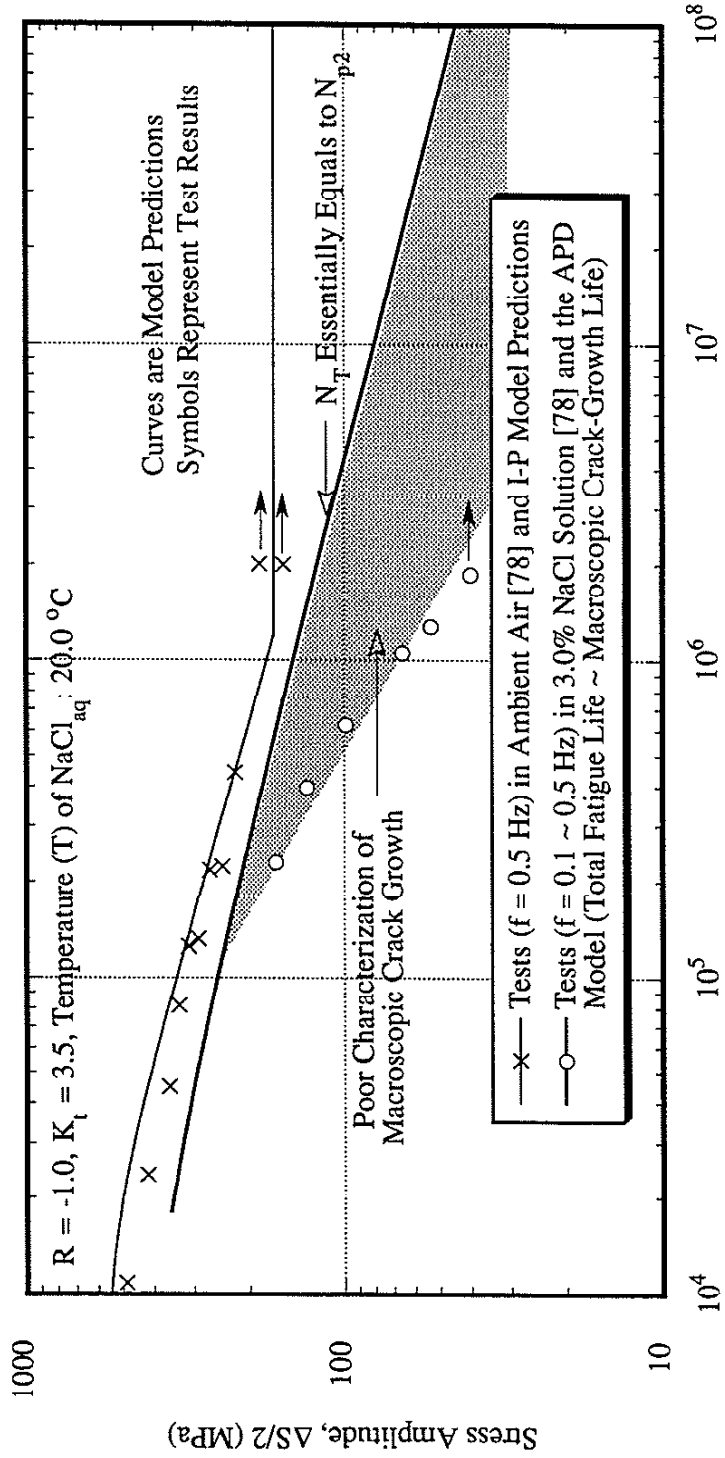

Figure 6.17 Comparison of corrosion-fatigue S-N behavior of notched (K_t = 3.5) JIS SM50A steel tested (f = 0.1 ~ 0.5 Hz) under reversed bending (R = -1.0) in 3.0% NaCl solution at 20 °C with test (f = 0.5 Hz) results in ambient air, and the APD model simulations (data taken from reference [78], sinusoidal wave).

APPENDIX A: CYCLIC-STRAIN-INDUCED CHEMICAL-NOTCHING KINETICS

A.1 STRAINING INDUCED SWEEPING POTENTIAL

As sketched in Fig. 6.10, an externally applied strain raises the corrosion susceptibility of an electrode by depressing its redox potential (E_{eq}) toward active (more negative) potential. The free-corrosion current density (i_{corr}) as obtained from the mixed-electrode theory increases [141-142] accordingly accompanying with a dropping free-corrosion potential (E_{corr}) [143-145]. Assuming that an electrode responds to the external straining with a dropping redox potential of a sweeping velocity (v):

$$E'_{eq} = E_{eq} - v\,t \tag{A.1}$$

and that the dissolving metal ion concentration in the vicinity of a static electrode can be characterized by Nernst's equation [146]:

$$C_{M^+} = \exp\left(\frac{z\,F}{R'\,T} \left(E_{eq} - E^o \right) \right) \tag{A.2}$$

we can then correlate the dissolving metal ion concentration in the vicinity of straining electrode with that of a static electrode of zero strain by:

$$C'_{M^+} = C_{M^+} \exp\left(- \frac{z\,F\,v\,t}{R'\,T} \right) \tag{A.3}$$

where:

E'_{eq}	=	Redox potential of a straining electrode (volt)
E_{eq}	=	Redox potential of a static electrode of zero strain (volt)
v	=	Straining induced sweeping velocity of redox potential (volt/sec)
C_{M^+}	=	Dissolving metal ion concentration in the vicinity of a static electrode of zero strain (mole/cm^3)
z	=	Valence of a dissolving cation
F	=	Faraday's constant (coulomb/mole)
R'	=	Gas constant (joule/mole °K)
T	=	Fluid temperature (°K)
E^o	=	Redox potential of a static electrode at its standard state (volt)
C'_{M^+}	=	Dissolving metal ion concentration in the vicinity of a straining electrode (mole/cm^3)

The perturbation of free-corrosion potential (E_{corr}) was observed in this investigation by fatigue straining API-S135 steel in seawater drilling fluids at 93.3 °C. The curved fitted relationships between stress range (ΔS) and sweeping potential velocity (v) are presented in Eq. A.4 and Eq. A.5 for the testing environments of seawater drilling fluid without and with adding polymeric inhibitor (Conquor 404), respectively:

$$v = -0.01 + 0.093 \left(\frac{\Delta S}{S_y} \right) \tag{A.4}$$

$$v = -0.03 + 0.093 \left(\frac{\Delta S}{S_y} \right) \tag{A.5}$$

where:

ΔS	=	Applied stress range (MPa)
S_y	=	Yield strength of material (0.2% offset) (MPa)

A.2 Transient Localized Electrochemical Dissolution

As shown in Fig. A.1, the redox potential (E_{eq}) fluctuates according to the fatigue strain applied to the electrode. The exponential decrease of metal ion concentration during loading reversal produces a current which conducts away the nearby excess metal ions to the surrounding dilute electrolyte ($[C_{M^+}] \sim 0$). Assuming that this conducting current is an irreversible process, the electrode must thus recharge its local environment to satisfy the exponential demand of metal ions for rising redox potential during unloading reversal. We further assume that the surface of the straining electrode is saturated with dissolving cations, and the extra amount of dissolution (beyond uniform corrosion) to recharge the local environment is fulfilled through a localized dissolution process. A transient peak-current density (i^*) of localized dissolution can then be calculated by relating the recharging current in Fig. A.1 with the ionic flux as following:

$$i^*(N) = \frac{z F D}{w} \int_0^{\frac{1}{2f}} \left[C^s_{M^+} - C_{M^+} \exp\left(- \frac{z F v}{2 f R' T} \right) \exp\left(\frac{z F v t}{R' T} \right) \right] dt \tag{A.6}$$

or equivalently in time base:

$$i^*(t) = \frac{z F D f}{w}\left[\frac{C^s_{M^+}}{2f} - \frac{C_{M^+} R' T}{z F v}\left(1 - \exp\left(- \frac{z F v}{2 R' T f} \right) \right) \right] \qquad (A.7)$$

where:

$i^*(N), i^*(t)$	=	Transient peak-charge (per cycle) and peak-current density of chemical-notching process, respectively (coulomb/cm^2, A/cm^2)
N	=	Number of fatigue cycles (cycles)
t	=	Time (sec)
D	=	Diffusion coefficient of dissolving metal ions (cm^2/sec)
w	=	Distance from a straining electrode where electrochemical potential was measured (cm)
f	=	Test frequency (cycles/sec)
C^s_{M+}	=	Saturation limit of dissolving metal ions (mole/cm^3)

A.3 Diffusion Limited Mass Transfer

Because the transient peak-current density computed in Eq. A.7 can not be sustained for long, the current-density trace must be limited by the ohmic drop or by ionic diffusion as chemical notches grow in size [130,147]. As shown in Fig. A.2, once the saturation of the dissolving cation occurs at the metal-solution interface after the initial transient period, a quasi-steady-state period of diffusional control commences. According to the most general description of mass transfer given by Nernst-Planck equation [146], the cation flux is composed of three contributions: concentration gradient, potential gradient and convection as seen in Eq. A.8:

$$J(x) = - D \frac{\partial C_{M^+}}{\partial x} - \frac{z F D C_{M^+}}{R' T} \frac{\partial E}{\partial x} + v C_{M^+} \qquad (A.8)$$

where:

J(x)	=	Dissolving metal ion flux (mole/cm^2 sec)
E	=	Electrochemical potential at position x (volt)
v	=	Flushing rate of electrolyte (cm/sec)

To simplify the mathematical treatment, we represent a three-dimensional ideal chemical notch by a two-dimensional model chemical notch shown in Fig. 3.4. The model chemical notch consists of an anodic base of uniform current density and two cathodic faces which isolate from the bulk electrolyte with a salt film of thickness (τ). This salt film behaves as a

diffusion buffer and provides a transition between the cation-saturated occluded zone ($C_{M^+} = C^s_{M^+}$ within a chemical notch) and the very dilute ($C_{M^+} = 0$) bulk electrolyte. The assumption of an uniform current-density distribution during active chemical notching should be justified because chemical notches grow in size but their shape remains almost unchanged (approximately a hemisphere) [148-149]. For an electrolyte of low flushing rate which preserves an intact diffusion buffer at the entrance of chemical notches, the convection term in Eq. A.8 could be ignored [130]. For a shallow chemical notch, we further assume no significant ohmic drop contribution [147]. Therefore, Eq. A.8 is reduced to the Fick's first law with an effective diffusion path of $a_{pit}+\tau$:

$$J(x) = -D\frac{\partial C_{M^+}}{\partial x} \tag{A.9}$$

therefore:

$$\frac{i(t)}{zF} = \frac{D\,C^s_{M^+}}{(a_{pit} + \tau)} \tag{A.10}$$

Assuming that the chemical notching proceeds mainly by anodic penetration from Faradic current, we use Faraday's law and obtain:

$$a_{pit} = \frac{M}{zF\rho}\int_0^t i(t)\,dt \tag{A.11}$$

Insert Eq. A.11 into Eq. A.10:

$$\frac{M}{zF\rho}\int_0^t i(t)\,dt + \tau = \frac{zF\,D\,C^s_{M^+}}{i(t)} \tag{A.12}$$

then differentiate both sides of Eq. A.12 with respect to time (t) and rearrange:

$$\frac{M\,i(t)}{zF\rho}\,dt = -zF\,D\,C^s_{M^+}\,i^{-2}(t)\,di(t) \tag{A.13}$$

The integration of Eq. A.13 gives:

$$i^{-2}(t) = i^{*-2} + \frac{2M}{z^2 F^2 \rho D C_{M^+}^s}\left(\frac{N}{f}\right) \qquad (A.14)$$

After inserting Eq. A.14 into Eq. A.11 and then solving the integration, the fatigue life (N_{pit}) required to produce a chemical notch of given depth (a_{pit}) can be estimated as:

$$N_{pit} = \frac{\rho f a_{pit}}{2M}\left[\frac{a_{pit}}{D C_{M^+}^s} + \frac{2zF}{i^*}\right] \qquad (A.15)$$

where:

$i(t)$	=	Trace of chemical-notching current density (A/cm^2)
a_{pit}	=	Depth of a chemical notch (cm)
τ	=	Thickness of diffusion buffer (salt film) (cm)
M	=	Atomic weight of material (g/mole)
ρ	=	Density of material (g/cm^3)
N_{pit}	=	Fatigue cycles to produce a chemical notch of a given depth (cycles)

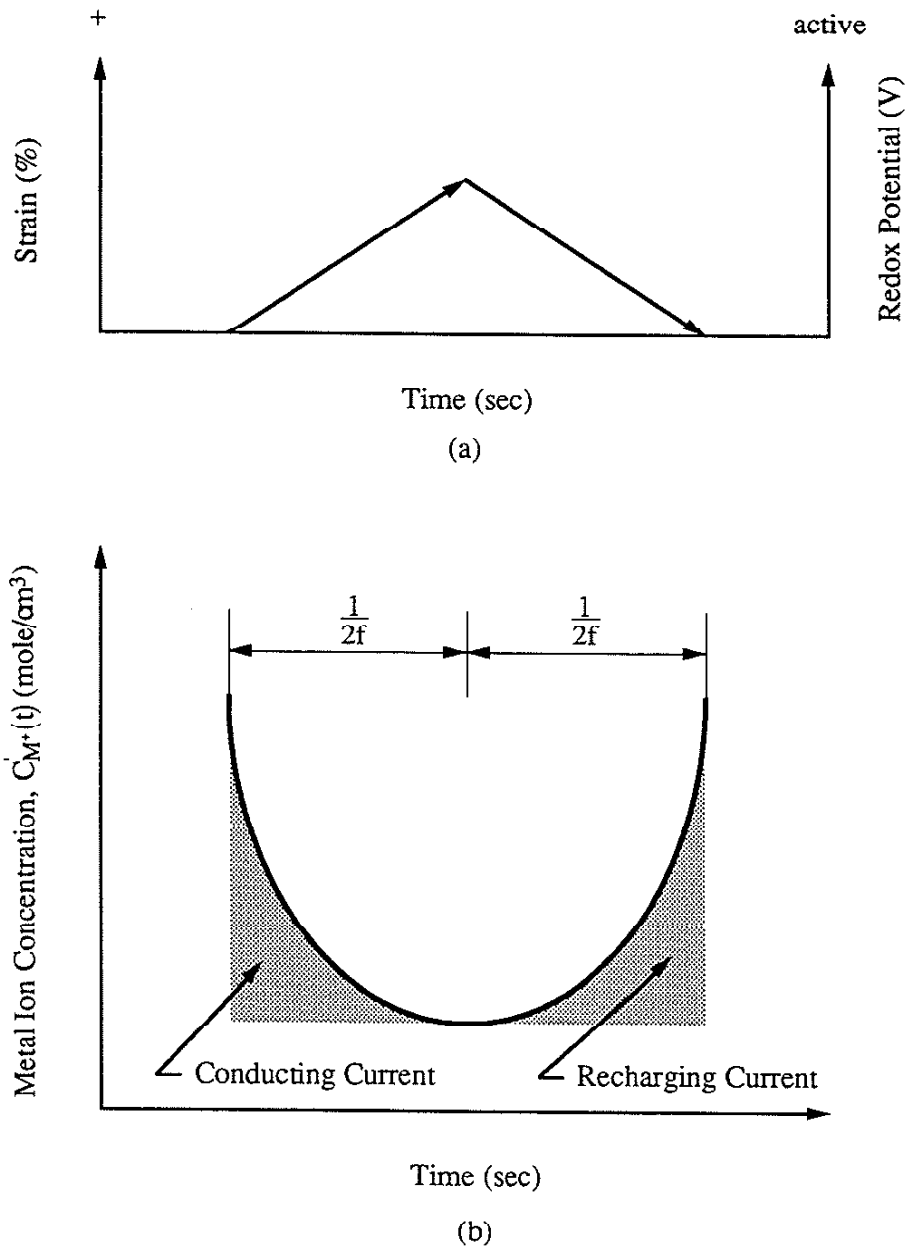

Figure A.1 Irreversible sweeping-potential electrochemical dissolution:
(a) cyclic strain and redox potential response;
(b) perturbation of cation concentration in the vicinity of the cyclically straining electrode.

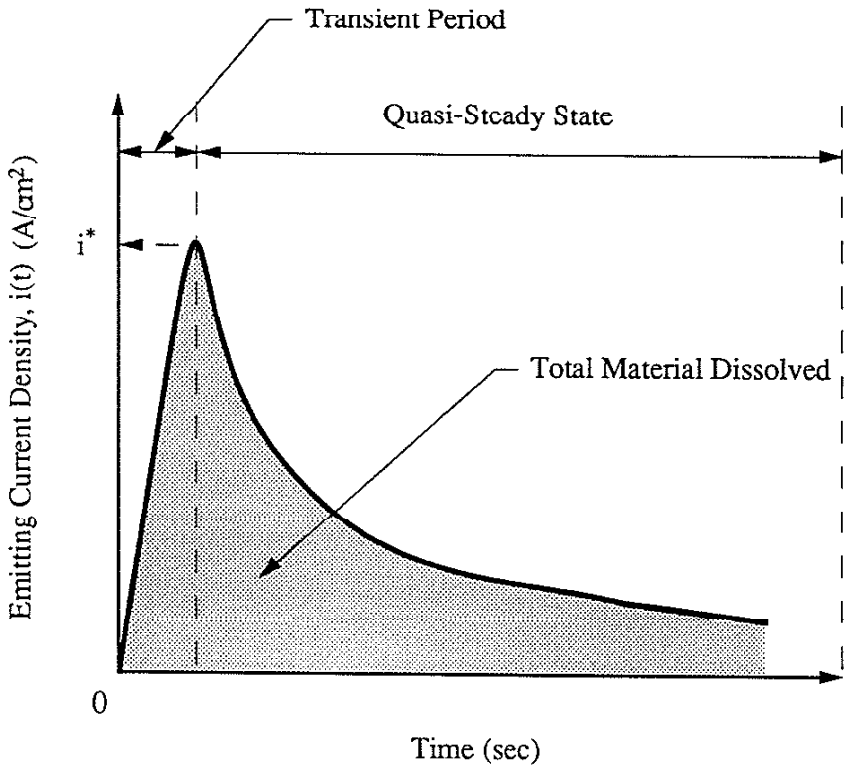

Figure A.2 The emitting current-density trace during active chemical-notching process.

APPENDIX B: COMPUTATION OF BARE-CRACK-TIP CURRENT DENSITY

B.1 MICRO-GALVANIC COUPLING AND ELECTROMIGRATION CONTINUITY

The bare-crack-tip current density (i_{bare}) after film rupture depends mainly on crack-tip electrochemical conditions, e.g., pH and electrochemical potential. Consider an idealized microcrack (as sketched in Fig. B.1) having a static crack-tip opening displacement (δ), an electromigration continuity must be established within any infinitesimal crack segment. The anode is assumed to be confined within crack tip which couples with passivated crack faces (cathodes) to complete an occluded micro-galvanic cell [139,150]. The development of microcracks is then associated with the anodic dissolution at bare crack tips, the diffusion of cations, anions, and the corresponding electromigration driven by the gradient of electrochemical potential. For a nearly static crack electrolyte, the mass transfer by ionic diffusion and convection would not be rate determining and hence will not be considered. Therefore, the electromigration continuity (see Fig. B.2), as originally proposed by Doig et al. [150-152] for stress-corrosion crack growth, can be written:

$$I_a + dI_a - I_a = 2\, i_c\, dx \tag{B.1}$$

$$\frac{dI_a}{dx} = 2\, i_c \tag{B.2}$$

where:

I_a	=	Anodic current flow (A/cm)
i_c	=	Cathodic current density at passivated crack faces (A/cm^2)
x	=	Distance from crack mouth (cm)

The anodic current flow is considered to be driven mainly by the gradient of electrochemical potential. Thus, the outcome anodic current flow must also satisfy Ohm's law [150-152]:

$$I_a = -\delta \eta \frac{dE_x}{dx} \tag{B.3}$$

After inserting Eq. B.3 into Eq. B.2 [150-152] we have:

$$\frac{d^2E_x}{dx^2} = -\frac{2\, i_c}{\delta \eta} \tag{B.4}$$

where:

δ	=	Crack-tip opening displacement (m)
η	=	Electrolytic conductivity of unit crack-tip opening ($\Omega^{-1}m^{-1}$)
E_x	=	Electrochemical potential at crack depth x (volt)

The crack-tip opening displacement under the maximum applied stress (S_{max}) can be obtained from Dugdale strip-yield model [153] seen in Fig. B.3:

$$\delta = \frac{8\,\sigma_{yc}\,a}{\pi\,\chi}\ln\left(\sec\left(\frac{\pi\,S_{max}}{2\,\sigma_{yc}}\right)\right) \tag{B.5}$$

Eq. B.5 can be simplified asymptotically for S_{max} less than 75% of material yield strength (S_y). Thus for a finite geometry under plane strain condition, the crack-tip opening displacement is:

$$\delta = \frac{K_{Imax}^2}{\chi\,\alpha\,\sigma_{yc}} \tag{B.6}$$

where:

σ_{yc}	=	Cyclic yield strength (MPa) (about 70% of monotonic yield strength)
a	=	Crack length (m)
χ	=	Elastic modulus of material (MPa)
S_{max}	=	Maximum applied tensile stress (MPa $\sqrt{m}$)
K_{Imax}	=	Maximum mode I stress-intensity factor (MPa $\sqrt{m}$)
α	=	Constraint factor for a plane strain condition (2.0-2.5)

The dissolution-current density of a corroding electrode under a given over-potential can be described by a well known Butler-Volmer equation seen in Eq. B.7. The derivation of Butler-Volmer equation can be found in any electrochemistry text [146]:

$$i_a = i_o\left[\exp\left(\frac{(1-\phi)\,z\,F}{R'\,T}(E_x - E_{eq})\right) - \exp\left(-\frac{\phi\,z\,F}{R'\,T}(E_x - E_{eq})\right)\right] \tag{B.7}$$

where:

i_a	=	Anodic dissolution-current density (corrosion rate) (A/cm^2)
i_o	=	Exchange current density of an electrode (A/cm^2)
ϕ	=	Symmetry factor

z	=	Valence of dissolving cations
F	=	Faraday's constant (coulomb/mole)
R'	=	Gas constant (joule/mole °K)
T	=	Fluid temperature (°K)
E_{eq}	=	Redox potential of a corroding electrode (V)

The first exponential function represents an oxidation reaction while the second a reduction reaction. By noting that the passivated crack faces are undergoing predominately a cathodic reaction, the cathodic current density (i_c) at these surfaces can be evaluated as:

$$i_c = i_o^{pass} \exp\left(-\frac{\phi z F}{R' T}\left(E_x - E_{eq}^c \right) \right) \tag{B.8}$$

i_o^{pass} (exchange current density) can not be derived from first principles and should be determined experimentally from passivated electrodes of a plastically-deformed material. By correlating with the experimentally observed cathodic Tafel's slope (β_c):

$$-\frac{\phi z F}{R' T} = \frac{2.3}{\beta_c} \tag{B.9}$$

and inserting Eqs. B.6, B.8, and B.9 into Eq. B.4, we obtain:

$$\frac{d^2 E_x}{dx^2} = -\frac{2 \chi \alpha \sigma_{yc} i_o^{pass}}{K_{Imax}^2 \eta} \exp\left(\frac{2.3}{\beta_c}\left(E_x - E_{eq}^c \right) \right) \tag{B.10}$$

where:

i_o^{pass}	=	Exchange current density of a cathodic reduction on passivated crack faces (A/cm^2)
E^c_{eq}	=	Redox potential of a cathodic redox couple (V)
β_c	=	Cathodic Tafel's slope of plastically-deformed passivated cathodes

Eq. B.10 can be solved numerically by the fourth-order Runge-Kutta algorithm to acquire the electrochemical potential at crack tips (E_{tip}) under the following boundary conditions:

$$\left[E_x \right]_{x=0} = E_{cm}; \qquad \left[\frac{dE_x}{dx} \right]_{x=0} = 0 \tag{B.11}$$

The anodic current density at bare crack tips (i_{bare}) can then be computed according to:

$$i_{bare} = i_o^{plastic} \exp\left(\left(1 - \phi \right) \frac{z F}{R' T} \left(E_{tip} - E^a_{eq} \right) \right) \tag{B.12}$$

$$\left(1 - \phi \right) \frac{z F}{R' T} = \frac{2.3}{\beta_a} \tag{B.13}$$

where:

E_{cm}	=	Electrochemical potential at crack mouth (volt)
i_{bare}	=	Bare-crack-tip current density (A/cm^2)
$i_o^{plastic}$	=	Exchange current density of an anodic dissolution at plastically-deformed crack tips (A/cm^2)
E_{tip}	=	Electrochemical potential at crack tips (volt)
E^a_{eq}	=	Redox potential of an anodic dissolution at crack tips (volt)
β_a	=	Experimentally observed anodic Tafel's slope of dissolving metal

B.2 Salt-Film Ohmic Drop and Crack-Mouth Potential

The gradient of electrochemical potential across the surrounding salt film in Fig. 3.4 is ignored during the development of active chemical notches discussed in Appendix A. As microcrack developing, the presence of this diffusional buffer becomes increasingly important and exhibits a significant ohmic transition (see Fig. B.4) between bulk solution and crack solution. Corrosion products tend to accumulate within this salt film due to the pH at crack mouth favors the precipitation (refer Pourbaix diagram) of metallic compounds. This effect makes the salt film electrolytically so resistant as must be integrated into consideration before the rational boundary conditions of electromigration continuity can be established.

From the Nernst-Einstein equation of one-dimensional mass conservation [146] we know:

$$D \frac{\partial^2 C_{M^+}}{\partial x^2} + \frac{z F}{R' T} D \left(\frac{\partial C_{M^+}}{\partial x} \frac{\partial E_x}{\partial x} + \frac{\partial^2 E_x}{\partial x^2} \right) = 0 \tag{B.14}$$

where:

D	=	Diffusion coefficient of dissolving metal ions (cm^2/sec)
C_{M^+}	=	Dissolving metal ion concentration near crack mouth ($mole/cm^3$)

By assuming a linear concentration gradient of dissolving metal ions within the salt film, Eq. B.14 is reduced to:

$$D\frac{\partial C_{M^+}}{\partial x}\frac{\partial E_x}{\partial x} + D\frac{\partial^2 E_x}{\partial x^2} = 0 \qquad \text{(B.15)}$$

Then from Eq. A.9 in Appendix A and Eqs. B.3-B.4, we have:

$$D\frac{\partial C_{M^+}}{\partial x} = -J(x) = -\frac{i_{out}}{z\,F} \qquad \text{(B.16)}$$

$$\frac{\partial E_x}{\partial x} = -i_{out}\,R_{film} \qquad \text{(B.17)}$$

$$\frac{\partial^2 E_x}{\partial x^2} = -\frac{2\,i_c\,R_{film}}{\delta} \qquad \text{(B.18)}$$

By substituting Eqs. B.16-B.18 into Eq. B.15 and assuming that the salt film of crack mouth (adjacent to crack solution) is saturated with the dissolving metal ions, the gradient of electrochemical potential within the salt film can then be written as:

$$\frac{\partial E_x}{\partial x} = \sqrt{\frac{2\,D\,C^s_{M^+}\,z\,F\,i_c}{\delta}}\,R_{film} \qquad \text{(B.19)}$$

The outcome current flow at film/bulk-solution interface should be driven mainly (as assumed) by the gradient of electrochemical potential, thus for a semi-circular microcrack:

$$i_{out} = \frac{(E_{bulk} - E_{cm})}{2\,a\,R_{film}} \qquad \text{(B.20)}$$

By inserting Eq. B.20 into Eq. B.17 and then equating Eq. B.17 with Eq. B.19, the electrochemical potential at crack mouth (E_{cm}) can be computed according to:

$$E_{cm} = E_{bulk} + \sqrt{\frac{2\,D\,C^s_{M^+}\,z\,F\,i_c}{\delta}}\,2\,a\,R_{film} \qquad \text{(B.21)}$$

where:

J(x) = Dissolving metal ion flux (mole/cm^2 sec)

i_{out}	=	Outcome current density at film/bulk-solution interface (A/cm^2)
R_{film}	=	Salt-film resistance (Ω m)
C^s_{M+}	=	Saturation limit of dissolving metal ions ($mole/cm^3$)
E_{bulk}	=	Electrochemical potential in bulk solution (volt)

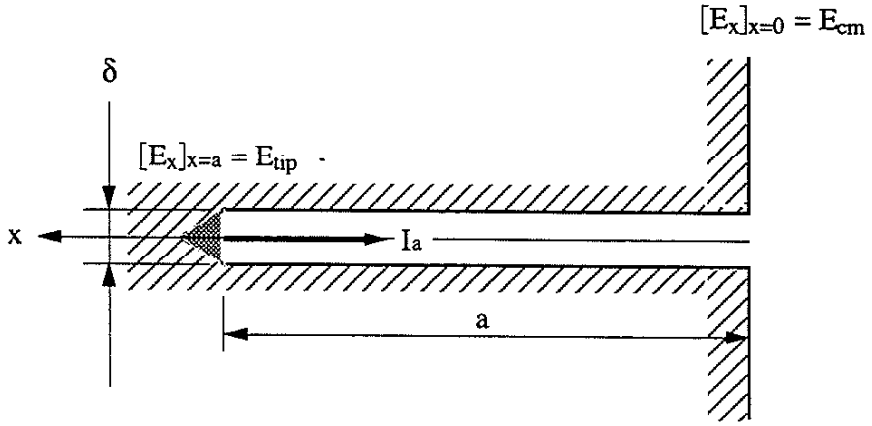

(a)

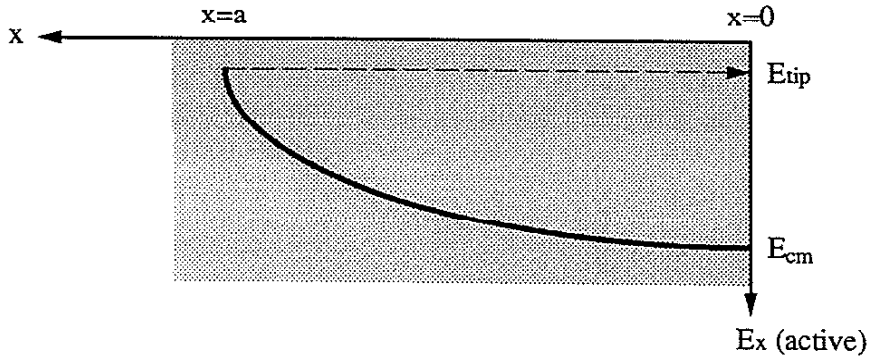

(b)

Figure B.1 Crack-tip dissolution and the gradient electrochemical potential within a microcrack:
(a) preferential dissolution of a microcrack tip;
(b) gradient of electrochemical potential across the microcrack.

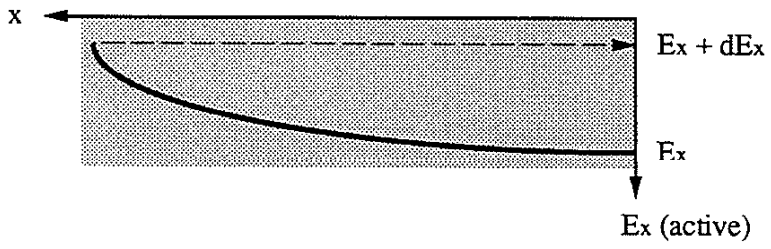

(a)

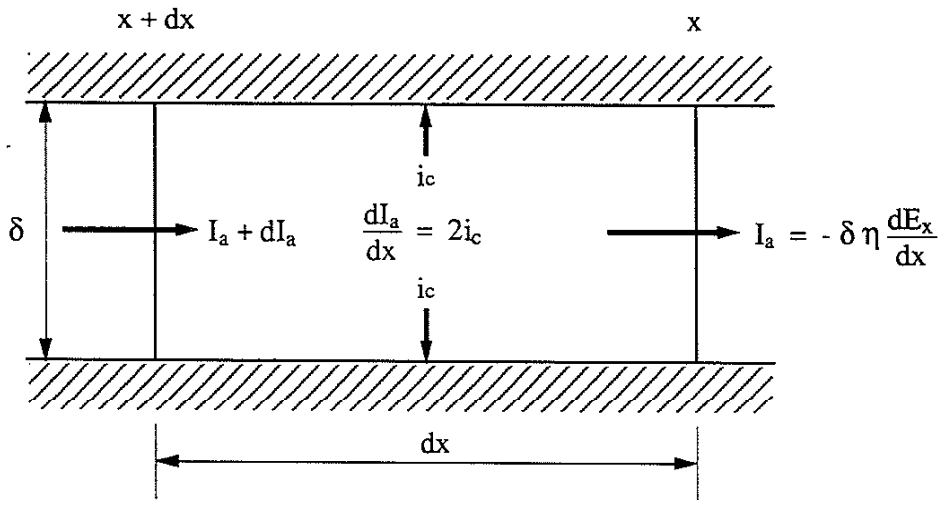

(b)

Figure B.2 Electromigration continuity within an infinitesimal crack segment:
(a) gradient of electrochemical potential across the crack segment;
(b) electromigration continuity of dissolution-charge carriers.

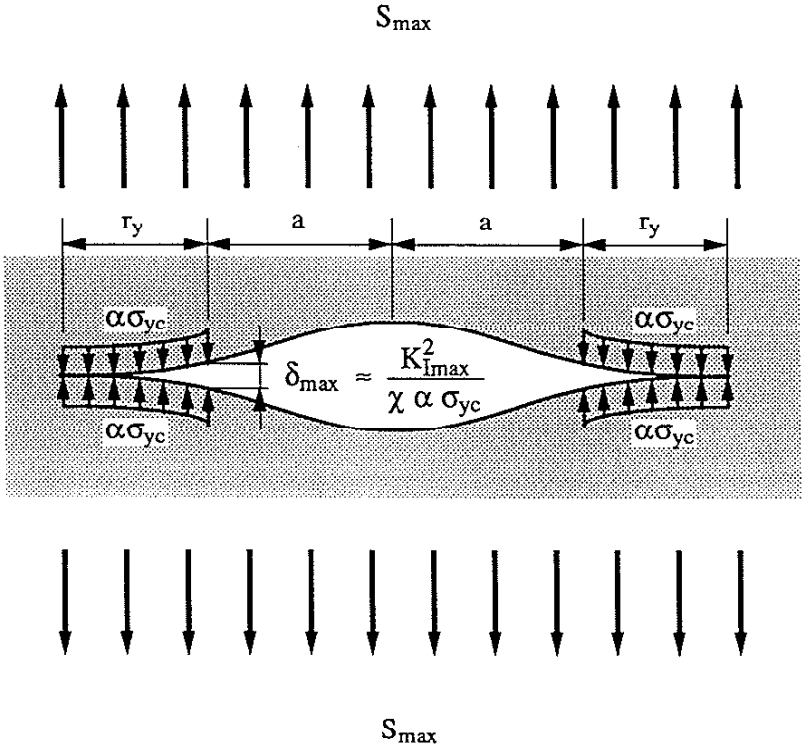

Figure B.3 The Dugdale strip-yield model [after 153]
(r_y is the size of plastic zone).

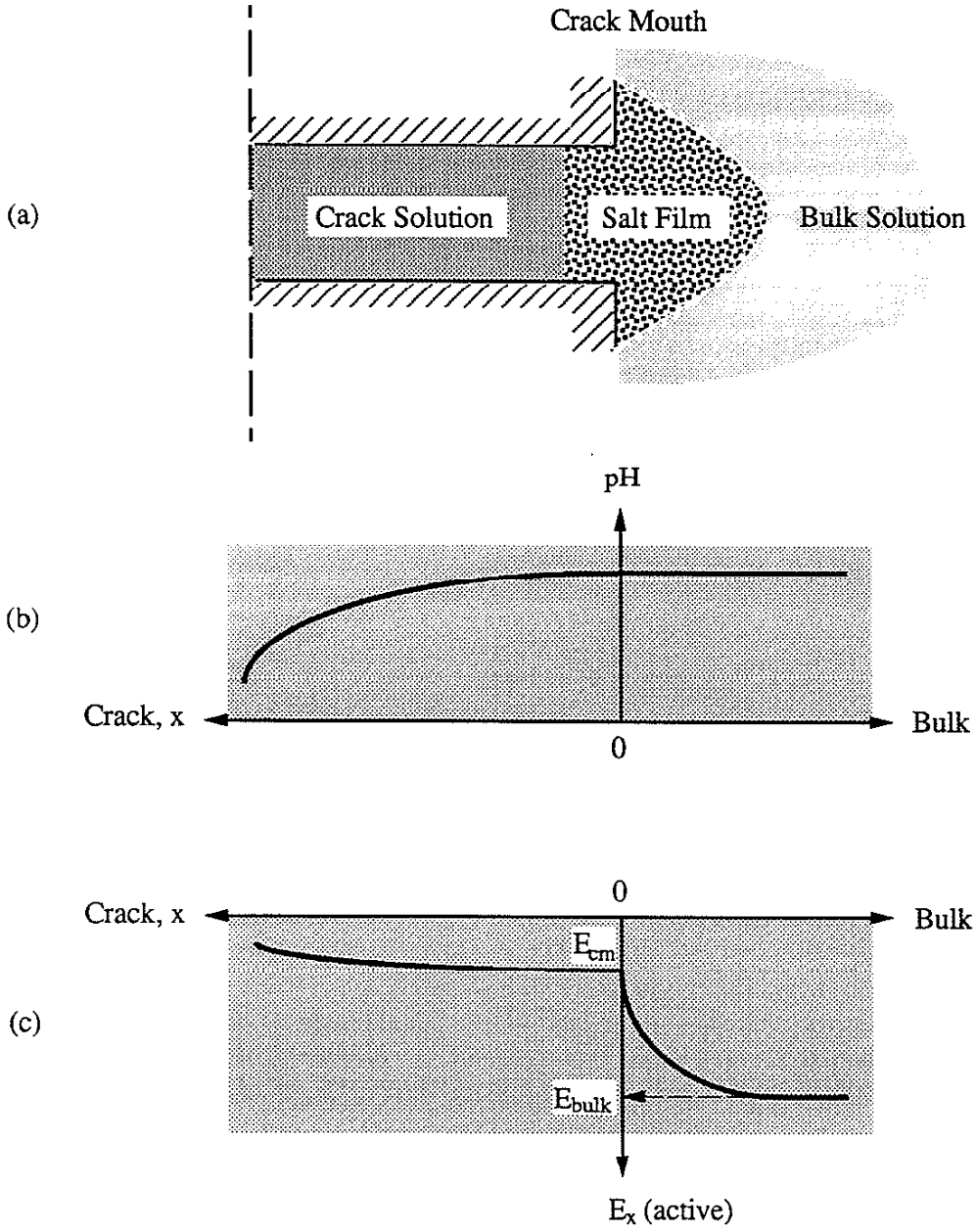

Figure B.4 Salt-film ohmic drop and crack-mouth potential:
(a) salt film at crack mouth; (b) pH profile;
(c) gradient of electrochemical potential at the entrance and in the interior of a microcrack.

APPENDIX C: DEGREE OF CFC SATURATION FOR CORROSION-ASSISTED MICROCRACK DEVELOPMENT

C.1 GENERAL

The following computation for the trace of crack-tip active area basically modifies the concept originally proposed by Masuda et al. [110]. Because the stress-corrosion cracking (SCC) is expected to be negligible for the corrosion-assisted microcrack development, only sinusoidal waveforms will be considered in the following modeling efforts.

C.2 MAXIMUM SURFACE AREA OF CRACK-TIP ACTIVE SITES (θ_{max}) AT PEAK LOAD

Assuming that the trace of rupture current density of crack-tip dissolution is closely related to the generation (slip process) and the diminishing (passivation) processes of crack-tip active sites [154] at the preferential dissolution zone ahead of a crack tip (see Fig. C.1), the surface area of crack-tip active sites at a given time instant ($t+\Delta t$) during loading reversal is given by:

$$\theta(t+\Delta t) \approx \theta(t) \exp(-\lambda \Delta t) + \mu \dot{\delta}_{tip} \Delta t \qquad (C.1)$$

where:

θ (t)	=	Trace of crack-tip active area (cm^2)
t	=	Time (sec)
λ	=	Current-density-decay exponent
μ	=	Proportional constant between active-site generation and crack-tip opening displacement
$\dot{\delta}_{tip}$	=	Crack-tip opening rate (mm/sec)
Δt	=	infinitesimal time increment (sec)

The crack-tip opening rate under a sinusoidal waveform loading can be approximated as:

$$\dot{\delta}_{tip} \approx 2 f (1 - R) \delta_{max} \qquad (C.2)$$

where:

f	=	Test frequency (1/sec)
R	=	Stress ratio of fatigue loading

δ_{max} = Crack-tip opening displacement at maximum applied stress (mm)

The infinitesimal change of crack-tip active area is thus:

$$d\theta(t) = \lim_{\Delta t \to 0} \left[\theta(t)\exp(-\lambda \Delta t) + 2 f \mu (1 - R) \delta_{max} \Delta t - \theta(t) \right] \quad (C.3)$$

To expand Eq. C.3 by Taylor's series, ignore high-order terms of Δt and then take a first-order derivative with respect to time (t), we get:

$$\frac{d\theta(t)}{dt} = -\lambda \theta(t) + 2 f \mu (1 - R) \delta_{max} \quad (C.4)$$

By solving Eq. C.4 with an initial condition: $\theta(t = 0) = 0$, the maximum surface area of crack-tip active sites (θ_{max}) corresponding to the bare-crack-tip current density (i_{bare}) at peak load becomes:

$$\theta_{max} = \theta(t = 1/2f) = \frac{2 f \mu (1 - R) \delta_{max}}{\lambda} \left[1 - \exp\left(-\frac{\lambda}{2 f} \right) \right] \quad (C.5)$$

C.3 SATURATED DIMINISHING PROCESS OF CRACK-TIP ACTIVE SITES

The diminishing rate of crack-tip active sites during unloading reversal can be obtained from a similar derivation. With an assumption of a fully irreversible slip process (an extreme case for a saturated corrosion fatigue) due to the presence of a corrosive environment, the diminishing rate of crack-tip active sites ($\theta^u_{sat}(t)$) during unloading reversal can be written as:

$$\frac{d\theta^u_{sat}(t)}{dt} = -\lambda \theta^u_{sat}(t) \quad (C.6)$$

The homogeneous solution of Eq. C.6 under an initial condition: $\theta^u_{sat}(t = 0) = \theta_{max}$ gives:

$$\theta^u_{sat}(t) = \theta_{max} \exp(-\lambda t) \quad (C.7)$$

where:

θ_{max} = Maximum surface area of crack-tip active sites (cm^2)

$\theta^{u}_{sat}(t)$ = Trace of crack-tip active area under a fully irreversible slip (saturated CFC) during unloading reversal (cm^2)

Eq. C.7 represents an extreme case in which a saturated corrosion fatigue has taken place. Under such a condition (e.g., low-frequency CFC), the operating reversible slip is so slow as allowing a fully corrosion attack to be accomplished before the close-up of crack walls. The reduction of crack-tip active sites owing solely to any reversible slip thus makes no significant contribution to the overall dissolution-current density at crack tips.

C.4 Partially-Saturated Diminishing Process of Crack-Tip Active Sites

Under usual circumstance in which only partially-saturated corrosion attack has taken place (e.g., high-frequency or low-temperature CFC), the reduction of crack-tip active sites due to reversible slip during unloading reversal can no longer be neglected but should contribute to the overall diminishing rate of crack-tip active area according to:

$$\frac{d\theta^{u}(t)}{dt} = -\lambda\,\theta^{u}(t) - 2f\mu(1-R)\delta_{max} \tag{C.8}$$

The solution of Eq. C.8 under an initial condition: $\theta^{u}(t=0) = \theta_{max}$ gives:

$$\theta^{u}(t) = \theta_{max}\exp(-\lambda t) - \frac{2f\mu(1-R)\delta_{max}}{\lambda}\left[1 - \exp(-\lambda t)\right] \tag{C.9}$$

Eq. C.9 would approach to null at a characteristic time (t_c) before unloading process completes. By setting Eq. C.9 to zero (as also given by Masuda et al. [110]), we express t_c and its limit as:

$$t_c = \frac{1}{\lambda}\ln\left(2 - \exp\left(-\frac{\lambda}{2f}\right)\right) \tag{C.10}$$

$$t_c \le \frac{1}{2f} \tag{C.11}$$

where:

$\theta^{u}(t)$ = Trace of crack-tip active area under a reversible slip (partially saturated CFC) during unloading reversal (cm^2)

t_c = Characteristic period from the onset of unloading to the complete disappearance of crack-tip active sites (sec)

C.5 DEGREE OF CFC SATURATION (φ)

The extent of crack-tip dissolution occurred within a fatigue cycle under a reversible slip process (partially-saturated CFC) can be evaluated by integrating the trace of crack-tip active area (Eq. C.9) within a duration of unloading from 0 to t_c:

$$\Theta = \int_0^{t_c} \theta^u(t)\,dt \tag{C.12}$$

or for simplicity, by integrating the trace of crack-tip active area in Eq. C.7 from 0 to t_c:

$$\Theta = \int_0^{t_c} \theta^u_{sat}(t)\,dt \tag{C.13}$$

For the case of a fully-irreversible slip process (a saturated CFC), area under the trace of Eq. C.7 within the whole duration of unloading reversal (see Fig. C.2) gives:

$$\Theta_{sat} = \int_0^{1/2f} \theta^u_{sat}(t)\,dt \tag{C.14}$$

The degree of CFC saturation (φ) during corrosion-assisted microcrack development can thus be defined as the ratio of the dissolution completed under partially saturated CFC process to which under a saturated CFC process as sketched in Fig. C.2. Therefore:

$$\varphi = \frac{\Theta}{\Theta_{sat}} \tag{C.15}$$

where:

Θ = Integrated surface area of crack-tip active sites under a reversible slip (partially saturated CFC) accumulated during unloading reversal (cm^2)

Θ_{sat} = Integrated surface area of crack-tip active sites under a fully irreversible slip (saturated CFC) accumulated during unloading reversal (cm^2)

φ = Degree of CFC saturation

After inserting Eqs. C.7, C.13, and C.14 into Eq. C.15, the degree of CFC saturation (φ) can then be written as:

$$\varphi = \frac{\left[1 - \exp\left(- \lambda t_c \right) \right]}{\left[1 - \exp\left(- \frac{\lambda}{2f} \right) \right]} \tag{C.16}$$

The degree of CFC saturation evaluated in Eq. C.16 has a value ranging from 0.5 to 1.0 for a fully-reversible slip ($\lambda = \infty$) and for a fully-irreversible slip process (saturated CFC, $\lambda = 0$, $t_c = 1/2f$), respectively. By combining Eq. C.16 with Eq. 3.12, Eq. 3.9 can then be explicitly expressed as:

$$\left(\frac{da}{dN} \right)_{pl} = \varphi \left(\frac{da}{dN} \right)_{cfc} = \frac{M\, i_{bare}}{z\, F\, \rho\, \lambda} \left(1 - \exp\left(- \lambda t_c \right) \right) \tag{C.17}$$

where:

$\left(\frac{da}{dN} \right)_{pl}$ = Rate of microcrack development (mm/cycle)

$\left(\frac{da}{dN} \right)_{cfc}$ = Crack growth rate from purely corrosion fatigue (mm/cycle)

M = Atomic weight of material (g/mole)

i_{bare} = Bare-crack-tip current density (A/cm^2)

z = Valence of dissolving cations

F = Faraday's constant (coulomb/mole)

ρ = Density of material (g/cm^3)

Eq. C.17 can be integrated into the modeling of the second CFC process (microcrack development) for simulating the corrosion-fatigue crack initiation at high test frequency (f), low fluid temperature (T), or in any other circumstances where a saturated CFC for the investigating systems does not likely to have been established.

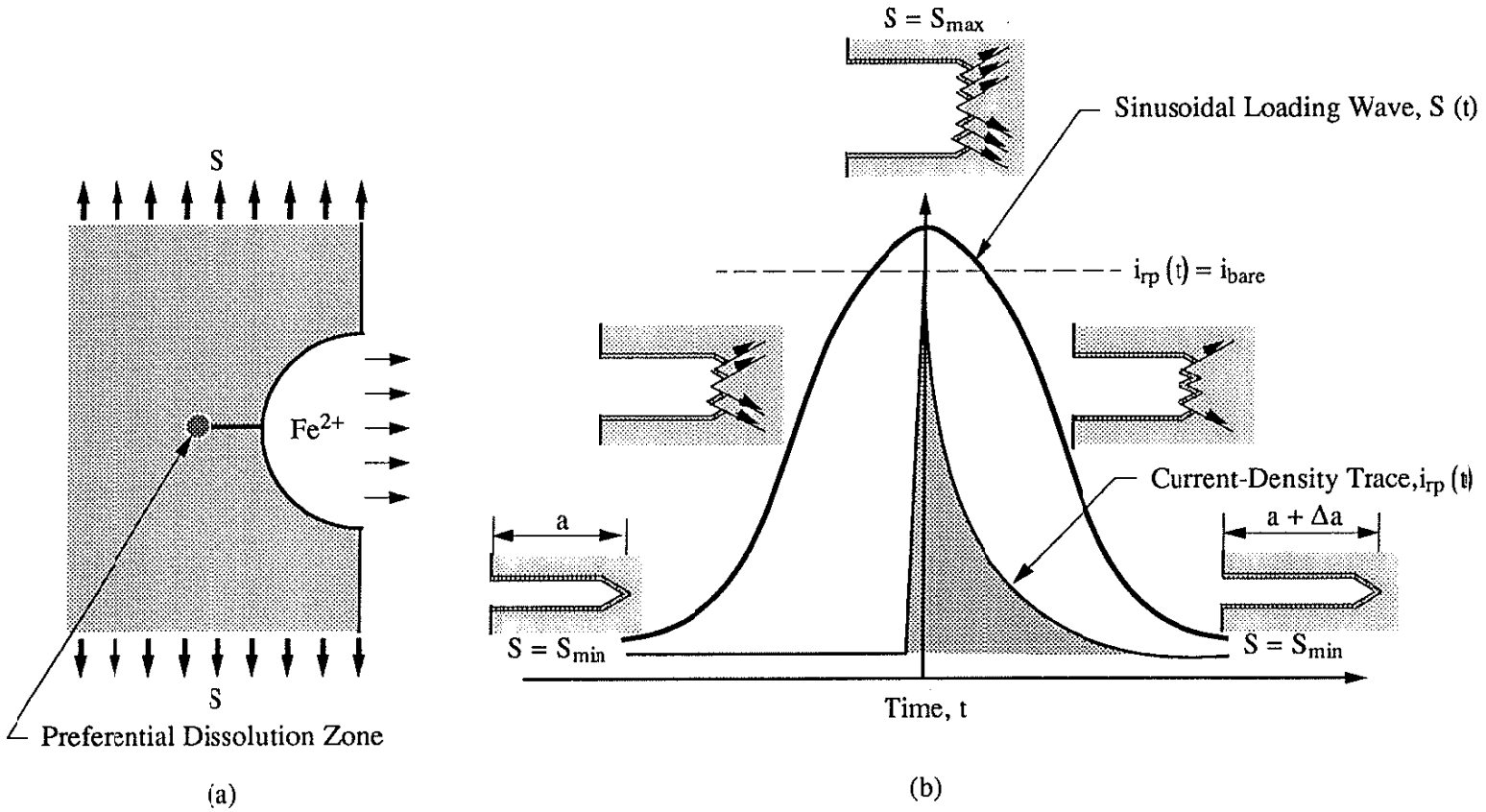

Figure C.1 Generaton of crack-tip active sites and the corrosion-assisted microcrack development:
(a) preferential dissolution zone at microcrack tip;
(b) generation of crack-tip active sites and the rupture current-density trace of crack-tip dissolution due to cyclic sinusoidal-waveform loading.

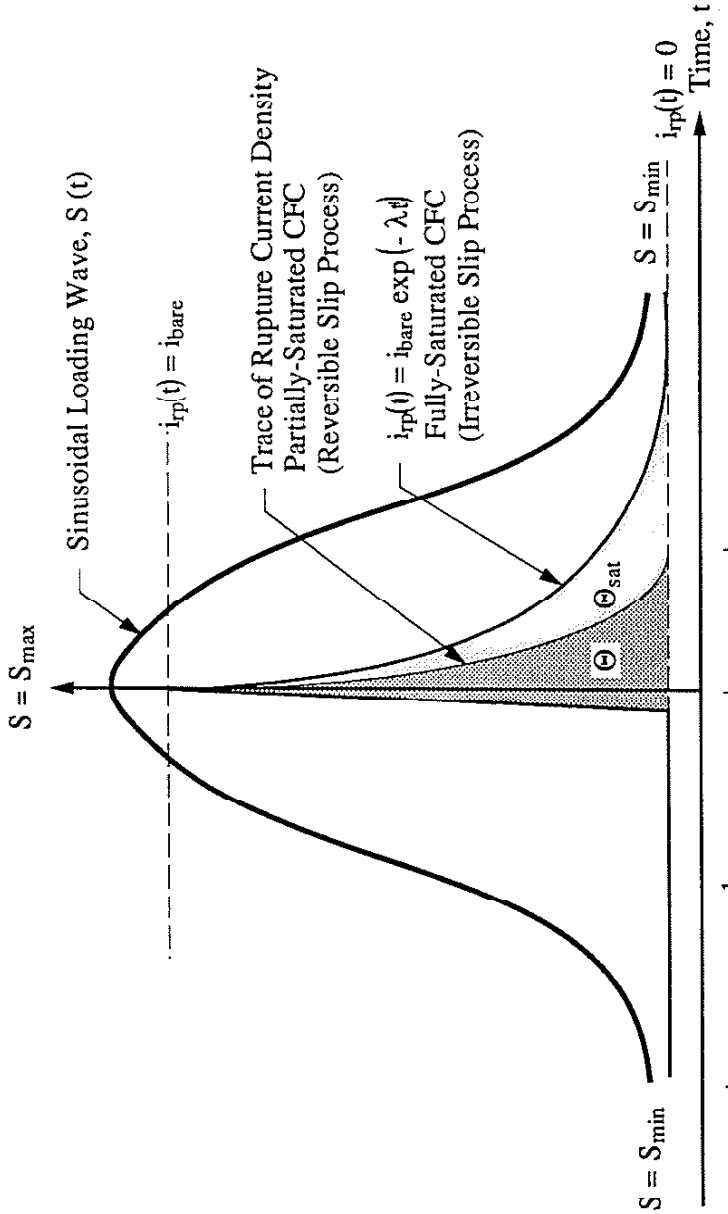

Figure C.2 Illustration of the rupture current-density trace of partially-saturated CFC for determining the degree of CFC saturation (Θ).

APPENDIX D: COMPUTATION OF SALT-FILM OHMIC-DROP COEFFICIENTS

D.1 BACKGROUND

Recalling Eq. B.21 in Appendix B:

$$E_{cm} = E_{bulk} + \sqrt{\frac{2\,D\,C^{s}_{M^+}\,z\,F\,i_c}{\delta}}\;2\,a\,R_{film} \qquad (B.21)$$

where:

E_{cm}	=	Electrochemical potential at crack mouth (volt)
E_{bulk}	=	Electrochemical potential in bulk solution (volt)
D	=	Diffusion coefficient of dissolving metal ions (cm^2/sec)
C^s_{M+}	=	Saturation limit of dissolving metal ions ($mole/cm^3$)
z	=	Valence of dissolving cations
F	=	Faraday's constant (coulomb/mole)
i_c	=	Cathodic current density at passivated crack faces (A/cm^2)
δ	=	Crack-tip opening displacement (cm)
a	=	Crack length (cm)
R_{film}	=	Electrolytic resistance of salt film (Ω cm)

Equation B.21 can be rewritten as:

$$E_{cm} = E_{bulk} + E_{\Omega}\left(\frac{a}{a_i}\right) \qquad (D.1)$$

$$E_{\Omega} = \sqrt{\frac{2\,D\,C^{s}_{M^+}\,z\,F\,i_c}{\delta}}\;2\,a_i\,R_{film} \qquad (D.2)$$

where:

E_{Ω}	=	Salt-Film Ohmic-Drop Coefficient (volt)
a_i	=	Initial crack length for LEFM integration (cm)

We calculate cathodic current density (i_c) by combining Eq. B.8 and Eq. B.9 as following:

$$i_c = i_o^{pass} \exp\left(\frac{2.3}{\beta_c}\left(E_{bulk} - E^{c}_{eq}\right)\right) \qquad (D.3)$$

where:

i_o^{pass}	=	Exchange current density of a cathodic reduction on passivated crack faces (A/cm^2)
E^c_{eq}	=	Redox potential of a cathodic redox couple (V)
β_c	=	Cathodic Tafel's slope on plastically-deformed passivated cathodes

The computation of salt-film ohmic-drop coefficients (E_Ω) will be illustrated in the following section for all corrosion-fatigue systems investigated in this study.

D.2 Salt-Film Ohmic-Drop Coefficients

For deaerated seawater drilling fluids at 93.3 °C, we have (refer to Table 5.3):

$\frac{D}{\delta} \approx 6.0 \times 10^{-6}$ (cm/sec) (assumed value for simplicity)

$C^s_{M^+} = 4.0 \times 10^{-3}$ (mole/cm^3)

$z = 2$

$F = 96500$ (coulomb/mole)

$a_i = 0.05$ (cm)

$R_{film} = 5500$ (Ω cm)

$i_o^{pass} = 1.0 \times 10^{-7}$ (A/cm^2)

$\beta_c = -0.18$

$E^c_{eq} = -0.37$ (V vs. SCE)

Case I: free corrosion in seawater drilling fluids at 93.3 °C

Under free-corrosion conditions, the electrochemical potential (E_{bulk}) at the onset of microcrack development is about -0.73 ~ -0.75 V (SCE). We calculate i_c and E_Ω using Eq. D.3 and Eq. D.2, respectively:

$i_c \approx 1.5 \times 10^{-5}$ (A/cm^2)

$E_\Omega = 0.19 \sim 0.20$ (V)

Case II: $E_{bulk} = -0.6$ V in deaerated seawater drilling fluid at 93.3 °C

$i_c \approx 1.9 \times 10^{-6}$ (A/cm^2)

$E_\Omega = 0.06 \sim 0.07$ (V)

Case III: E_{bulk} = -0.7 V in deaerated seawater drilling fluid at 93.3 °C

$i_c \approx 7.0 \times 10^{-6}$ (A/cm^2)

E_O = 0.13 ~ 0.14 (V)

Case IV: E_{bulk} = -0.8 V in deaerated seawater drilling fluid at 93.3 °C

$i_c \approx 3.0 \times 10^{-5}$ (A/cm^2)

E_O = 0.29 ~ 0.30 (V)

Case V: saline aqueous environments at ambient temperature (25 °C)

We have different electrochemical parameters for the effect of temperature (T) as tabulated in Table 5.4. They are:

β_c = -0.227

E^c_{eq} = -0.173 (V vs. SCE)

E_{bulk} = -0.55 ~ -0.56 (V)

Therefore:

$i_c \approx 6.0 \times 10^{-6}$ (A/cm^2)

E_O = 0.12 ~ 0.13 (V)

REFERENCES

[1] Congleton, J., Parkins, R. N., "Degradation of Mechanical Properties by Corrosion Fatigue", Proceeding of Institution of Mechanical Engineers, Vol. 203, Part C2, (1989), pp. 73-84.

[2] Turnbull, A., "Modeling of Environment Assisted Cracking", Corrosion Science, Vol. 34, No. 6, (1993), pp. 921-960.

[3] Ford, F. P., Emigh, P. W., "The Prediction of the Maximum Corrosion Fatigue Crack Propagation Rate in the Low Alloy Steel-Deoxygenated Water System at 288°C", Corrosion Science, Vol. 25, No. 8/9, (1985), pp. 673-692.

[4] Zhang, X. D., and Song, Y. J., "Crack Arrest Behaviour and a Proposed Model", International Journal of Fatigue, Vol. 13, No. 5, (1991), pp. 411-416.

[5] McAdam, D. J. Jr., and Geil, G. W., "Pitting and its Effect on the Fatigue Limit of Steels Corroded under Various Conditions", Proceedings of ASTM, Vol. 41, (1941), pp. 696-732.

[6] Ebara, R., Kai, T. and Inoue, K., "Corrosion-Fatigue Behavior of 13 Cr Stainless Steel in Sodium-Chloride Aqueous Solution and Steam Environment", Corrosion-Fatigue Technology, ASTM STP 642, H. L. Craig, Jr.,, T. W. Crooker, and D. W. Hoeppner, Eds., (1978), pp. 155-168.

[7] Kitagawa, H., Fujita, T., and Miyazawa, K., "Small Randomly Distributed Cracks in Corrosion", Corrosion-Fatigue Technology, ASTM STP 642, H. L. Craig, Jr.,, T. W. Crooker, and D. W. Hoeppner, Eds., (1976), pp. 98-114.

[8] Hoeppner, D. W., "Model for Prediction of Fatigue Lives Based Upon a Pitting Corrosion Fatigue Process", Fatigue Mechanisms, ASTM STP 675, J. T. Fong, Ed., (1979), pp. 841-870.

[9] Isaacs, H. S., "The Localized Breakdown and Repair of Passive Surfaces During Pitting", Corrosion Science, Vol. 29, No. 23, (1989), pp. 313-323.

[10] Jones, D. A., "Localized Corrosion", Chapter 4, Corrosion Process, R. N. Parkins, Ed., Applied Science Publishers, (1982), pp. 161-207.

[11] Wranglen, G., "Review Article on the Influence of Sulphide Inclusions on the Corrodibility of Fe and Steel", Corrosion Science, Vol. 9, No. 8, (1969), pp. 585-602.

[12] Boukerrou, A., Cottis, R. A., "Crack Initiation in the Corrosion Fatigue of Structural Steels in Salt Solutions", Corrosion Science, Vol. 35, No. 1-4, (1993), pp. 577-585.

[13] Szklarska-Smialowska, Z., "Review of Literature on Pitting Corrosion Published Since 1960", Corrosion-NACE, Vol. 27, No. 6, (1971), pp. 223-233.

[14] Pourbaix, M., "The Electrochemical Basis for Localized Corrosion", U. R. Evans Conference on Localized Corrosion NACE-3, R. W. Staehle, B. F. Brown, J. Kruger, and A. Agrawal, Eds., (1974), pp. 12-33.

[15] Parkins, R. N., "Environment Sensitive Fracture and its Prevention", British Corrosion Journal, Vol. 14, No. 1, (1979), pp. 5-14.

[16] Briant, C. L., "Brittle Failures Caused by Atomic Species- II: Hydrogen Embrittlement", Chapter 4, Metallurgical Aspects of Environmental Failures, Elsevier Science Publishing Company INC., (1985), pp. 71-94.

[17] Asayama, Y., Ibaragi, M., and Kawase, Y., "Delayed Failure of PH13-8Mo Steel plated with Al-IVD", Metallurgical Transactions, Vol. 22A, No. 12, (1991), pp. 2935-2945.

[18] Ray, G. P., Jarman, R. A., and Thomas, J.G.N., "Some Aspects of Crack Initiation in Mild Steel under Corrosion-Fatigue Condition", Journal of Material Science, Vol. 29, No. 1:1, (1994), pp. 47-53.

[19] Simmons, G. W., Pao, P. S., and Wei, R. P., "Fracture Mechanics and Surface Chemistry Studies of Subcritical Crack Growth in AISI 4340 Steel", Metallurgical Transactions A, Vol. 9A, No. 8, (1978), pp. 1147-1158.

[20] Hancock, G. G., and Johnson, H. H., "Hydrogen, Oxygen, and Subcritical Crack Growth in a High-Strength Steel", Transactions of the Metallurgical Society of AIME, Vol. 236, No. 4, (1966), pp. 513-516.

[21] Gangloff, R. P., "Crack Size Effects on the Chemical Driving Force for Aqueous Corrosion Fatigue", Metallurgical Transaction A, Vol. 16, No. 5, (1985), pp. 953-969.

[22] Ouchi, H., Kobayashi, J., Soya, I., and Okamota, K., "Fatigue Crack Growth in a High Tensile Strength in Seawater and Several Other Environments", ISIJ International, Vol. 34, No. 5, (1994), pp. 451-459.

[23] Laird, C. and Duquette, D. J., "Mechanisms of Fatigue Crack Nucleation", Corrosion Fatigue: Chemistry, Mechanics and Microstructure, NACE International Corrosion Conference Series, A. J. McEvily, and R. W. Staehle, Eds., (1972), pp. 88-117.

[24] Duquette, D. J., "Environmental Effects I: General Fatigue Resistance and Crack Nucleation in Metals and Alloys", Fatigue and Microstructure, ASM, (1979), pp. 335-363.

[25] Duquette, D. J., "A Mechanistic Understanding of the Effects of Environment on fatigue Crack Initiation and Propagation", Environment-Sensitive Fracture of Engineering Materials, Proceedings of Symposium of the Metallurgical Society of AIME, Z. A. Foroulis, Ed., (1979), pp. 521-537.

[26] Lynch, S. P., "Mechanisms of Fatigue and Environmental Assisted Fatigue", Fatigue Mechanisms, ASTM STP 675, J. T. Fong, Ed., (1979), pp. 174-213.

[27] Müller, M., "Theoretical Considerations on Corrosion Fatigue Crack Initiation", Metallurgical Transactions A, Vol. 13A, No. 4, (1982), pp. 649-655.

[28] Daeubler, M. A., Warren, G. W., Bernstein, I. M., and Thompson, A. W., "Modeling of Corrosion Fatigue Crack Initiation under Passive Electrochemical Conditions", Metallurgical Transactions A, Vol. 22A, No. 2, (1991), pp. 521-529.

[29] Markfield, A., Ph.D. Thesis, UMIST (1986).

[30] Jaske, C. E., Payer, J. H., and Balint, V. S., "Background for Corrosion Fatigue in Marine Environments", Corrosion Fatigue of Metals in Marine Environments Chapter 2, Metals and Ceramics Information Center, Battelle Memorial Institute, (1981), pp. 3-34.

[31] Turnbull, A., Dolphin, A. S., and Rackley, F. A., "Experimental Determination of the Electrochemistry in Corrosion-Fatigue Cracks in Structural Steel in Artificial Seawater", Corrosion-NACE, Vol. 44, No. 1, (1988), pp. 55-61.

[32] Turnbull, A., Ferriss, D. H., "Mathematical Modeling of the Electrochemistry in Corrosion Fatigue Cracks in Steel Corroding in Marine Environments", Corrosion Science, Vol. 27, No. 12, (1987), pp. 1323-1350.

[33] Turnbull, A., "Theoretical Analysis of Influence of Crack Dimensions and Geometry on Mass Transport in Corrosion-Fatigue Cracks", Material Science and Technology, Vol. 1, No. 9, (1985), pp. 700-710.

[34] Smith, J. A., Peterson, M. H., and Brown, B. F., "Electrochemical Conditions at the Tip of an Advancing Stress Corrosion Crack in AISI 4340 Steel", Corrosion-NACE, Vol. 26, No. 12, (1970), pp. 539-542.

[35] En-Hou, H., and Wei, K., "Chemical and Electrochemical Conditions within Corrosion Fatigue Cracks", Corrosion Science, Vol. 35, No. 1-4, (1993), pp. 599-610.

[36] Deluccia, J. J., "Electrochemical Aspects of Hydrogen in Metals", Hydrogen Embrittlement: Prevention and Control, ASTM STP 962, L. Raymond, Ed., (1988), pp. 17-34.

[37] Wei, R. P., "Electrochemical Considerations of Crack Growth in Ferrous Alloys", Advances in Fracture Research, Vol. 2, 7th International Conference on Fracture, K. Salama, K. Ravi-Chandar, D. M. R. Taplin, P. R. Rao, Eds., (1989), pp. 1525-1544.

[38] Wei, R. P. and Gangloff, R. P., "Environmentally Assisted Crack Growth in Structural Alloys: Perspectives and New Directions", Fracture Mechanics, Perspective and Directions, ASTM STP 1020, R. P. Wei, R. P. Gangloff, Eds., (1989), pp. 233-264.

[39] Gangloff, R. P., and Turnbull, A., "Crack Electrochemistry Modeling and Fracture Mechanics Measurement of the Hydrogen Embrittlement Threshold in Steel", Modeling Environmental Effects on Crack Growth Process, Proceedings of a Symposium Sponsored by the Metallurgical Society in Toronto, Canada, R. H. Jones, and W. W. Gerberich, Eds., (1985), pp. 55-81.

[40] Scott, P. M., Thorpe, T. W., and Silvester, D. R. V., "Rate-Determining Processes for Corrosion Fatigue Growth in Ferritic Steels in Seawater", Corrosion Science, Vol. 23, No. 6, (1983), pp. 559-575.

[41] Birnbaum, H. K., "Mechanisms of Hydrogen-Related Fracture of Metals", Environment-Induced Cracking of Metals, R. P. Gangloff, and M. B. Ives, Eds., NACE, (1990), pp. 21-30.

[42] Lynch, S. P., "Environmentally Assisted Cracking: Overview of Evidence for an Adsorption-Induced Localized Slip Process", Journal of Material Science, Vol. 21, No. 2, (1986), pp. 692-704.

[43] Sullivan, A. M. and Crooker, T. W., "Fatigue Crack Growth in A516-60 Steel - Effects of Specimen Thickness, Saline Environment, and Electrochemical Potential", Proceedings of International Conference on Fracture Mechanics and Technology, Vol. 1, (1977), pp. 687-698.

[44] Vosikovsky, O., "Fatigue-Crack Growth in an X-65 Line-Pipe Steel at Low Cyclic Frequencies in Aqueous Environments", Journal of Engineering Material and Technology, ASME Transaction, Vol. 97, No. 4, (1975), pp. 298-304.

[45] Vosikovsky, O., "Effects of Stress Ratio on Fatigue Crack Growth Rates in X70 Pipeline Steel in Air and Saltwater", Journal of Testing and Evaluation, Vol. 8, No. 2, (1980), pp. 68-73.

[46] Vosikovsky, O, "Frequency, Stress Ratio, and Potential Effects on Fatigue Crack Growth of HY-130 Steel in Salt Water", Journal of Testing and Evaluation, Vol. 6, No. 3, (1978), pp. 175-182.

[47] Fujii, C. T., and Smith, J. A., "Environmental Influences on the Aqueous Fatigue Crack Growth Rates of HY-130 Steel", Corrosion Fatigue, ASTM STP 801, T. W. Crooker, and B. N. Leis, Eds., (1983), pp. 390-402.

[48] Kitagawa, H., "A Fracture Mechanics Approach to Ordinary Corrosion Fatigue of Unnotched Steel Specimens", Corrosion Fatigue: Chemistry, Mechanics and Microstructure, NACE International Corrosion Conference Series, A. J. McEvily, and R. W. Staehle, Eds., (1972), pp. 521-528.

[49] Ishiguro, T., "Corrosion Fatigue Strength of Steels for Marine Structures", Nippon Steel Technical Report, Vol. 9, (1977), pp. 27-36.

[50] Lee, H. H., and Uhlig, H. H., "Corrosion Fatigue of Type 4140 High Strength Steel", Metallurgical Transaction, Vol. 3, No. 11, (1972), pp. 2949-2957.

[51] Endo, K., Komai, K., and Imashiro, N., "Environmental Effects on Initiation and Propagation of Fatigue Cracks in High Strength Structural Steel", Bulletin, Japanese Society of Mechanical Engineers, Vol. 20, No. 143, (1977), pp. 513-520.

[52] Masumoto, I., Akaishi, T., "Study of Corrosion Fatigue of Steel Plates and Welded Joints in 3% NaCl Aqueous Solution - 2nd Report: Effect of Grain Size and Cementite Configuration of Steels on the Corrosion Fatigue of Steel", Journal of Japan Welding Society, Vol. 44, No. 9, (1975), pp. 734-738.

[53] Congleton, J., and Craig, I. H., "Corrosion Fatigue", Chapter 5 of Corrosion Process, R. N. Parkins, Ed., Applied Science Publishers, (1982), pp. 209-269.

[54] Jaske, C. E., Broek, D., Slater, J. E., and Anderson, W. E., "Corrosion Fatigue of Structural Steels in Seawater and for Offshore Applications", Corrosion-Fatigue Technology, ASTM STP 642, H. L. Craig, Jr.,, T. W. Crooker, and D. W. Hoeppner, Eds., (1978), pp. 19-47.

[55] Endo, K., Miyao, Y., "Effects of Cyclic Frequency on the Corrosion Fatigue Strength", Bulletin, Japanese Society of Mechanical Engineers, Vol. 1, (1958), pp. 374-380.

[56] Endo, K., Komai, K., and Nakagaki, K., "Plastic Strain Fatigue of High Tensile Strength Steel in Corrosive Media", Bulletin, Japanese Society of Mechanical Engineers, Vol. 11, No. 47, (1968), pp. 791-797.

[57] Pettit, D. E., Hoeppner, D. W., and Hyler, W. S., "Evaluation of Methods to Alleviate Corrosion Fatigue in Type 135 Drill-Pipe Steel for Offshore-Drilling Applications", Effects of Environment and Complex Load History on fatigue Life, ASTM STP 462, (1970), pp. 241-257.

[58] Endo, K., and Komai, K., "Influence of Secondary Stress Fluctuations of Small Amplitude on Low-Cycle Corrosion Fatigue", Corrosion-Fatigue Technology, ASTM STP 642, H. L. Craig, T. W. Crooker, and D. W. Hoeppner, Eds., (1978), pp. 74-97.

[59] Endo, K., Komai, K., "Effects of Stress Wave Form and Cycle Frequency on Low Cycle Corrosion Fatigue", Corrosion Fatigue: Chemistry, Mechanics and Microstructure, NACE International Corrosion Conference Series, A. J., McEvily, and R. W. Staehle, Eds., (1972), pp. 437-450.

[60] Gould, A. J., "The Influence of Temperature on the Severity of Corrosion Fatigue", Engineering, Vol. 141, May 8, (1936), pp. 495-496.

[61] Dugdale, D. S., "Corrosion Fatigue of Sharply Notched Steel Specimens", Metallurgica, Jan., (1972), pp. 27-28.

[62] Watanabe, M., and Mukai, Y., "Corrosion Fatigue Properties of Structural Steel and its Welded Joints in Sea Water - Properties under High Amplitude and Slow Rate of Cyclic Stressing", Proceedings of International Conference on Welding in Offshore Constructions, Welding Institute, Abington, Vol. 1, (1974), pp. 46-53.

[63] Jolliff, J. V., and Thiruvengadam, A., "Effect of Hydrostatic Pressure on Corrosion-Fatigue at High Frequency", ASME Transactions, Journal of Engineering for Industry, Series B, Vol. 96, No. 3, (1974), pp. 1085-1088.

[64] Duquette, D. J., and Uhlig, H. H., "Effect of Dissolved Oxygen and NaCl on Corrosion Fatigue of 0.18% Carbon Steel", Transactions of the ASM, Vol. 61, (1968), pp. 449-456.

[65] Masumoto, I., and Akaishi, T., "Study on Corrosion Fatigue of Steel Plates and Welded Joints in 3% NaCl Aqueous Solution - Report 3", Journal of Japan Welding Society, Vol. 44, No. 10, (1975), pp. 822-825.

[66] Velden, R., Ewalds, H. L., Schultze, W. A., and Punter, A., "Anomalous Fatigue Crack Growth Retardation in Steels for Offshore Application", Corrosion Fatigue, ASTM STP 801, T. W. Crooker, and B. N. Leis, Eds., (1983), pp. 64-80.

[67] Duquette, D. J., and Uhlig, H. H., "The Critical Reaction Rate for Corrosion Fatigue of 0.18% Carbon Steel and the Effect of pH", ASM Transactions, Vol. 62, (1969), pp. 839-845.

[68] Radd, F. J., Crowder, L. H., and Wolfe, L. H., "Effect of pH in the Range 6.6-14.0 on the Aerobic Corrosion Fatigue of Steel", Corrosion-NACE, Vol. 16, No. 8, (1960), pp. 415-418.

[69] Nichols, J. L., "Cathodic Protection Reduces Corrosion Fatigue Cracking of Steel in Sea Water", Material Protection, Vol. 2, No. 2, (1963), pp. 46-53.

[70] Hudgins, C. M., Jr., Casad, B. M., Schroeder, R. L., and Patton, C. C., "The Effect of Cathodic Protection on the Corrosion Fatigue Behavior of Carbon Steel in Synthetic Sea Water", Journal of Petroleum Technology, Vol. 23, No. 3, (1971), pp. 283-293.

[71] Hooper, W. C., and Hartt, W. H., "The Influence of Cathodic Polarization upon Fatigue of Notched Structural Steel in Seawater", Corrosion-NACE, Vol. 34, No. 9, (1978), pp. 320-323.

[72] Hartt, W. H., Martin, P. E., and Hooper, W. C., "Endurance Limit Enhancement of Notched 1018 Steel in Sea Water - Specimen Size and Frequency Effects", Corrosion-NACE, Vol. 36, No. 3, (1980), pp. 107-112.

[73] Wacker, G. A., "Effects of Marine Environment on High-Strength Steels", ASTM STP 445, (1969), pp. 68-87.

[74] Vassilaros, M. G., and Czyryca, E. J., "Low-Cycle Fatigue Crack Initiation in HY-130 System Metals; Effects of Marine Environments, Cathodic Protection, Frequency, and Hold-Time", Research and Development Report MAT-77-57, (1977).

[75] Hutchings, J., and Sanderson, G., "The Influence of Tempering Temperature, Minor Alloying Elements, and Cathodic Polarization on the Low Frequency Fatigue Resistance of 18% Ni Maraging Steel", Corrosion Science, Vol. 16, No. 8, (1976), pp. 545-549.

[76] Kirk, W. W., Covert, R. A., and May, T. P., "Corrosion Behavior of High-Strength Steels in Marine Environments", Metal Engineering Quartly, Vol. 8, No. 4, (1968), pp. 31-38.

[77] Taniguchi, K., Oda, T., Ueda, S., and Nakajima, M., "Development of New High Strength Special Steel Propeller for Big Ship", Japan Shipbuilding and Marine Engineering, Jan. (1969), pp. 20-28.

[78] Nishioka, K., Hirakawa, K., and Kitaura, I., "Low Frequency Corrosion Fatigue Strength of Steel Plate", The Sumitomo Search, No. 16, (1976), pp. 40-54.

[79] Levy, M., and Morrossi, J. L., "Corrosion-Fatigue Behavior of Coated 4340 Steel for Blade Retention Bolts of the AH-1 Helicopter", ASTM STP 642, H. L. Craig, Jr., T. W. Crooker, and D. W. Hoeppner, Eds., (1978), pp. 300-312.

[80] Ratcliffe, M. L., "Corrosion Fatigue and Air Fatigue Tests on 85-Ton Aircraft Steel", National Engineering Laboratory Report 38/60, (1961).

[81] Congleton, J. H., Craig, I. H., Denton, B. K., and Parkins, R. N., "Crack Growth in HY80 and HY130 Steels by Corrosion Fatigue", Metal Science, Vol. 13, No. 7, (1979), pp. 436-443.

[82] Scott, P. M., "Chemistry Effects in Corrosion Fatigue", Corrosion Fatigue, ASTM STP 801, T. W. Crooker, and B. N. Leis, Eds., (1983), pp. 319-350.

[83] Murakami, R., and Ferguson, W. G., "The Effects of Cathodic Potential and Calcareous Deposits on Corrosion Fatigue Crack Growth Rate in Seawater for Two

Offshore Structural Steels", Fatigue and Fracture of Engineering Materials and Structures, Vol. 9, No. 6, (1987), pp. 477-488.

[84] Li, M.-Q., Wei, Z.-W., Zhang, F.-S., and Tang, J.-Q., "The Corrosion Fatigue of Medium Strength Structural Steels", Corrosion Science, Vol. 34, No. 9, (1993), pp. 1403-1410.

[85] Ritchie, R. O., "Role of the Environment in Near-Threshold Fatigue Crack Growth in Engineering Materials", Environment-Sensitive Fracture of Engineering Materials, Proceeding of Symposium of AIME, Z. A. Foroulis, Ed., (1979), pp. 538-563.

[86] Thomas, J. P., and Wei, R. P., "Corrosion Fatigue Crack Growth of Steels in Aqueous Solutions I: Experimental Results and Modeling the Effects of Frequency and Temperature", Material Science and Engineering, Vol. A159, No, 2, (1992), pp. 205-221.

[87] Kawai, S., and Koibuchi, "Effect of Waveform on Corrosion Fatigue Crack Growth", Fatigue of Engineering Materials and Structures, Vol. 1, No. 4, (1979), pp. 395-407.

[88] Barsom, J. M., "Effect of Cyclic Stress Form on Corrosion Fatigue Crack Propagation Below K_{Iscc} in a High Yield Strength Steel", Corrosion Fatigue: Chemistry, Mechanics and Microstructure, NACE International Corrosion Conference Series, A. J., McEvily, and R. W. Staehle, Eds., (1972), pp. 424-436.

[89] Yokobori, A. T., Yokobori, T., Kosumi, T., and Takasu, N., "Effects of Frequency, Stress Rising Time and Stress Holding Time on Corrosion Fatigue Crack Growth Behaviour of Low Alloy Cr-Mo Steel", Corrosion Cracking, Conference Proceedings, ASM, V. S. Goel, Ed., (1986), pp. 1-9.

[90] Miller, G. A., Hudak, S. J., and Wei, R. P., "The Influence of Loading Variables on Environment-Enhanced Fatigue Crack Growth in High Strength Steels", Journal of Testing and Evaluation, Vol. 1, No. 11, (1973), pp. 524-531.

[91] Yokobori, A. T., Jr., Chiba, N., Yamada, T., Kosumi, T., and Yokobori, T., "Effect of Stress Rising, Holding and Descending Time on fatigue Crack Growth in a Corrosive Environment", Fracture Mechanics, Current Japanese Materials Research, Vol. 8, H. Okamura, and K. Ogura, Eds., (1991), pp. 125-143.

[92] Bardal, E., Sondenfor, J. M., and Gartland, P. O., "Slow Corrosion Fatigue Crack Growth in a Structural Steel in Artificial Sea Water at Different Potentials, Crack Depths and Loading Frequencies", Proceedings of Offshore Steels Conference, Welding Institute, England, (1978), pp. 415-438.

[93] Jones, B. F., "The Influence of Crack Depth on the Fatigue Crack Propagation Rate for a Marine Steel in Seawater", Journal of Material Science, Vol. 17, No. 2, (1982), pp. 499-507.

[94] Nakai, Y., Tanaka, K., and Wei, R. P., "Short-Crack Growth in Corrosion Fatigue for a High Strength Steel", Engineering Fracture Mechanics, Vol. 24, No. 3, (1986), pp. 433-444.

[95] Tanaka, K., and Wei, R. P., "Growth of Short Fatigue Cracks in HY-130 Steel in 3.5% NaCl Solution", Engineering Fracture Mechanics, Vol. 21, No. 2, (1985), pp. 293-305.

[96] Johnson, R., Bretherton, I., Tomkins, B., Scott, P. M., and Silvester, D. R. V., "The Effect of Sea Water Corrosion in Fatigue Crack Propagation in Structural Steel", Proceedings of Offshore Steels Conference, Welding Institute, England, Nov., (1978), pp. 387-414.

[97] Ryder, J. T., Gallagher, J. P., "Temperature Influence on Corrosion Fatigue Behavior of 5Ni-Cr-Mo-V Steel", Journal of Testing and Evaluation, Vol. 2, No. 3, (1974), pp. 180-189.

[98] Ryder, J. T., "Temperature Characterization of the Below K_{Iscc} Corrosion Fatigue Behavior of HY-130 Steel", Ph.D. Thesis, University of Illinois at Urbana-Champaign, (1972).

[99] Scott, P. M., and Silvester, D. R. V., "The Influence of Seawater on Fatigue Crack Propagation Rates in Structural Steel", Department of Energy, UK Offshore Steels Research Project, Interim Technical Report UKOSRP 3/03, (1975).

[100] Misawa, T., and Kobayashi, Y., "Effect of pH on Corrosion Fatigue Crack Propagation in a Low Carbon Steel", Boshoku Gijutsu, Vol. 25, No. 8, (1976), pp. 493-497.

[101] Austen, I. M., West, J. M., and Brook, R., "Corrosion Fatigue in Nickel Steels", Metal Science, Vol. 12, No. 2, (1978), pp. 77-82.

[102] Bogar, F. D., and Crooker, T. W., "Influence on Bulk-Solution-Chemistry Conditions on Marine Corrosion-Fatigue Crack Growth Rate", Journal of Testing and Evaluation, Vol. 7, No. 3, (1979), pp. 155-159.

[103] Crooker, T. W., Bogar, F. D., and Cares, W. R., "Effects of Flowing Natural Seawater and Electrochemical Potential on Fatigue-Crack Growth in Several High-Strength Marine Alloys", Corrosion Fatigue, Technology ASTM STP 642, H. L. Craig, Jr., T. W. Crooker, and D. W. Hoeppner, Eds., (1978), pp. 189-201.

[104] Kondo, Y., "Prediction of Fatigue Crack Initiation Life Based on Pit Growth", Corrosion, Vol. 45, No. 1, (1989), pp. 7-11.

[105] Wei, R. P., "On Understanding Environment Enhanced Fatigue Crack Growth - A Fundamental Approach", Fatigue Mechanisms, ASTM STP 675, J. T. Fong, Ed., (1979), pp. 816-840.

[106] Duquette, D. J., "Fundamental of Corrosion Fatigue Behaviors of Metals and Alloys", Hydrogen Embrittlement and Stress Corrosion Cracking, R. Gibala, and R. F. Hehemann, Eds., ASM, (1984), pp. 249-270.

[107] Weiss, M. P., "Estimating Fatigue Cracks from the Onset of Loading in Smooth AISI 4340 Specimens under Cyclic Stresses", International Journal of Fatigue, Vol. 14, No. 2, (1992), pp. 91-96.

[108] Imhof, E. J., and Barsom, J. M., "Fatigue and Corrosion Fatigue Crack Growth of 4340 Steel at Various Yield Strengths", Progress in Flaw Growth and Fracture Toughness Testing, ASTM STP 536, (1973), pp. 182-205.

[109] Wei, R. P., Gao, M., "Reconstruction of the Superposition Model for Environmentally Assisted Fatigue Crack Growth", Scripta Metallurgica, Vol. 17, (1983), pp. 959-962.

[110] Masuda, H., Matsuoka, S., Nishijima, S., and Shimodaria, M., "The Role of Corrosion in Fatigue Crack Propagation for Structural Alloys in 3% NaCl Solution", Corrosion Science, Vol. 28, No. 5, (1988), pp. 433-447.

[111] Harlow, D. G., Wei, R. P., "A Mechanistically Based Approach to Probability Modeling for Corrosion Fatigue Crack Growth", Engineering Fracture Mechanics, Vol. 45, No. 1, (1993), pp. 79-88.

[112] Choi, D. and Was, G. S., "Development of a Pit Growth Resistance Parameter for the Study of Pit Growth in Alloy 600", Corrosion, Vol. 48, No. 4, (1992), pp. 292-296.

[113] Hashimoto, M., Miyajima, S., and Murata, T., "An Experimental Study of Potential Fluctuation During Passive Film Breakdown and Repair on Iron", Corrosion Science, Vol. 33, No. 6, (1992), pp. 905-915.

[114] Rollins, V., Arnold, B., Lardner, E., "Corrosion Fatigue in High Carbon Steel", British Corrosion Journal, Vol. 5, No. 1, (1970), pp. 33-40.

[115] Ting, C.-H., and Lawrence, F. V., "A Model for the Long-Life Fatigue Behavior of Small Notches", Ph.D. Thesis, University of Illinois at Urbana-Champaign, (1991).

[116] Hagn, L., "Life Time Prediction for Parts in Corrosion Environments", Corrosion in Power Generating Equipment, (1983).

[117] Ahn, S.-H., Lawrence, F. V., and Metzger, M. M., "Corrosion Fatigue of an HSLA Steel", Fatigue & Fracture of Engineering Materials and Structures, Vol. 15, No. 7, (1992), pp. 625-642.

[118] Newman, J. C., Phillips, E. P., Swain, M. H., and Everett, R. A., "Fatigue Mechanics: an Assessment of a Unified Approach to Life Prediction", Advances in Fatigue Life Predictive Techniques, ASTM STP 1122, M. R. Mitchell, and R. W. Laudgraf, Eds., (1992), pp. 5-27.

[119] Saxena, A., Wilson, W. K., Roth, L. D., and Liaw, P. K., "The Behavior of Small Fatigue Cracks at Notches in Corrosive Environments", International Journal of Fracture, Vol. 28, No. 2, (1985), pp. 69-82.

[120] Barbosa, M., "A Model for the Kinetics of Repassivation I-Straining Electrodes", Corrosion, Vol. 43, No. 5, (1987), pp. 309-318.

[121] Bannantine, J. A., Comer, J. J., and Handrock, J. L., "Fundamentals of Metal Fatigue Analysis", Prentice Hall, (1990).

[122] Ishihara, S., Shiozawa, K., Miyao, K., and Miwa, H., "Computer Simulation of Corrosion Fatigue Process Considering Stress Relaxation Due to Initiation and Propagation of Multiple Cracks", JSME-International Journal, Series I, Vol. 35, No. 1, (1992), pp. 78-83.

[123] Nevill, B. T., "An Alternative to Cadmium: Ion Vapor Deposition of Aluminum", Plating and Surface Finishing, Jan., (1993), pp. 14-19.

[124] Ahmed, N. A. G., "Ion Plating: Optimum Surface Performance and Material Conservation", Thin Solid Films, Vol. 241, (1994), pp. 179-187.

[125] Technical Report on Fatigue Properties, Journal the Society of Automotive Engineers, Feb. (1975).

[126] Itoh, Y. Z. and Kashiwaya, H., "Low-Cycle Fatigue Properties of Steels and Their Weld Metals", Journal of Engineering Materials and Technology, Vol. 111, No. 10, (1989), pp. 431-437.

[127] Kang, K. J., Song, J. H., and Earmme, Y. Y., "Fatigue Crack Growth and Closure Through a Tensile Residual Stress Field under Compressive Applied Loading", Fatigue and Fracture of Engineering Materials and Structures, Vol. 12, No. 5, (1989), pp. 363-376.

[128] Bethune, A. J. and Loud, N. S., Standard Electrode Potentials and Temperature Coefficients at 25 °C, Clifford A. Hampel, (1964).

[129] Stern, M., "The Electrochemical Behavior, Including Hydrogen Overvoltage, of Iron in Acid Environment", Journal of Electrochemical Society, Vol. 102, No. 11, (1955), pp. 609-616.

[130] Beck, T. R., and Chan, S. G., "Experimental Observations and Analysis of Hydrodynamic Effects on Growth of Small Pits", Corrosion-NACE, Vol. 37, No. 11, (1981), pp. 665-671.

[131] Kuo, H. C. and Landolt, D., "Rotating Disk Electrode Study of Anodic Dissolution or iron in Concentrated Chloride Media", Electrochimica Acta, Vol. 20, (1975), pp. 393-399.

[132] Simonen, E. P., Jones, R. H., and Danielson, M. J., "Predicted Salt Film Formation Effects on Stage I Stress Corrosion Cracking of Anodically Polarized Nickel", Corrosion Science, Vol. 34, No. 6, (1993), pp. 899-914.

[133] Stulen, F. B., and Schulte, W. C., "The Fatigue Analysis of the Mohole Drill Pipe and Associated Problems", Report No. C-2951, Curtiss Division, Curtiss-Wright Corp., (1965).

[134] Schuetz, A. E., Hyler, W. S., Jackson, L. R., and Boyd, W. K., "A Study of Fatigue and Other Related Problems Associated with Drill Pipe and Casing Materials for Project Mohole", Summary Report to Brown & Root, Inc., Battelle Memorial Institute, (1964).

[135] Hoeppner, D. W., Groeneveld, T. P., Keppenhafer, A. C., Hyler, W. S., and Elsea, A. R., "A Study of Fatigue and Other Related Problems Associated with Drill Pipe and Casing Materials for Project Mohole", Summary Report II to Brown & Root, Inc., Battelle Memorial Institute, (1964).

[136] Iwai, Y., Eya, H., Itoh, Y., Arai, Y., and Takeuchi, K., "Measurement and Correlation of Solubilities of Oxygen in Aqueous Solutions Containing Salts and Sucrose", Fluid Phase Equilibria, Vol. 83, Feb., (1993), pp. 271-278.

[137] Kautek W., "The Galvanic Corrosion of Steel Coatings: Aluminum in Comparison to Cadmium and Zinc", Corrosion Science, Vol. 28, No. 2, (1988), pp. 173-199.

[138] Soboyejo, W. O., Knott, J. F., "An Investigation of Environmental Effects on Fatigue Crack Growth in Q1N (HY80) Steel", Metallurgical Transactions A, Vol. 21A, No. 11, (1990), pp. 2977-2983.

[139] Wilhelm, S. M., "Galvanic Corrosion Caused by Corrosion Products", Galvanic Corrosion, ASTM STP 978, H. P. Hack, Ed., (1988), pp. 23-34.

[140] Thomas, J. P., and Wei, R. P., "Corrosion Fatigue Crack Growth of Steels in Aqueous Solutions II: Modeling the Effects of ΔK", Material Science and Engineering, Vol. A159, No. 2, (1992), pp. 223-229.

[141] Buck, O., and Ranjan, R., "Evaluation of a Crack-Tip-Opening Displacement Model under Stress-Corrosion Conditions", Modeling Environmental Effects on Crack Growth Process, R. H. Jones, and Gerberich, W .W., Eds., (1986), pp. 209-223.

[142] Sato, E., and Murata, T., "Effect of Chloride ion on Straining Electrode Behavior of Austenitic Stainless Steel", Corrosion, Vol. 46, No. 11, (1990), pp. 921-923.

[143] Funk, A. G., Giddings, J. C., Christensen, C. J., and Eyring, H., "Strain Electrometry and Corrosion I. General Considerations on Interfacial Electrical Transients", National Academy of Science, Vol. 43, (1957), pp. 421-429.

[144] Funk, A. G., Chakravarty, D. N., Eyring, H., and Christensen, C. J., "Strain Electrometry, Corrosion and Catalysis III. The Iron Electrode", Zeitschrift Fur Physikalische Chemie, Vol. 15, (1958), pp. 67-74.

[145] Giddings, J. C., Funk, A. G., Christensen, C. J., and Eyring, H., "Strain Electrometry and Corrosion, IV Film Properties and Strain Potential", Journal of Electrochemical Society, Vol. 106, No. 2, (1959), pp. 91-95.

[146] Bard, A. J., and Faulkner, L. R, "Electrochemical Methods, Fundamentals and Applications", John Wiley & Sons, (1980).

[147] Tester, J. W., and Isaacs, H. S., "Diffusional Effects in Simulated Localized Corrosion", Journal of Electrochemistry Society, Vol. 122, No. 11, (1975), pp. 1438-1445.

[148] Kitagawa, H., Tsuji, K., Hisada, T., and Hashimoto, Y., "An Analysis of Random Pits in Corrosion Fatigue: A Statistical Three-Dimensional Evaluation of an Irregularly Corroded Surface", Corrosion Fatigue, ASTM STP 801, T. W. Crooker, and B. N. Leis, Eds., (1983), pp. 147-158.

[149] Ishihara, S., Shiozawa, K., Miyao, K., and Inoue, M., "Effects of Fluid Flow Rate and Stress Amplitude on the Initiation and Growth Behavior of Corrosion Pits on an Annealed Carbon Steel", JSME International Journal, Series I, Vol. 35, No. 3, (1992), pp. 367-373.

[150] Doig, P., and Flewitt, P.E.J., "The Significance of External Polarization on Stress Corrosion Crack Growth by Anodic Dissolution", Corrosion, Vol. 37, No. 7, (1981), pp. 378-383.

[151] Doig, P., and Flewitt, P.E.J., "The Influence of Crack Length on Stress Corrosion Crack Velocity", Metallurgical Transactions A, Vol. 14A, No. 5, (1983), pp. 978-983.

[152] Melville, P. H., "Variation of Potential in Stress Corrosion Cracks", British Corrosion Journal, Vol. 14, No. 1, (1979), pp. 15-19.

[153] Hellan, K., Introduction to Fracture Mechanics, McGraw-Hill Book Company, (1984).

[154] Hoar, T. P., and West, J. M., "Mechano-Chemical Anodic Dissolution of Austenitic Stainless Steel in Hot Chloride Solution", Proceedings Royal Society of London, Series A, Vol. 268, No. 1334, (1962), pp. 304-315.